

UNIVERSITY OF PADOVA

DEPARTMENT OF INDUSTRIAL ENGINEERING (DII)

MASTER THESIS IN MECHANICAL ENGINEERING

**APPLICATION OF LOCAL APPROACHES BASED ON NSIFs
CALCULATED WITH THE PSM ON A STEEL TUBE-TUBE
JOINT UNDER COMBINED LOADING**

Supervisor: Prof. Giovanni Meneghetti, Prof. Michael Vormwald

Co-supervisor: Eng. Alberto Campagnolo

Candidate: Giulio Nante

ACADEMIC YEAR 2017/2018

To my parents

INDEX

SUMMARY:	5
CHAPTER 1:	7
Fatigue of weld ends under combined loading	7
1.1 Introduction	7
1.2 Nomenclature.....	8
1.3 Specimens and testing	9
1.3 Collected data	12
1.4 Results	22
1.5 The out-of-phase effect	23
1.6 The EESH approach	23
1.6.1 Evaluation of result.....	25
1.7 The SSCH approach	27
1.8 The NuMeSiS approach	36
1.9 A new combined approach.....	38
1.10 Application to testing data	39
CHAPTER 2:	43
The NSIF approach	43
2.1 Recall of linear elastic fracture mechanics.....	43
2.2 Fatigue of welded joints: from a nominal approach to a local one based on NSIFs	50
2.3 The strain energy density (SED) approach.....	52
2.4 The Peak Stress Method (PSM).....	54
2.5 A link between the Peak Stress Method and the averaged value of the local strain energy density (SED)	59
2.6 Design scatter bands according to PSM.....	61
2.7 Fatigue assessments with the Peak Stress Method.....	63
2.7 The equivalent peak stress in special cases.....	66
CHAPTER 3:	71
Application of the Peak Stress Method to steel welded joints.	71
3.1 introduction	71
3.2 Experimental data	72
3.3 FEM models to estimate the Mode I NSIF precisely.	74
3.4 Evaluation of results	87
3.5 FEM models to estimate the approximated Mode I NSIF value using the Peak Stress Method (PSM).....	90
3.6 Evaluation of results.....	95

CHAPTER 4:	99
Application of the Peak Stress Method to the welded joint	99
4.1 Axis symmetric model	99
4.2 Idealised 3D weld geometry	109
4.3 CAD model creation	112
4.4 FEM Mainmodel creation	116
4.5 FEM Submodel creation	124
4.6 Validation of results with SED approach.....	138
4.7 Procedure flow chart	146
4.8 Comparison of experimental results with PSM-design scatter bands.....	147
CONCLUSIONS:	153
REFERENCES:	155
APPENDIX:	159
ACKNOWLEDGMENTS:	167

SUMMARY

The aim of this thesis is to verify the effectiveness of the Peak Stress Method (PSM) on a welded steel tube-tube joint under combined loading. The experimental data, provided by Vormwald in terms of applied loads and cycles to failure, have been evaluated in terms of equivalent peak stress and compared with PSM design scatter bands.

The procedure necessary to do that is particularly challenging and it requires to face up to a lot of issues. First, the experimental data considers a lot of different scenarios: stress-relieved and as-welded specimens, uni-axial and multiaxial cases with two different biaxiality ratio, two different cycle ratios and also in-phase and out-of-phase loading conditions.

In chapter one, the specimens' geometry and experimental data were analysed and discussed in order to re-obtain the published SN curves and to calculate the ranges of the applied stresses on the inner tube, because this is where the loads will be applied in the Finite Elements Analysis (FEA). Furthermore, it was investigated the method proposed by Vormwald to take into account the out-of-phase effect in the calculation of the equivalent stress. In fact, theoretically this effect would result in a fatigue life reduction and it is important to understand if it is negligible or not in this case, because the Peak Stress Method does not consider it and potentially could lead to unreliable results.

In chapter two, the linear elastic fracture mechanics (LEFM) was recalled to introduce the local approach based on the Notch Stress Intensity Factors (NSIFs) to properly study the stress state around a sharp V-notch. Then, the focus switches to an energetic approach, using the NSIFs values to calculate the Strain Energy Density (SED) that brings the possibility to compare the fatigue life of notches with different opening angles. The next step is introducing the Peak Stress Method, that allows an easy and rapid calculation of the Notch Stress Intensity Factors (NSIFs) and recalling the SED definition it results in the formulation of the equivalent peak stress. Eventually, the equivalent peak stress design scatter bands are presented and these will be resumed in the end of the thesis to verify if the Peak stress Method is effective in this particular case.

In chapter three, an application of the Peak Stress Method to cruciform specimens is presented, to underline how this approach makes it possible to calculate the NSIFs with FE meshes far less refined. In addition, several experimental data given in terms of nominal stress range were evaluated in terms of equivalent peak stress and compared with the design scatter bands.

In chapter four, the core of the thesis is discussed, first with 2D models, then with 3D ones characterized by articulated and complex shapes. At the beginning, to study the state of tension around the root tip, two axis-symmetric geometries were modelled and solved, one for the pure axial loading condition and the other for the torsional case. The next step is the description of the 3D CAD creation and its analysis with the Ansys software. The extraction of the equivalent peak stresses of both loading cases has required several FEM models and a lot of procedures aimed to their validations. These extracted values are necessary to evaluate the experimental data in terms of equivalent peak stress and make a comparison with the design scatter bands.

In the end of the thesis, the result of all operations, here briefly discussed, will be shown in a single SN diagram, but it has not to be forgotten that a lot of different factors are taken into account and the outcome could have a lot of different explanations.

CHAPTER 1:

Fatigue of weld ends under combined loading

1.1 Introduction

Nowadays an interesting topic of research is represented by fatigue behaviour of weld ends under multi-axial load conditions. The automotive industry is committed in discovering the fatigue life of some welded parts, like steel tube-tube joints that were analysed by Shams and Vormwald in [1]. In this research project it has been taken into account not only the geometrical and statistical size effect but also the out-of-phase effects on fatigue strength using a multi-axial criterion. In literature it is known that in case of a discontinuous welding the critical zone is represented by the weld start and end points. This kind of failure happens in the fatigue application, due to the notch effect, and in order to be avoided the knowledge of S-N curves is strictly necessary. However, these curves are known only in uniaxial cases and rely on an idealized model obtained by a high precision 3D-scanning with notch radii of $r_{toe}=0,20$ mm and $r_{root}=0,05$ mm. The corresponding fatigue lives and hence the S-N curves were determined experimentally. Today different S-N curves are assigned to weld toe and weld root failure scenarios. Shams and Vormwald work, [1], proposed a method to develop S-N curves valid for the determination of fatigue life of weld ends under multi-axial loading conditions.

1.2 Nomenclature

a_w	Throat thickness	δ	Phase shift
A_ψ	Corresponding surface to the node ψ	κ	Weibull exponent
$d_{a,1}$	External diameter of inner tube	λ	Ratio of semi-axes of ellipses
$d_{a,2}$	External diameter of outer tube	ρ	Non proportionality parameter
F_\perp	Normal force	ρ^*	Micro-structural length
$I_{A,ref}$	Highly stressed reference surface	σ_a	Nominal normal stress amplitude
I_{A,ρ^*}	Stress integral based on effective stress	σ_{eq}	Equivalent stress
k	Slope of S-N curve	σ_x	Normal stress in x direction
l_w	Weld length	σ_y	Normal stress in y direction
r_{root}	Radius at weld root	$\sigma_{\rho^*,SSCH}$	Effective stress including out-of-phase effects
r_{toe}	Radius at weld toe	$\sigma_{\rho^*,\kappa}$	Weighted effective stress
R	Load ratio	$\sigma_{\rho^*,\psi}$	Effective stress
$s(x, y, z)$	Direction of highest stress gradient	τ_a	Nominal shear stress amplitude
t_1	Thickness of inner tube	τ_{xy}	Shear stress
t_2	Thickness of outer tube	ψ	Node on a critical surface
σ_w	Normal stress referring to the weld throat area	$\Delta\sigma_n$	Range of normal stress referring to the inner tube
τ_w	Shear stress referring to the weld throat area	$\Delta\tau_n$	Range of shear stress referring to the inner tube

1.3 Specimens and testing

The experimental part of this research involved 16 series of tests (in total 142 tests) with tube-tube joints under pure axial force, pure torsional moment and combined in-phase as well as out-of-phase loadings. Specimens consisted in welded tube-tube joints from fine-grained and engineering steels (outer tube: S340+N and inner tube: E355+N) under constant amplitude loading in the range of 10^4 – $5 \cdot 10^6$ cycles to failure. The 490 mm-long test specimen consists of two tubes with an overlap length of 60 mm. The external diameters of the inner and outer tubes are $d_{a,1} = 40$ mm and $d_{a,2} = 45$ mm, respectively. The inner tube has a sheet thickness of $t_1 = 2.0$ mm; while the sheet thickness of the outer tube is $t_2 = 2.5$ mm. Two seam welds at opposing quadrants joined the two tubes, see Fig. 1.1. The tube-tube joints were manufactured using gas shielded metal arc welding. The welding was carried out in a twin-robot system, where two robots work simultaneously.

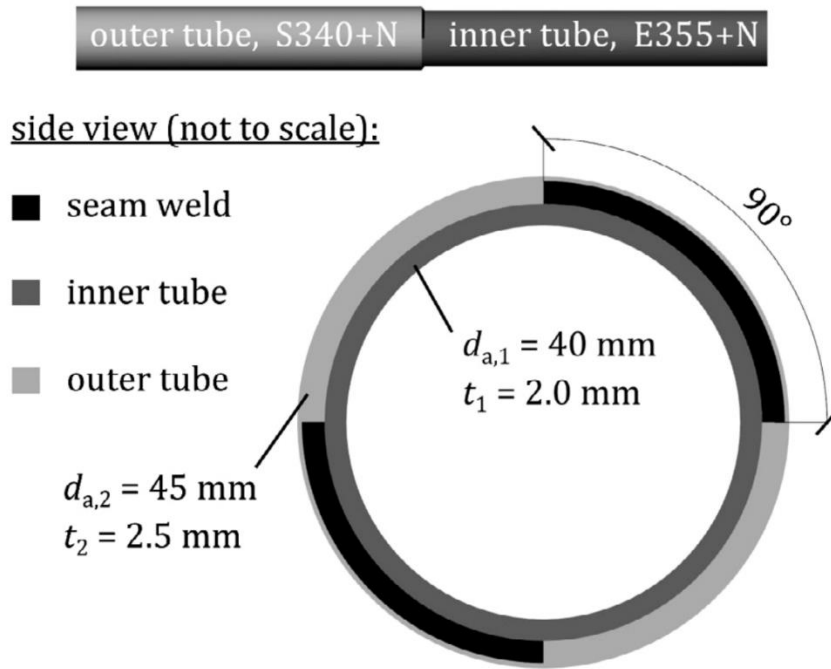


Figure 1.1: Overlapped tube-tube specimen [1].

Regarding the applied loads, in the case of combined loading two ratios were considered for the torsional moment to the axial force amplitudes $M_{t,a}/F_{\perp,a}$. This ratio assumes two values: 28 Nm/kN and 17.9 Nm/kN. Herein, dimensionless ratios expressed by nominal stress amplitudes τ_a/σ_a are also given. The normal stress is calculated from the value of axial force considering the weld throat area, fig 1.2:

$$\sigma_w = \frac{F_{\perp}}{2 a_w l_w} \quad (1.1)$$

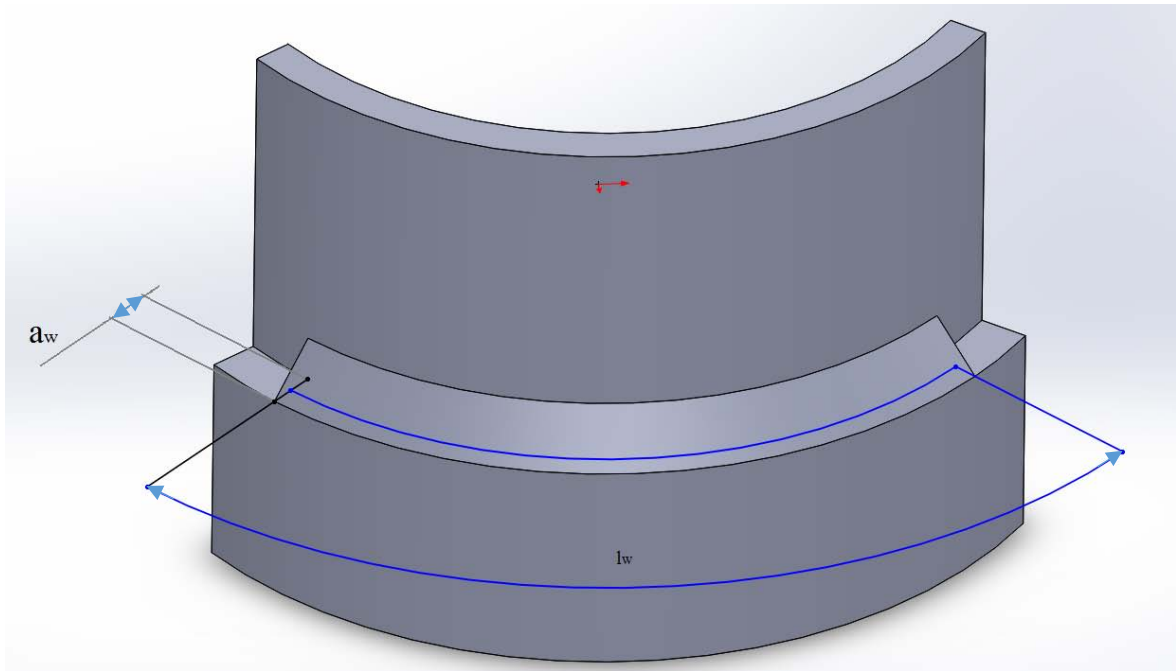


Figure 1.2: Rough weld idealized model.

Furthermore, considering a couple of forces producing the torsional moment, the shear stress could be derived from equation:

$$\tau_w = \frac{M_T}{d_{a,1} a_w l_w} \quad (1.2)$$

Finally, considering $d_{a,1} = 40$ mm, the ratio between shear stress and normal stress results:

$$\frac{\tau_w}{\sigma_w} = \frac{1}{20 \text{ mm}} \frac{M_T}{F_{\perp}} \quad (1.3)$$

Taking into account this last expression it results that a ratio $M_{t,a}/F_{\perp,a}$ of 28 Nm/kN corresponds to a τ_a/σ_a equal to 1.4; while, with a $M_{t,a}/F_{\perp,a}$ of 17.9 Nm/kN, the stress ratio results 0.895.

The experiments have been conducted using a servo-hydraulic multi-axial test rig with testing frequencies of 8–10 Hz for uniaxial and 1–2 Hz for multiaxial loading conditions. The experimental set-up is depicted in Fig. 1.3.

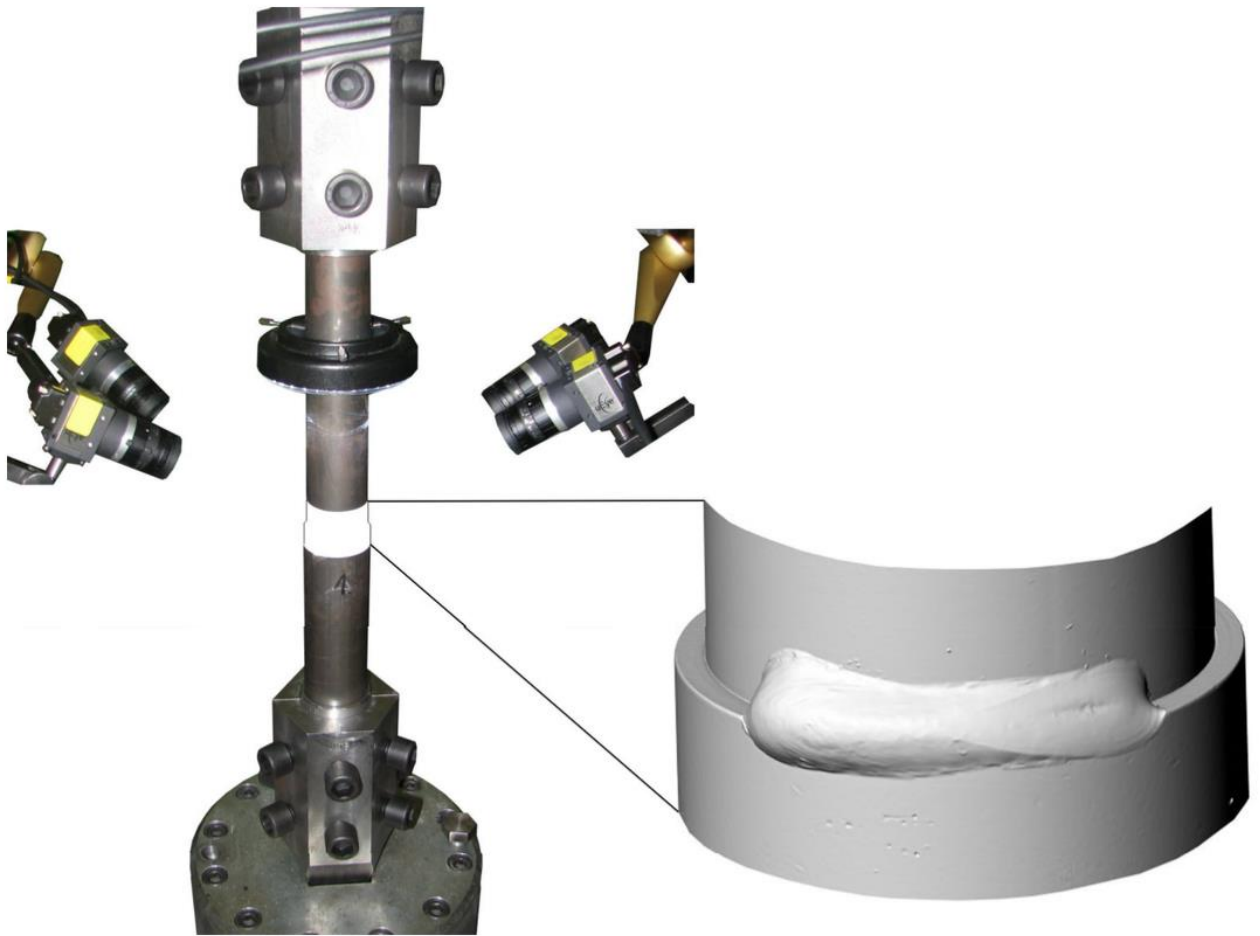


Figure 1.3: Experimental set-up (a), scan of the weld (b), [1].

Prior to testing, the specimens were sprayed using a scan spray in order to ease the optical detectability of both formation and growth of fatigue cracks after the test. During testing, the fatigue cracks were monitored by taking photographs of the four existing weld start and end points at predefined numbers of cycles. If predefined upper and lower limits for deformation values were exceeded, the experiment was terminated.

The failure criterion was established setting limits for deformation values to ± 8 mm and ± 5 degrees. The corresponding number of cycles was considered to plot the data in the S-N space.

1.3 Collected data

In the following tables all the series are represented, making a distinction in terms of condition and nominal load ratio. In particular, any effect of residual welding stresses in series 01–12 is excluded because all specimens were stress-relieved by heat treatment (600 C° for 6 h and followed by slow cooling) prior to testing. Furthermore, four test series (series 13–16) were not exposed to any heat treatment, so that they have been tested in an as-welded condition in order to investigate the influence of residual stresses on fatigue resistance. In series 01-06 a load ratio R equal to zero is considered, while in the others R is always -1. In-phase as well as out-of-phase loading conditions have been considered, and the phase value will be indicated with the letter δ and expressed in degrees.

Regression lines are added for a 50% probability of survival.

Series	Condition	R	δ	M_T/F_{\perp} [Nm/kN]	τ_w/σ_w	Number of specimens
01	Stress-relieved	0	-	-	-	12
02	Stress-relieved	0	-	-	-	12
03	Stress-relieved	0	0°	28.0	1.40	12
04	Stress-relieved	0	0°	17.9	0.895	12
05	Stress-relieved	0	90°	28.0	1.40	12
06	Stress-relieved	0	90°	17.9	0.895	12

Table 1.1: Test program series 01-06.

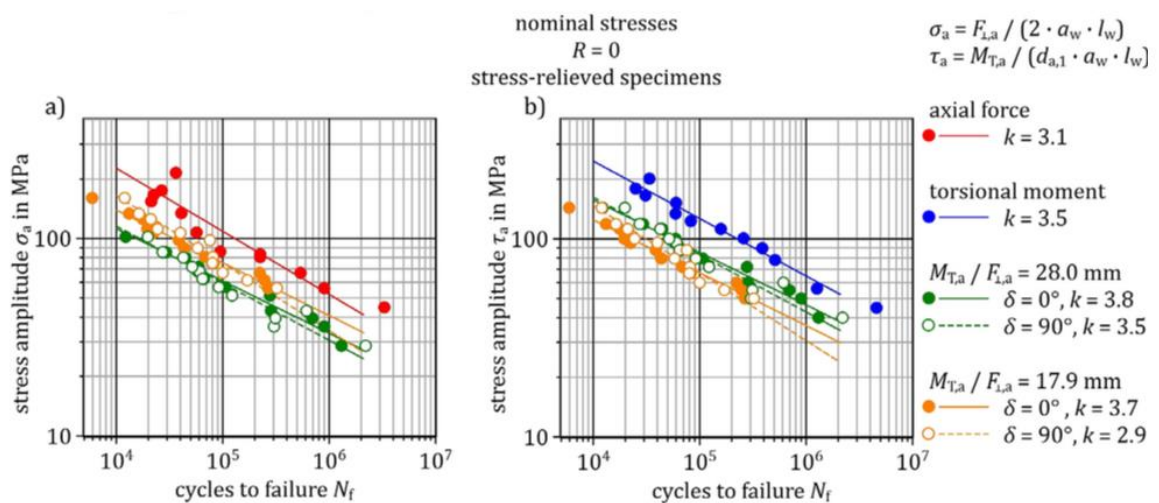


Figure 1.4: S-N curves for pulsating loading and stress-relieved specimens, [1].

Series	Condition	R	δ	M_T/F_{\perp} [Nm/kN]	τ_w/σ_w	Number of specimens
07	Stress-relieved	-1	-	-	-	7
08	Stress-relieved	-1	-	-	-	7
09	Stress-relieved	-1	0°	28.0	1.40	7
10	Stress-relieved	-1	0°	17.9	0.895	7
11	Stress-relieved	-1	90°	28.0	1.40	7
12	Stress-relieved	-1	90°	17.9	0.895	7

Table 1.2: Test program series 07-12.

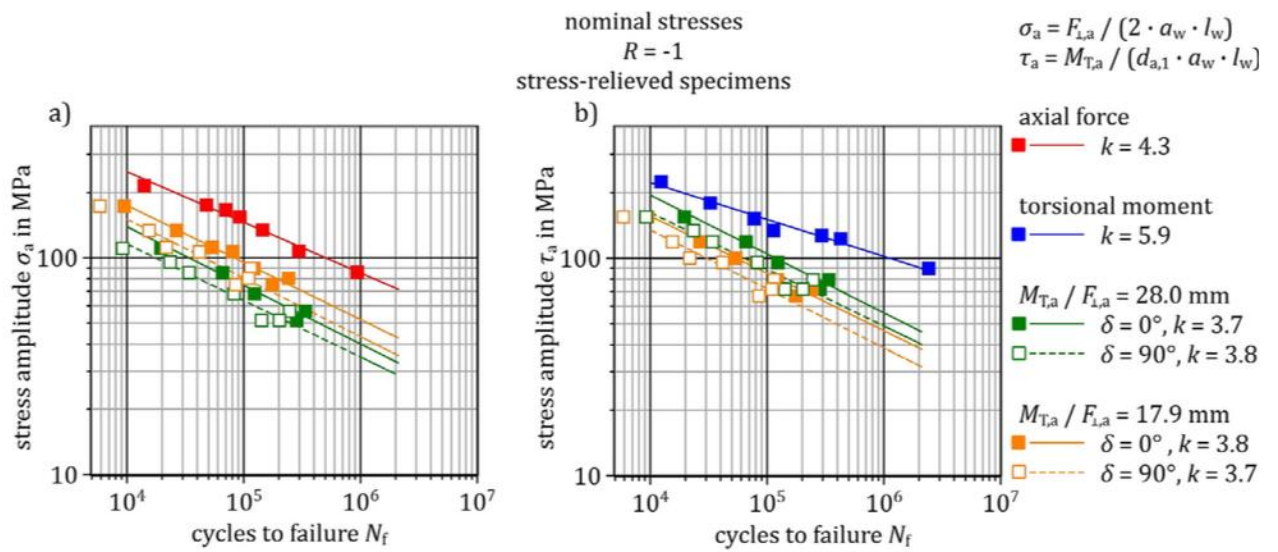


Figure 1.5: S-N curves for alternating loading and stress-relieved specimens, [1].

Series	Condition	R	δ	M_T/F_{\perp} [Nm/kN]	τ_w/σ_w	Number of specimens
13	As-welded	-1	-	-	-	7
14	As-welded	-1	-	-	-	7
15	As-welded	-1	0°	28.0	1.40	7
16	As-welded	-1	90°	28.0	1.40	7

Table 1.3: Test program series 13-16.

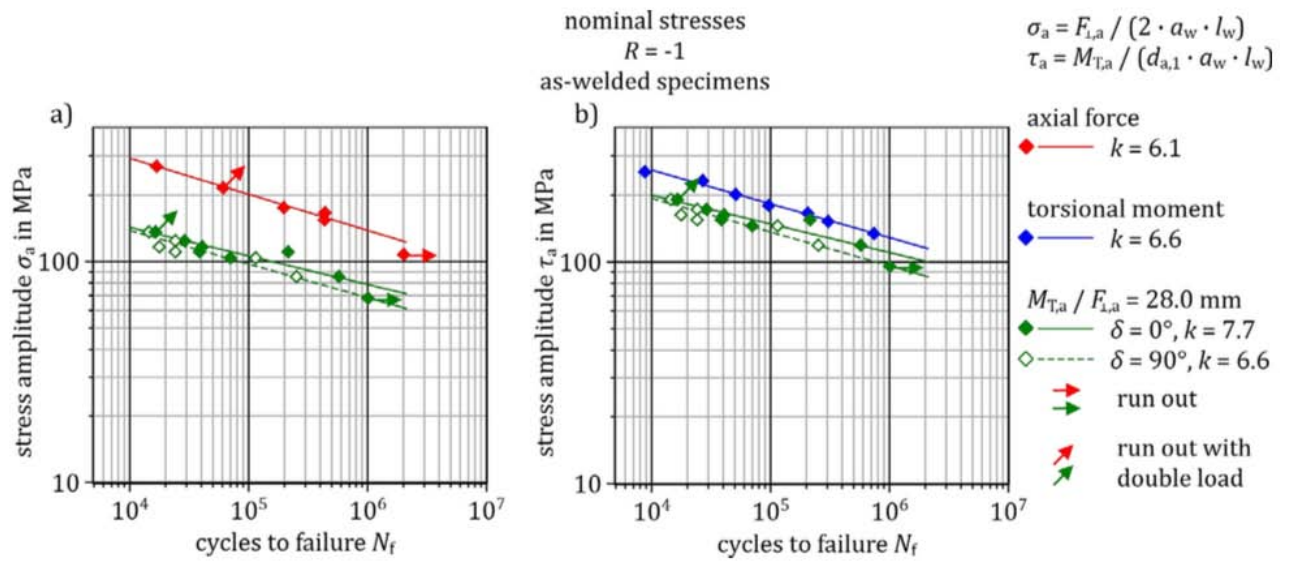


Figure 1.6: S-N curves for alternating loading and as-welded specimens, [1].

When no cracks could be detected after 10^6 load cycles in the case of combined loadings or after $2 \cdot 10^6$ load cycles otherwise the corresponding experimental results have been defined as run out and they have been indicated with horizontal arrows in Fig. 1.6. In the case of run out tests, the applied load(s) have then been doubled and the test was repeated. These data have been indicated with inclined arrows in Fig. 1.6.

All the load amplitudes applied to the specimens, reported in the German report, have been re-analysed in terms of stress range, calculated into the inner tube according to the following expressions: **CHECK DE DI**

$$\Delta\sigma_n = \frac{\Delta F}{A_{inner\ tube}} = \frac{2F_a}{\frac{\pi}{4}(d_e^2 - d_i^2)} \quad (1.4)$$

$$\Delta\tau_n = \frac{\Delta M_t}{W_{t, inner\ tube}} = \frac{2M_{t,a}}{\frac{\pi}{16} \frac{d_{a,1}^4 - (d_{a,1} - 2t)^4}{d_e}} \quad (1.5)$$

Using these new definitions for the range of stresses, the two values of the ratio τ_n/σ_n become 1.55 and 0.99. All the data have been resumed in the following table, where all test series are represented along with details about the loading conditions, Tab 1.4.

Series	Specimen	$F_{\perp,a}$ [kN]	σ_w [MPa]	σ_n [MPa]	$M_{T,a}$ [Nm]	τ_w [MPa]	τ_n [MPa]	N_f
1	1	15.0	135.1	125.65				39500
	2	5.0	45.02	41.88				3246185
	3	12.0	108	100.52				53000
	4	9.0	81.03	75.39				220000
	6	6.3	56.27	52.35				887000
	7	17.3	155.3	144.91				19500
	8	9.6	86.43	80.42				90000
	9	18.5	166.6	154.97				15000
	10	9.3	83.73	77.90				221000
	11	19.5	175.6	163.34				18000
	12	24.0	216.1	201.04				30000
	2	1				400	180.1	185.12
2					300	135.1	138.84	50000
3					200	90.03	92.56	316500
4					125	56.27	57.85	547000
5					250	112.5	115.70	135500
6					100	45.02	46.28	3405000
7					175	78.78	80.99	297000
8					225	101.3	104.13	206000
9					450	202.6	208.26	32500
10					340	153.1	157.35	35500
11					275	123.8	127.27	64000
12					370	166.6	171.23	23000
3	2	4.0	36.01	33.51	112	50.42	51.83	842000
	3	3.2	28.81	26.81	89,6	40.33	41.47	1068000
	4	7.6	68.42	63.66	213	95.88	98.58	51500
	5	9.5	85.53	79.58	266	119.7	123.10	20000
	6	4.8	43.22	40.21	134,4	60.5	62.20	221000
	7	4.4	39.61	36.86	123,2	55.46	57.02	586000
	8	5.8	51.77	48.17	161	72.48	74.51	168000
	9	11.4	102.6	95.49	320	144.1	148.09	10000
	10	7.0	63.02	58.64	196	88.23	90.71	41000
	11	8.0	72.03	67.01	224	100.8	103.67	54000
	12	9.0	80.58	74.97	250,6	112.8	115.98	40500
	4	2	7.5	67.52	62.82	134,4	60.5	62.20
3		11.9	107.1	99.68	213	95.88	98.58	18000
4		10.0	89.58	83.35	178	80.13	82.38	39000
5		17.9	161.2	149.94	320	144.1	148.09	5000
6		6.3	56.27	52.35	112	50.42	51.83	244000
7		6.9	61.94	57.63	123,2	55.46	57.02	233000

	8	9.0	81.03	75.39	161	72.48	74.51	66000
	9	8.4	75.45	70.20	150	67.52	69.42	78000
	10	11.0	98.58	92.14	196	88.23	90.71	36000
	11	12.5	112.5	104.71	224	100.8	103.67	17500
	12	14.0	126	117.27	250,6	112.8	115.98	13500
5	1	6.4	57.09	53.19	178	80.02	82.38	80000
	2	4.0	35.96	33.51	112	50.35	51.83	170000
	3	3.2	28.77	26.81	89,6	40.28	41.47	1406000
	4	7.6	68.33	63.66	213	95.75	98.58	59500
	5	9.5	85.41	79.58	266	119.6	123.10	26000
	6	4.8	43.16	40.21	134	60.42	62.01	281000
	7	4.4	39.56	36.86	123	55.38	56.92	308000
	8	5.8	51.7	48.17	161	72.37	74.51	121000
	9	11.4	102.5	95.49	320	143.9	148.09	19500
	10	7.0	62.93	58.64	196	88.11	90.71	64000
	11	8.0	71.93	67.01	224	100.7	103.67	50000
	12	9.0	80.47	74.97	251	112.7	116.16	42500
6	1	14.9	134.2	124.81	266	119.7	123.10	16000
	2	7.5	67.52	62.82	134	60.5	62.01	96000
	3	11.9	107.2	99.68	213	95.88	98.58	25500
	4	10.0	89.58	83.35	178	80.13	82.38	57000
	5	17.9	161.2	149.94	320	144.1	148.09	11500
	6	6.3	56.27	52.35	112	50.42	51.83	319000
	7	6.9	61.94	57.63	123	55.46	56.92	167000
	8	9.0	81.03	75.39	161	72.48	74.51	79000
	9	8.4	75.45	70.20	150	67.52	69.42	80000
	10	11.0	98.58	92.14	196	88.23	90.71	75000
	11	12.5	112.5	104.71	224	100.8	103.67	23500
	12	14.0	126	117.27	251	112.8	116.16	21000
7	1	19.5	175.6	163.34			0.00	46500
	2	17.3	155.3	144.91			0.00	91000
	3	15.0	135.1	125.65			0.00	143000
	4	12.0	108	100.52			0.00	292000
	5	9.6	86.43	80.42			0.00	930000
	6	24.0	216.1	201.04			0.00	13500
	7	18.5	166.6	154.97			0.00	69000
8	1				500	225.1	231.40	9000
	2				400	180.1	185.12	26500
	3				300	135.1	138.84	87000
	4				200	90.03	92.56	1600000
	5				340	153.1	157.35	51000

	6				275	123.8	127.27	332000
	7				285	128.3	131.90	209000
9	1	12.4	111.2	103.87	346	155.8	160.13	19000
	2	9.5	85.53	79.58	266	119.7	123.10	62500
	3	7.6	68.42	63.66	213	95.88	98.58	115000
	4	6.4	57.17	53.19	178	80.13	82.38	277000
	5	5.8	51.77	48.17	161	72.48	74.51	212000
10	1	19.3	173.8	161.67	346	155.8	160.13	9000
	2	14.9	134.2	124.81	266	119.7	123.10	24000
	3	11.9	107.1	99.68	213	95.88	98.58	79000
	4	10.0	89.58	83.35	178	80.13	82.38	113000
	5	9.0	81.03	75.39	161	72.48	74.51	193000
	6	12.5	112.5	104.71	224	100.8	103.67	52000
11	1	12.4	111.2	103.87	346	155.8	160.13	9000
	2	9.5	85.53	79.58	266	119.7	123.10	33000
	3	7.6	68.42	63.66	213	95.88	98.58	81000
	4	6.4	57.17	53.19	178	80.13	82.38	240000
	5	5.8	51.77	48.17	161	72.48	74.51	140000
	6	10.7	96.33	89.63	300	135.1	138.84	23000
	7	5.8	51.77	48.17	161	72.48	74.51	200000
12	1	19.3	173.8	161.67	346	155.8	160.13	5500
	2	14.9	134.2	124.81	266	119.7	123.10	15000
	3	11.9	107.1	99.68	213	95.88	98.58	41000
	4	10.0	89.58	83.35	178	80.13	82.38	143000
	5	9.0	81.03	75.39	161	72.48	74.51	108000
	6	12.5	112.5	104.71	224	100.8	103.67	21000
	7	8.4	75.45	70.20	150	67.52	69.42	84000
13	2	24.0	216.1	201.04			0.00	60434
	3	19.5	175.6	163.34			0.00	194758
	4	30.0	270.1	251.30			0.00	16615
	5	17.3	155.3	144.91			0.00	431699
	7	18.5	166.5	154.97			0.00	435631
14	1				300	135.1	138.84	736789
	2				400	180.1	185.12	95893
	3				520	234.1	240.65	26663
	4				340	153.1	157.35	302999
	5				450	202.6	208.26	50567
	6				370	166.6	171.23	205146
	7				570	256.6	263.79	8670
15	1	15.2	136.9	127.32	426	191.8	197.15	16312
	2	9.5	85.53	79.58	266	119.7	123.10	570627

	3	13.8	124.2	115.60	386	173.8	178.64	28872
	4	12.4	111.2	103.87	346	155.8	160.13	213300
	5	11.6	104.4	97.17	325	146.3	150.41	69429
	6	13.0	117	108.90	364	163.9	168.46	40546
	7	12.4	111.2	103.87	346	155.8	160.13	38122
16	1	15.2	136.9	127.32	426	191.8	197.15	14348
	2	9.5	85.53	79.58	266	119.7	123.10	249139
	3	13.8	124.2	115.60	386	173.8	178.64	23857
	4	12.4	111.2	103.87	346	155.8	160.13	23992
	5	11.6	104.4	97.17	325	146.3	150.41	113527
	6	13.0	117	108.90	364	163.9	168.46	17653

Table 1.4: Test program series

Only few specimens are missing in previous table because of invalid test procedures or run-out data. Starting from these values, Wohler curves have been re-determined in this contribution by performing a statistical analysis and obtaining the same values already published in [1]. Only the slopes of S-N curves, k , are slightly different, this could be due to a possible different interpolation method, as an example a different confidence adopted in the statistical analysis. However, this difference could be ignored considering the scatter band of the statistical distribution.

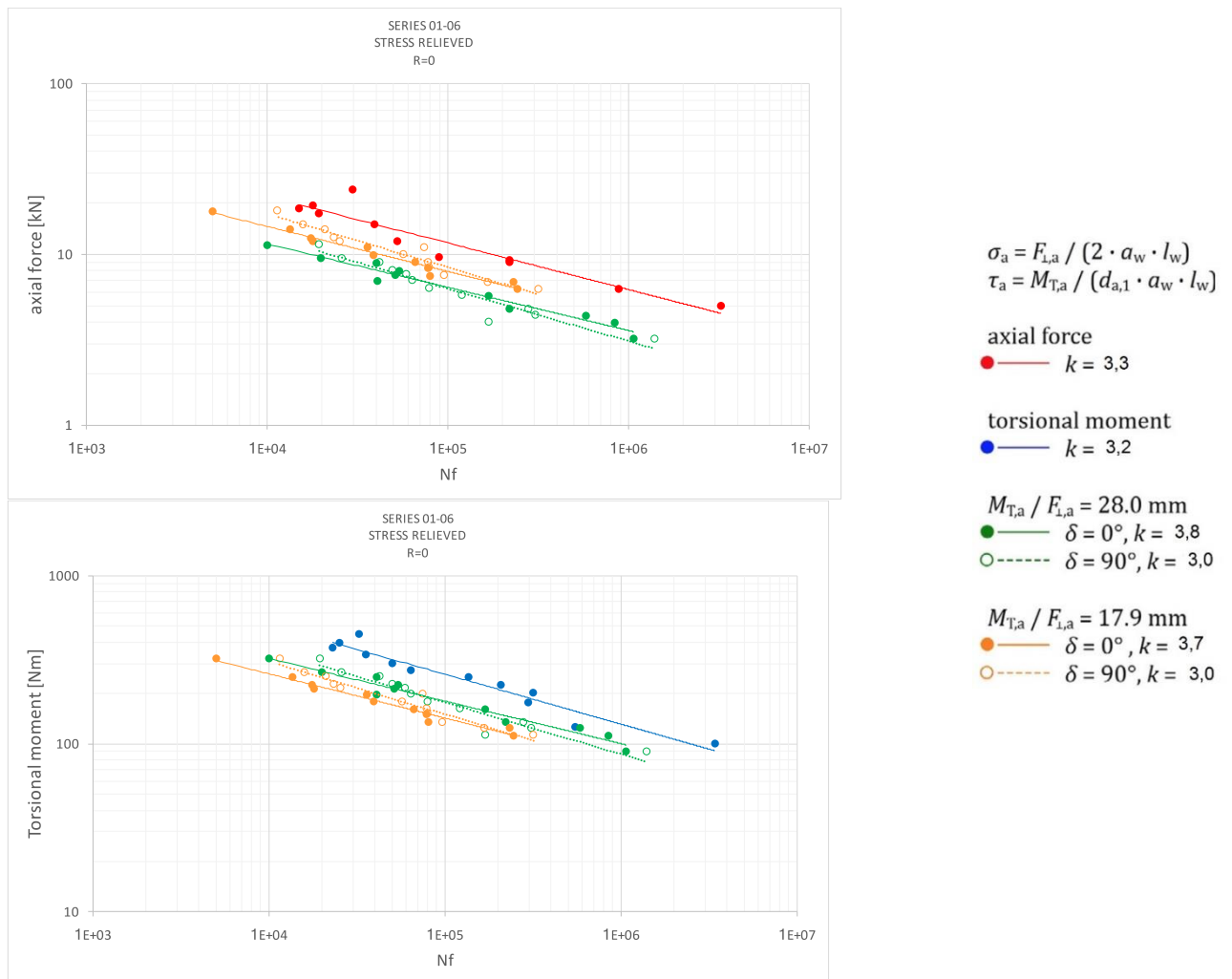


Figure 1.7: S-N curves for pulsating loading and stress-relieved specimens.

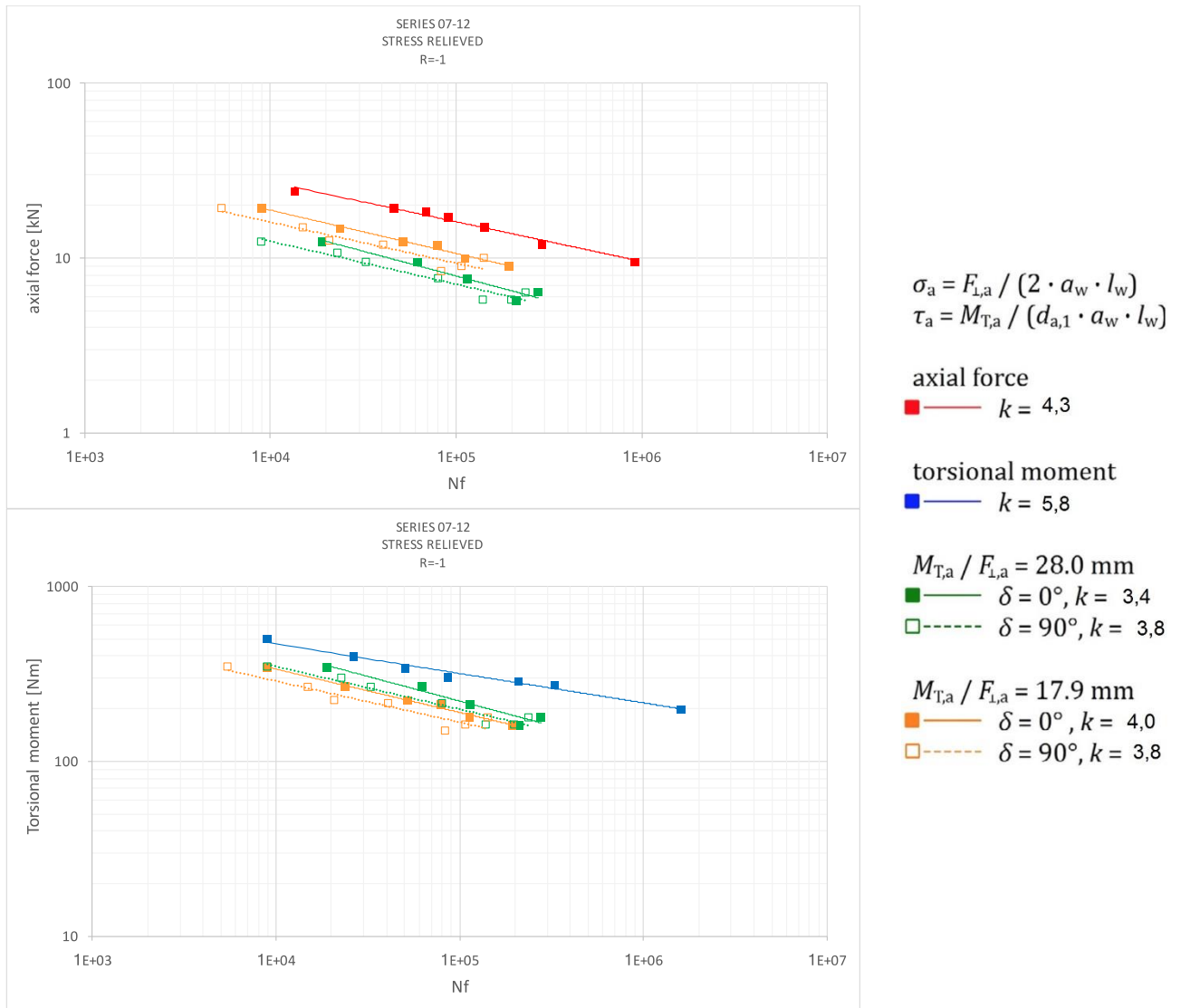


Figure 1.8: S-N curves for alternating loading and stress-relieved specimens.

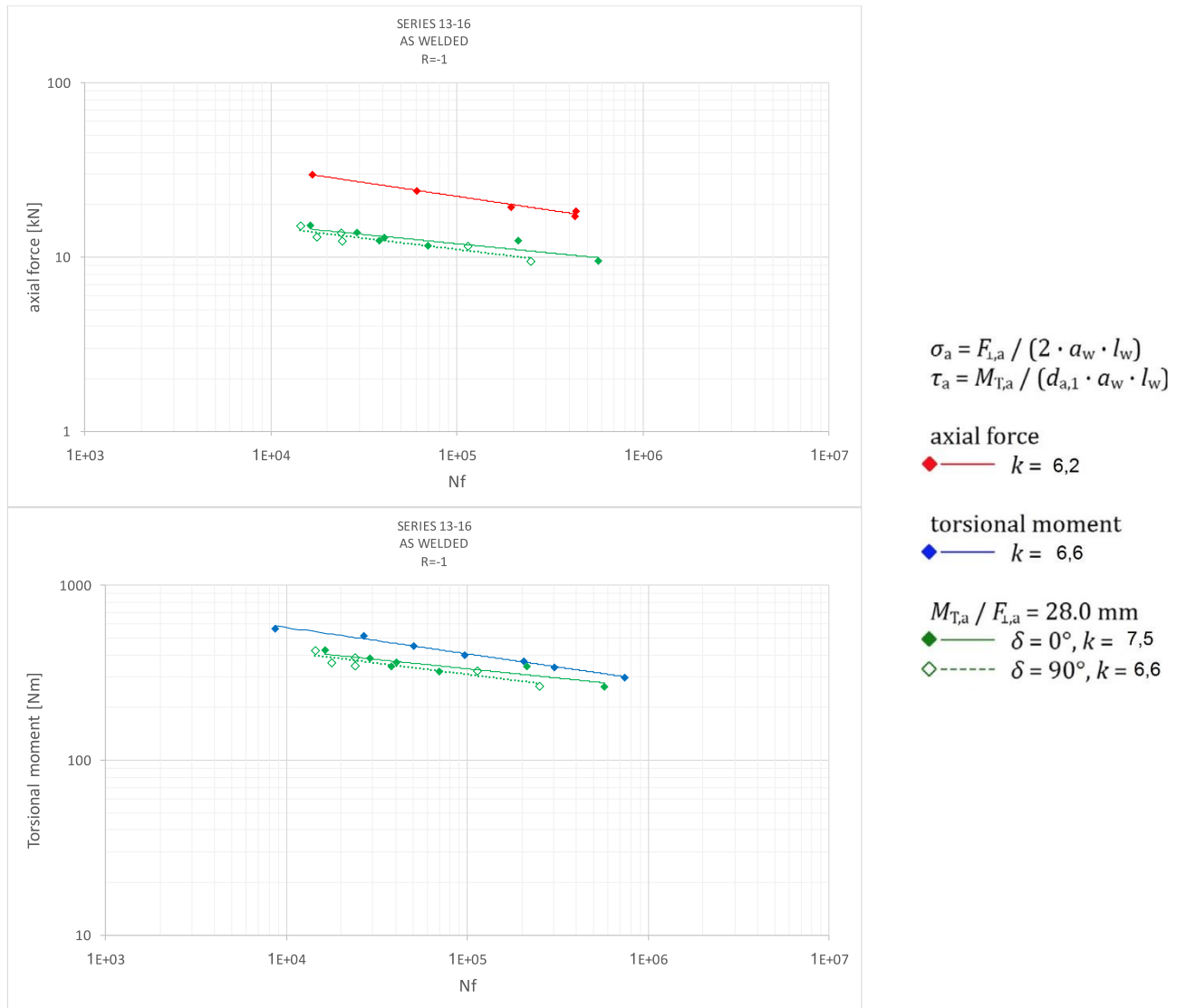


Figure 1.9: S-N curves for alternating loading and as-welded specimens.

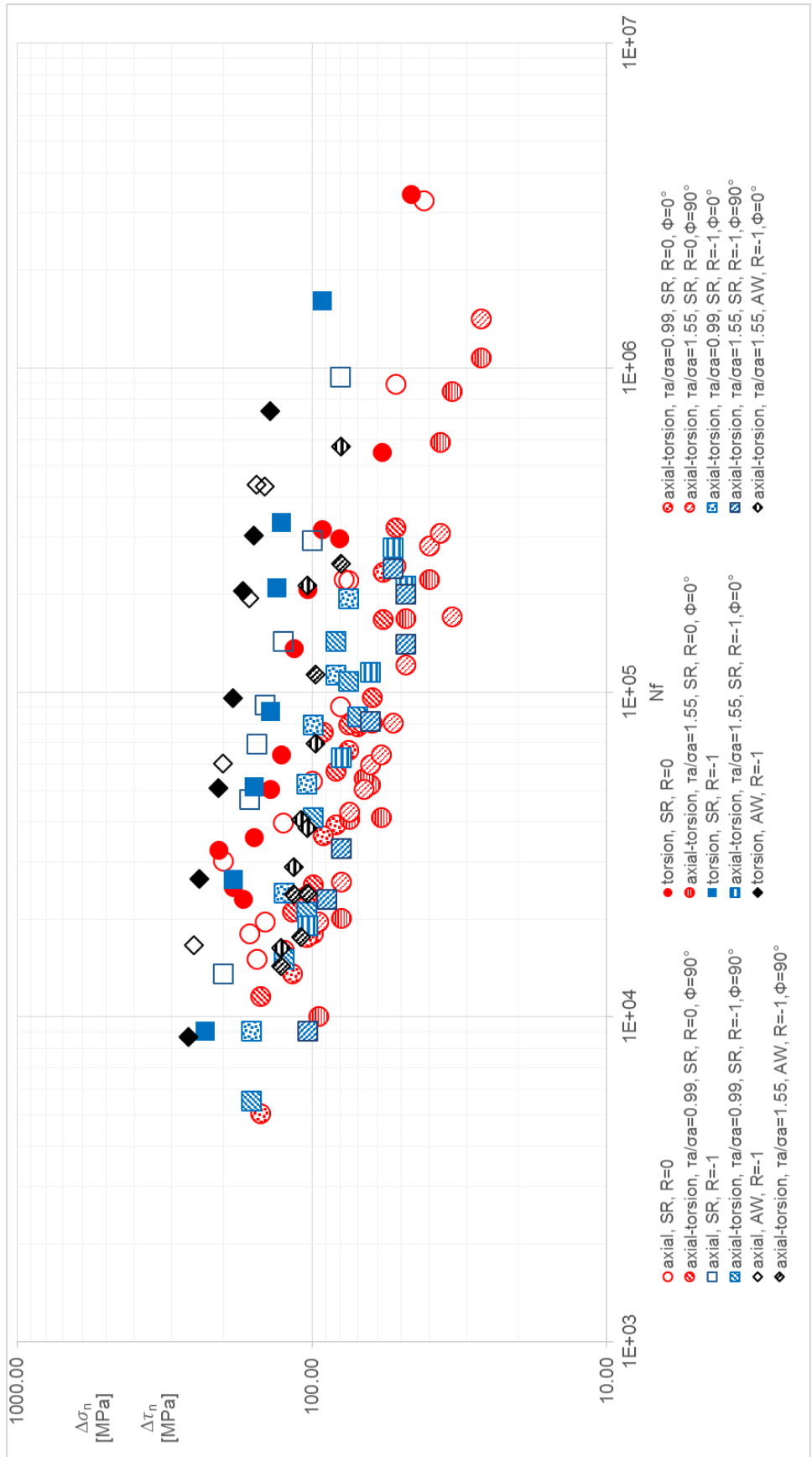


Fig. 1.10. Experimental results collected in terms of range of stress and cycles to failure. In the multiaxial cases and in the pure axial ones, the normal stress has been plotted, while for the pure torsional case, the shear stress has been presented. In the legend, the abbreviations mean: SR for stress relieved and AW for as-welded

1.4 Results

Typical failures of specimens under pulsating uniaxial and multiaxial loading are shown in Fig. 1.11. Fatigue cracks initiated at the transition area between weld toe and root in all tested specimens, either at the weld start or at the weld end position.

- In the case of specimens under pure axial loading, the fatigue cracks were initiated in both the weld start and end locations. The crack fronts spread toward each other at the weld toe on the outer tube side during cyclic loading and finally coalesced into one crack, Fig. 1.11a.
- In specimens subjected to torsional moment the cracks spread to the inner and outer tube halves, Fig. 1.11b.
- In the case of combined in-phase loading the fatigue cracks spread either into the outer pipe or through the weld metal, Fig. 1.11c.
- In contrast, the welds failed only with crack spreading through the weld metal when force and moment were phase-shifted by 90° , Fig. 1.11d.

Similar results were achieved for the case of nominal load ratio equal to -1.

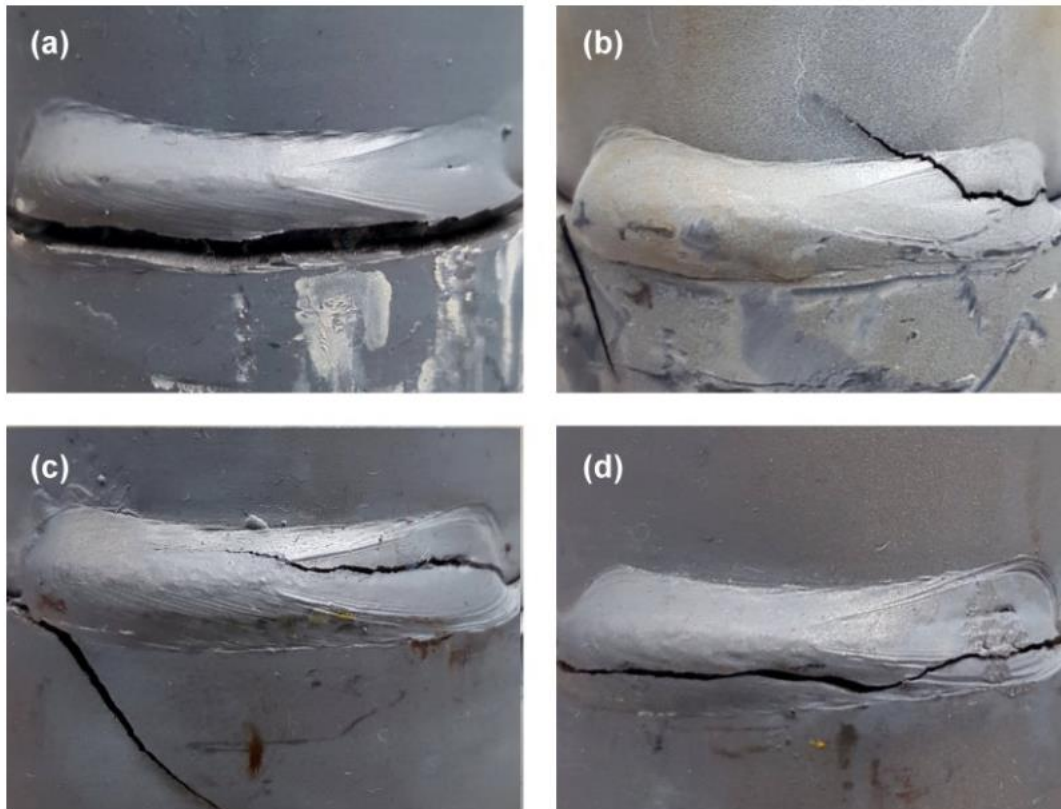


Fig. 1.11. Failure modes of welded joints under axial force (a), torsional moment (b) and proportional (c) as well as non-proportional (d) combinations, $R = 0$.

Referring to the data re-calculated in terms of nominal stress range into the inner tube and not to the published ones, some considerations could be drawn. The slopes of the S-N curves, when described by a power law, vary within the range of 3.2–5.9 for stress-relieved specimens. The slopes of S-N curves are higher and vary between $6.3 \leq k \leq 9.4$ for specimens tested in the as-welded conditions.

The specimens in the as-welded condition provide higher fatigue strengths as compared to stress-relieved specimens, especially in the area of higher fatigue lives. This could indicate the existence of compressive residual stresses resulting from the welding process which allow to obtain longer fatigue lives for a given loading condition.

Regarding out-of-phase behaviour, the reduction of fatigue life, typically observed in the literature, is not remarkably relevant. However, its effect could be seen as a k reduction in three cases, and in particular:

1. in series 01-06, considering the amplitude ratio $M_{t,a}/F_{\perp,a}$ of 17,9 Nm/kN with a k reduction from 3,7 to 3,0.
2. in series 01-06, considering the amplitude ratio $M_{t,a}/F_{\perp,a}$ of 28 Nm/kN with a k reduction from 3,8 to 3,0.
3. in series 12-16, considering the amplitude ratio $M_{t,a}/F_{\perp,a}$ of 28 Nm/kN with a k reduction from 7,5 to 6,6.

1.5 The out-of-phase effect

During multi-axial loading conditions, the specimens' lifetime is decreased by the effect of out-of-phase loading. In fact, for proportional loading the principal stress directions remain constant while, in case of non-proportional loading, they may change over time, which apparently causes the classic fatigue lifetime previsions procedures to fail. Figure 1.12 shows why the principal stress approach fails for non-proportional loading. The calculated stress range is smaller for this case (b), when compared to proportional loading (a), which indicates that it would be less damaging. However, practice shows that the opposite is generally the case, i.e. that non-proportional loading is more damaging than proportional loading.

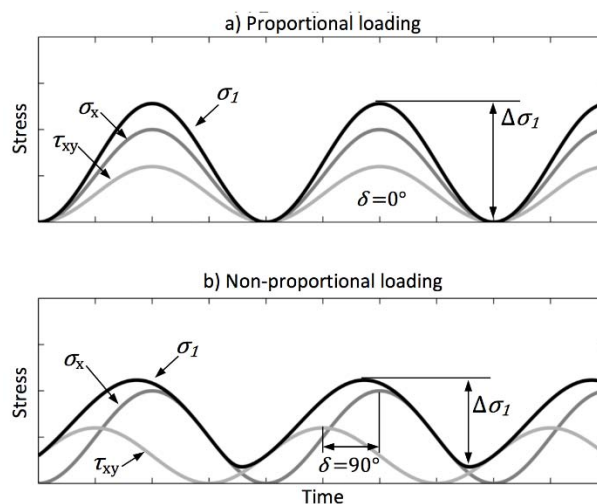


Figure 1.12: The range of principal stress is smaller for non-proportional loading than for proportional, [2].

The literature provides an abundance of criteria for assessment of welded joints under multiaxial loads, typically based on either stress interaction equations or critical plane approaches. Pedersen in [2] discussed about the reliability of these criteria and found out that the best ones to describe the effects of out-of-phase loading were the Effective Equivalent Stress Hypothesis (EESH) proposed by Sonsino in [3] and the IIW approach presented in [4].

1.6 The EESH approach

The first step is considering that conventional criteria such as Von Mises and Tresca are not representative of the state of tension in the case of out-of-phase stresses with variable stress directions. Sonsino, in his research [3], studied welded cruciform specimens and tube-tube joints under biaxial constant-amplitude loading in the range of 10^3 to 5×10^6 cycles to crack initiation and breakthrough respectively. All his specimens were relieved by heat treatment to be sure that residual stresses won't interfere. The results showed that in all notch cases phase displacement results in a decrease of fatigue life. The influence of a combined in-phase load on the fatigue life could be

predicted in a satisfactory manner on the basis of the Von Mises equivalent stress:

$$\sigma_{eq,VM} = \sqrt{\sigma_x^2 + \sigma_y^2 - \sigma_x\sigma_y + 3\tau_{xy}^2} \quad (1.6)$$

However, this hypothesis failed in case of out-of-phase stresses with variable principal stress directions: depending on the notch case, the fatigue life was overestimated by a factor of 4.5-70. The application of Von Mises criteria failed because like all other conventional hypothesis it considers local stresses while only focusing on an effective equivalent stress promises a satisfying solution.

Referring to a biaxial loading composed by torque and axial stress, this hypothesis considers an interference plane, shown in figure 1.13.

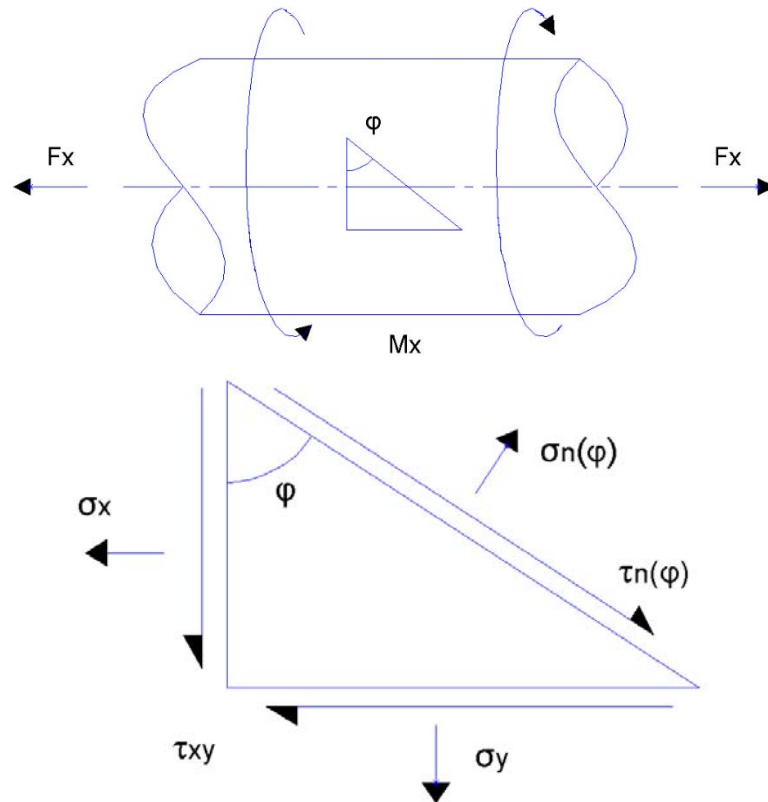


Figure 1.13: interference plane and stresses.

Stress tensor of the biaxial stress-state:

$$[\sigma] = \begin{bmatrix} \sigma_x & \tau_{xy} \\ \tau_{xy} & \sigma_y \end{bmatrix} \quad (1.7)$$

Stresses of the biaxial-state:

$$\sigma_n(\varphi) = \frac{\sigma_x + \sigma_y}{2} + \frac{\sigma_x - \sigma_y}{2} \cos(2\varphi) + \tau_{xy} \sin(2\varphi) \quad (1.8)$$

$$\tau_n(\varphi) = \frac{\sigma_x - \sigma_y}{2} \sin(2\varphi) - \tau_{xy} \cos(2\varphi) \quad (1.9)$$

The stresses acting in this plane could also be written:

$$\sigma_n(\varphi) = \sigma_x \cos^2 \varphi + \sigma_y \sin^2 \varphi + 2\tau_{xy} \cos \varphi \sin \varphi \quad (1.10)$$

$$\tau_n(\varphi) = \tau_{xy}(\cos^2\varphi - \sin^2\varphi) - (\sigma_x - \sigma_y)\cos\varphi \sin\varphi \quad (1.11)$$

According to EES the cause of crack initiation is represented by a shear stress $\tau_n(\varphi)$. The interaction of shear stresses in various interference planes φ , in particular in the case of variable principal stress directions is considered by an effective shear stress:

$$\tau_{arith} = \frac{1}{\pi} \int_0^\pi \tau_n(\varphi) d\varphi \quad (1.12)$$

The effective shear stress is then used for determining the effective equivalent stress:

$$\sigma_{eq}(\delta) = \sigma_{eq}(\delta = 0) * \frac{\tau_{arith}(\delta)}{\tau_{arith}(\delta = 0)} * \sqrt{G \exp[1 - \left(\frac{\delta - 90^\circ}{90^\circ}\right)^2]} \quad (1.13)$$

with:

$$EESH \text{ OUT OF PHASE FACTOR} = \frac{\tau_{arith}(\delta)}{\tau_{arith}(\delta = 0)} \quad (1.14)$$

$$\sigma_{eq}(\delta = 0) = \sqrt{\sigma_x^2 + \sigma_y^2 - \sigma_x\sigma_y + f_G^2 3\tau_{xy}^2} \quad (1.15)$$

$$f_G = \frac{\sqrt{\sigma_x^2 + \sigma_y^2 - \sigma_x\sigma_y}}{\sqrt{3}\tau_{xy}} \quad (1.16)$$

f_G is the size effect factor that reflects the influence of the maximum stressed material volume on the supportable local stress. G is a factor that derives from the stress concentration factors that in case of complex geometries could be determined using the finite element analysis. In general G expression is given by eq (1.17), where the stress concentration factors were derived for a mean radius of $r_m = 0.45$ mm for the un-machined flange-tube and tube-tube connections and for a mean radius of $r_m = 2.25$ mm for the machined flange-tube connections.

$$G = \frac{1 + K_{ta}}{1 + K_{tt}} \text{ or } \frac{1 + K_{tb}}{1 + K_{tt}} \quad (1.17)$$

Where K_{ta} is the stress concentration factor for axial stress, K_{tb} for bending and K_{tt} for torsion.

The root in equation 1.13 considers the influence of the material volume affected by rotating principal stress and principal strain axes in the case of a phase displacement. In fact, according to equation 1.13, if δ is different from zero the exponential function is not equal to one.

1.6.1 Evaluation of result

To explain the effectiveness of this approach it could be useful to analyse a S-N curve in terms of nominal stress and then another curve considering the equivalent one calculated by equation 1.13 and evaluating the reduction of the scatter range. Sonsino in his work [3], considered welded machined tube-tube connections under pure bending and combined bending and torsion (in-phase and out-of-phase) loading conditions. The result of the experimental procedure is shown in fig. 1.14, considering the nominal stress.

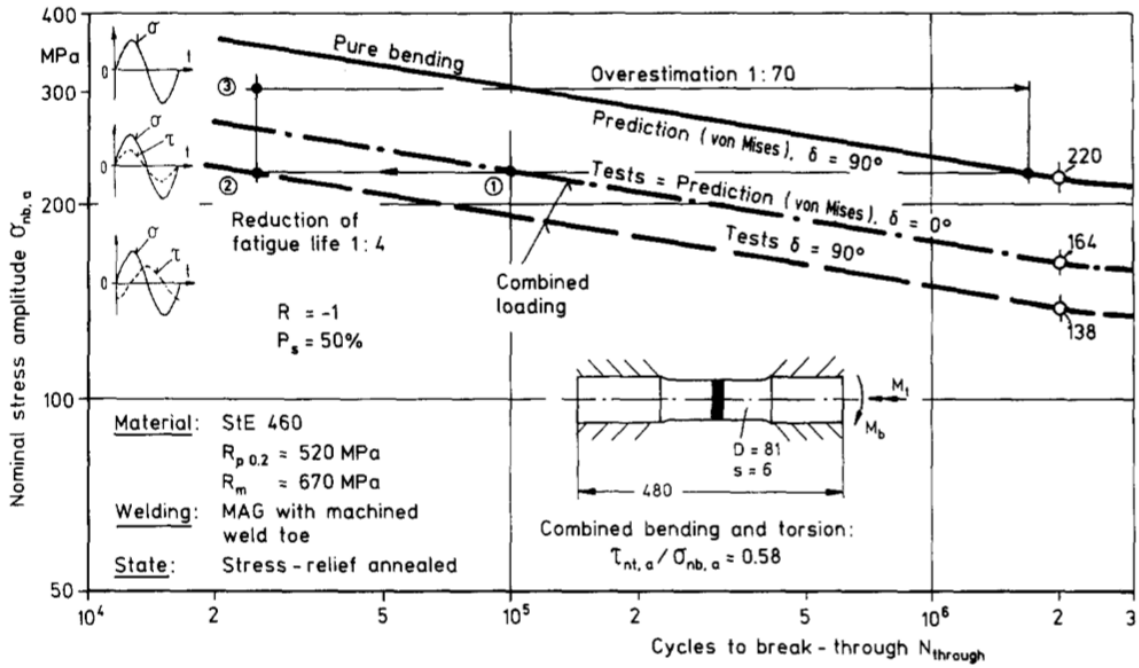


Figure 1.14: Fatigue strength of welded machined tube-tube connections under multiaxial loading, [3].

As it is shown in figure 1.14, it is quite obvious that with combined loading there is a decrease of the fatigue life and this reduction is remarked in case of a 90° phase between the two loading conditions. In order to unify all the experimental data within a single scatter range, Sonsino produced a S-N curve in terms of equivalent stress, eq 1.13. The specimens were the same of fig 1.14, however this new approach allow the pure bending curve to be representative also for the combined (in-phase and out-of-phase loading conditions). Regression lines were added for a 10% and 90% probability of survival and the outcome is a great reduction of the scatter range, if compared to fig 1.15.

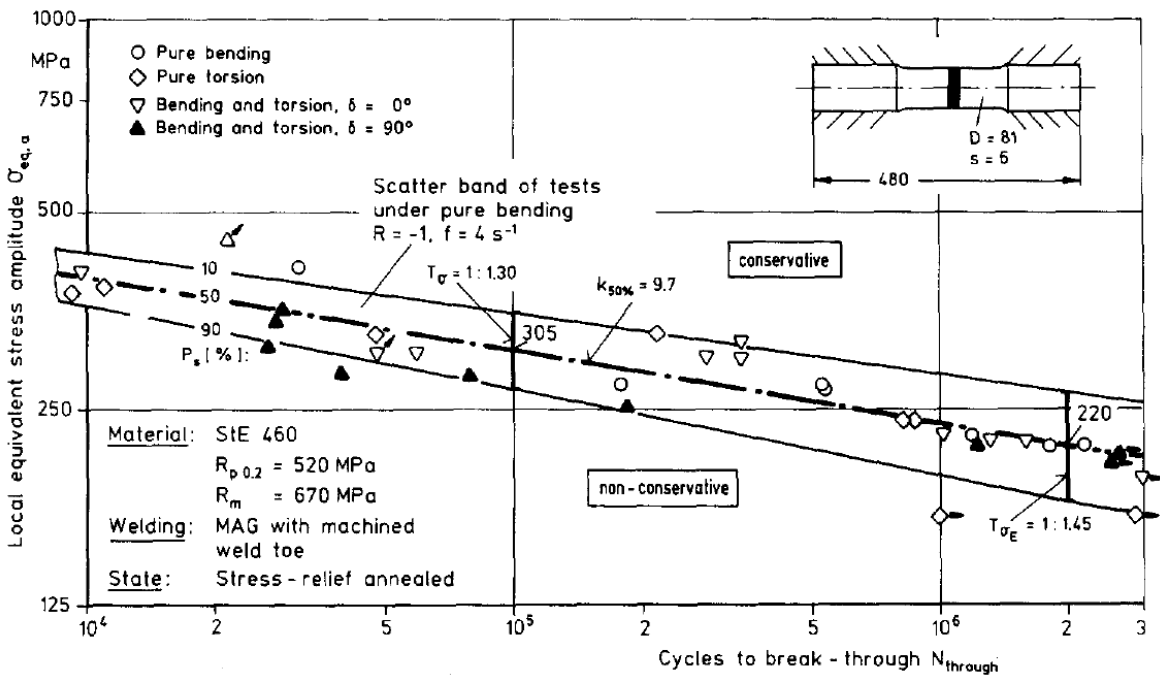


Figure 1.15: Evaluation of multiaxial stress states with the hypothesis of effective equivalent stress (EES) for welded, machined tube-tube connections, [3].

In conclusion, the equivalent effective stress (EES) is based on local coordinate stresses in weld toes and considers the maximum stressed material volume governed by the stress gradient and the phase displacement between the local normal and shear stresses. The effectiveness of this method is shown by the capability of transferring the local normal and shear stresses and the local multiaxial stress states with constant and variable principal stress directions into a S-N curve determined under uniaxial load, irrespective of the stress concentration level given by the geometry and the machining of the welded joint.

1.7 The SSCH approach

In 2010, a new approach was proposed in [5] and called: “stress space curve hypothesis”, which includes the EESH as a particular case. This criterion is worth being noticed also because it includes a lot of classical approaches for special testing situations. The first step of the SSCH idea is represented by the generalization of classical approaches like Von Mises, eq. 1.18, and Tresca, eq. 1.19, with eq. 1.20.

$$\sigma_{eq,VMises} = \sqrt{\sigma_x^2 + \sigma_y^2 - \sigma_x\sigma_y + 3\tau_{xy}^2} = \sqrt{I_1^2 - 3I_2} \quad (1.18)$$

$$\sigma_{eq,Tresca} = \sqrt{\sigma_x^2 + \sigma_y^2 - 2\sigma_x\sigma_y + 4\tau_{xy}^2} = \sqrt{I_1^2 - 4I_2} \quad (1.19)$$

$$\sigma_{eq} = \sqrt{I_1^2 - (4 - \alpha)I_2} = \sqrt{\sigma_x^2 + \sigma_y^2 - (2 - \alpha)\sigma_x\sigma_y + (4 - \alpha)\tau_{xy}^2} \quad (1.20)$$

with I_1 and I_2 invariants of the biaxial stress tensor.

$$I_1 = \sigma_x + \sigma_y \quad (1.21)$$

$$I_2 = \sigma_x\sigma_y - \tau_{xy}^2 \quad (1.22)$$

Because of a formulation using the invariants I_1 and I_2 , the resulting equivalent stress is also invariant against rotations of the coordinate system. If α equals 0 the equivalent stress turns out to be Tresca, while if it equals 1 the equivalent stress is the Von Mises' one. The biaxial stress tensor may be decomposed into two parts, eq. 1.23, described by Mohr's stress components:

$$\begin{bmatrix} \sigma_x & \tau_{xy} \\ \tau_{xy} & \sigma_y \end{bmatrix} = \begin{bmatrix} p & 0 \\ 0 & p \end{bmatrix} + \begin{bmatrix} q & \tau_{xy} \\ \tau_{xy} & -q \end{bmatrix} \quad (1.23)$$

With:

$$p = \frac{\sigma_x + \sigma_y}{2} \quad \text{and} \quad q = \frac{\sigma_x - \sigma_y}{2} \quad (1.24)$$

p is the quasi-hydrostatic stress component, while q and τ_{xy} are both deviatoric stress components.

$$p = \frac{3}{2}\sigma_h \quad \text{with} \quad \sigma_h = \frac{\sigma_x + \sigma_y + \sigma_z}{3} \quad (1.25)$$

Rewriting the equivalent stress, introducing p and q , with different weighting factors α and β for the two kind of stresses, it results, eq 1.26:

$$\sigma_{eq} = \sqrt{\alpha p^2 + \beta q^2 + \beta \tau_{xy}^2} = \sqrt{\alpha p^2 + \beta (q^2 + \tau_{xy}^2)} \quad (1.26)$$

Taking into account uniaxial conditions $\sigma_{eq} = \sigma_x$ with $\sigma_y = 0$ and $\tau_{xy} = 0$, the relation $\alpha + \beta = 4$ must be satisfied, so that the following equation can be obtained:

$$\sigma_{eq} = \sqrt{\alpha p^2 + (4 - \alpha)(q^2 + \tau_{xy}^2)} \quad (1.27)$$

At this point it was introduced the idea of representing the state of tension in a p, q, τ stress space. Periodic stress-time histories lead to closed curves whose shapes are invariant against a rotation of the coordinate system. In case of uniaxial and proportional loadings, the p - q - τ -space signals result in straight line segments, as it is shown in figure 1.16.

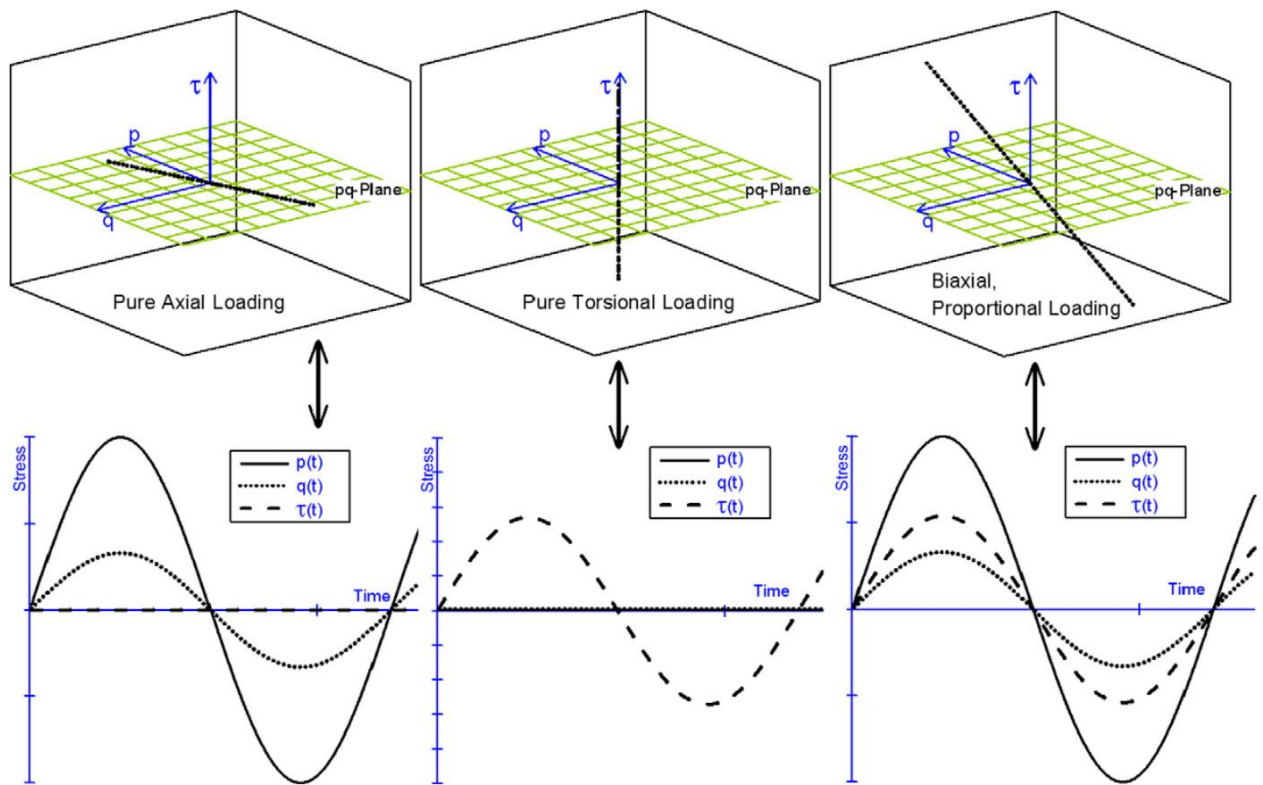


Figure 1.16: p - q - s -space signals for uniaxial and proportional loadings, [5].

The basic idea is that the length of such stress space segments is the damage-relevant variable. This means that different types of uniaxial loadings with the same lifetime should lead to lines with the same length. To fulfil this condition, the stress variables are multiplied by weighting factors, which are given in the following equation:

$$p \rightarrow p * \sqrt{\alpha} \quad (1.28)$$

$$q \rightarrow q * \sqrt{4 - \alpha} \quad (1.29)$$

$$\tau \rightarrow \tau * \sqrt{4 - \alpha} \quad (1.30)$$

In this way the stress space has been rescaled and considering the variable amplitude to rewrite the equivalent stress, it is now the half-length of the line segment.

$$\sigma_{eq,SSCH} = \sqrt{(\sqrt{\alpha} * p_a)^2 + (\sqrt{4 - \alpha} * q_a)^2 + (\sqrt{4 - \alpha} * \tau_{xy,a})^2} \quad (1.31)$$

The determination of the scaling factor α is not immediate. First of all, it depends on the material and the geometry but another observation needs to be done. Comparing the basic S-N curve for pure axial and pure torsional loading, the previous formula leads to a proportional coherency between these two types of loadings (assumption: $\sigma_y = \nu \sigma_x$; at the surface in the case of the sharp notch effect in the fatigue critical area of the weld root).

$$\sigma_{eq,SSCH,Axial} = \sigma_{x,a} \sqrt{1 + \nu^2 + (\alpha - 2)\nu} \quad (1.32)$$

$$\sigma_{eq,SSCH,Torsion} = \tau_{xy,a} \sqrt{4 - \alpha} \quad (1.33)$$

If α is a constant parameter, this would lead to a torsional S-N curve parallel to the axial one even though, in most cases, the slopes are different. To correct this, the constant α is now considered to depend on the lifetime. This means that the fatigue processes may be based on different damage mechanisms, depending on the load level. The function $\alpha(N)$ is shown in Fig. 1.17 for three investigated materials in the welded state. Equation 1.37 represents the modified SSCH approach for sinusoidal, constant amplitude signals. It must be solved numerically on condition that the point $(\sigma_{eq,SSCH}(N); N)$ has to fit onto the reference S-N curve.

$$\sigma_{eq,SSCH,Axial}(N) = \sigma_{eq,SSCH,Torsion}(N) \quad (1.34)$$

$$\sigma_{x,a} \sqrt{1 + \nu^2 + (\alpha(N) - 2)\nu} = \tau_{xy,a} \sqrt{4 - \alpha(N)} \quad (1.35)$$

$$\alpha(N) = 4 - \frac{(1 + \nu)^2}{\nu + \tau_{xy,a}^2(N) / \sigma_{x,a}^2(N)} \quad (1.36)$$

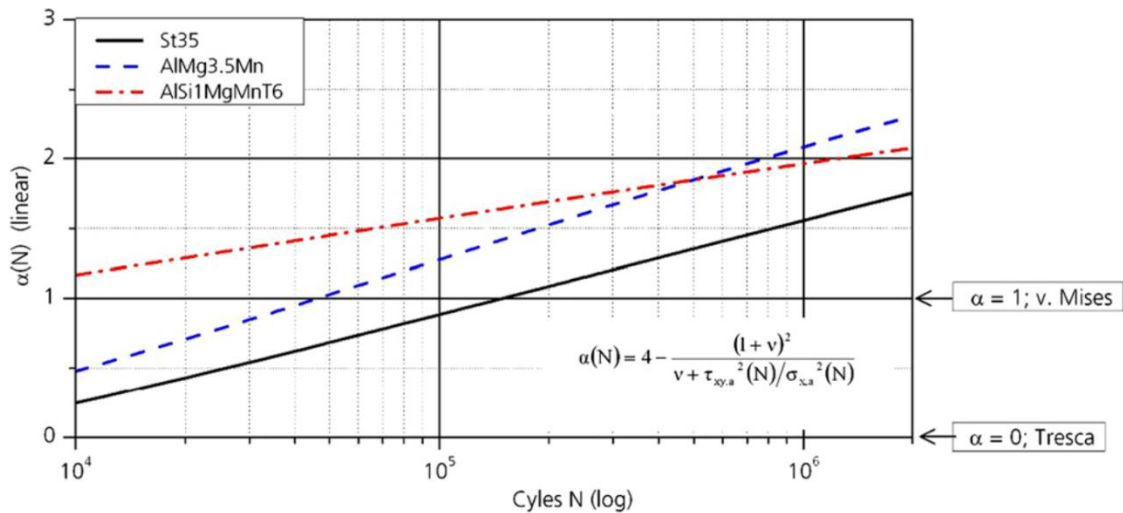


Figure 1.17: $\alpha(N)$ as a function of cycles to failure, [5].

hence the equivalent stress is:

$$\sigma_{eq,SSCH} = \sqrt{\alpha(N) * p^2 + (4 - \alpha(N)) * (q^2 + \tau_{xy}^2)} \quad (1.37)$$

Regarding out-of-phase loadings this hypothesis works, just with few adjustments. The effect of a phase different from zero is to result in an ellipse in the p-q- τ space, invariant against a rotation of the coordinate system.

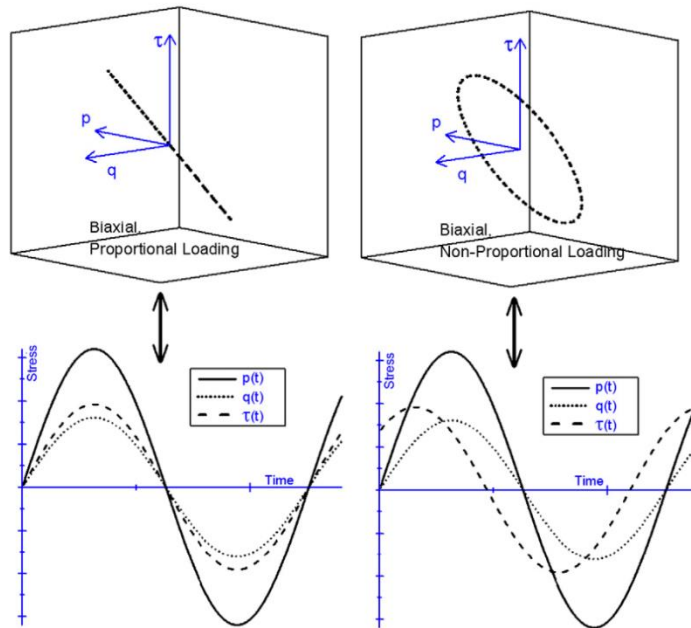


Figure 1.18: p-q-s-space signals for proportional and non-proportional loadings. , [5].

Applying the same stress amplitudes σ_{xa} , σ_{ya} , τ_{xya} but changing the phase ϕ_{xy} , three observations could be done:

- 1- The length of the semi-major axis b decreases with increasing phase shifts and the length of the semi-minor axis a increases, Fig. 1.19.

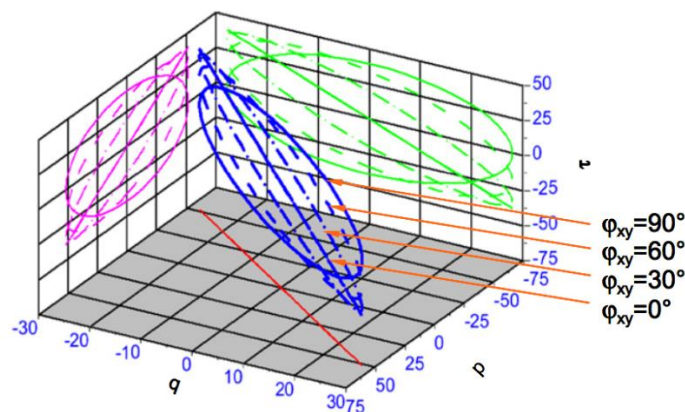


Figure 1.19: Influence of phase shifts ϕ_{xy} on stress ellipses, [5].

- 2- For each of these ellipses, a circumscribing rectangle can be constructed. The diagonal

lengths of these rectangles are constant, i.e. all the corner points are located on a circle, and can be calculated from any ellipse, Fig 1.20.

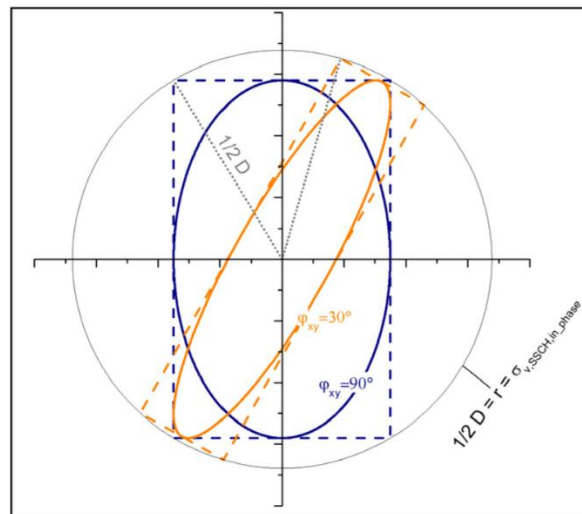


Figure 1.20: Circumscribing rectangles of stress ellipses, [5].

- 3- The enveloping rectangle from the $\phi_{xy} = 90^\circ$ ellipse encloses and touches all ellipses, Fig. 1.21.

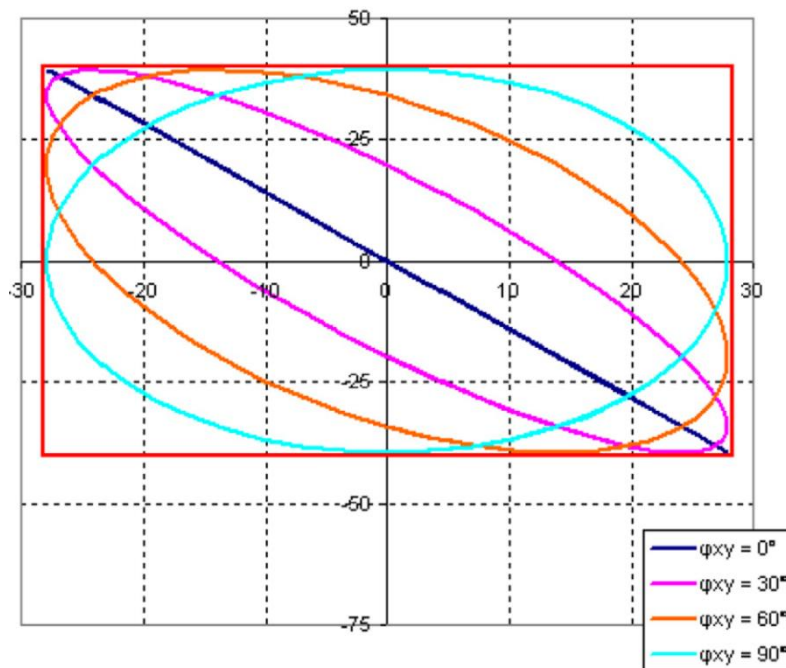


Figure 1.21: Enveloping rectangle of stress ellipses. [5].

The idea of the length of the straight-line segments that results from the uniaxial and proportional cases as being the damage-relevant variable can now be generalized for out-of-phase signals. One possible idea would be to consider it as a special case of the ellipses semi-major axis b , because the semi-major axis of the stress ellipse indicates the largest stress range. However, ductile materials react on loads, that cause a significant change over time of principal stress directions, with a reduction of fatigue life. Hence, the semi-major axis of the ellipse would be a disadvantageous value for ductile materials in deriving an equivalent stress, because the length of the semi-major axis

decreases with increasing phase shifts while, in experiments, the fatigue life is reduced. In order to properly represent the stress state it has been proposed to consider both semi-minor and semi-major axes of the stress ellipses. To achieve this the half diagonal is recommended as an assessment criterion, Fig 1.22.

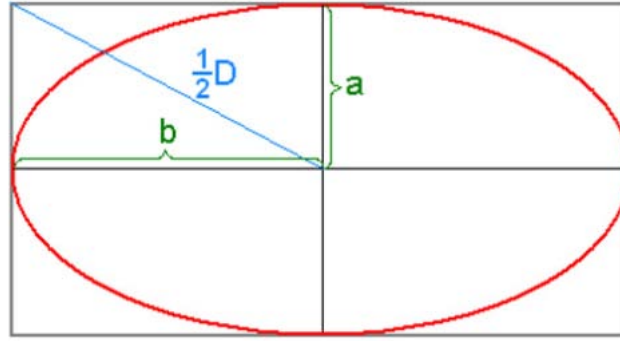


Figure 1.22: Stress ellipse with semi-minor and semi-major axes as assessment criterion, [5].

The equivalent stress formula is the same of the proportional case, but obviously the quasi-hydrostatic stress component and the deviatoric ones take into account the corresponding phases.

$$\frac{1}{2}D = \sqrt{a^2 + b^2} = \sigma_{eq,SSCH} = \sqrt{\alpha p^2 + (4 - \alpha)(q^2 + \tau_{xy}^2)} \quad (1.38)$$

The relationship between $\sigma_x(t)$, $\sigma_y(t)$ and $p(t)$, $q(t)$ is represented below ($\tau_{xy}(t)$ remains the same).

$$\sigma_x(t) = \sigma_{xa} * \sin(\omega t) \quad p(t) = p_a * \sin(\omega t + \varphi_p) \quad (1.39)$$

$$\sigma_y(t) = \sigma_{ya} * \sin(\omega t + \varphi_y) \quad q(t) = q_a * \sin(\omega t + \varphi_q) \quad (1.40)$$

$$\tau_{xy}(t) = \tau_{xya} * \sin(\omega t + \varphi_{xy}) \quad (1.41)$$

with:

$$p_a = \sqrt{(\sigma_{xa} + \sigma_{ya} * \cos(\varphi_y))^2 + (\sigma_{ya} * \sin(\varphi_y))^2} \quad (1.42)$$

$$\varphi_p = \arctan\left(\frac{\sigma_{ya} * \sin(\varphi_y)}{\sigma_{xa} + \sigma_{ya} * \cos(\varphi_y)}\right) \quad (1.43)$$

$$q_a = \sqrt{(\sigma_{xa} - \sigma_{ya} * \cos(\varphi_y))^2 + (\sigma_{ya} * \sin(\varphi_y))^2} \quad (1.44)$$

$$\varphi_q = \arctan\left(\frac{-\sigma_{ya} * \sin(\varphi_y)}{\sigma_{xa} - \sigma_{ya} * \cos(\varphi_y)}\right) \quad (1.45)$$

However, in practice it would be complex to use these notations so an easier way to express both in-phase and out-of-phase effects is here proposed. An additional factor $f = f(\lambda)$ has been introduced

and it is a function of λ , the ratio between the semi-minor axis and the semi-major axis of the ellipse in the p-q- τ space.

$$\underbrace{\sigma_v}_{\text{proportional case}} \rightarrow \underbrace{\sigma_v \cdot f}_{\text{non-proportional case}} \quad (1.46)$$

The additional factor $f(\lambda)$ has to fulfil several conditions:

1. $f(\lambda = 0) = 1$, because the proportional and uniaxial equivalent stresses should remain unchanged. This is the case without out-of-phase loadings.
2. For $\phi_{xy} = 90^\circ$, $f(\lambda_{max})$, should be at a maximum for ductile materials and at a minimum for brittle materials. (For semi-ductile materials, $f(\lambda) = \text{const.} = 1$). The global maximum for λ is always $\lambda = 1$, standing for a circle as a special case of a stress ellipse.
3. The function f should be monotonically increasing for ductile materials, monotonically decreasing for brittle materials, but still $f(\lambda) > 0$ must always be fulfilled.

These conditions can be fulfilled with the approach in the following equation.

$$f(\lambda) = f(a/b) = \left(1 + \frac{\rho * a * b}{a^2 + b^2}\right) = \left(1 + \frac{\rho * \lambda}{1 + \lambda^2}\right) \quad (1.47)$$

The additional parameter ρ depend on the specimen material and its sign cover all three kinds of out-of-phase behaviour. In fact in case of a ductile material the out-of-phase effect is a decrease of lifetime so ρ will be positive, while in a brittle material it results in an increasing of lifetime and ρ will be negative. Last but not the least, the semi-ductile material is not influenced by the existence of a phase between loadings, so ρ results equal to zero. These considerations are derived from experimental data, in fact tests demonstrate that steel is more sensitive to a phase shift than aluminium alloys. All these cases are resumed in the following table.

Material	ρ	$f(\lambda)$	Out-of-phase behaviour
Ductile	> 0	≥ 1	Decr. lifetime
Semi-ductile	$= 0$	1	Neutral
Brittle	< 0	≤ 1	Incr. lifetime

Table 1.5: out-of-phase behaviour of different materials.

Graphically the function $f(\lambda)$ modifies the ellipse by changing the length of both semi axes in the p, q, τ space. The non-proportionality function $f(\lambda)$ lead to an equivalent stress formula, eq. 1.48, suitable for the analysis of multiaxial stresses.

$$\sigma_{eq,SSCH} = \frac{1}{2}D * f(\lambda) = \sqrt{a^2 + b^2} * f(\lambda) = \sqrt{\alpha p^2 + (4 - \alpha)(q^2 + \tau_{xy}^2)} * \left(1 + \frac{\rho * \lambda}{1 + \lambda^2}\right) \quad (1.48)$$

The last expression of this equivalent stress is the one used to analyse the fatigue life of the steel tube-tube joints that were under investigation by Shams and Vormwald in [1]. The importance of the SSCH method is validated by the fact that with this approach it could be possible to approximate the Equivalent Stress Hypotheses EESH, discussed in the previous paragraph. The quasi-hydrostatic stress is not considered by the EESH, so instead of the special stress ellipse, only the projection onto q, τ space is taken into account. In fact the EESH approach considers that the cause of failure is represented only by shear stress $\tau_n(\varphi)$ and the phase effect corresponds in a decrease of the lifetime (true only in ductile materials). Considering a factor $\rho = 0,22$, the function $f(\lambda)$ approximate very well the EESH out of phase factor:

$$\frac{\tau_{arith}(\varphi)}{\tau_{arith}(\varphi = 0)} \approx f(\lambda_{q\tau}; \rho = 0,22) = \left(1 + \frac{0,22 * \lambda_{q\tau}}{1 + \lambda_{q\tau}^2}\right) \quad (1.49)$$

EESH OUT-OF-PHASE FACTOR

The goodness of this approximation is represented by a low value of the error, as it is shown in the graphic below.

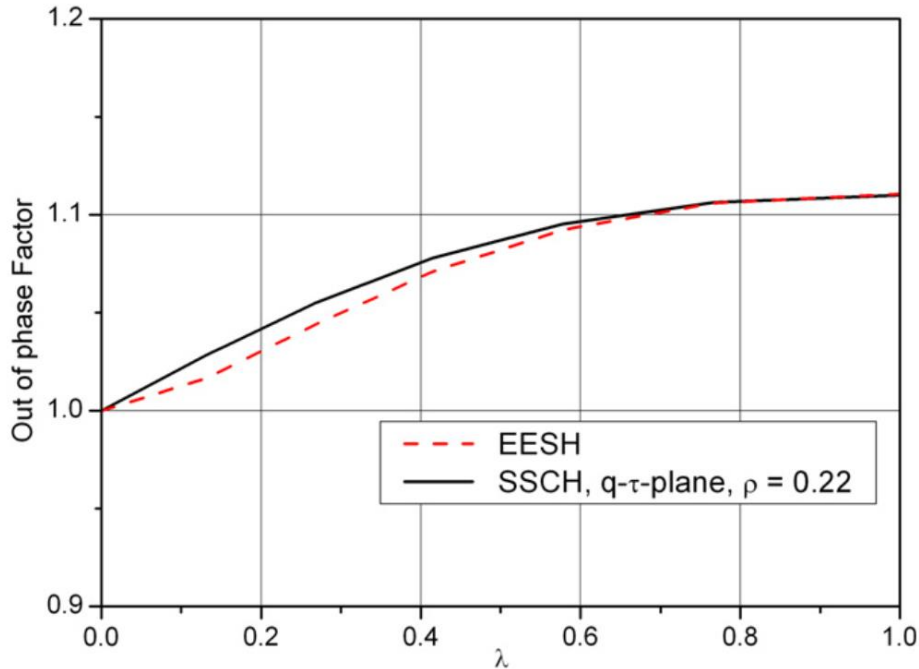


Figure 1.23: Comparison of different out-of-phase factors from EESH and SSCH approaches, [5].

The data collected show that the out-of-phase effect is more relevant in steels than aluminium alloys, in terms of fatigue life reduction. The calculations with SSCH lead to a satisfactory estimation that tends more to the conservative side than to the non-conservative side and places the results in a tight scatter band. Below are reported examples of a St35, Fig 1.24, and an aluminum alloy, Fig 1.25.

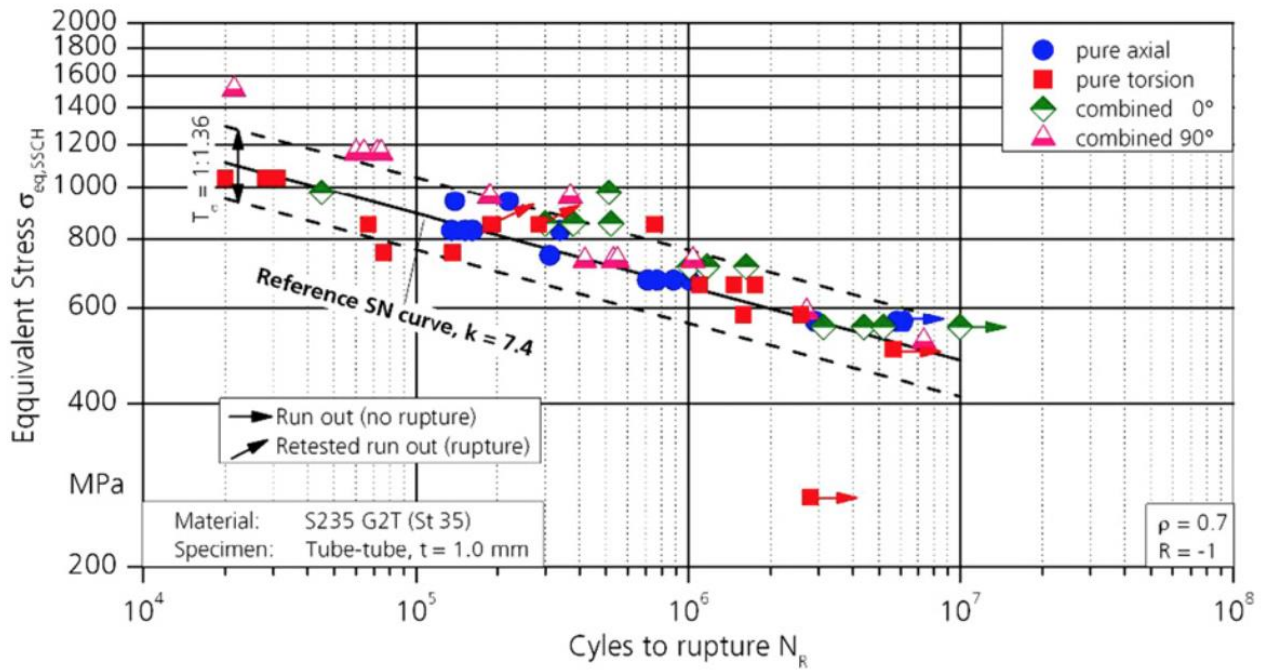


Figure 1.24: Local equivalent stresses for the steel joints according to the SSCH hypothesis versus fatigue life, [5].

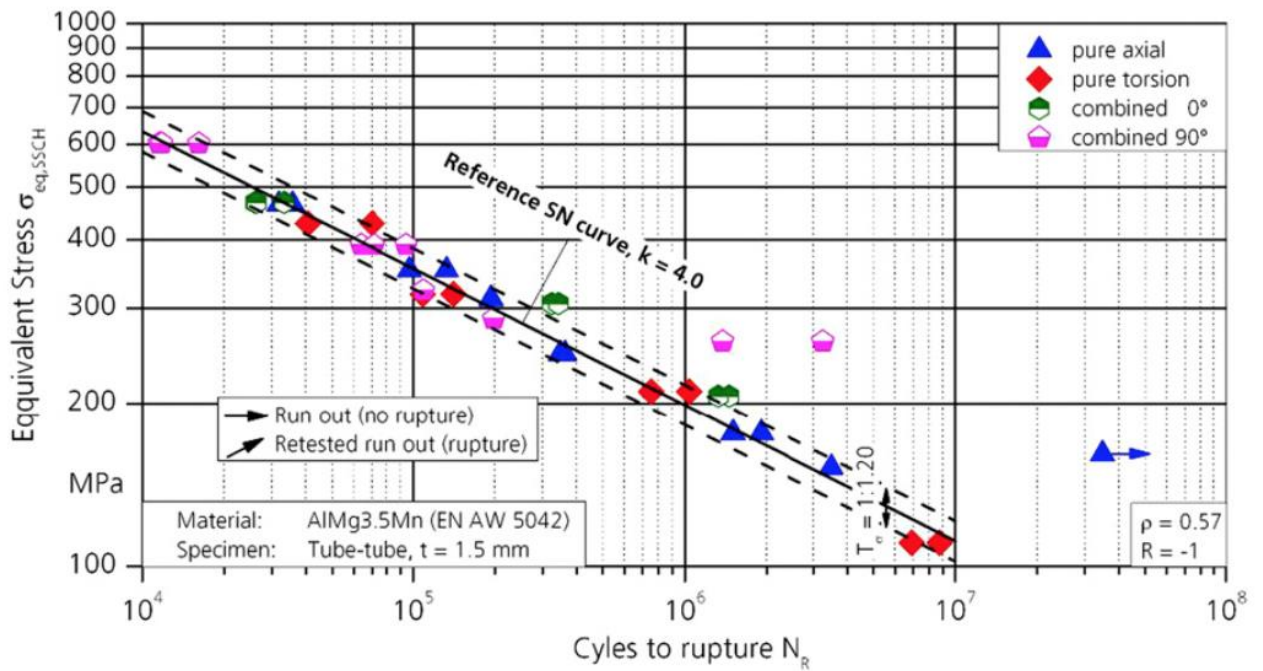


Figure 1.25: Local equivalent stresses for the aluminium joints of the alloy AlMg3.5Mn according to the SSCH hypothesis versus fatigue life, [5].

After all considerations the SSCH criteria was adopted to estimate the out-of-phase effects, but it is necessary to introduce another theory to take into account the size effects. This new theory is called NuMeSiS.

1.8 The NuMeSiS approach

Regarding welded joints, there is a great variety of Wöhler curves, depending on the structural shape and size. In order to unify structures different in shape and in size, a lot of theories have been produced, like the one proposed by Lazzarin et al. [7], based on the strain energy density. The NuMeSiS approach aims to determine a standardised notch stress considering a combination of geometrical and statistical size effect. With geometrical size effect we refer to the inhomogeneous stress distribution, while the statistical size effect relies on the fact that larger specimens have higher probability of defect. This method considers the micro-support effect according to Neuber for the geometrical size effect and weakest link model according to Weibull for the statistical size effect.

Generally speaking, regarding the size effect, we know that in a structure proportionally scaled down but loaded with the same nominal and notch stress, the fatigue life of the smaller structure will be higher than the fatigue life of the larger one.

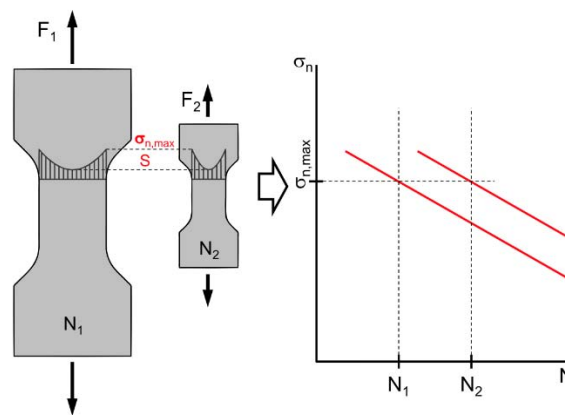


Figure 1.26: Influence of size effect on fatigue life, [6].

First of all, the size effect could be derived from the fact that in reality properties scale non-proportionally and can be divided into two components:

- Notch sharpness: Geometric shape of the notch (rounding and opening angle) will determine the stress inhomogeneity.
- Notch area: a large notch length (i.e. a long seam weld compared to short seam weld with identical weld toe rounding) will lead to larger highly stressed surface and thus decrease the probability of survival.

In order to use this method, we need to refer to an effective stress, calculated by integrating the $\sigma_{eq,VM}$ over the micro-structural length ρ^* (to consider the geometrical size effect) in direction of the highest stress gradient $s(x, y, z)$, see fig 1.27.

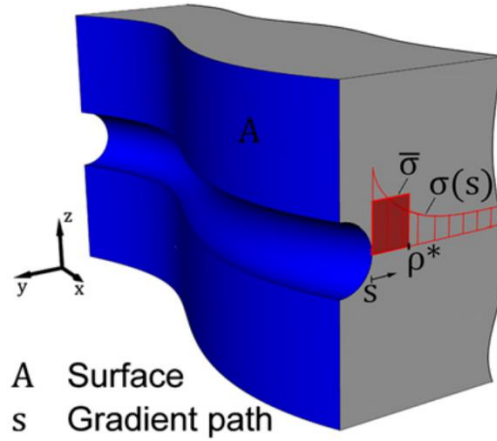


Figure 1.27: Combination of geometrical and statistical size effect, [6].

Kaffenberger and Vormwald reported this method in [6], starting from the averaged effective stress, obtained by dividing the integrated stress by ρ^* , eq 1.50.

$$\bar{\sigma}(x, y, z) = \frac{1}{\rho^*} \int_0^{\rho^*} \sigma(s(x, y, z)) ds \quad (1.50)$$

Then to consider the statistical size effect we consider Weibull's weakest link theory, which refers to the probability of finding a weak link in a certain volume. This means that the higher is the volume considered, the higher is the probability to find a defect. The probability of survival for specimens with inhomogeneous distribution is obtained using the Weibull distribution function, eq 1.51.

$$P_S(V_0) = e^{-\left(\frac{\sigma}{\sigma_0}\right)^\kappa} \quad (1.51)$$

$P_S(V_0)$ is the survival probability of a specimen with volume V_0 with an applied stress equal to σ . κ is the Weibull's modulus and σ_0 the normalization parameter. To relate the survival probability with the highly stressed surface instead of the highly stressed volume, the surface has to be divided into areas with homogeneous stress distributions so that a stress integral I_a could be calculated. It results:

$$P_S(A) = e^{\left[-\frac{I_A}{I_{A0}} \left(\frac{\sigma_{max}}{\sigma_0}\right)\right]^\kappa} \quad (1.52)$$

The stress integral could be written referring to the effective stresses from eq 1.53, instead of elastic ones.

$$I_{A,\rho^*} = \int \frac{\bar{\sigma}(x, y, z)}{\bar{\sigma}_{max}} dA \quad (1.53)$$

$\bar{\sigma}_{max}$ is the maximum effective stress while I_a represents the highly stressed surface, obtained by addition of weighted surface fractions. The integral could be expressed also with a summation, where A_ψ is the corresponding surface at node ψ .

$$I_{A,\rho^*} \approx \sum_{\psi} \left\{ \left(\frac{\sigma_{\psi}}{\sigma_{max}} \right)^\kappa A_{\psi} \right\} \quad (1.54)$$

Considering the depth of ρ^* we could derive an highly stressed volume:

$$I_{V,\rho^*} = \rho^* \int \frac{\bar{\sigma}(x,y,z)}{\bar{\sigma}_{max}} dA \quad (1.55)$$

The correction factor $n_{\rho^*,\kappa}$ is introduced to include both geometrical and statistical size effect; it is obtained by equating identical survival properties of two specimens of different size:

$$n_{\rho^*,\kappa} = \left(\frac{I_{V,\rho^*}}{I_A * \rho^*} \right)^{-\frac{1}{\kappa}} = \left(\frac{I_{A,\rho^*}}{I_{A,ref}} \right)^{-\frac{1}{\kappa}} \quad (1.56)$$

Finally, a weighted effective stress could be derived by eq 1.57:

$$\sigma_{\rho^*,\kappa} = \frac{\bar{\sigma}_{max}}{n_{\rho^*,\kappa}} \quad (1.57)$$

Inserting eq 1.53 in 1.55 afterwards in 1.57 the weighted effective stress could be written in eq 1.58.

$$\sigma_{\rho^*,\kappa} = \left\{ \sum_{\psi} \left(\sigma_{\rho^*,\psi}^{\kappa} \frac{A_{\psi}}{I_{A,ref}} \right) \right\}^{\frac{1}{\kappa}} \quad (1.58)$$

ρ^* : micro-structural length, material property.

κ : scatter parameter of Weibull distribution, material property.

A_{ψ} : corresponding surface for each node ψ .

$I_{A,ref}$: highly stressed reference surface, obtained by minimizing the scatter range of the S-N curve.

1.9 A new combined approach

The aim of the combination between the SSCH and the NuMeSiS is to propose an equivalent stress that takes into account not only the out-of-phase phenomenon, but also the geometrical and statistical size effects. The first problem is that the stress space curve hypothesis refers to two-dimensional stress state while the NuMeSiS hypothesis considers weighted effective stress belonging to critical surfaces. In particular, it fails in the calculation of the effective stress because in the notch proximity in the planar case we have a plane stress, while in a 3D notch the inside notch length is represented by plane strain. The solution is considering the free parameter α equal to one, obtaining the equivalent Von Mises stress multiplied by the out-of-phase factor, eq 1.59.

$$\sigma_{eq,SSCH} = \sigma_{eq,VM} * \left(1 + \frac{\rho * \lambda}{1 + \lambda^2} \right) \quad (1.59)$$

Once solved the problem with the SSC hypothesis it is time to deal with NuMeSiS. From the previous paragraph it is clear the higher it is κ , the lesser the statistical size effect is considered. So to turn off the statistical size effect it is necessary to allow exponent κ to approach infinite.

$$\lim_{\kappa \rightarrow \infty} \sigma_{\rho^*,\kappa} = \sigma_{\rho^*,max} \quad (1.60)$$

It is important to remark that $\sigma_{\rho^*,\kappa}$ is the maximum effective stress and, generally, it is different from the maximum Von Mises stress $\sigma_{eq,VM,max}$. In the new approach the maximum effective stress and the non-proportionally function, both based on Von Mises stresses, are combined. The resulting stress, including the geometrical size effect and the non-proportionally behaviour, is given in eq. 1.61.

$$\sigma_{\rho^*,SSCH} = \sigma_{\rho^*,max} * \left(1 + \frac{\rho * \lambda}{1 + \lambda^2} \right) \quad (1.61)$$

ρ^* : micro-structural length, material property.

ρ : non proportionally parameter, reference to tab 1.5.

1.10 Application to testing data

Vormwald in [1] calculated the equivalent stress, according to eq 1.61, and reported all the result in the report [8]. At this point it is possible to plot all the data of tested specimens in Wohler diagrams. The parameters were set: $\alpha=1$; $\rho^*=0,2$ mm and $\rho=1,6$. The graph below refers to a survival property of 50%, fig. 1.24. The scatter range of the scatter band with survival probabilities of 10% and 90% in strength direction was determined from the S-N curves.

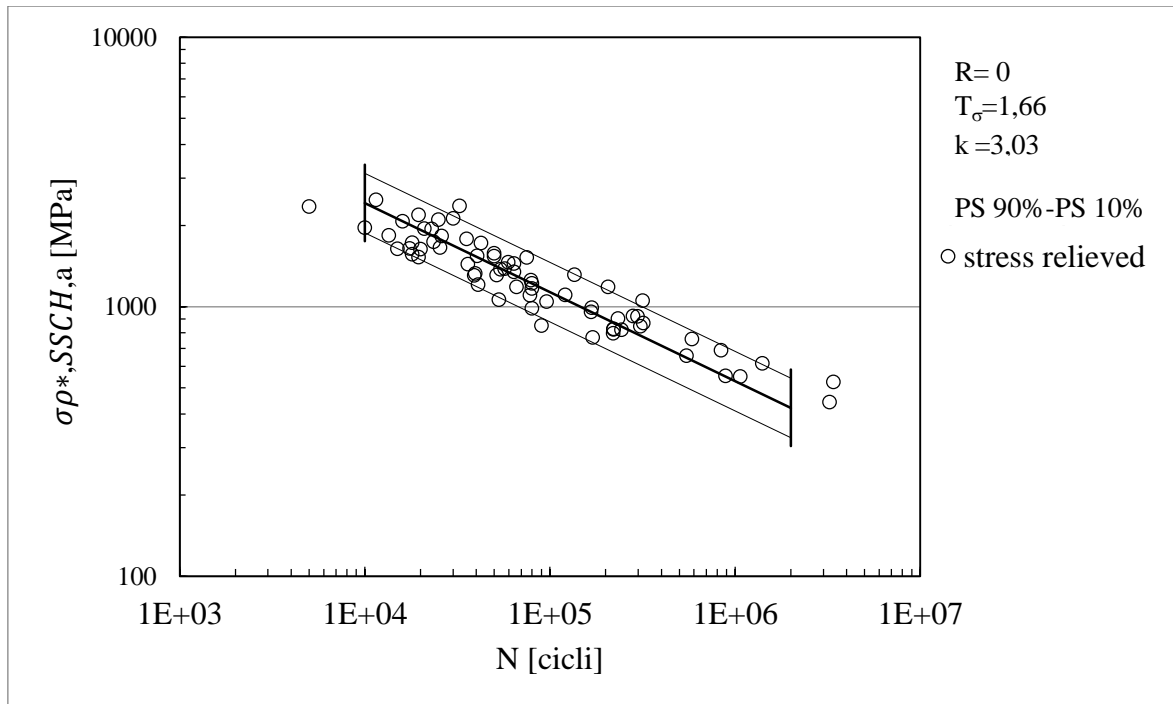


Figure 1.28: S-N curves for stress-relieved with cycle ratio R = 0.

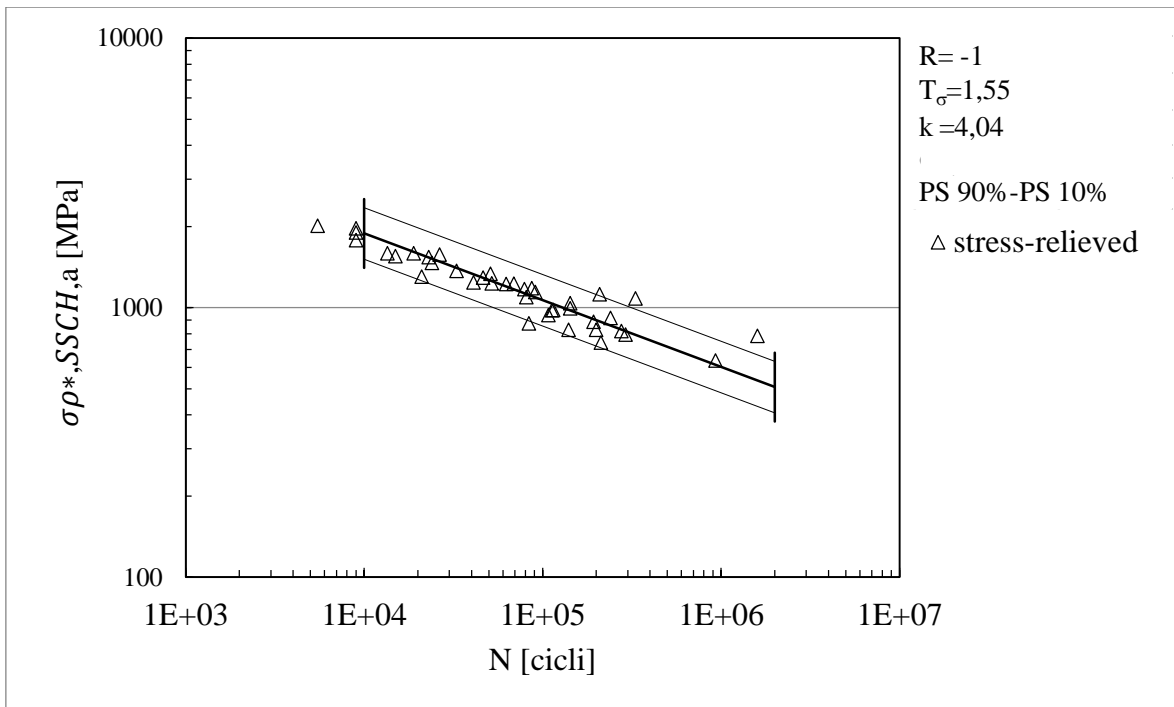


Figure 1.29: S-N curves for stress-relieved with cycle ratio $R = -1$.

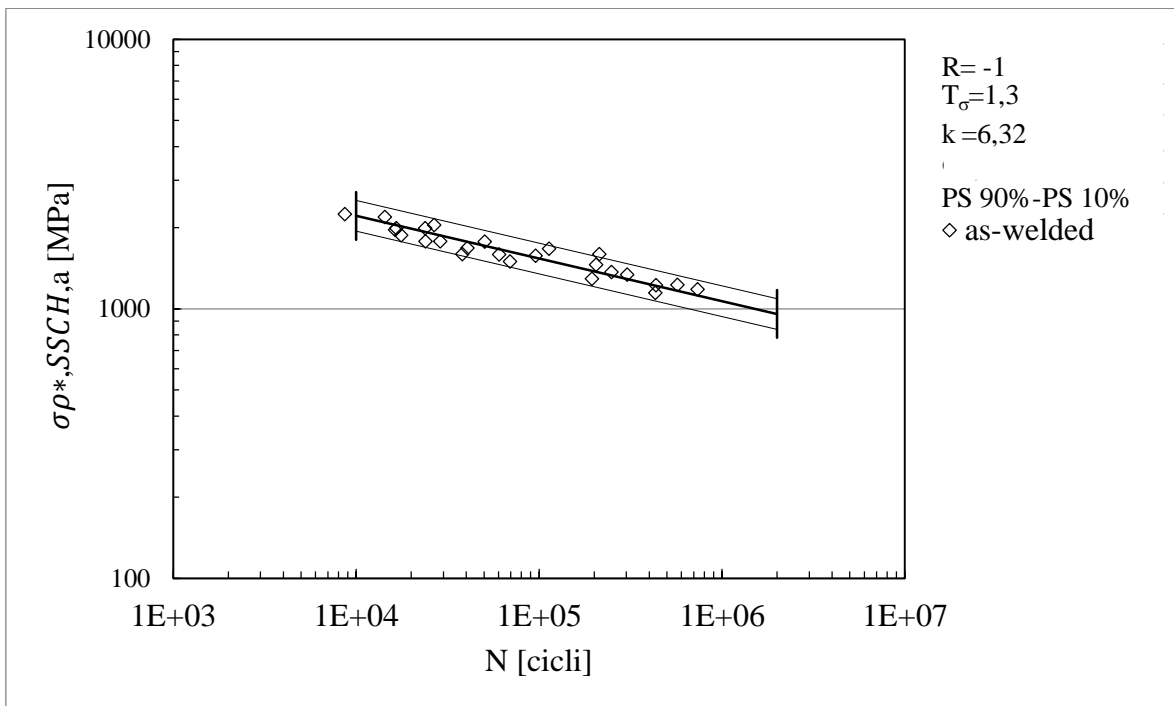


Figure 1.30: S-N curves for stress-relieved with cycle ratio $R = -1$.

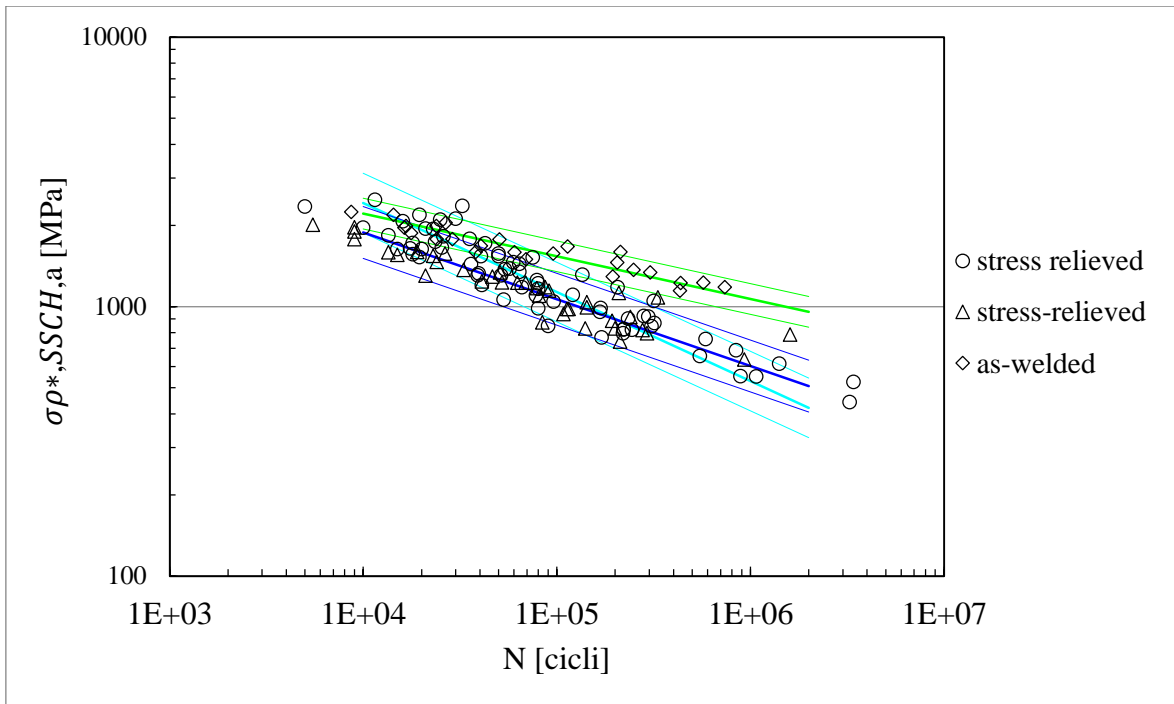


Figure 1.31 S-N curves for as-welded and stress-relieved specimens.

The application of NuMeSiS does not provide better scatter values than the conventional strength hypothesis like Tresca or Von Mises. However, thanks to the combined approach with SSCH, a satisfactory scatter range of 1,3 for specimens in as-welded condition could be achieved by setting the parameters: $\alpha=1$; $\rho^*=0,2$ mm and $\rho=1,6$.

CHAPTER 2:

The NSIF approach

2.1 Recall of linear elastic fracture mechanics

In many mechanical components there are sharp notches, for example in welded joints or in shafts housing sealing ring where even though there is a tip radius different from zero, its value is so small that the rounded notch has the same structural behaviour of a sharp one. Dealing with components weakened by a sharp V-notch, the fatigue life assessment needs to be studied in a different way from a point-wise approach. Indeed, when considering a sharp V notch the stress state will be infinite at the tip of the notch and this would lead to the impossibility for the component to carry any kind of loads, from the point of view of a point-wise approach. However, practice shows that even with a sharp V notch a certain amount of strength resistance is still available. In order to estimate it, here Williams equations are recalled by considering a polar coordinate system centred at the notch tip.

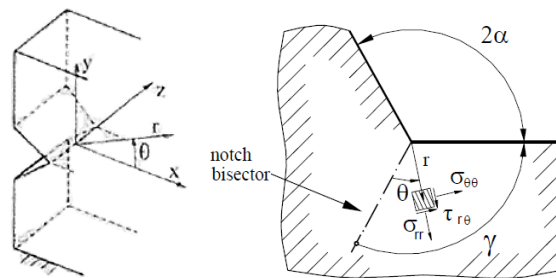


Figure 2.1: Sharp V-notch geometry and local coordinate system, [19].

2.1.1 Mode I: Opening

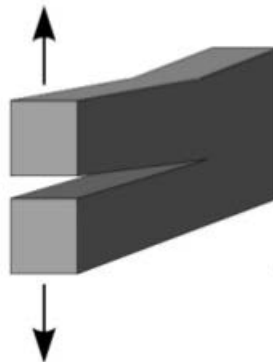


Figure 2.2: Mode I loaded structure.

$$\begin{Bmatrix} \sigma_{\theta\theta} \\ \sigma_{rr} \\ \tau_{r\theta} \end{Bmatrix} = \lambda_1 r^{\lambda_1-1} a_1 \left[\begin{Bmatrix} (1 + \lambda_1)\cos(1 - \lambda_1)\vartheta \\ (3 - \lambda_1)\cos(1 - \lambda_1)\vartheta \\ (1 - \lambda_1)\sin(1 - \lambda_1)\vartheta \end{Bmatrix} + \chi_1(1 - \lambda_1) \begin{Bmatrix} \cos(1 + \lambda_1)\vartheta \\ -\cos(1 + \lambda_1)\vartheta \\ \sin(1 + \lambda_1)\vartheta \end{Bmatrix} \right] \quad (2.1)$$

$$\chi_1 = \frac{-\sin[(1 - \lambda_1)\gamma]}{\sin[(1 + \lambda_1)\gamma]} \quad (2.2)$$

2.1.2 Mode II: in-plane shear

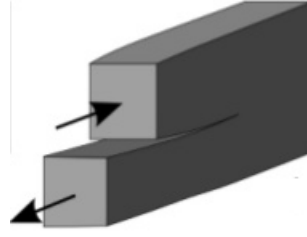


Figure 2.3: Mode II loaded structure.

$$\begin{Bmatrix} \sigma_{\theta\theta} \\ \sigma_{rr} \\ \tau_{r\vartheta} \end{Bmatrix} = \lambda_2 r^{\lambda_2-1} a_2 \left[\begin{Bmatrix} (1 + \lambda_2) \sin(1 - \lambda_2) \vartheta \\ (3 - \lambda_2) \sin(1 - \lambda_2) \vartheta \\ (1 - \lambda_2) \cos(1 - \lambda_2) \vartheta \end{Bmatrix} + \chi_2 (1 - \lambda_2) \begin{Bmatrix} \sin(1 + \lambda_2) \vartheta \\ -\sin(1 + \lambda_2) \vartheta \\ \cos(1 + \lambda_2) \vartheta \end{Bmatrix} \right] \quad (2.3)$$

$$\chi_2 = \frac{-\sin[(1 - \lambda_2)\gamma]}{\sin[(1 + \lambda_1)\gamma]} \quad (2.4)$$

λ_1 and λ_2 are Williams' eigenvalues, function of the notch opening angle, derived from the following equations and plotted in the graph below:

$$\begin{aligned} \lambda_1 \sin 2\gamma + \sin 2\lambda_1 \gamma &= 0 && \text{for mode I loading} \\ \lambda_2 \sin 2\gamma - \sin 2\lambda_2 \gamma &= 0 && \text{for mode II loading} \end{aligned}$$

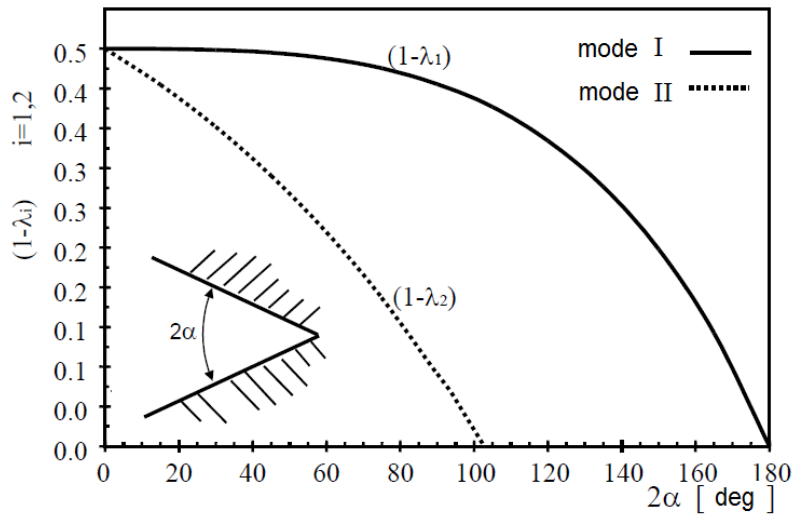


Figure 2.4: stress singularity in the proximity of a sharp V-notch.

Where $\gamma = \pi - \alpha$. In these equations the a_1 and the a_2 are parameters dependant on the loads and geometry. In order to estimate their values Gross and Mendelson defined the Notch Stress Intensity factors (NSIFs) with the following hypotheses: sharp V-notch, linear elastic isotropic and homogenous material and plane stress or plane strain condition. It results, respectively for mode I and II:

$$K_1^V = \sqrt{2\pi} \lim_{r \rightarrow 0^+} r^{1-\lambda_1} \sigma_{\theta\theta}(r, \vartheta = 0) \quad (2.5)$$

$$K_2^V = \sqrt{2\pi} \lim_{r \rightarrow 0^+} r^{1-\lambda_2} \tau_{r\vartheta}(r, \vartheta = 0) \quad (2.6)$$

Both NSIFs are calculated along the notch bisector line ($\vartheta = 0$), in this condition K_1^V depends only on the $\sigma_{\theta\theta}$ stress component, and K_2^V only on the $\tau_{r\vartheta}$ one; in any other zone near the notch there will be a relation between them. It is possible to calculate the a_1 and a_2 in relation to NSIFs, from eq 2.1 and eq 2.3:

$$\sigma_{\theta\theta}(r, \vartheta = 0) = \lambda_1 r^{\lambda_1 - 1} a_1 [(1 + \lambda_1) + \chi_1(1 - \lambda_1)] \quad (2.7)$$

$$\tau_{r\vartheta}(r, \vartheta = 0) = \lambda_2 r^{\lambda_2 - 1} a_2 [(1 - \lambda_2) + \chi_2(1 - \lambda_2)] \quad (2.8)$$

Inserting these last two equations in the NSIFs definitions, a_1 and a_2 are determined:

$$a_1 = \frac{K_1^V}{\sqrt{2\pi}\lambda_1[(1 + \lambda_1) + \chi_1(1 - \lambda_1)]} \quad (2.9)$$

$$a_2 = \frac{K_2^V}{\sqrt{2\pi}\lambda_2[(1 - \lambda_2) + \chi_2(1 - \lambda_2)]} \quad (2.10)$$

Eventually, inserting in Williams equations, it results:

Mode I:

$$\begin{Bmatrix} \sigma_{\theta\theta} \\ \sigma_{rr} \\ \tau_{r\vartheta} \end{Bmatrix} = \frac{r^{\lambda_1 - 1} K_1^V}{\sqrt{2\pi}[(1 + \lambda_1) + \chi_1(1 - \lambda_1)]} \left[\begin{Bmatrix} (1 + \lambda_1)\cos(1 - \lambda_1)\vartheta \\ (3 - \lambda_1)\cos(1 - \lambda_1)\vartheta \\ (1 - \lambda_1)\sin(1 - \lambda_1)\vartheta \end{Bmatrix} + \chi_1(1 - \lambda_1) \begin{Bmatrix} \cos(1 + \lambda_1)\vartheta \\ -\cos(1 + \lambda_1)\vartheta \\ \sin(1 + \lambda_1)\vartheta \end{Bmatrix} \right] \quad (2.11)$$

Mode II:

$$\begin{Bmatrix} \sigma_{\theta\theta} \\ \sigma_{rr} \\ \tau_{r\vartheta} \end{Bmatrix} = \frac{r^{\lambda_2 - 1} K_2^V}{\sqrt{2\pi}[(1 - \lambda_2) + \chi_2(1 - \lambda_2)]} \left[\begin{Bmatrix} (1 + \lambda_2)\sin(1 - \lambda_2)\vartheta \\ (3 - \lambda_2)\sin(1 - \lambda_2)\vartheta \\ (1 - \lambda_2)\cos(1 - \lambda_2)\vartheta \end{Bmatrix} + \chi_2(1 - \lambda_2) \begin{Bmatrix} \sin(1 + \lambda_2)\vartheta \\ -\sin(1 + \lambda_2)\vartheta \\ \cos(1 + \lambda_2)\vartheta \end{Bmatrix} \right] \quad (2.11)$$

In literature the last equations are resumed summing mode I and mode II contributes and simplified naming the terms in brackets as follows, eq 2.12:

$$\begin{Bmatrix} \sigma_{\theta\theta} \\ \sigma_{rr} \\ \tau_{r\vartheta} \end{Bmatrix} = \frac{K_1}{r^{1 - \lambda_1}} \begin{Bmatrix} \tilde{\sigma}_{\vartheta\vartheta}(\vartheta) \\ \tilde{\sigma}_{rr}(\vartheta) \\ \tilde{\tau}_{r\vartheta}(\vartheta) \end{Bmatrix}_1 + \frac{K_2}{r^{1 - \lambda_2}} \begin{Bmatrix} \tilde{\sigma}_{\vartheta\vartheta}(\vartheta) \\ \tilde{\sigma}_{rr}(\vartheta) \\ \tilde{\tau}_{r\vartheta}(\vartheta) \end{Bmatrix}_2 \quad (2.12)$$

2.1.3 Mode III: out-of-plane shear

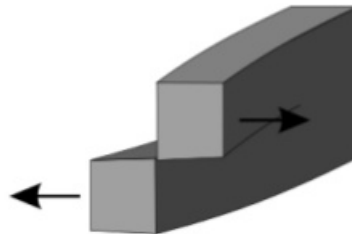


Figure 2.5: Mode III loaded structure.

The local distributions for mode III loading referred to a polar reference system (r, θ) centred at the V notch tip are the following:

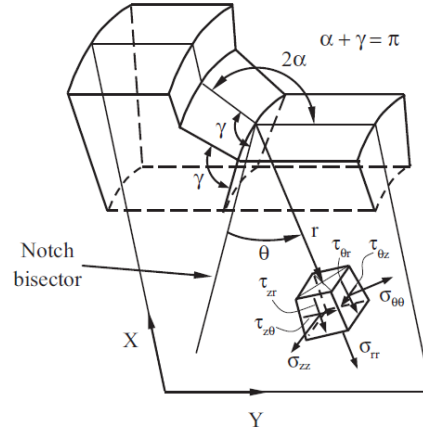


Figure 2.6: Polar reference system centered at the weld toe of a typical tube-to-flange welded joint geometry, [17].

$$\begin{Bmatrix} \tau_{\theta z} \\ \tau_{rz} \end{Bmatrix}_{\rho=0} = \frac{K_3}{\sqrt{2\pi}} r^{1-\lambda_3} \begin{Bmatrix} \cos(\lambda_3 \vartheta) \\ \sin(\lambda_3 \vartheta) \end{Bmatrix} \quad (2.13)$$

The mode III NSIF, K_3 , can be defined by extending the definitions of mode I and II NSIFs proposed by Gross and Mendelson:

$$K_3 = \sqrt{2\pi} \lim_{r \rightarrow 0^+} r^{1-\lambda_3} \tau_{\theta z}(r, \vartheta = 0) \quad (2.14)$$

Where λ_3 is the stress singularity exponent, which depends on the notch-opening angle 2α ($\gamma = \pi - \alpha$), according to eq 2.15:

$$\cos(\lambda_3 \gamma) = 0 \quad (2.15)$$

$$\lambda_3 = \frac{\pi}{2\gamma} \quad (2.16)$$

At this point it is possible to plot λ_1 , λ_2 and λ_3 in the same graph in function of the notch angle, plotted on the graph below, Fig. 2.7.

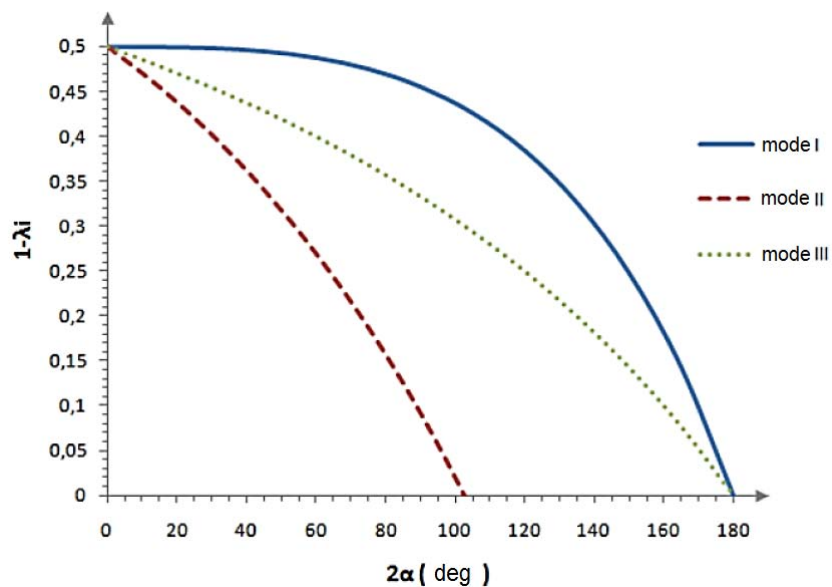


Figure 2.7: stress singularity in the proximity of a sharp V-notch, [20].

What is remarkable from this diagram is that with an opening angle equal or major than 102° the mode II is not singular anymore and its influence could be neglected. Meneghetti and Lazzarin have studied this last statement in [22] restricting this problem to non-load carrying fillet-welded joints having the geometry shown in fig 2.8 with $t = T$, $\phi = 45^\circ$, $h/T = 0.6$.

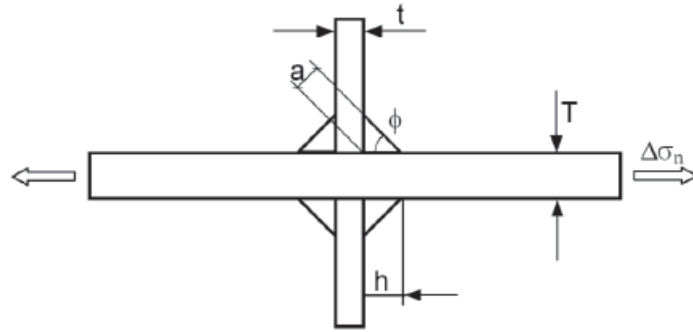


Figure 2.8: geometry of the non-load carrying fillet-welded joints.

The aim of this research was to bound the region where local stresses are described with good approximation only by the Mode I contribution. The circumstances in which Mode II stresses are negligible should be investigated for any radial line departing from the weld toe, not only along the free surface. This negligible condition could be interpreted by imposing the Mode II stresses 10% of the applied nominal stress as follows.

$$\frac{K_2}{r^{1-\lambda_2}} \left\{ \begin{array}{l} \tilde{\sigma}_{\vartheta\vartheta}(\vartheta) \\ \tilde{\sigma}_{rr}(\vartheta) \\ \tilde{\tau}_{r\vartheta}(\vartheta) \end{array} \right\}_2 = 0.1 \sigma_n \quad (2.17)$$

Mode II stress intensity factor has the following engineering expression:

$$K_2 = k_2 \sigma_n T^{1-\lambda_2} \quad (2.18)$$

k_2 is a non-dimensional coefficient given in [23], which depends on the joint geometry and the external loading mode. Substitution of Equation 2.18 into Equation 2.17 leads the following equations:

$$\frac{k_2}{\left(\frac{r}{T}\right)^{1-\lambda_2}} \left\{ \begin{array}{l} \tilde{\sigma}_{\vartheta\vartheta}(\vartheta) \\ \tilde{\sigma}_{rr}(\vartheta) \\ \tilde{\tau}_{r\vartheta}(\vartheta) \end{array} \right\}_2 = 0.1 \quad (2.19)$$

Which can be solved for the non-dimensional distance r/T as a function of the polar coordinate θ . Results are reported in fig 2.9 under the hypothesis of $\lambda_2 = 1.302$ ($2\alpha = 135^\circ$). Inside the dashed areas the following condition holds true, and then, in principle the contribution to the local stresses due to Mode II cannot be considered negligible:

$$\frac{K_2}{r^{1-\lambda_2}} \left\{ \begin{array}{l} \tilde{\sigma}_{\vartheta\vartheta}(\vartheta) \\ \tilde{\sigma}_{rr}(\vartheta) \\ \tilde{\tau}_{r\vartheta}(\vartheta) \end{array} \right\}_2 \geq 0.1 \sigma_n \quad (2.20)$$

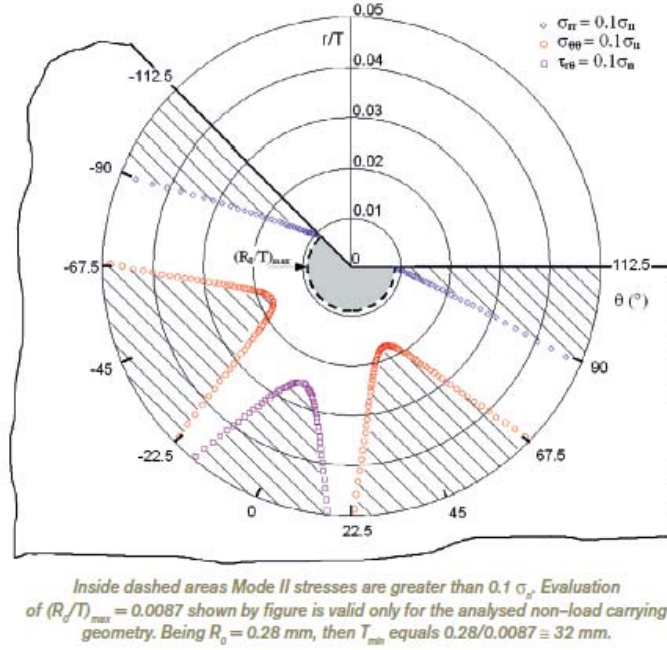


Figure 2.9: Limit paths where mode II stress components are ten percent the applied nominal stress, [22].

In the figure is shaded the maximus circle where eq (2.20) is still valid. The corresponding $(R_0/T)_{\max}$ value is $0.28/32 = 0.00875$. However, Figure 2.9 shows that even with a lower T , Mode II stresses are higher than 10% the applied nominal stress only in a very small region. Then it is believed that ignoring the non-singular contribute doesn't make a big concern in this particular geometry.

There are also cases where including the singular contributes of Mode I and Mode II is not enough, for example in the case of thin welded lap joints. In fact, Williams' equations have been simplified before, theoretically they would comprehend other terms:

$$\begin{Bmatrix} \sigma_{\theta\theta} \\ \sigma_{rr} \\ \tau_{r\vartheta} \end{Bmatrix} = \frac{K_I}{r^{1-\lambda_1}} \begin{Bmatrix} \tilde{\sigma}_{\vartheta\vartheta}(\vartheta) \\ \tilde{\sigma}_{rr}(\vartheta) \\ \tilde{\tau}_{r\vartheta}(\vartheta) \end{Bmatrix}_1 + \frac{K_{II}}{r^{1-\lambda_2}} \begin{Bmatrix} \tilde{\sigma}_{\vartheta\vartheta}(\vartheta) \\ \tilde{\sigma}_{rr}(\vartheta) \\ \tilde{\tau}_{r\vartheta}(\vartheta) \end{Bmatrix}_2 + \text{higher order terms} \quad (2.21)$$

Considering cracks ($2\alpha = 0^\circ$) and not sharp open V-notches we could distinguish the T-stress contribute, between all the others higher order terms, as follows on eq. 2.22.

$$\begin{Bmatrix} \sigma_{\theta\theta} \\ \sigma_{rr} \\ \tau_{r\vartheta} \end{Bmatrix} = \frac{K_I}{\sqrt{2\pi r}} \begin{Bmatrix} \cos^3\left(\frac{\vartheta}{2}\right) \\ -\frac{1}{4}\cos\left(\frac{3}{2}\vartheta\right) + \frac{5}{4}\cos\left(\frac{\vartheta}{2}\right) \\ \frac{1}{4}\sin\left(\frac{\vartheta}{2}\right) + \frac{1}{4}\sin\left(\frac{3}{2}\vartheta\right) \end{Bmatrix} + \quad (2.22)$$

$$+ \frac{K_{II}}{\sqrt{2\pi r}} \begin{Bmatrix} -3\sin\left(\frac{\vartheta}{2}\right)\cos^2\left(\frac{\vartheta}{2}\right) \\ \frac{3}{4}\sin\left(\frac{3}{2}\vartheta\right) - \frac{5}{4}\sin\left(\frac{\vartheta}{2}\right) \\ \frac{1}{4}\cos\left(\frac{\vartheta}{2}\right) + \frac{3}{4}\cos\left(\frac{3}{2}\vartheta\right) \end{Bmatrix} + T \begin{Bmatrix} \cos^2(\vartheta) \\ \sin^2(\vartheta) \\ -\frac{1}{2}\sin(2\vartheta) \end{Bmatrix} + O(r^{\frac{1}{2}})$$

Where K_I and K_{II} are the Stress Intensity factors, defined by Gross and Mendelson by means of eq. 2.23 and 2.24.

$$K_I = \sqrt{2\pi} \lim_{r \rightarrow 0^+} r^{0.5} \sigma_{\theta\theta}(r, \vartheta = 0) \quad (2.23)$$

$$K_{II} = \sqrt{2\pi} \lim_{r \rightarrow 0^+} r^{0.5} \tau_{r\vartheta}(r, \vartheta = 0) \tag{2.24}$$

The constant term T is a slit-parallel tensile or compressive stress, named ‘‘T-stress’’ by Larsson and Carlsson and can be defined by the following equation:

$$T = \lim_{r \rightarrow 0^+} [\sigma_{rr}(r, \vartheta = 0) - \sigma_{\theta\theta}(r, \vartheta = 0)] \tag{2.25}$$

The T-stress influence is relevant at the crack tip stress state and, not only in crack cases but also in presence of a sharp V-notch its contribute has to be studied properly. A very recent research shows that in case of short cracks the T-stress must be taken in account. We are in this conditions if:

$$\frac{a}{R_0} < 10 \tag{2.26}$$

Thanks to the definitions of NSIFs we can describe the stress state near the notch tip taking advantage of a finite number avoiding the singularity problem (i.e. infinite stress). These numbers could be used as a failure criterion: if one of them is major than a critical value the cracked or notched component will break. Because of the definitions of NSIFs, we are dealing with a local approach that takes into account the stress state at the notch tip and it is irrelevant which kind of load is the cause of it, the only thing that matters is the local stress state. Here it is a first problem: stress states belonging to different geometries, in terms of opening angles, could not be compared with NSIFs, it would not make a sense because of a different unit of measurement (Williams’ eigenvalues change with different opening angles).

Another issue is that the NSIFs are calculated considering the points located in the notch bisector line ($\theta=0$) and their calculation requires very refined meshes with an element size near the tip of the notch close to 10^{-5} mm. The procedure becomes more time-consuming in case of 3D components that cannot be analysed by means of two-dimensional models.

However, the NSIFs approach is valuable to summarize a lot of fatigue test data belonging to different geometries keeping constant the opening angle.

For example, many tests have been performed by Maddox, Gurney, Kihl and Sarkani of fillet welded joints with an opening angle of 135° and it is possible to plot these results in terms of mode I NSIF and cycles to failure. Here are reported the results for both structural steels and aluminium alloys as well. Concerning the steel joints, we recall here that the main plate thickness varied in a wide range, from 6 mm to 100 mm, while the attachment to main plate thickness ratio ranged from 0.03 to 8.8. The welded joints were made of structural steels with a yield stress varying from 360 to 670 MPa. Concerning the aluminum joints the main plate thickness varied from 3 to 24mm, while the attachment to main plate thickness ratio ranged from 0.25 to 1. The aluminum alloys belonged to the 5000 and 6000 series with a yield stress varying from 250 and 304 MPa. All fatigue results considered here are from welded joints under ‘as welded’ conditions, tested with a nominal load ratio close to zero.

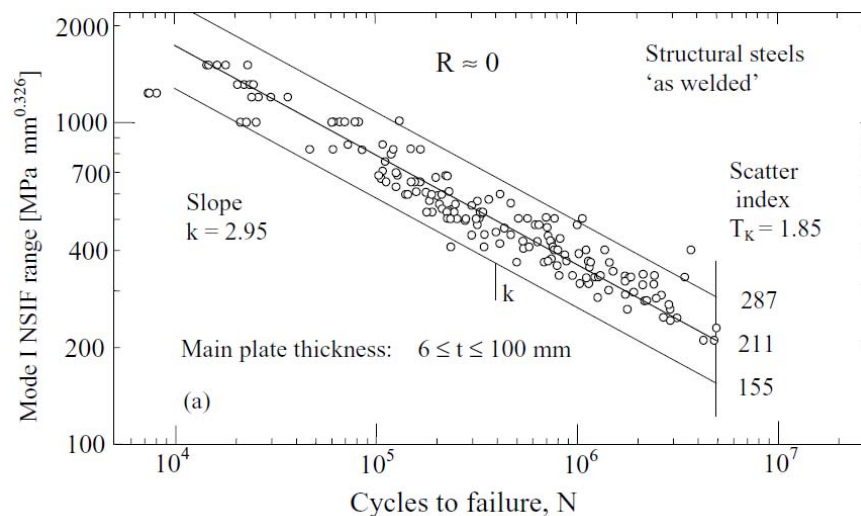


Figure 2.10 Fatigue strength of fillet-welded joints made of structural steels in terms of the Mode I NSIF [18].

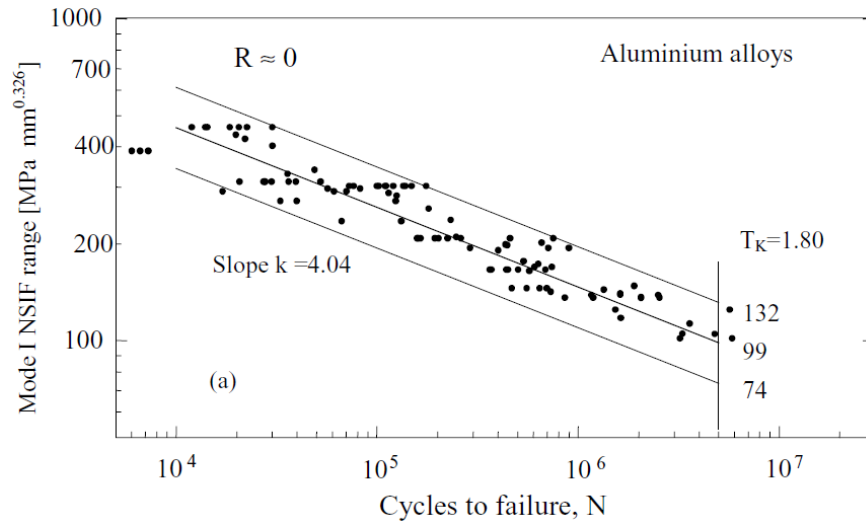


Figure 2.11 Fatigue strength of fillet-welded joints made of aluminium alloys in terms of the Mode I NSIF [18]

The scatter index was evaluated considering the 97.7% and the 2.3% probability of survival. These graphs show the capability of the NSIF approach to summarize the fatigue strength data in a single scatter band taking into account the size effect for both steel and aluminium alloy.

2.2 Fatigue of welded joints: from a nominal approach to a local one based on NSIFs

A first good application of the local approach is represented by the fatigue life assessment of transverse non-load-carrying fillet welds in an “as welded” condition. The 12 series exhibited large variations of plate thickness (from 13 to 100 mm), attachment size and bead height (see Table 2.1). Plotting the number of cycles to failure versus nominal stress ranges, as is usual in S–N diagrams, due to large variations in the geometrical parameters, the scatter of the experimental data is obviously very pronounced. In the same figure, the fatigue strength data are also given in terms of mode I NSIF neglecting the Mode II influence (very low in these kinds of joints, it is not singular). It is evident that the scatter greatly decreases, in particular in the high cycle fatigue. The same series were separately analyzed using the least squares method to determine mean curves and their intercepts for 5 000 000 cycles (Table 2.1). The scatter in fatigue strength of different geometries reduces from $\pm 40\%$ (the variation referring to the mean of the overall distribution) to $\pm 10\%$, assuming K_1 is a meaningful parameter in fatigue strength predictions. It is worth noting that we have forced the N-SIF approach to lifetime predictions and no longer to estimation of crack initiation, because it can give stress distributions along all directions and therefore also take into account the stress distribution along the actual crack propagation path.

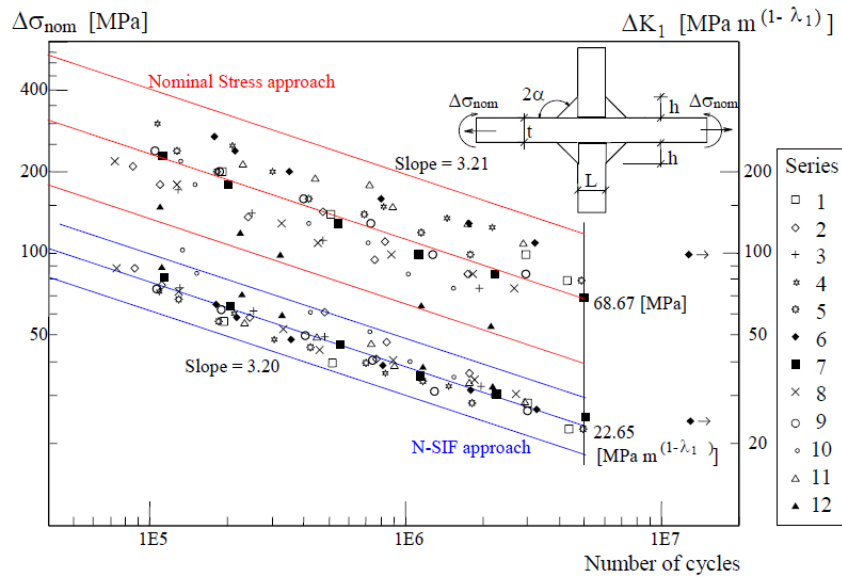


Figure 2.12. Fatigue strength in terms of nominal stress and N-SIF ranges, [22].

Series	t [mm]	h [mm]	L [mm]	$\Delta\sigma$ [MPa]	$\Delta\%$	ΔK_I [MPa m ^{0.326}]	$\Delta\%$
1	13	8	10	79.52	16	22.04	-3
2	50	16	50	59.64	-13	25.02	10
3	100	16	50	55.47	-19	23.56	4
4	13	5	3	91.70	34	21.62	-5
5	13	10	8	76.68	12	21.24	-6
6	25	5	3	93.92	37	22.19	-2
7	25	9	32	66.02	-4	23.04	2
8	25	15	220	59.72	-13	23.59	4
9	38	8	13	68.89	0	20.84	-8
10	38	15	220	45.46	-34	20.86	-8
11	100	5	3	95.70	39	24.34	7
12	100	15	220	40.09	-42	23.22	2

Table 2.1. Transverse non-load-carrying welded joints (Refs [10,11]) giving geometrical parameters, fatigue strength ranges at 5×10^6 cycles and differences in percent with respect to the mean value of the overall distribution, [22].

As it was said before, a comparison in terms of NSIFs requires a constant opening angle to guarantee the same unit of measurement. For example considering a transverse load-carrying fillet welds there will be one crack initiation point at the toe ($2\alpha=135^\circ$; NSIF's measurement unit is $\text{MPa m}^{0.326}$) and a second one at the root ($2\alpha=0^\circ$; NSIF's measurement unit is $\text{MPa m}^{0.5}$).

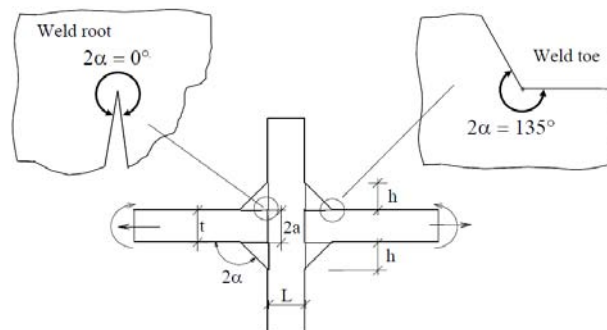


Figure 2.13: load carrying cruciform joint, [22].

It is necessary a further step to solve this problem and the solution is given by an energetic approach: the strain energy density (SED).

2.3 The strain energy density (SED) approach

The energetic criterion was first proposed by Lazzarin and Zambardi in [20] to restore the comparability of potential crack initiation points. Lazzarin et al. assumed a structural volume having circular shape with radius R_0 as shown in Fig. 2.14 and provided the closed-form expression of the averaged SED parameter as a function of the relevant NSIFs.

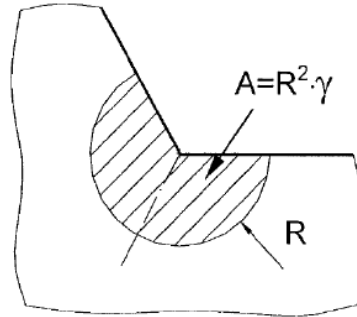


Figure 2.14: Structural volume for the calculation of SED

Dealing with a general multiaxial fatigue loading situation (mixed mode I + II + III loading), the Strain Energy Density averaged over the control volume can be expressed as follows:

$$\Delta\bar{W} = c_{w1} \frac{e_1}{E} \left[\frac{\Delta K_1}{R_0^{1-\lambda_1}} \right]^2 + c_{w2} \frac{e_2}{E} \left[\frac{\Delta K_2}{R_0^{1-\lambda_2}} \right]^2 + c_{w3} \frac{e_3}{E} \left[\frac{\Delta K_3}{R_0^{1-\lambda_3}} \right]^2 \quad (2.26)$$

Where E is the modulus of elasticity, e_1 , e_2 and e_3 are known parameters which depend on the notch opening angle 2α and on the Poisson's ratio ν , while ΔK_1 , ΔK_2 and ΔK_3 are the ranges of the NSIFs (maximum value minus minimum value). Relation 2.27 is not valid in case of short cracks, when the T-stress contribute cannot be neglected. We are in this conditions if:

$$\frac{a}{R_0} < 10 \quad (2.27)$$

Where a is the crack length and R_0 the control radius. Dealing with mixed mode crack problems under plane strain conditions and in case of as-welded specimens, the updated expression for the Strain Energy Density, eq. 2.28, is:

$$\Delta\bar{W} = \frac{e_1 K_I^2}{E R_0} + \frac{e_2 K_{II}^2}{E R_0} + \frac{1-\nu^2}{2E} T^2 + \frac{8\sqrt{2}}{15 * (\pi)^{3/2}} \frac{(1+\nu)(2-5\nu)}{E} \frac{K_I T}{\sqrt{R_0}} \quad (2.28)$$

Where K_I , K_{II} and K_{III} are the Stress Intensity Factors (SIFs) and T is the constant defined by eq. 2.25. In Eq.2.27, strain energies due to mode I, II and III, respectively, can be simply summed up, mutual terms being null. Below, in table 2.2, are reported the values of the coefficients for selected notch opening angles 2α and with reference to two values of the Poisson's ratio, namely $\nu=0.33$ (aluminium alloys) and $\nu=0.3$ (structural steels); e_1 , e_2 and e_3 are referred to plane strain conditions. Lazzarin and Livieri in 2005 demonstrated that the control radius R_0 was 0.28 mm for arc-welded joints made of structural steel and 0.12 mm for those made of aluminium alloy. These values are obtained imposing the equality of strain energy density between a smooth specimen and a notched one. It is worth remarking that in this last calculation the welded structures' properties were considered because during a welding process all the local material characteristics are altered.

2α (°)	λ_1	$R_0=0.12$ mm e_1	$R_0=0.28$ mm e_1
0	0.500	0.125	0.133
90	0.544	0.138	0.145
120	0.616	0.124	0.129
135	0.674	0.113	0.118

Table 2.2: Values of Mode I constants, [21].

2α (°)	λ_2	$R_0=0.12$ mm e_2	$R_0=0.28$ mm e_2
0	0.500	0.337	0.340

Table 2.3: Values of Mode II constants, [21].

2α (°)	λ_3	$R_0=0.12$ mm e_3	$R_0=0.28$ mm e_3
0	0.500	0.423	0.414
90	0.666	0.317	0.310
120	0.750	0.282	0.276
135	0.800	0.265	0.259

Table 2.4: Values of Mode III constants, [21].

Lazzarin, Sonsino and Zambardi in 2004 dealt with the c_w coefficient, discovering that is dependent on the nominal load ratio R , according to the following expression:

$$c_w(R) = \begin{cases} \frac{1 + R^2}{(1 - R)^2} & \text{if } -1 \leq R \leq 0 \\ \frac{1 - R^2}{(1 + R)^2} & \text{if } 0 \leq R < 1 \end{cases} \quad (2.29)$$

These equations are valid in stress-relieved conditions, while in case of as-welded structures $c_w=1$, because the experimental evidence shows that their fatigue behavior is independent from the load ratio of the applied external loads. In particular in stress relieved specimens, the parameter c_w equals 0.5 for $R=-1$.

Thanks to the knowledge of all these parameters it is possible to calculate the Strain Energy Density in every fatigue crack initiation point, for example in a transverse welded joint. In particular SED restores the possibility of comparing fatigue root and toe failures because of the same unit of measurement (that of an energy). In Fig 2.15 900 fatigue failure data at the root side as well as at the toe side are reported in the same graph.

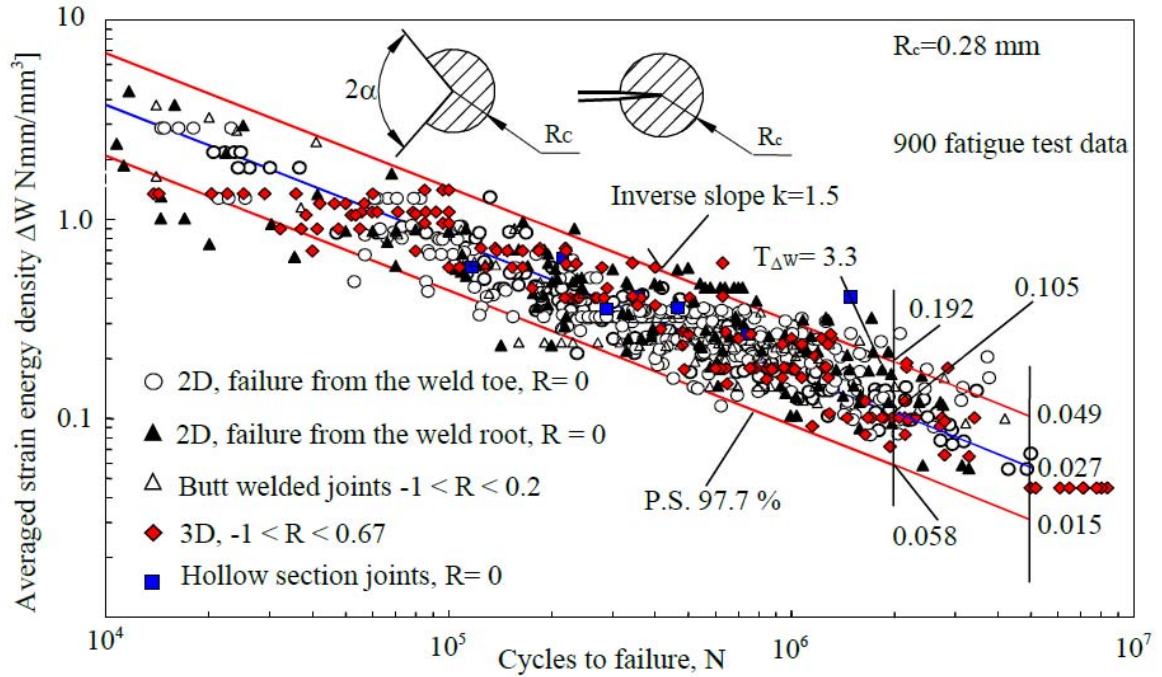


Figure 2.15: Design scatter band using the SED approach.

The Strain Energy Density is proportional to the square of the nominal stress, so in a double logarithmic scale the inverse slope will be the half of the one proposed in literature, so it will be 1.5. Lazzarin and co-workers demonstrated that it is possible to calculate the averaged SED numerically by adopting coarse meshes with few elements within the control volume. However, even though the calculations will be less time-consuming, the control volume must be modelled. A further development is represented by the Peak Stress Method (PSM), that gives the possibility of calculating the NSIFs without the control volume and with coarser meshes. Moreover, the PSM evaluates only the singular linear elastic peak stresses evaluated at the V-notch tip.

2.4 The Peak Stress Method (PSM)

The Peak Stress Method is a simplified, FE method to quickly estimate the NSIFs values using coarse meshes. This approach was originally proposed by Nisitani and Teranishi to estimate the Mode I SIF (Stress Intensity Factor) of cracks, then Meneghetti and Lazzarin extended this method for sharp V notches. More precisely the authors who originally proposed the method showed that the linear elastic peak stress evaluated at the crack tip is proportional to the Mode I SIF. A further step forward was made widening this theory to sharp V-shaped notches where the local stress parameters, called NSIFs, were discovered to be dependent to the elastic peak stress as well. The PSM expressions estimate the NSIFs K_I , K_{II} and K_{III} from the singular, linear elastic, opening ($\sigma_{\theta\theta, \theta=0, peak}$), in-plane shear ($\tau_{r\theta, \theta=0, peak}$) and out-of-plane shear ($\tau_{\theta z, \theta=0, peak}$) FE peak stresses, which are referred to the V-notch bisector line. In more detail the following expression were previously validated:

$$K_{FE}^* = \frac{K_I}{\sigma_{\theta\theta, \theta=0, peak} d^{1-\lambda_1}} \quad (2.30)$$

$$K_{FE}^{**} = \frac{K_{II}}{\tau_{r\theta, \theta=0, peak} d^{0.5}} \quad (2.31)$$

$$K_{FE}^{***} = \frac{K_{III}}{\tau_{\theta z, \theta=0, peak} d^{1-\lambda_3}} \quad (2.32)$$

Dealing with the Mode II case, the Peak Stress Method is valid only in crack cases, not for sharp V notches. In previous equations, d is “the global element size”, which is the average size of the finite elements to input in the numerical code before running the free mesh generation algorithm. The values of NSIFs are intended to be the “right” ones calculated from the definition, eqs. 2.5, 2.6 and 2.14. Firstly, these equations were calibrated by using Ansys® FE code (a is the crack length and d the global element size) and their values are:

$$K_{FE}^* = 1.38 \pm 3\% \tag{2.33}$$

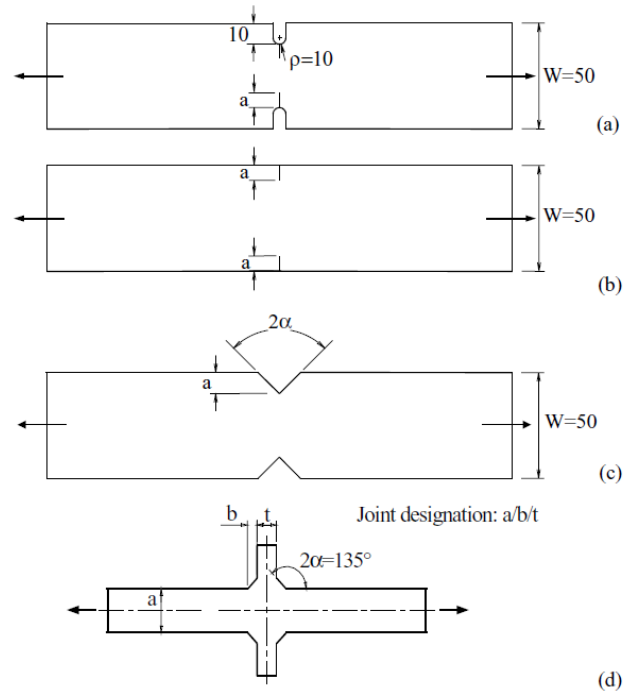


Figure 2.16: sharply notched geometries used to investigate the range of applicability of the peak stress method (all dimensions in mm), [18].

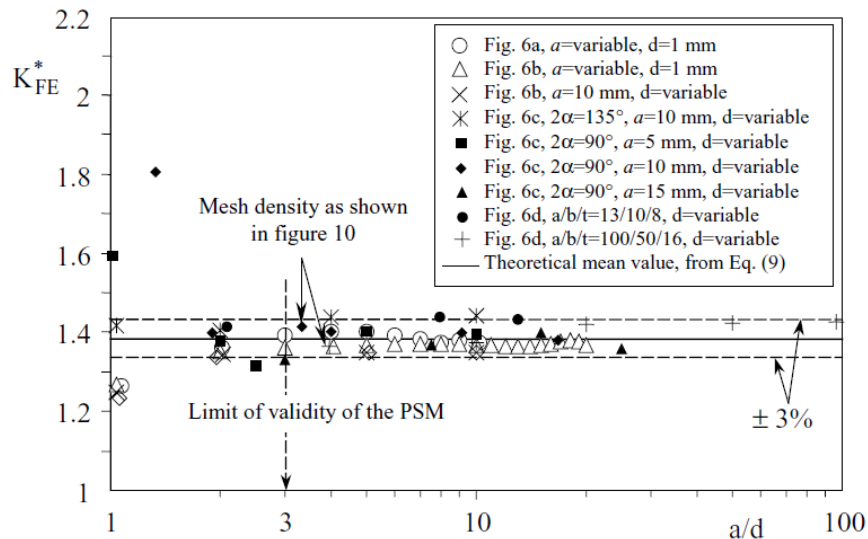


Figure 2.17: Non-dimensional K_{FE}^* ratio as evaluated from 61 FE analyses (see Fig. 6 for all models), [18].

$$K_{FE}^{**} = 3.38 \pm 3\% \quad (2.34)$$

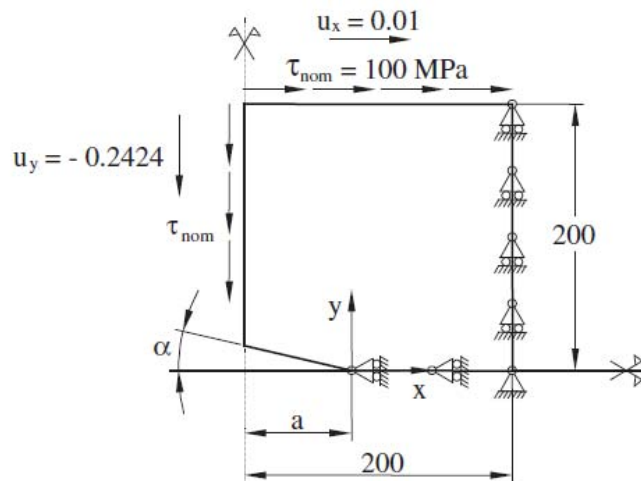


Figure 2.18: Geometry and loading condition of the analysed mode II crack problem. Dimensions and applied displacements in mm, [18].

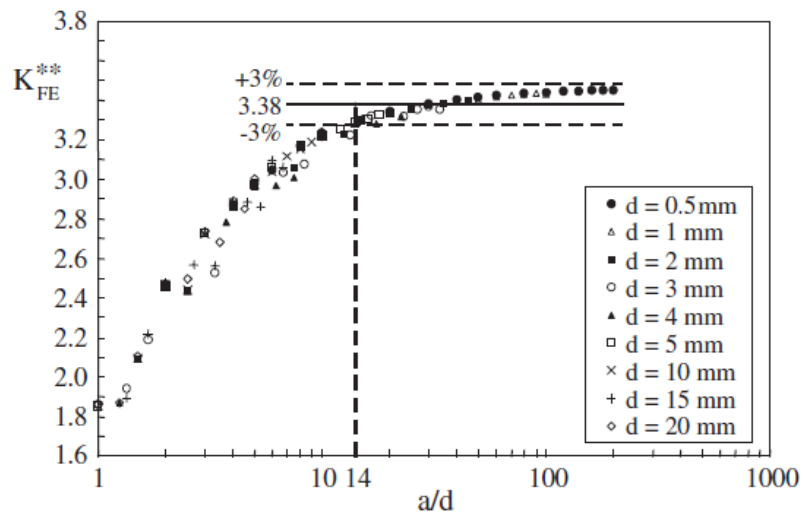


Figure 2.19: Calibration of the PSM approach for a crack ($2\alpha = 0^\circ$) under mode II loading. Finite element analyses performed by using the free mesh algorithm (as implemented in Ansys® code) with a mean element size d , [18].

$$K_{FE}^{***} = 1.93 \pm 3\% \quad (2.35)$$

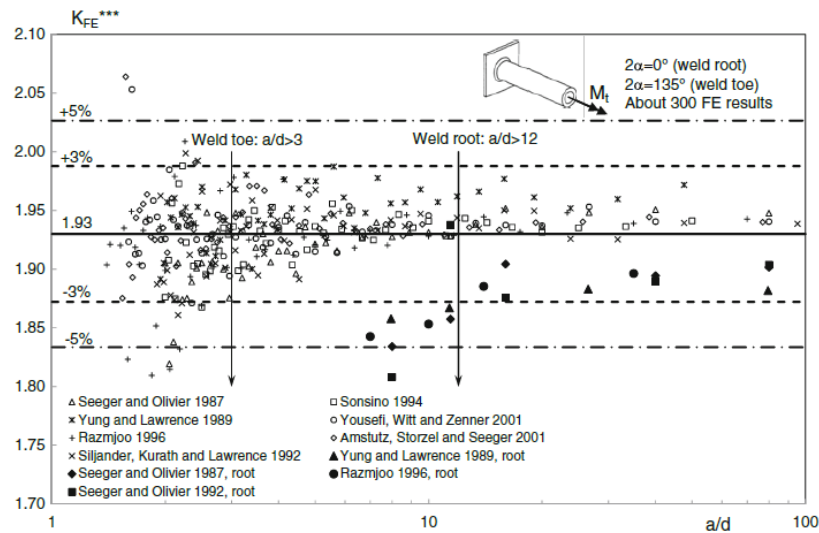


Figure 2.20: Calibration of the PSM applied at the weld toe ($2\alpha=135^\circ$) and at the weld root ($2\alpha=0^\circ$) of tube-to-plate welded joints (a is the tube thickness). The two-dimensional, axisymmetric geometries were discretized with a free mesh of PLANE 25 FE elements available in the Ansys® element library (d is the mean value of the FE size), [17].

Latest articles update these three values in case of different FEM software, for example Abaqus, Nastran and Straus7. Dealing with Ansys® the calibration constants were obtained under four hypothesis; each of them must be fulfilled to recalculate these factors.

1. Concerning Eqs. (2.30) and (2.31), use of two-dimensional, 4-node quadrilateral finite elements with linear shape functions, as implemented in ANSYS FE code (PLANE 42 or alternatively PLANE 182 with K-option 1 set to 3). Concerning Eq. (2.26), use of two-dimensional, harmonic, 4-node linear quadrilateral elements, as implemented in ANSYS FE code (PLANE 25). Finally, the use of three-dimensional, eight-node brick elements (SOLID 185 with K-option 2 set to 3 of Ansys Element Library) is allowed for all loading modes, i.e. for Eqs. (2.30)–(2.32);
2. The FE mesh pattern close to the notch or crack tip must be generated following these instructions: four elements must share the node located at the notch tip if the notch opening angle 2α is equal to or lower than 90° (typically at the weld root $2\alpha = 0$), while two elements must share the node at notch tip when the notch opening angle is greater than 90° (typically at the toe side $2\alpha = 135^\circ$). The mesh patterns, according to the PSM, are automatically generated by the free mesh generation algorithm available in ANSYS_ software, so that only the 'global element size' parameter d must be input by the FE analyst.
3. Eqs. (2.30) and (2.32) can be applied to V-notches with an opening angle 2α between 0° and 135° ; while Eq. (2.31) is restricted to the crack case ($2\alpha = 0^\circ$);
4. For mode I loading (Eq. 2.31), the mesh density ratio a/d that can be adopted in FE analyses must exceed 3 to obtain $K_{FE}^* = 1.38 \pm 3\%$. For mode II loading more refined meshes are needed, the mesh density ratio a/d having to be greater than 14 to obtain $K_{FE}^{**} = 3.38 \pm 3\%$. Finally, in the case of mode III loading (Eq. (2.32)), the mesh density ratio must be $a/d \geq 3$ at the weld toe (where $2\alpha = 135^\circ$) and $a/d \geq 12$ at the root side (where $2\alpha = 0^\circ$), to get $K_{FE}^{***} = 1.93 \pm 3\%$. In previous definitions of the ranges of applicability, the reference dimension a has the following meanings: when the root side is of interest, a is the minimum between the crack length (l in Fig. 2.21), the ligament length (z in Fig. 2.21) and the thickness (t in Fig. 3), while a is always the thickness (t in Fig. 2.21) when assessing the toe side.

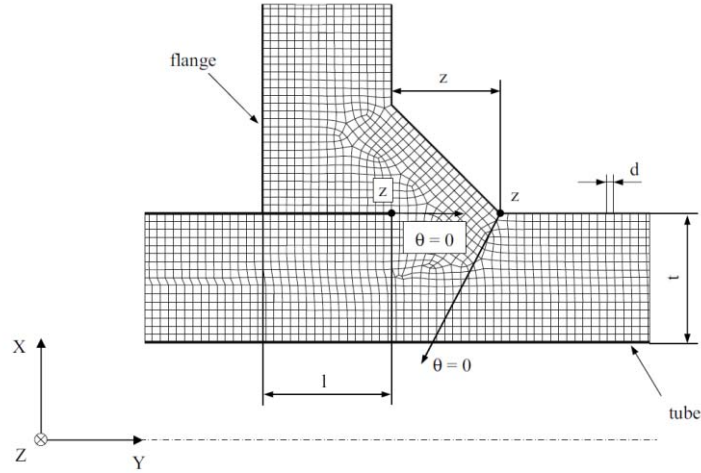


Figure 2.21. Typical 2D FE mesh to apply the PSM; the example reported in the figure shows a tube-to-flange fillet welded joint. Four-node, quadrilateral, harmonic PLANE 25 elements available in Ansys® Element Library were adopted to generate the free mesh shown in the figure. The Y-axis is the axis of the tube, [21].

2.4.1 The peak stress method using 3D finite element models

Originally the PSM was calibrated with 2D models and only in recent studies it was extended to 3D FE models. In summary it was demonstrated that K_{FE} values given by expressions 2.30 and 2.31 using 3D FE models meshed with eight-node brick elements are equal to those calculated from four node quadrilateral elements. Considering 2D plane elements with four node, the displacement field is described by means of linear shape functions according to the classical formulation:

$$u(\xi; \eta) = \sum_{i=1}^4 N_i(\xi; \eta) u_i \quad (2.36)$$

$$N_i(\xi; \eta) = \frac{1}{4} (1 + \xi \xi_i) (1 + \eta \eta_i) \quad (2.37)$$

According to Fig. 2.22a, $u = u(\xi; \eta)$ is the displacement field in the element, ξ and η are the natural element coordinates varying between -1 and +1, $N_i(\xi; \eta)$ are the element's shape functions and $u_i = u(\xi_i, \eta_i)$ is the displacement at node i .

Considering now an eight-node, 3D FE, as shown in Fig. 2.22b, the displacement field in the element is described by the following expression:

$$u(\xi; \eta; \zeta) = \sum_{i=1}^8 N_i(\xi; \eta; \zeta) u_i \quad (2.38)$$

$$N_i(\xi; \eta; \zeta) = \frac{1}{8} (1 + \xi \xi_i) (1 + \eta \eta_i) (1 + \zeta \zeta_i) \quad (2.39)$$

Where (ξ, η, ζ) are the natural element coordinates varying between -1 and +1. If a plane having constant $\zeta = \bar{\zeta}$ coordinate is considered, expression 2.37 becomes:

$$\bar{u} = \sum_{i=1}^4 \frac{2}{8} (1 + \xi \xi_i) (1 + \eta \eta_i) \frac{(1 - \bar{\zeta}) u_i + (1 + \bar{\zeta}) u_{i+4}}{2} \quad (2.40)$$

By indicating:

$$\bar{u}_i = \frac{(1 - \bar{\zeta}) u_i + (1 + \bar{\zeta}) u_{i+4}}{2} \quad i = 1, \dots, 4 \quad (2.41)$$

The displacement evaluated along the element edge between node i and node $i + 4$ at the point where $\xi = \bar{\xi}$, Eq. 2.40 becomes:

$$\bar{u} = \sum_{i=1}^4 \frac{1}{4} (1 + \xi \bar{\xi}_i)(1 + \eta \eta_i) \bar{u}_i \quad (2.42)$$

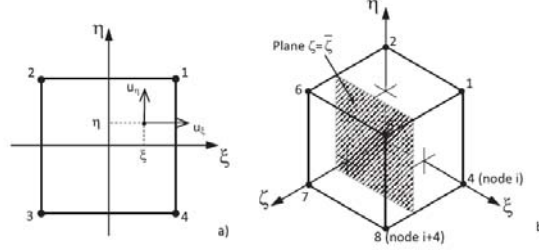


Figure 2.22: Four-node plane element (a); eight-node solid element and cutting plane where local stresses are evaluated (b), [16].

What is worth noting in this last expression is that it coincides with the displacement field of the four-node element Eq 2.36. Therefore, for the same in-plane mesh pattern and under pure plane stress or pure plane strain conditions, 2D models meshed with four-node elements and 3D models meshed with eight-node elements will deliver the same elastic peak stresses. In case of complex 3D models it is recommended to use a coarse mesh of 10-node pyramid elements for the main model geometry, and a sub-model meshed with 8-node brick elements to respect PSM hypothesis. Furthermore, where is possible, the sub-model mesh or, in general, the one surrounding the notch tip is suggested being obtained by extrusion of a 2D mesh created with the free mesh generator algorithm, using as input the so-called global element size. Sometimes, in case of particular geometries, mapped meshes are required worsening the reliability of the Peak Stress Method, increasing errors in range from 6% to 7%.

2.5 A link between the Peak Stress Method and the averaged value of the local strain energy density (SED)

The PSM proposes an alternative formulation of the exact NSIFs that could be insert in the expression of the averaged SED that will be function of the singular, linear elastic FE peak stresses $\sigma_{\vartheta\vartheta, \vartheta=0, peak}$, $\tau_{r\vartheta, \vartheta=0, peak}$ and $\tau_{\vartheta z, \vartheta=0, peak}$. Furthermore, in plane strain condition, an equivalent peak stress can be expressed as follows:

$$\begin{aligned} \Delta \bar{W} = & c_{w1} \frac{e_1}{E} \left[K_{FE}^* \Delta \sigma_{\vartheta\vartheta, \vartheta=0, peak} \left(\frac{d}{R_0} \right)^{1-\lambda_1} \right]^2 \\ & + c_{w2} \frac{e_2}{E} \left[K_{FE}^{**} \Delta \tau_{r\vartheta, \vartheta=0, peak} \left(\frac{d}{R_0} \right)^{1-\lambda_2} \right]^2 \\ & + c_{w3} \frac{e_3}{E} \left[K_{FE}^{***} \Delta \tau_{\vartheta z, \vartheta=0, peak} \left(\frac{d}{R_0} \right)^{1-\lambda_3} \right]^2 \rightarrow = \frac{1-v^2}{2E} \Delta \sigma_{eq, peak}^2 \end{aligned} \quad (2.43)$$

Therefore the following expression of the equivalent peak stress is obtained:

$$\Delta \sigma_{eq, peak} = \sqrt{c_{w1} f_{w1}^2 \Delta \sigma_{\vartheta\vartheta, \vartheta=0, peak}^2 + c_{w2} f_{w2}^2 \Delta \tau_{r\vartheta, \vartheta=0, peak}^2 + c_{w3} f_{w3}^2 \Delta \tau_{\vartheta z, \vartheta=0, peak}^2} \quad (2.44)$$

If we are dealing just with Mode I:

$$\Delta \sigma_{eq, peak} = f_{w1} \Delta \sigma_{\vartheta\vartheta, \vartheta=0, peak} \quad (2.45)$$

The correction parameters f_{w1} , f_{w2} and f_{w3} weight the peak stress both around the tip and along the radial direction, θ and r coordinates respectively. Their expressions are:

$$f_{w1} = K_{FE}^* \sqrt{\frac{2e_1}{1-\nu^2}} \left(\frac{d}{R_0}\right)^{1-\lambda_1} \quad (2.46)$$

$$f_{w2} = K_{FE}^{**} \sqrt{\frac{2e_2}{1-\nu^2}} \left(\frac{d}{R_0}\right)^{1-\lambda_2} \quad (2.47)$$

$$f_{w3} = K_{FE}^{***} \sqrt{\frac{2e_3}{1-\nu^2}} \left(\frac{d}{R_0}\right)^{1-\lambda_3} \quad (2.48)$$

Tables 1–3 report the values of f_{w1} , f_{w2} and f_{w3} , respectively where three values of the average FE size, namely $d = 0.2$ mm, 0.50 mm and 1 mm, different notch opening angles 2α and two values of the control radius for SED evaluation (i.e. $R_0 = 0.28$ mm for structural steels and 0.12 mm for aluminium alloys, have been taken into account).

2α (°)	λ_1	$R_0=0.12$ mm		$R_0=0.28$ mm	
		$f_{w1,d=0.2mm}^b$	$f_{w1,d=1mm}^b$	$f_{w1,d=0.5mm}^c$	$f_{w1,d=1mm}^c$
0	0.500	0.944	2.109	0.997	1.410
90	0.544	0.969	2.019	1.015	1.392
120	0.616	0.886	1.644	0.918	1.198
135	0.674	0.821	1.387	0.849	1.064

^b values calculated with $\nu=0.33$, $K_{FE}^* = 1.38$

^c values calculated with $\nu=0.3$, $K_{FE}^* = 1.38$

Table 2.5: values of Mode I constants, [21].

2α (°)	λ_2	$R_0=0.12$ mm		$R_0=0.28$ mm	
		$f_{w2,d=0.2mm}^b$	$f_{w2,d=1mm}^b$	$f_{w2,d=0.5mm}^c$	$f_{w2,d=1mm}^c$
0	0.500	3.795	8.480	3.904	5.522

^b values calculated with $\nu=0.33$, $K_{FE}^{**} = 3.38$

^c values calculated with $\nu=0.3$, $K_{FE}^{**} = 3.38$

Table 2.6: values of Mode II constants, [21].

2α (°)	λ_3	$R_0=0.12$ mm		$R_0=0.28$ mm	
		$f_{w3,d=0.2mm}^b$	$f_{w3,d=1mm}^b$	$f_{w3,d=0.5mm}^c$	$f_{w3,d=1mm}^c$
0	0.500	2.428	5.431	2.459	3.478
90	0.666	1.931	3.303	1.933	2.436
120	0.750	1.745	2.610	1.737	2.065
135	0.800	1.649	2.273	1.634	1.877

^b values calculated with $\nu=0.33$, $K_{FE}^{***} = 1.93$

^c values calculated with $\nu=0.3$, $K_{FE}^{***} = 1.93$

Table 2.7: values of Mode III constants, [21].

It should be noted that while parameters f_{w1} , f_{w2} and f_{w3} as well as the peak stresses depend on the adopted FE size d , the equivalent peak stress defined by Eq. 2.44 does not. When stress components tied to mode II loading are null (for example: pure mode I loading at the weld root) or non-singular (for example: at the toe side as far as $2\alpha > 102^\circ$), the expression of the equivalent peak stress can be simplified as follow:

$$\Delta\sigma_{eq,peak} = \sqrt{c_{w1}f_{w1}^2\Delta\sigma_{\theta\theta,\theta=0,peak}^2 + c_{w3}f_{w3}^2\Delta\tau_{\theta z,\theta=0,peak}^2} \quad (2.49)$$

In case of as-welded joints the correction factors $c_{wi} = 1$, so the equivalent peak stress turns out to be:

$$\Delta\sigma_{eq,peak} = \sqrt{f_{w1}^2 \Delta\sigma_{\vartheta\vartheta,\vartheta=0,peak}^2 + f_{w3}^2 \Delta\tau_{\vartheta z,\vartheta=0,peak}^2} \quad (2.50)$$

2.6 Design scatter bands according to PSM

Many experimental results have been analysed, in order to be able to properly calibrate the design scatter bands in terms of equivalent stress and cycles to failure. The aim of this work was to create three design curves, one valid for the Mode I and II loaded conditions, one for the Mode III and another one valid for the combination of Mode I, II and III (multiaxial case). In the last loading condition, where the contributes of Mode I, II and III are present, the design scatter bands were obtained by considering the slope of the Mode III curves and some characteristics of the other curve (T_σ , $\Delta\sigma_{A,50\%}$). This approach was proposed by Livieri and in this way a new standardized curve was created, valid for the multiaxial case.

Below are reported the characteristics of the equivalent peak stress curves for steel divided in the three different cases:

1. Mode I and Mode II;
2. Pure Mode III;
3. Mode I, Mode II and Mode III.

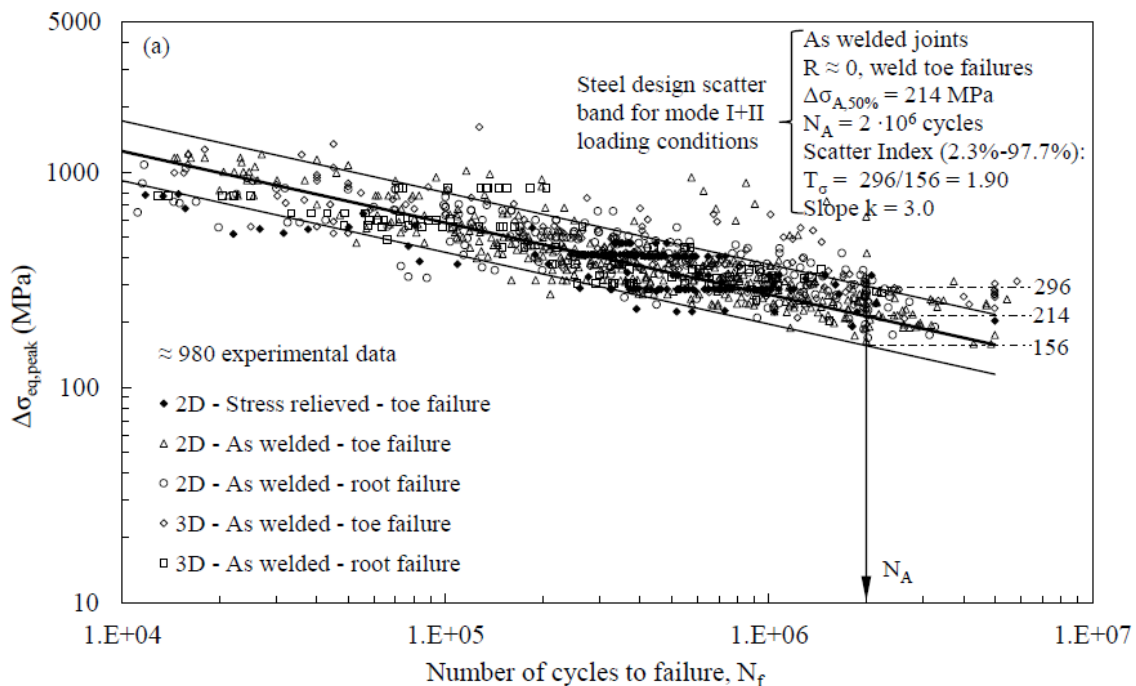


Figure 2.23: Steel design scatter band for Mode I and Mode II loading conditions, [21].

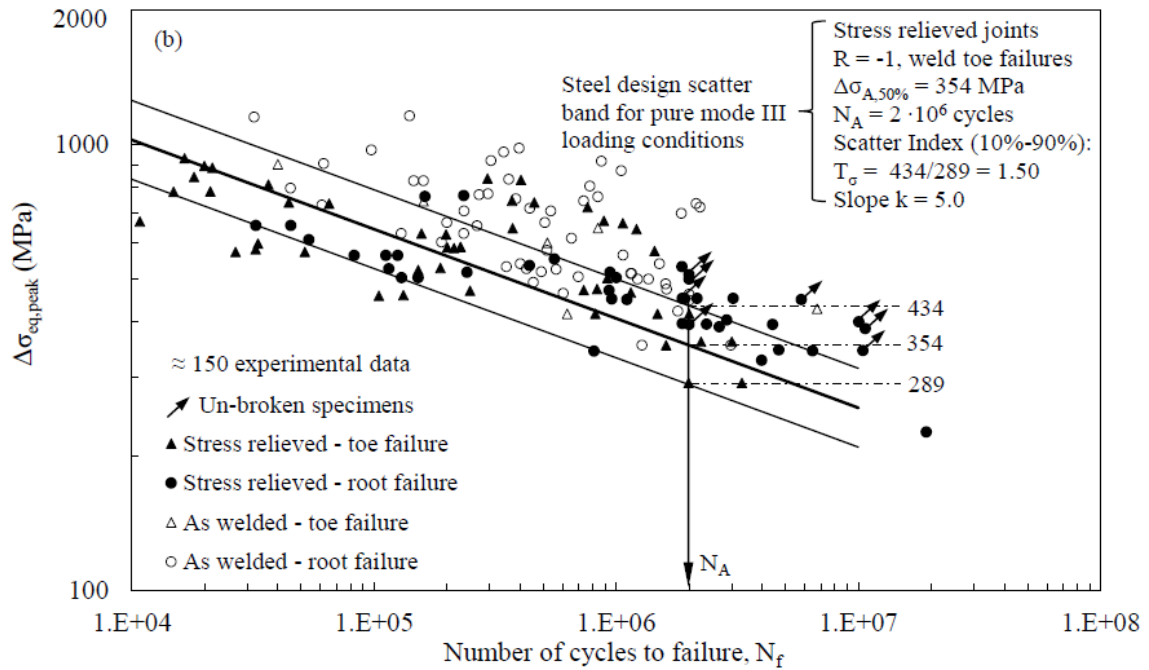


Figure 2.24: Steel design scatter band for pure Mode III loading conditions, [21].

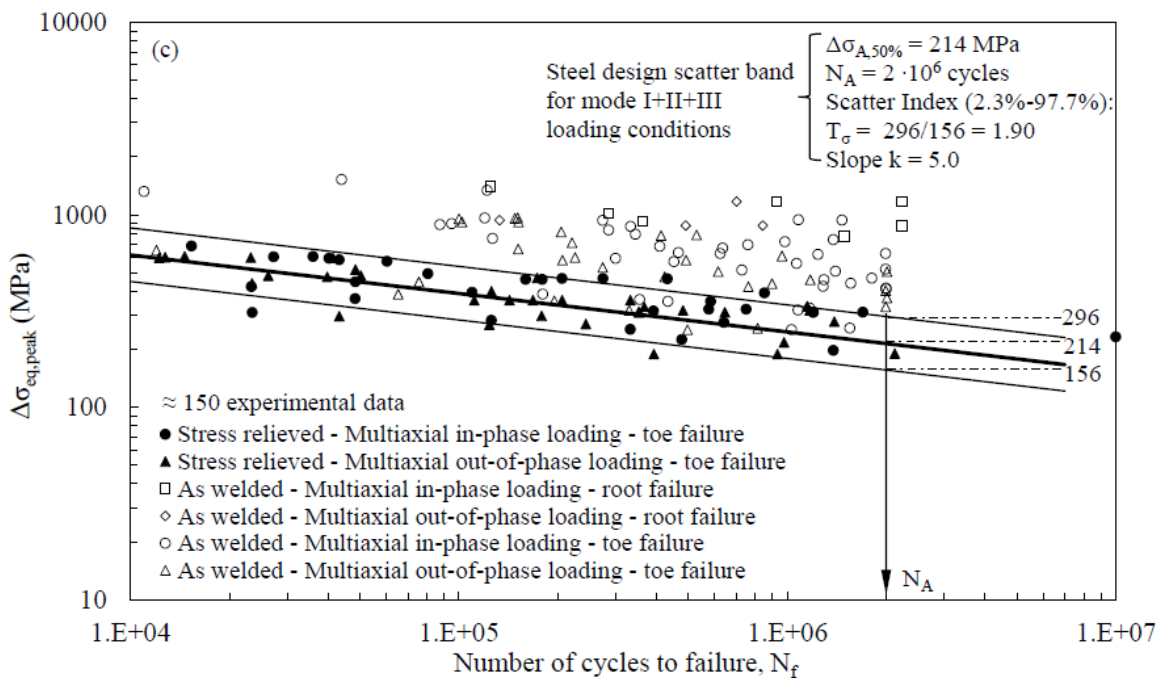


Figure 2.25: Steel design scatter band for Mode I, Mode II and Mode III loading conditions, [21].

The general conservatism of steel welded joints under as welded conditions could be explained by high residual compressive state at the weld toe and at the weld root sites. These curves have been validated by over 1300 experimental results and might be useful to design engineers engaged in fatigue assessment of welded joints.

2.7 Fatigue assessments with the Peak Stress Method

Previously the Strain Energy Density was introduced to restore the comparability of notches with different opening angles that NSIFs were not able to guarantee. The new expression of the equivalent peak stress, obtained from the combination of SED and PSM, is still able to compare failures relative to different notch geometries. A first application of this last statement is reported by a research considering welded joints failing from the weld root or the weld toe. In particular, weld root failures were generated from testing load-carrying cruciform fillet-joints under axial or bending loading. Due to this particular geometry, Mode II stresses were negligible at the root, so that eq. 2.45 could be used. Concerning weld toe failures, the flank angle ranged from 30° to 70° (2α from 150° to 110°) and then, again, eq. 2.45 was applied because the Mode II is not singular. Fig. 2.28 shows a comparison between the experimental results and the design scatter band previously calibrated on fatigue failures from the weld toe with flank angles around 45° .

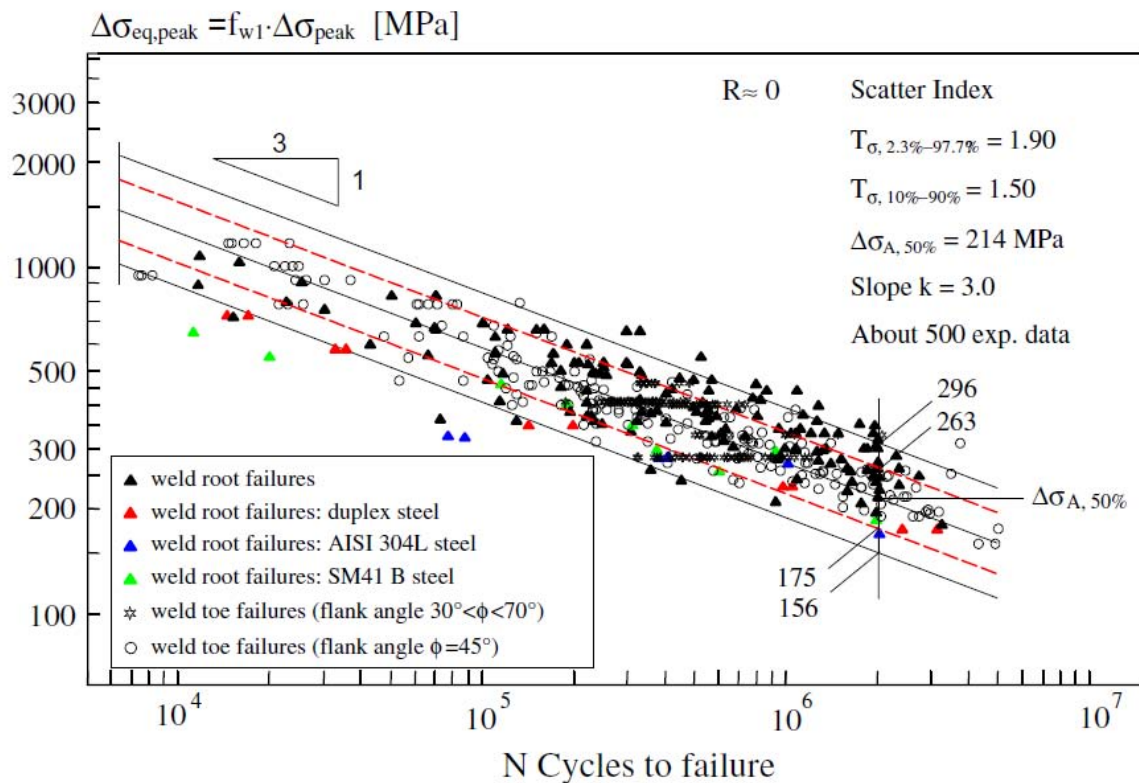



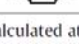


Figure 2.27. Fatigue strength of steel welded joints with weld toe or weld root failures in terms of the equivalent peak stress evaluated by using a finite element size equal to $d = 1$ mm. Scatter bands related to mean values \pm two standard deviations ($T_\sigma = 296/156 = 1.90$) or to $P_s = 10\text{--}90\%$ ($T_\sigma = 263/175 = 1.50$), [18].

It is worth noting that most of the data fall within the scatter range previously calibrated as a demonstration of the goodness of this method.

A step forward is considering steel welded geometries where the mode II contribute is not negligible. Fatigue tests were performed on load-carrying lap joints (L) and partial load-carrying cover plates (C). The weld throat thickness was 3 mm (L3 and C3 series) or 6 mm (L6 and C6 series). A total of 40 specimens have been analysed keeping the load ratio constant to 0.1. The geometries and the failure position are resumed in table 2.8.

Joint geometry	Failure position (number of specimens)	$\Delta\sigma_{A,50\%}^a$ (MPa)	$\Delta\sigma_{A,97.7\%}^a$ (MPa)	k	$T_{\sigma,10-90\%}$
L3 	Root (9) and toe (1)	66.9	53.2	3.88	1.34
C3 	Toe (11)	76.8	54.9	2.89	1.54
L6 	Toe (8) and root (2)	84.6	75.1	3.07	1.17
C6 	Toe (11)	83.1	60.1	2.88	1.52

^a Values calculated at $N_A = 2 \times 10^6$ cycles to failure; $\Delta\sigma_{A,97.7\%}$ evaluated with a confidence level of 95%.

Table 2.8: Summary of fatigue tests results on welded lap joints (L) and cover plates (C), [18].

Plane strain, two-dimensional analyses of the welded joints were performed by using four-node quadrilateral elements as implemented in Ansys® code (PLANE 42 elements of the Ansys® element library). A free mesh was adopted, the only parameter used to drive the mesh generation being the so-called “global element size” which was set to $d = 1$ mm. A friction-free contact between main and cover plates was simulated by means of a symmetry boundary condition applied to the contact surface of the cover plates, as shown in Fig. 2.28.

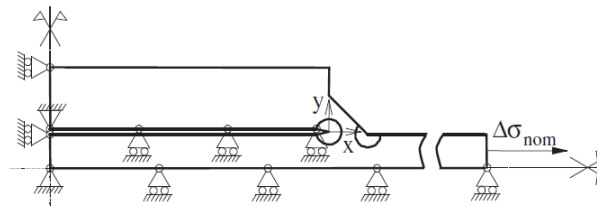


Figure 2.28: geometry of the welded lapped joint with the applied restraints, [18].

By so doing, linear elastic finite element analyses could be performed. It should be noted that the transverse displacement of the cover plates due to contraction of the main plate is prevented, which implies an approximation with respect to the actual structural behavior of the joint. To investigate this point, the joints tested by the authors have been analyzed also by using friction-free contact elements between main plate and cover plate. As a result, it could be verified that the equivalent peak stresses at the point of crack did not change by more than 7% with respect to the linear elastic analysis. Then the approximation introduced by the linear elastic finite element analysis was considered acceptable. Table 2.9 reports the peak stresses calculated at the root and at the toe along with the resulting equivalent peak stresses. It can be seen that except for the case L6, the equivalent peak stress correctly identifies the crack initiation point.

Series	ΔK_I	ΔK_{II}	ΔK_I	ΔW [N mm/mm ³]				$\Delta\sigma_{yy,peak}$	$\Delta\tau_{xy,peak}$	$\Delta\sigma_{11,peak}$	$\Delta\sigma_{eq,peak}$		Failure position
	Root	Toe	Toe	Root ^a	Toe ^b	Root ^c	Toe ^c	Root	Toe	Root ^d	Toe ^e		
L3	36.07	235.9	417.2	3.31×10^{-1}	2.58×10^{-1}	3.36×10^{-1}	2.27×10^{-1}	24.60	84.90	305.9	469.9	325.5	Root (9) and toe (1)
C3	47.64	108.4	306.5	7.46×10^{-2}	1.39×10^{-1}	8.03×10^{-2}	1.23×10^{-1}	30.10	42.50	226.1	238.4	240.6	Toe (11)
L6	26.56	155.4	300.1	1.44×10^{-1}	1.33×10^{-1}	1.46×10^{-1}	1.18×10^{-1}	11.40	52.10	217.9	288.0	231.8	Toe (8) and root (2)
C6	38.11	64.60	263.0	2.80×10^{-2}	1.02×10^{-1}	3.24×10^{-2}	9.08×10^{-2}	18.20	25.70	190.9	144.2	203.1	Toe (11)

^a Calculated by means of eq (2.27), considering Mode I and Mode II contributors.

^b Calculated by means of eq (2.27), considering Mode I contribute.

^c Calculated directly from accurate FE analysis

^d Calculated by means of eq (2.43), considering Mode I and Mode II contributors.

^e Calculated by means of eq (2.43), considering Mode I contribute.

Table 2.9. Stress parameters calculated at the toe and at the root of the joints tested in the present work. The nominal stress applied to the main plate is $\Delta\sigma_{nom} = 100$ MPa. The FE-based energy values were calculated by means of the same refined mesh adopted to calculate the NSIFs. Peak stresses evaluated by means of a free mesh, mean finite element size $d = 1$ mm and four-node quadrilateral elements (PLANE 42 of the Ansys Element library), [18].

In parallel very refined FE meshes with an element size on the order of 10^{-5} mm were generated to calculate the NSIFs at the weld root and weld toe. Having in hands the NSIFs, the mean value of the SED could be evaluated considering the two first terms of eq. 2.26 at the root or considering just the first one for the toe. The SED was also evaluated directly from the FE analyses by using the same

numerical models adopted to evaluate the NSIFs. All results are reported in Table 2.9. In particular it is seen that the maximum difference between the SED parameter evaluated analytically (eq. 2.26) and numerically (by FEM) is about 15% at the root of C6 joints, which means that the influence of higher order terms can be neglected in this case, at least from an engineering point of view.

Two additional points are worth mentioning:

1. It has been shown that the direct evaluation of the SED parameter by means of a finite element analysis does not require a very refined mesh. In fact Lazzarin and co-workers were able to show that only four element having size 0.28 mm placed inside the structural volume can deliver a reasonably correct value of the SED parameter;
2. In case of thin sheet lap joints (widely used in the automotive industry), the influence of higher order stress terms cannot be neglected inside the structural volume. Therefore the degree of accuracy of eq. 2.26 decreases if no extra-terms are included; conversely, the direct evaluation of the SED parameter by means of a finite element analysis leads to correct results.

Additional experimental results were taken by literature and evaluated in terms of equivalent peak stress, considering the contribute of Mode I and Mode II. Fig 2.29 compares all the available data with the design scatter band previously calibrated, showing a fair agreement.

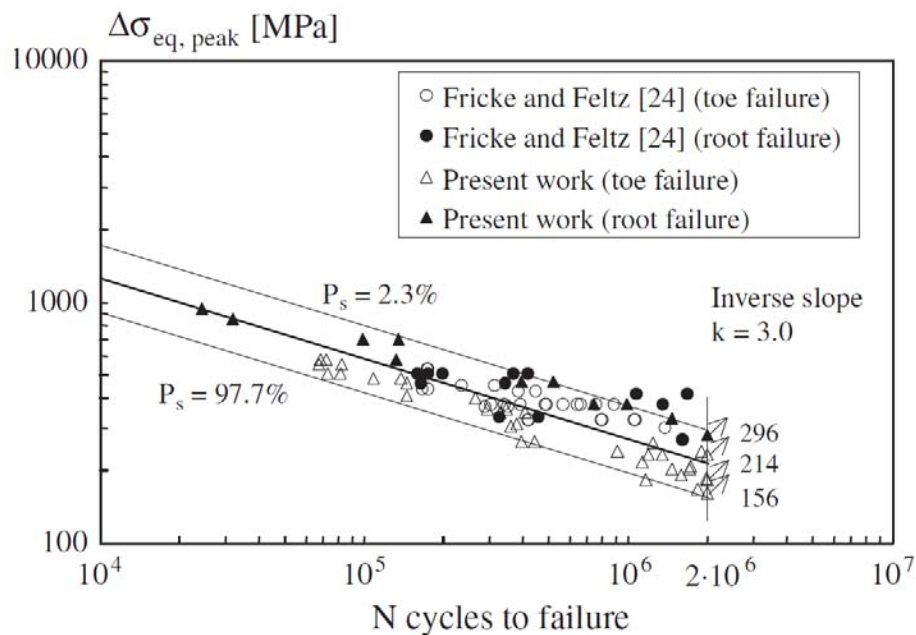


Figure 2.29: Fatigue test results in terms of equivalent peak stress evaluated by means of finite element analyses with mean element size $d = 1$ mm, [18].

At this point, we dealt with Mode I and Mode II fatigue life assessment using the PSM, a further step is considering Mode III loaded geometries. In [17] are reported the experimental data of tube-to-flange specimens under torsional loading evaluated in terms of equivalent peak. The aim of this work was, to validate the Mode III design scatter band and Fig 2.30 shows that it results a good agreement between the experimental data and the calibrated curve.

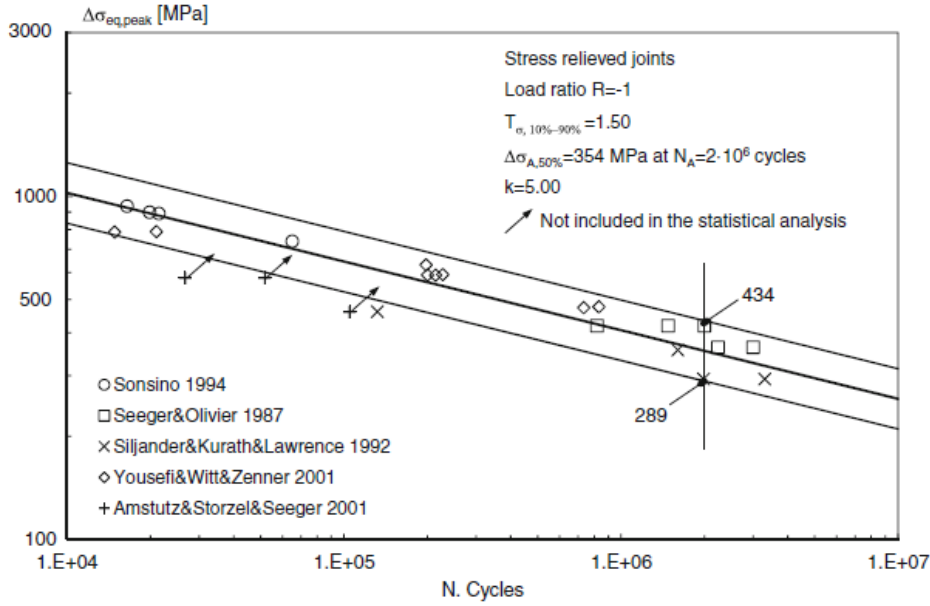


Figure 2.30: Fatigue test results in terms of range of the equivalent peak stress evaluated according to eqs (8) and (10). Data refer only to weld toe failures. Scatter band fitted on experimental results by setting k equal to 5.00 and $T_{\sigma,10-90\%}$ equal to 1.5 [17].

2.7 The equivalent peak stress in special cases

There are three cases where the PSM expression, eq. 2.44, is not valid anymore. The first exception occurs when the weld toe profile cannot be assumed as sharp V-notch because the tip radius is large enough to induce full notch sensibility. In the multiaxial case, the equivalent peak stress at the weld toe must be updated according to the following expression:

$$\bar{W} = c_{w1} \frac{1 - \nu^2}{2E} \Delta\sigma_{max}^2 + c_{w3} \frac{1 + \nu}{E} \Delta\tau_{max}^2 \rightarrow \frac{1 - \nu^2}{2E} \Delta\sigma_{eq,peak}^2 \quad (2.51)$$

$$\Delta\sigma_{eq,peak} = \sqrt{c_{w1} \Delta\sigma_{max}^2 + c_{w3} \frac{2\Delta\tau_{max}^2}{1 - \nu}} \quad (2.52)$$

Where σ_{max} and τ_{max} are the maximum value of tension and torsion stresses evaluated at the weld toe with sufficiently refined FE meshes, as it is required to evaluate the stress concentration factor.

Another special case is that of a box-beam fillet-welded joints under combined bending and torsion multiaxial fatigue loadings reported in fig. 2.32.

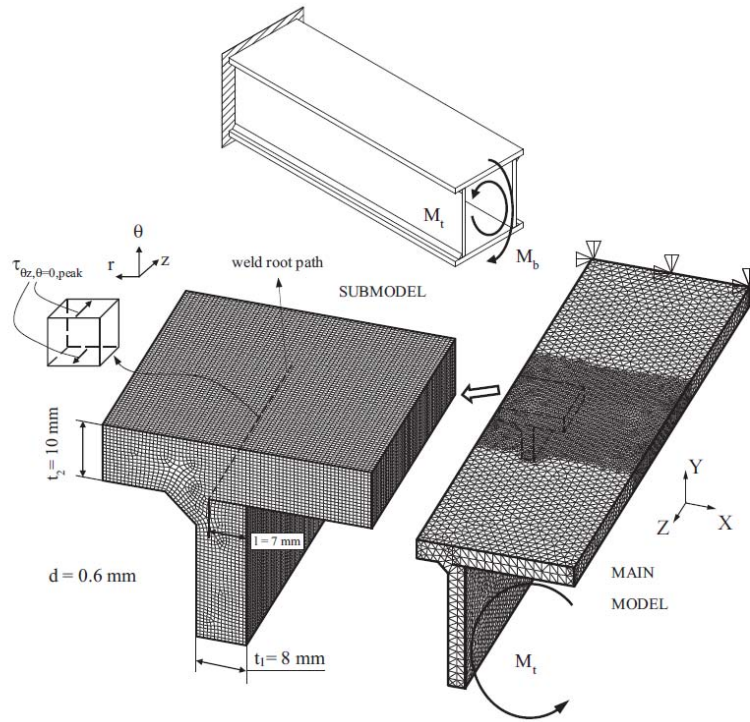


Figure 2.31: 3D FE mesh to apply the PSM according to Eq. (2.51); the example reported in the figure shows a box-beam fillet-welded joint [47]. Eight node brick SOLID 185 elements (with K-option 2 set to 3) available in Ansys# Element Library were adopted to generate the 3D mesh of the submodel shown in the figure, [21].

In this case, Mode I bending stresses are not singular either at the weld toe and at the weld root because they are parallel to the weld toe as well as to the weld root paths. The equivalent peak stress can be evaluated by means of the following expression, which takes into account the mode I, non-singular, nominal bending stress and the mode III, singular, torsional shear stress:

$$\Delta \bar{W} = c_{w1} \frac{\Delta \sigma_{nom}^2}{2E} + c_{w3} \frac{e_3}{E} \left[K_{FE}^{***} \Delta \tau_{\theta z, \theta=0, peak} \left(\frac{d}{R_0} \right)^{1-\lambda_3} \right] = \frac{1-\nu^2}{2E} \Delta \sigma_{eq, peak}^2 \quad (2.53)$$

$$\Delta \sigma_{eq, peak} = \sqrt{c_{w1} \frac{\Delta \sigma_{nom}^2}{1-\nu^2} + c_{w3} f_{w3}^2 \Delta \tau_{\theta z, \theta=0, peak}^2} \quad (2.54)$$

Where σ_{nom} can be evaluated by Navier distribution, while the singular one ($\Delta \tau_{\theta z, \theta=0, peak}$) must be calculated from FE analyses according to PSM recommendations.

The last special case occurs when dealing with geometries where the Mode I, Mode II and Mode III contribution to the strain energy density are not independent each other. Mutual work must be taken in account, inserting coupling terms. An example of such condition is represented by a plate having a box-welded joint subjected to biaxial fatigue loading due to two orthogonal forces (F_x and F_y in Fig 2.30).

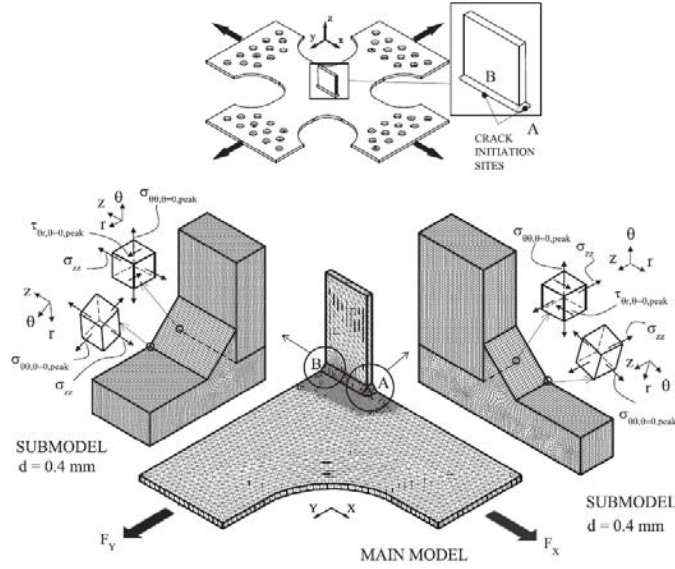


Figure 2.32. 3D FE mesh of a plate having a box-welded (wrap-around) joint [49]. Eight node brick SOLID 185 elements (with K-option 2 set to 3) available in Ansys(R) Element Library were adopted to generate the 3D mesh of the submodels shown in the figure, [21].

First the contribute of each force to the strain energy is calculated, then all contributes are summed up. Let us consider the weld root side at point A. The single force F_x generates mode I and mode II singular stresses; the single force F_y generates mode I, mode II singular stresses and also σ_{zz} non-singular stresses. Considering the root side at point B, the single force F_x generates mode I, mode II singular stresses and σ_{zz} non-singular stresses, while F_y generates mode I and mode II singular stresses. According to the approximate approach adopted here, the total averaged SED, $\Delta\bar{W}$, is evaluated by summing up the contributions due to the forces F_x and F_y applied individually:

$$\Delta\bar{W} = \Delta\bar{W}_{F_x} + \Delta\bar{W}_{F_y} \quad (2.55)$$

Where:

$$\Delta\bar{W}_{F_x} = c_{w,F_x} \left\{ \frac{e_1}{E} \left[K_{FE}^* \Delta\sigma_{\theta\theta,\theta=0,peak} \left(\frac{d}{R_0} \right)^{1-\lambda_1} \right] + \frac{e_2}{E} \left[K_{FE}^{**} \Delta\tau_{r\theta,\theta=0,peak} \left(\frac{d}{R_0} \right)^{1-\lambda_2} \right]^2 + \frac{\Delta\sigma_{zz}^2}{2E} \right\}_{F_x} \quad (2.56)$$

$$\Delta\bar{W}_{F_y} = c_{w,F_y} \left\{ \frac{e_1}{E} \left[K_{FE}^* \Delta\sigma_{\theta\theta,\theta=0,peak} \left(\frac{d}{R_0} \right)^{1-\lambda_1} \right] + \frac{e_2}{E} \left[K_{FE}^{**} \Delta\tau_{r\theta,\theta=0,peak} \left(\frac{d}{R_0} \right)^{1-\lambda_2} \right]^2 + \frac{\Delta\sigma_{zz}^2}{2E} \right\}_{F_y} \quad (2.57)$$

The non-singular contribute resulted negligible, so the equivalent peak stress turns out to be:

$$\Delta\bar{W} = \frac{1-\nu^2}{2E} \Delta\sigma_{eq,peak}^2 \quad (2.58)$$

CHAPTER 3:

Application of the Peak Stress Method to steel welded joints.

3.1 introduction

In the previous chapter, the NSIFs approach was presented and, in particular, its summarizing capability was underlined. To be more precise, it was reported the example of transverse non-load-carrying fillet welds in an “as welded” condition to emphasize how a switch from a nominal to a local approach could reduce significantly the scatter band. The calculation of the exact NSIF requires very refined meshes but thanks to the Peak Stress Method, with an acceptable range of error, we could calculate the approximated ΔK_I with coarser meshes. Taking as a reference point the article of G. Meneghetti and P. Lazzarin [10], four different geometries have been investigated to validate the results shown in this work, with a traction or bending load. The software Ansys® has been utilized, fulfilling all the PSM hypothesis. Dealing with weld toe failures, the notch opening angle is $2\alpha = 135^\circ$ for every geometry, so the Mode II contribute is not singular and it will be considered negligible. The aim of this investigation is to estimate the Mode I NSIF value both with refined meshes, applying the definition, both applying the PSM using coarser meshes. Eventually, there will be a discussion evaluating the results and judging if there is an acceptable match with the published values or not.

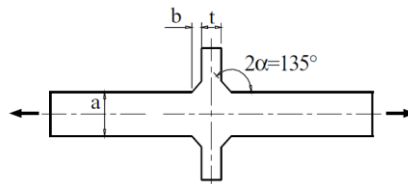


Figure 3.1: transverse non-load-carrying joint. [10].

Series	Joint geometry	a (mm)	t (mm)	b (mm)	Load type ^b	K_I^V/σ_g (mm ^{0.326})	σ_{peak}/σ_g	K_{FE}^*
1	Cruciform-nlc	13	10	8	T	2.633	1.870	1.408
2	Cruciform-nlc	50	50	16	T	3.927	2.818	1.394
3	Cruciform-nlc	100	50	16	T	3.962	2.941	1.347
4	Cruciform-nlc	13	3	5	T	2.235	1.646	1.358
5	Cruciform-nlc	13	10	8	T	2.633	1.870	1.408
6	Cruciform-nlc	25	3	5	T	2.247	1.667	1.348
7	Cruciform-nlc	25	32	9	T	3.293	2.347	1.403
8	Cruciform-nlc	25	220	15	T	3.881	2.882	1.347
9	Cruciform-nlc	38	13	8	T	2.859	2.139	1.337
10	Cruciform-nlc	38	220	15	T	4.609	3.350	1.376
11	Cruciform-nlc	100	3	5	T	2.307	1.672	1.380
12	Cruciform-nlc	100	220	15	T	5.704	4.222	1.351
13	Cruciform-nlc	25	3	5	B	2.247	1.618	1.389
14	Cruciform-nlc	50	3	5	B	2.363	1.696	1.393
15	Cruciform-nlc	100	3	5	B	2.325	1.694	1.372
16	Cruciform-nlc	100	13	8	B	3.051	2.131	1.432
17	Cruciform-nlc	6	6	2.2	T	1.991	1.796 ^a	1.389
18	Cruciform-nlc	19	19	7.1	T	2.899	2.084	1.391
19	Cruciform-nlc	25	25	9.4	T	3.170	2.277	1.392
20	Cruciform-nlc	11	11	4.1	T	2.426	1.765	1.374
21	Cruciform-nlc	11	11	4.1	T	2.426	1.765	1.374
22	Cruciform-nlc	6	6	6	T	2.152	1.496	1.439
23	T-nlc	6	6	6	B	1.793	1.272	1.410
24	Cruciform-lc	6	6	6	T	2.600	2.302 ^a	1.416

^a Calculated by means of an element size $d = 0.5$ mm.

^b T = traction; B = bending.

Table 3.1: Stress parameters for the analysed steel welded joints. The elastic peak stress was calculated by means of an element size $d = 1$ mm, [10].

3.2 Experimental data

Referring to the previous table, a nomenclature system to refer to the four joints has been established:

- “T” for transverse non load carrying joints/ a / t / b.
- “C” for cruciform non load carrying joints/ a / t / b.

For each of the selected series range of stresses and the corresponding cycles to failure have been provided, see table 3.1. These experimental results bring the possibility of filling a Wohler diagram in terms of range of tension and cycles to failure. What emerges is the clear size effect on the fatigue life assessment that is showed by the different disposition of the different series within this diagram. Only series 1 and 16 seem to be overlapped, perhaps a possible explanation is that two out of three geometrical parameters (t and b) are very similar so it is the fatigue behavior.

Series	a (mm)	Nf	$\Delta\sigma$ [MPa]
1	13	192000	200
	13	507000	140
	13	2937000	100
	13	4297000	80
12	100	109000	150
	100	224000	120
	100	322000	100
	100	1153000	65
	100	2147000	55
16	100	120000	260
	100	200000	220
	100	302000	180
	100	744000	140
	100	1180000	120
	100	2158000	110
23	6	135000	300
	6	237000	260
	6	407000	200
	6	573000	190
	6	665000	180
	6	1525000	160
	6	1534000	150
	6	2601000	140

Table 3.2: experimental results for four different series, [10].

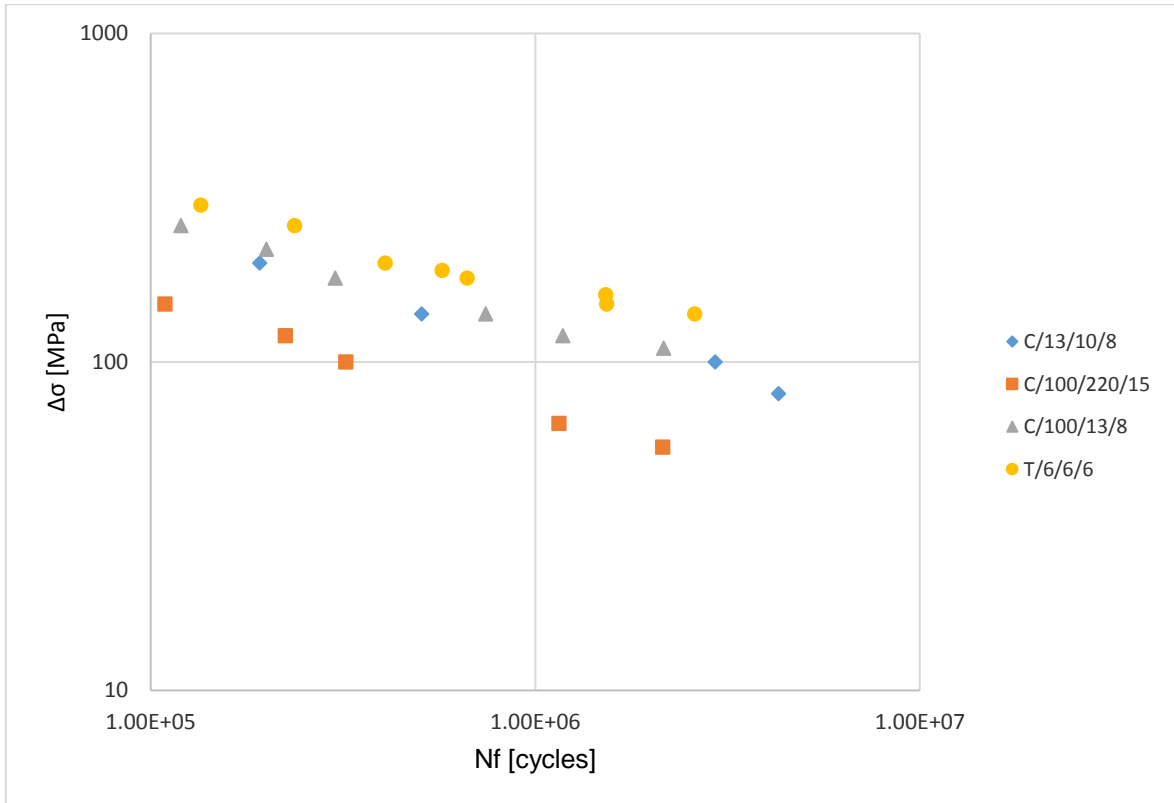


Figure 3.2: S-N graph for every analyzed series.

Running a statistical analysis, the outcome is a very high value of the scatter index (10%-90%), equal to 3.57 obtained imposing the inverse slope equal to 3; as shown in fig 3.3.

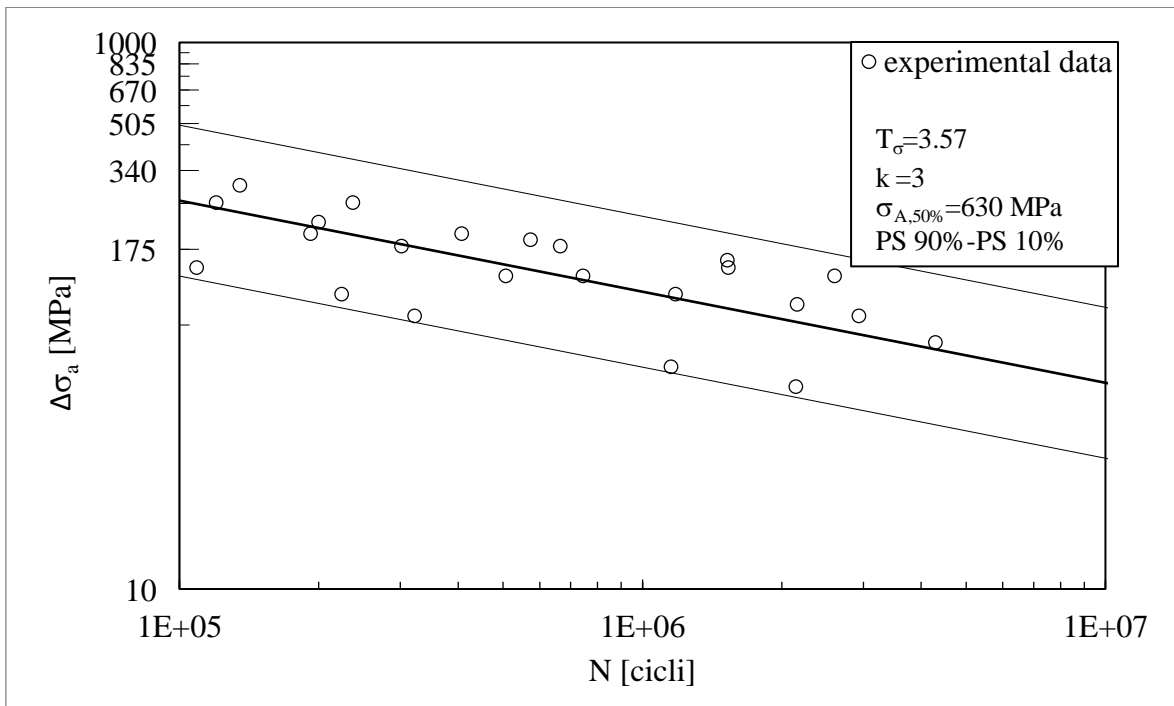


Figure 3.3: statistical analysis of the experimental data.

3.3 FEM models to estimate the Mode I NSIF precisely.

To correctly estimate the Mode I NSIF, K_1 , very refined meshes are required in the V-notch tip proximity. Since we are dealing with sharp V-notched geometries the tip radius is null, leading to a singular stress distribution. Looking at the maximum principal stress at the notch tip will be meaningless: the lower is the tip element size, the higher will be the stress. Theoretically, with an element size extremely low, near zero, the first principal stress will be infinite. The only way to estimate the stress distribution near the notch is to apply the NSIF definition, eq 3.1, which gives a finite value in relation to a local polar coordinate system centered in the notch tip, fig. 3.4.

$$K_1^V = \sqrt{2\pi} \lim_{r \rightarrow 0^+} r^{1-\lambda_1} \sigma_{\theta\theta}(r, \vartheta = 0) \quad (3.1)$$

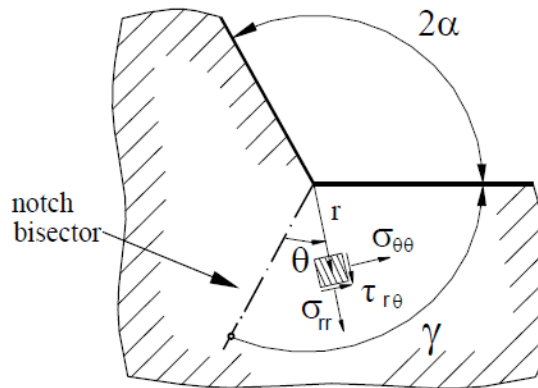


Figure 3.4: Sharp V-notch geometry and local coordinate system, [11].

In the present work, thanks to the specimens' geometry, plane models have been considered, avoiding the time-consuming problem of a 3D mesh. In order to build suitable meshes to apply the NSIF definition, a particular technique was adopted in all models, drawing two circles around the notch tip. The bigger circle has a 0.28 mm radius while the smaller one just a 0.0001 mm radius. In the smaller circle, a specific mesh tool of Ansys code called "concentration keypoint" was adopted to guarantee a circular and uniform element disposition around the notch.

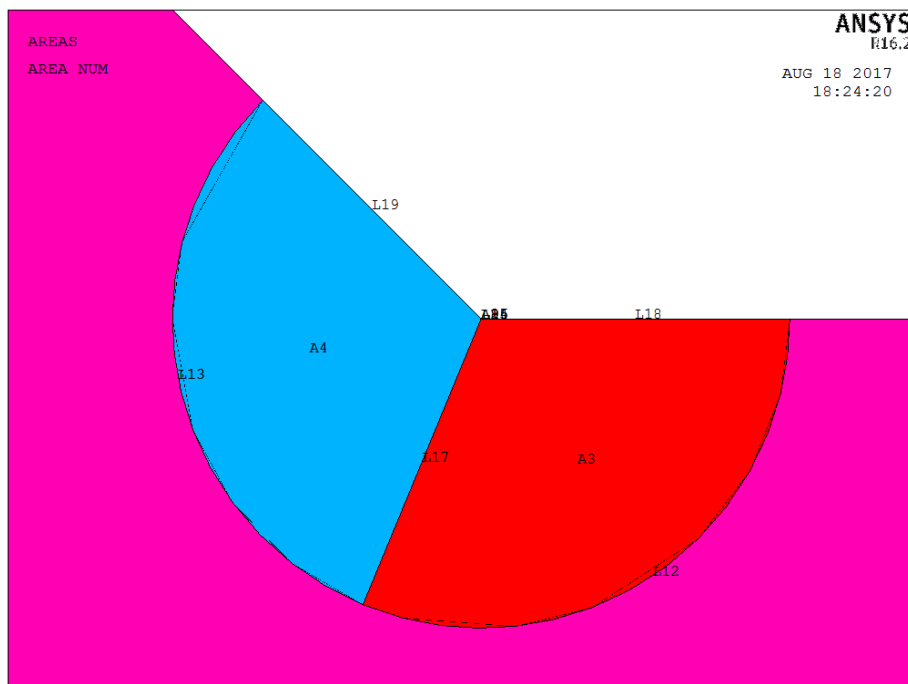


Figure 3.4: Bigger circle, radius = 0.28 mm.

Line number	Number of divisions	Spacing ratio
12	10	1
13	10	1
17	100	1500
18	100	1500
19	100	1500

Table 3.3: meshed lines characteristics of the bigger circle.

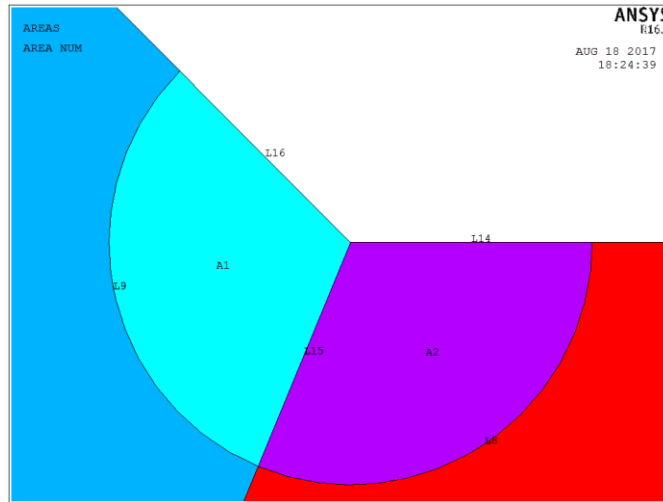


Figure 3.5: smaller circle, radius = 0.0001 mm

Line number	Number of divisions	Spacing ratio
8	10	1
9	10	1
14	5	1
15	5	1
16	5	1

Table 3.4: meshed lines characteristics of the smaller circle.

Only after having divided the area like it is showed in figs. 3.4 and 3.5 it is possible to create a “concentration Keypoint”. The command is located in the following path:

MAIN MENU → PREPROCESSOR → MESHING →
→ SIZE CNTRLs → CONCENTRATION KPS → CREATE.

The input to be insert to successfully accomplish this operation are:

- NPT: number of concentration keypoint
- DELR: Radius of first row of elements derived from the radius value (10^{-4}) divided by the number of divisions (5), it results: $2e-5$ mm)
- NTHET: number of elements around the circumference (10)

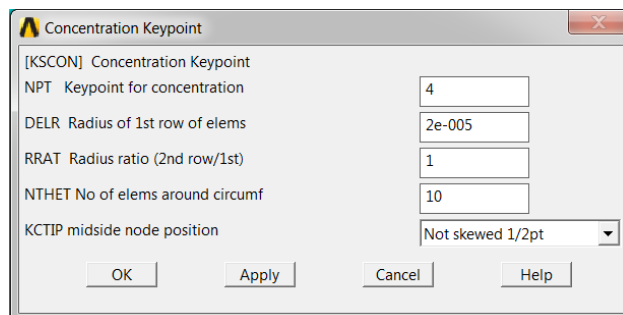


Figure 3.6: Ansys' window for concentration keypoints creation.

Following these indication step by step, the output in the smaller circle will be the one shown in fig 3.7. Concerning the mesh creation in the bigger one, the mesh is generated only imposing the lines divisions, the spacing ratios and launching the mapped mesh generator algorithm, the result is plot in figure 3.8.

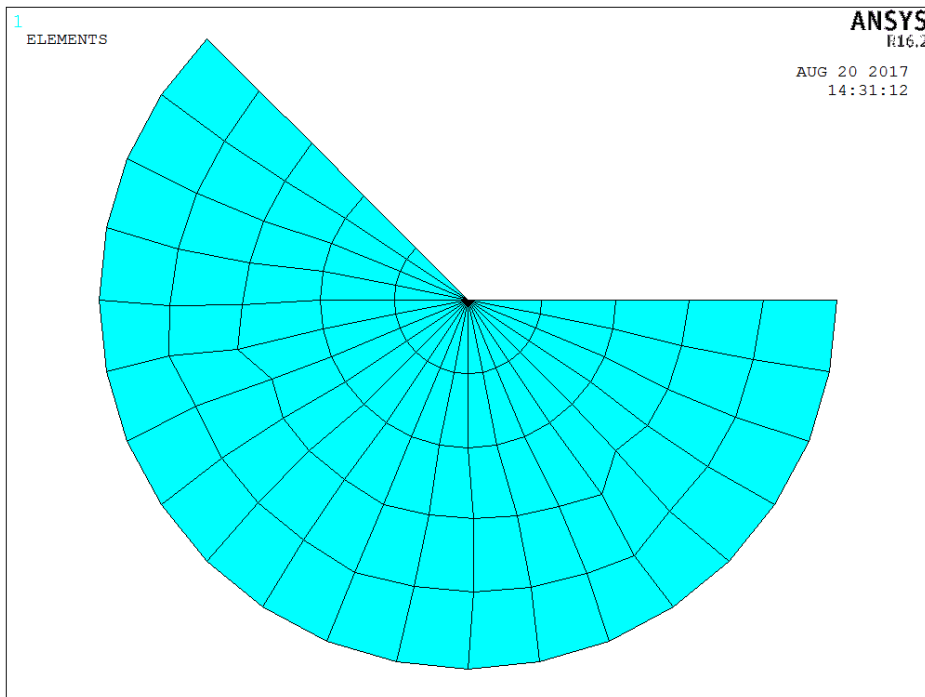


Figure 3.7: mesh of the smaller circle derived by the concentration Keypoint definition.

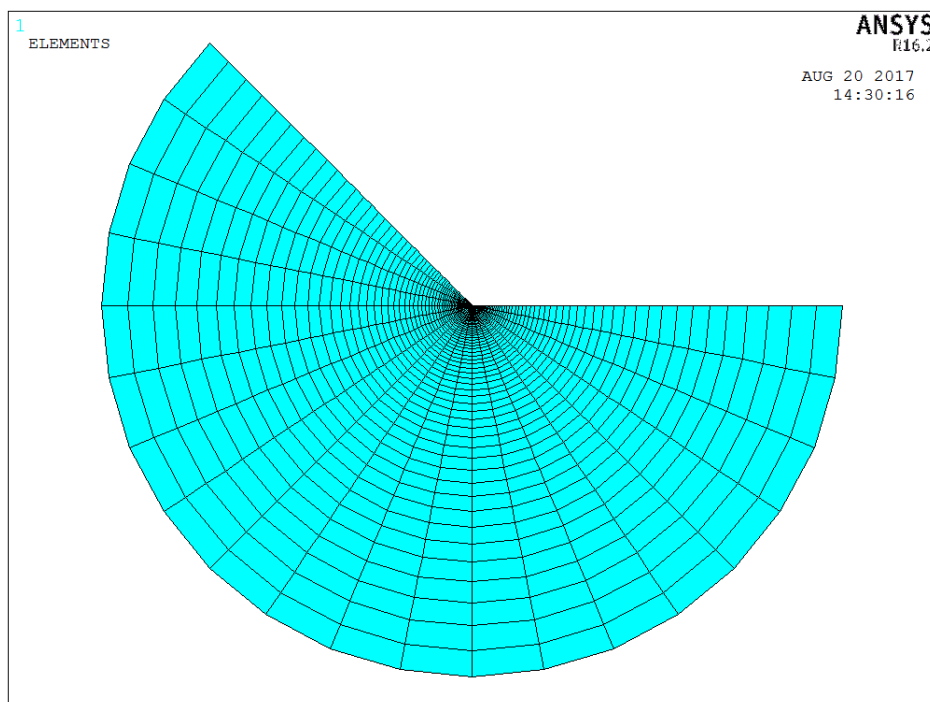


Figure 3.8: mesh of the bigger circle.

At this point the area near the V-notch tip is well meshed, what has still to be defined is the elements creation in the other areas. To create an homogenous mesh, every line has been studied in terms of number of divisions and spacing ratio, and after few attempts, all four geometries are characterized by an element size that decrease in the notch tip direction. This mesh generation path has been followed in all four studied cases, and the results will show a good match with the published ones, confirming the goodness of the here proposed FEM models.

3.3.1 Series 1

The geometry of this series is a cruciform non load carrying fillet welded joint subjected to a traction load. The dimensions have been taken by table 3.1 and it has been modelled using the double symmetry on the XZ and YZ plane, taking as a reference system the one showed in fig 3.9. The traction load was equal of 1 MPa.

FEM Characteristics:

- Element type: PLANE 183
- Keyoptions: K1 Simple enhanced strain; K3 Plane strain
- Poisson's ratio: 0.3
- Young's modulus: 206000 MPa
- Minimum element size: $2 \cdot 10^{-5}$ mm

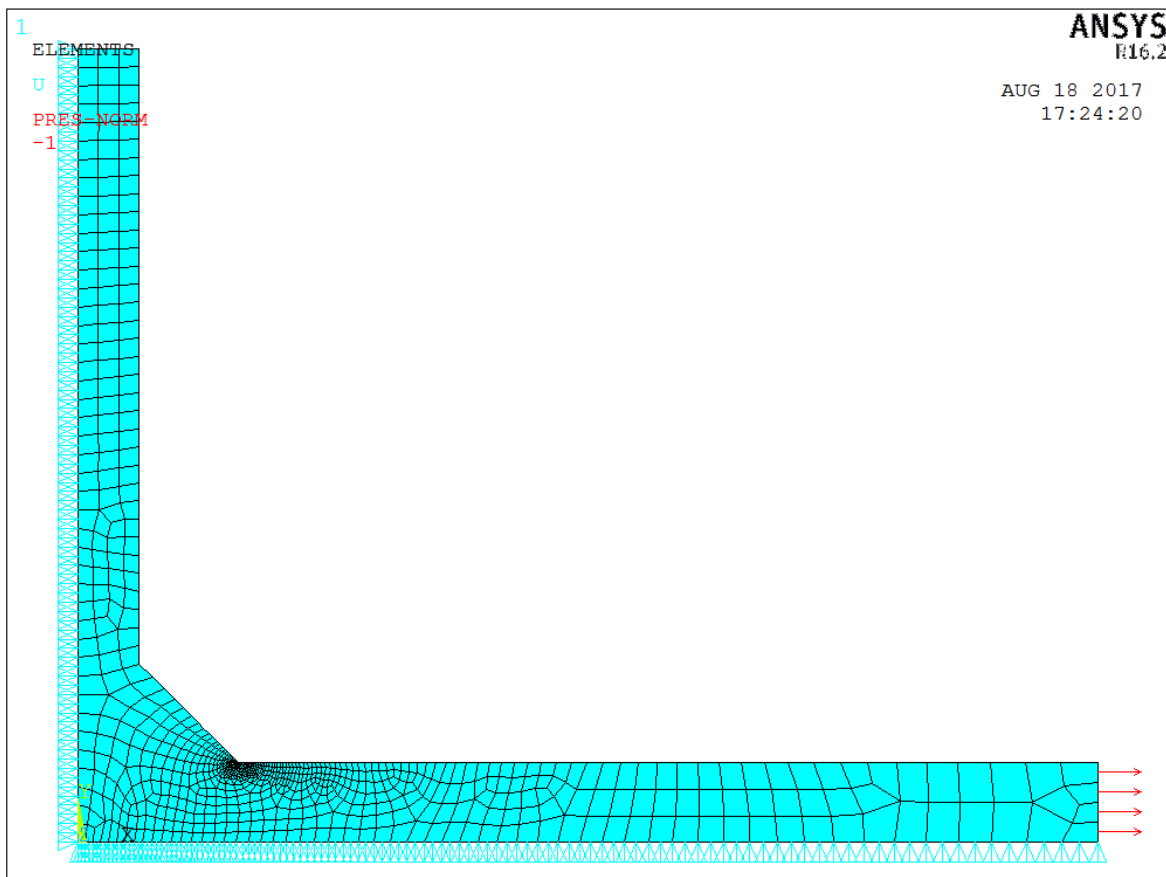


Figure 3.9: Geometry, constraints and loads of the series 1 FEM model.

Once the structure has been solved, the output of the results has been displayed referring to a local Cartesian coordinate system located at the notch tip and with the x-axis aligned with the notch bisector line.

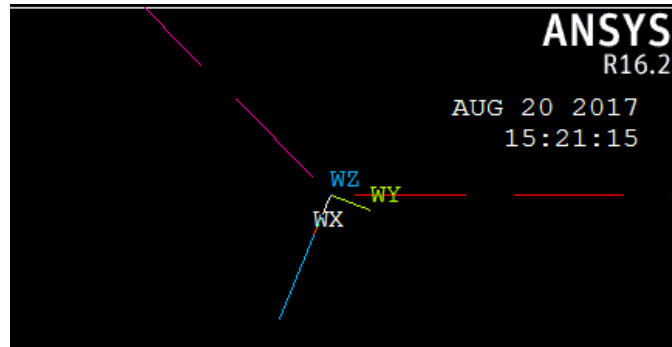


Figure 3.10: Local Cartesian coordinate system.

The nodes belonging to the bisector line, within the bigger circle radius were selected and used to define a path with exception to the nodes belonging to the smaller circle because heavily sensitive to the singularity distortion. In this reference system the stress σ_y act like the $\sigma_{\theta\theta}(r, \vartheta = 0)$ of the NSIF definition, eq. 3.1, so it was plotted in relation to the tip distance, fig 3.11.

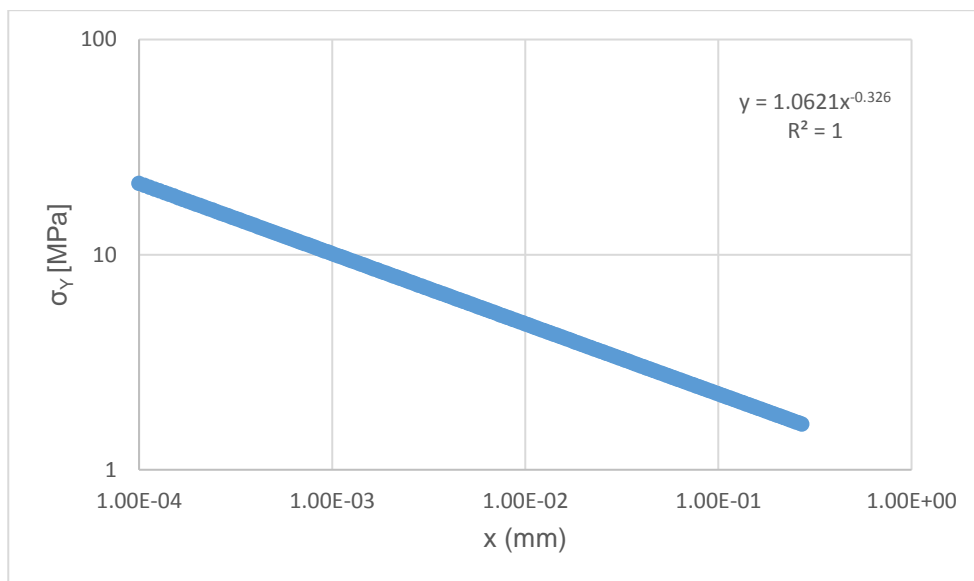


Figure 3.11: Y-stress distribution referred to the local coordinate system in fig. 3.10.

The modulus of exponent of interpolation line (power law) is 0.326 confirming Williams eigenvalue. Having the stress distribution, the Mode I NSIF definition can be derived and what emerges is its finite and constant value within the considered distance.

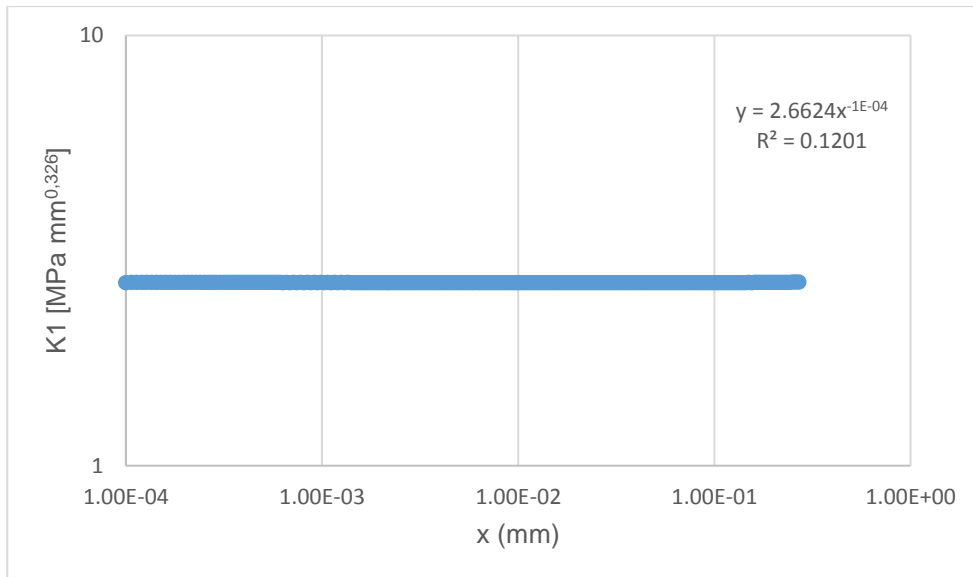


Figure 3.12: NSIF value of the selected nodes belonging to the notch bisector line and within the bigger circle radius.

The exponent of the power of law interpolation line is extremely low, so the NSIF value, considered constant is 2.6624.

3.3.2 Series 12

The geometry of this series is a cruciform non load carrying fillet welded joint subjected to a traction load. The dimensions have been taken by table 3.1 and it has been modelled using the double symmetry on the XZ and YZ plane, taking as a reference system the one showed in fig 3.13. The traction load was equal of 1 MPa.

FEM Characteristics:

- Element type: PLANE 182
- Keyoptions: K1 Simple enhanced strain; K3 Plane strain
- Poisson ratio: 0.3
- Young modulus: 206000 MPa
- Minimum element size: $2 \cdot 10^{-5}$ mm

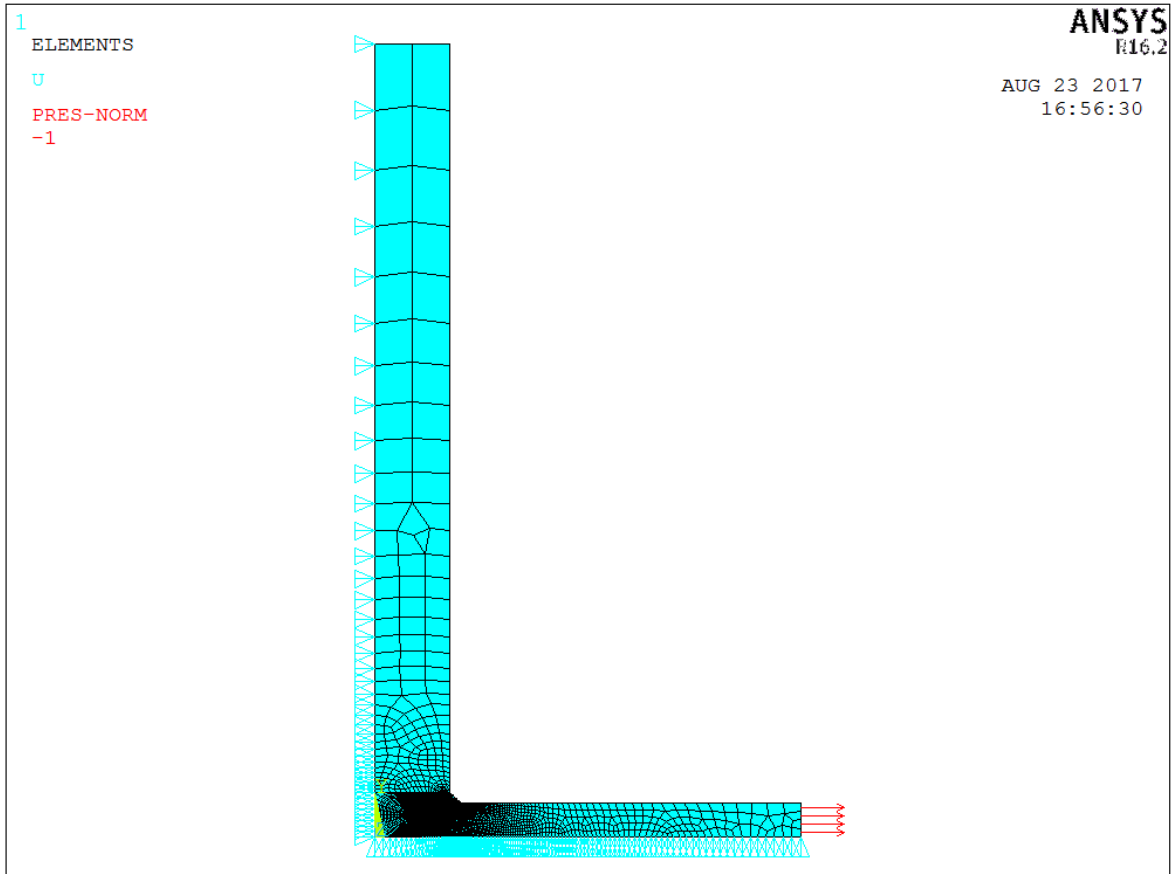


Figure 3.13: Geometry, constraints and loads of the series 12 FEM model.

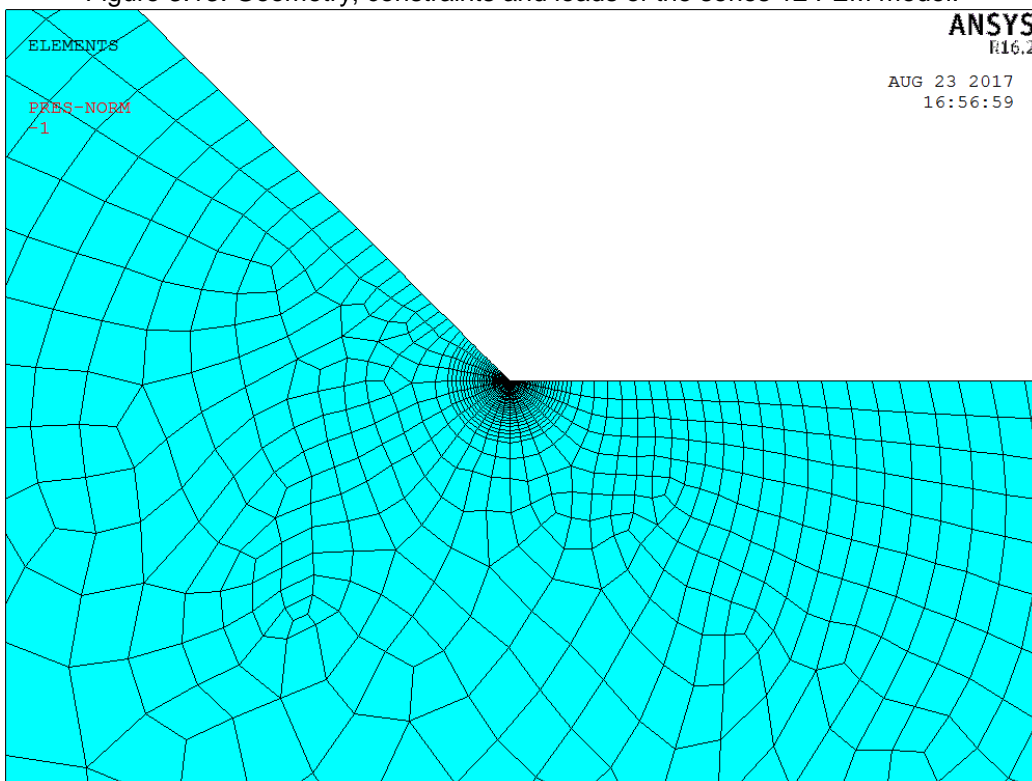


Figure 3.14 Zoom around the notch tip of the series 12 FEM model.

Once the structure has been solved, the output of the results has been displayed referring to a local Cartesian coordinate system located at the notch tip and with the x-axis aligned with the notch bisector line.

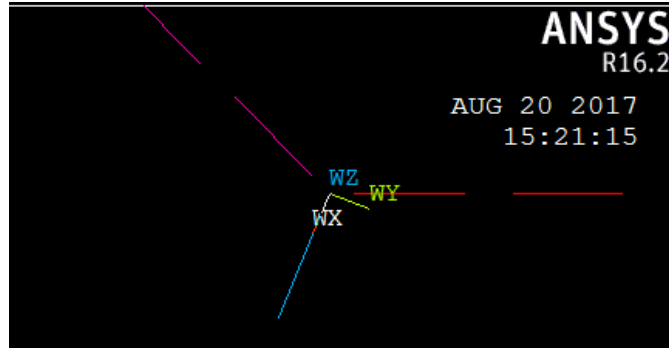


Figure 3.15: Local Cartesian coordinate system.

The nodes belonging to the bisector line, within the bigger circle radius were selected and used to define a path with exception to the nodes belonging to the smaller circle because heavily sensitive to the singularity distortion. In this reference system the stress σ_y act like the $\sigma_{\theta\theta}(r, \vartheta = 0)$ of the NSIF definition, eq. 3.1, so it was plotted in relation to the tip distance, fig 3.16.

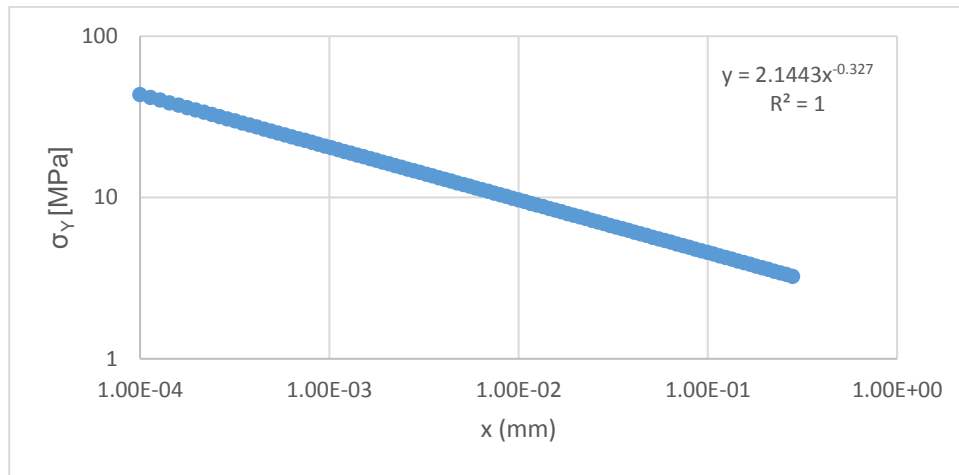


Figure 3.16: Y-stress distribution referred to the local coordinate system in fig. 3.15.

The modulus of exponent of interpolation line (power law) is 0.327 confirming Williams eigenvalue. Having the stress distribution, the Mode I NSIF definition can be applied and what emerges is its finite and constant number within the considered distance.

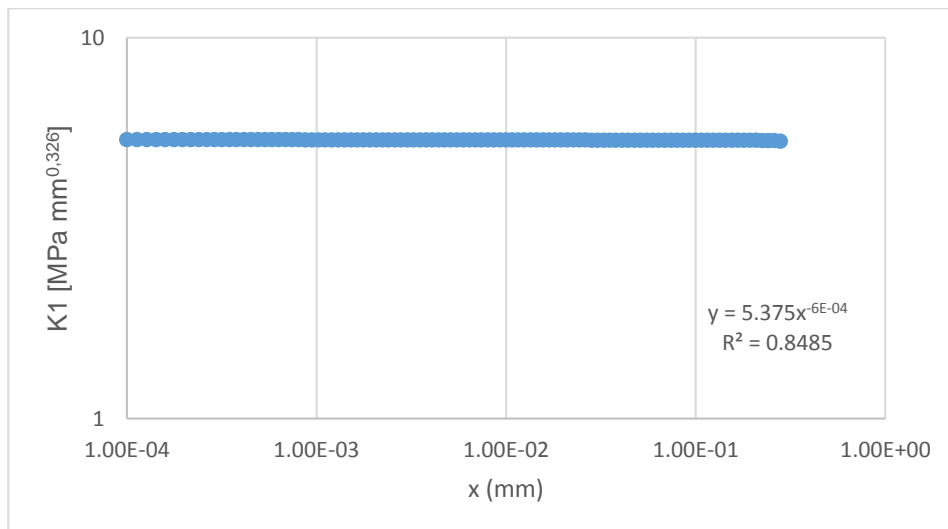


Figure 3.17: NSIF value of the selected nodes belonging to the notch bisector line and within the bigger circle radius.

The exponent of the power of law interpolation line is extremely low, so the NSIF value, considered constant is 5.375.

3.3.3 Series 16

The geometry of this series is a cruciform non load carrying fillet welded joint subjected to a bending load. The dimensions have been taken by table 3.1 and it has been modelled using the symmetry YZ plane, and the anti-symmetry on the XZ plane, taking as a reference system the one showed in fig 3.18. Furthermore, the displacement on the node in position (0; 0; 0) has been restrained in the y direction.

FEM Characteristics:

- Element type: PLANE 182
- Keyoptions: K1 Simple enhanced strain; K3 Plane strain
- Poisson ratio: 0.3
- Young modulus: 206000 MPa
- Minimum element size: $2 \cdot 10^{-5}$ mm

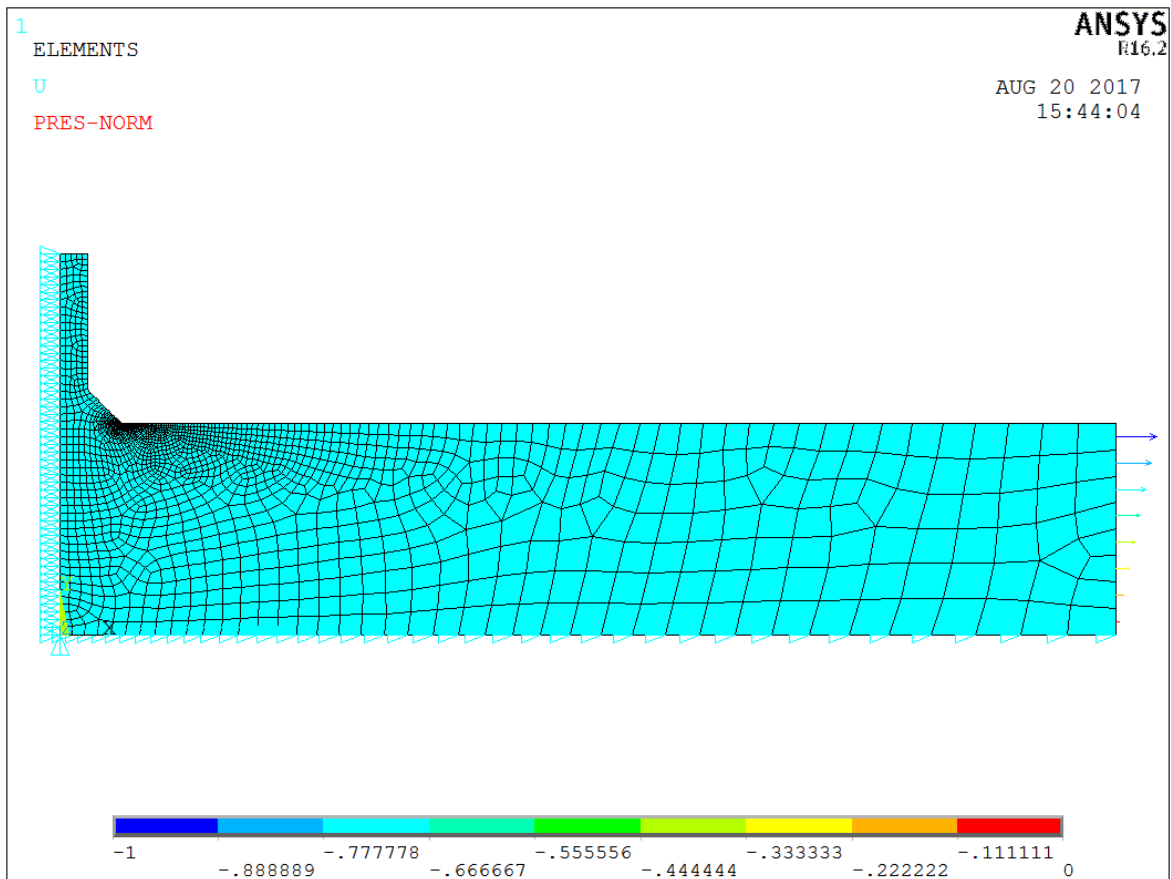


Figure 3.18: Geometry, constraints and loads of the series 16 FEM model.

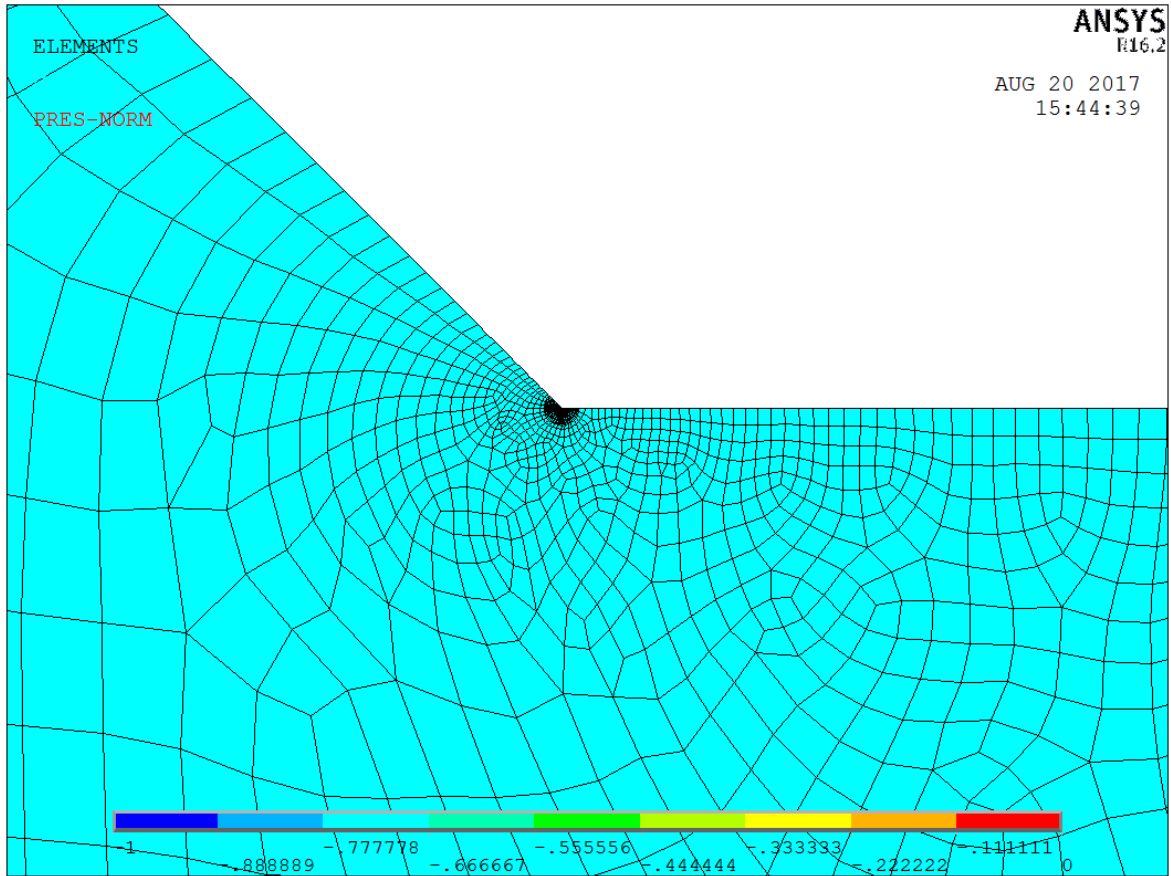


Figure 3.19: zoom around the notch tip of series 16 FEM model

Once the structure has been solved, the output of the results has been displayed referring to a local Cartesian coordinate system located at the notch tip and with the x-axis aligned with the notch bisector line.

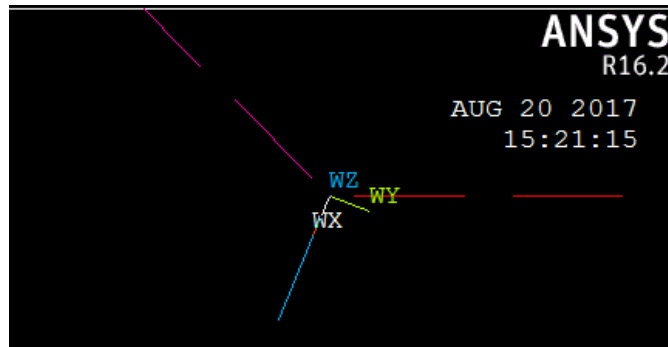


Figure 3.20: Local Cartesian coordinate system.

The nodes belonging to the bisector line, within the bigger circle radius were selected and used to define a path with exception to the nodes belonging to the smaller circle because heavily sensitive to the singularity distortion. In this reference system the stress σ_y act like the $\sigma_{\theta\theta}(r, \vartheta = 0)$ of the NSIF definition, eq. 3.1, so it was plotted in relation to the tip distance, fig 3.21.

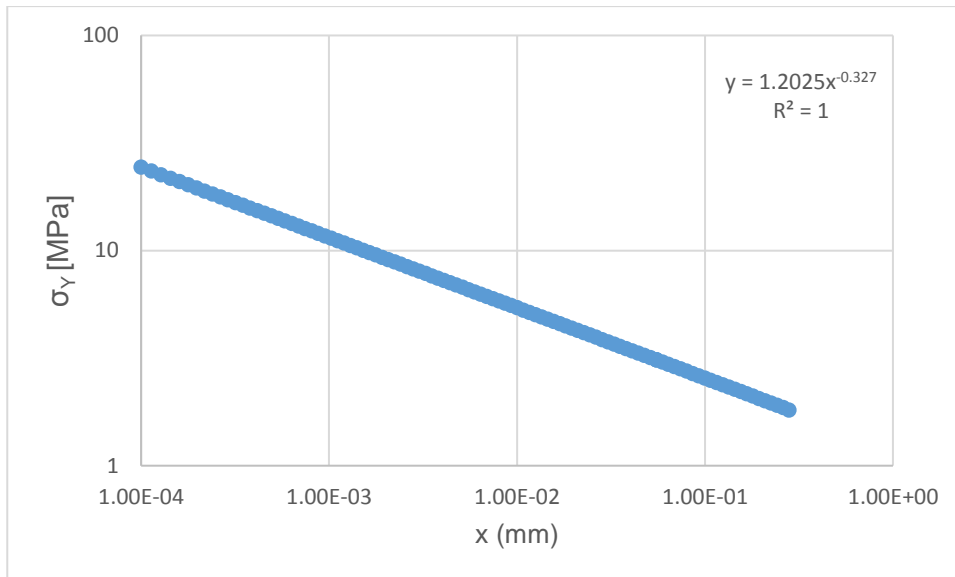


Figure 3.21: Y-stress distribution referred to the local coordinate system in fig. 3.20.

The modulus of exponent of interpolation line (power law) is 0.327 confirming Williams eigenvalue. Having the stress distribution, the Mode I NSIF definition can be applied and what emerges is its finite and constant number within the considered distance.

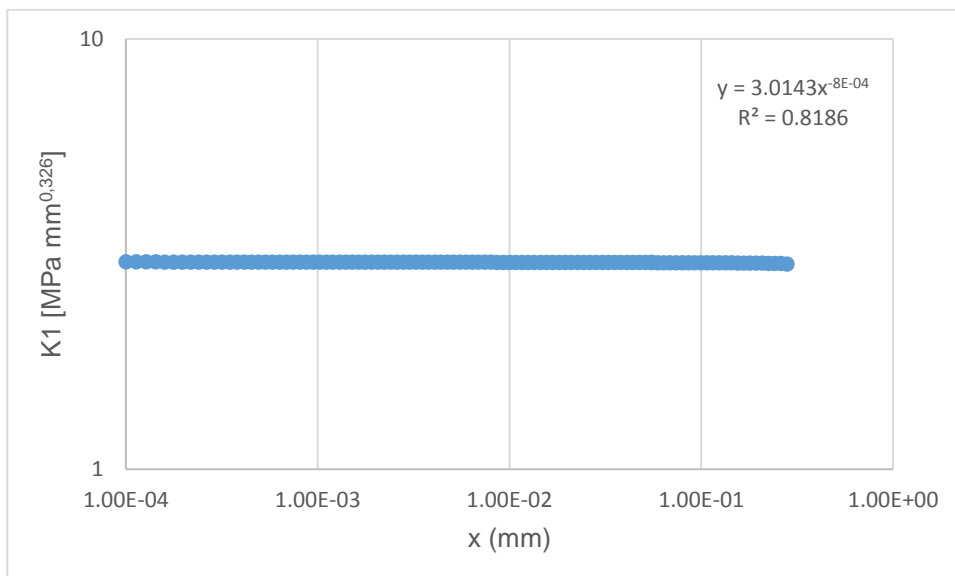


Figure 3.22: NSIF value of the selected nodes belonging to the notch bisector line and within the bigger circle radius.

The exponent of the power of law interpolation line is extremely low, so the NSIF value, considered constant is 3.014.

3.3.4 Series 23

The geometry of this series is a T non load carrying fillet welded joint subjected to a bending load. The dimensions have been taken by table 3.1 and it has been modelled using the symmetry on the YZ plane, taking as a reference system the one showed in fig 3.23. Furthermore, the displacement on the node in position (0; 0; 0) has been restrained in the y direction.

FEM Characteristics:

- Element type: PLANE 182
- Keyoptions: K1 Simple enhanced strain; K3 Plane strain
- Poisson ratio: 0.3
- Young modulus: 206000 MPa
- Minimum element size: $2 \cdot 10^{-5}$ mm

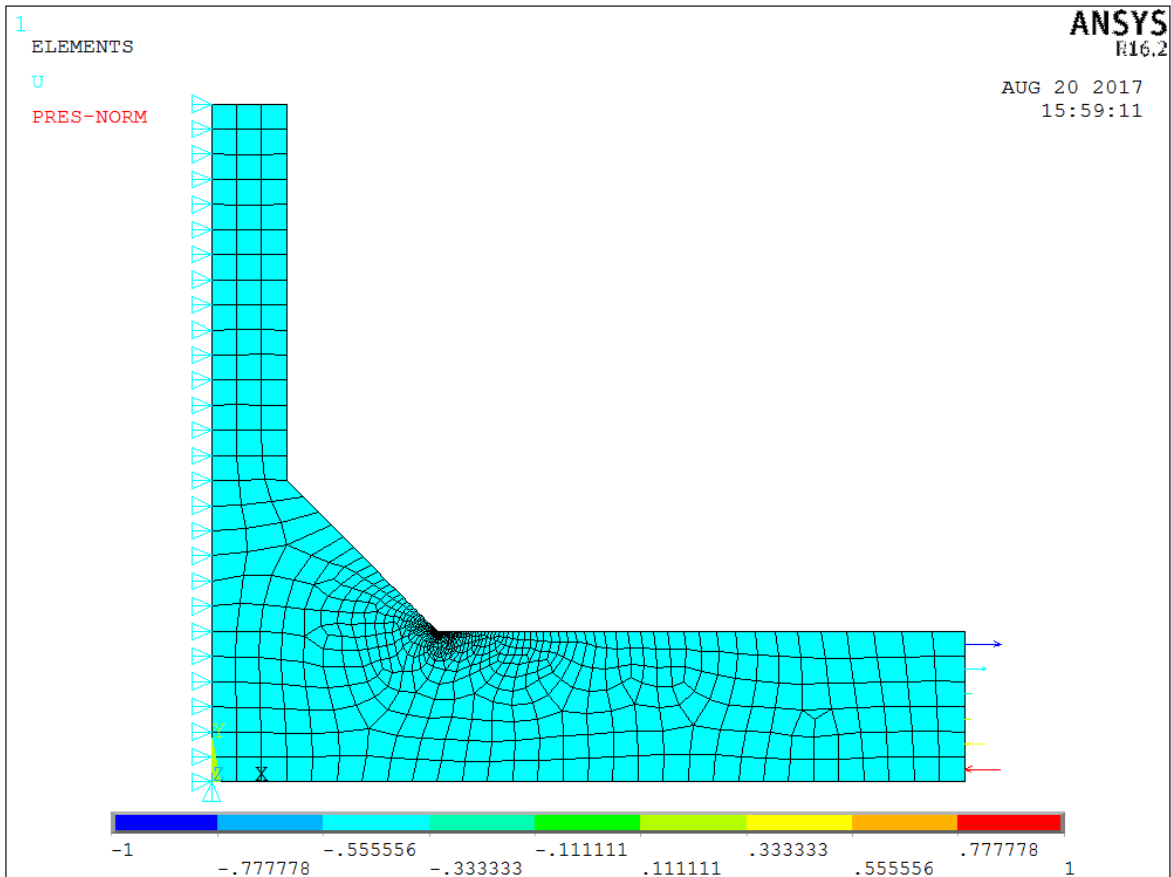


Figure 3.23: Geometry, constraints and loads of the series 12 FEM model.

Once the structure has been solved, the output of the results has been displayed referring to a local Cartesian coordinate system located at the notch tip and with the x-axis aligned with the notch bisector line.

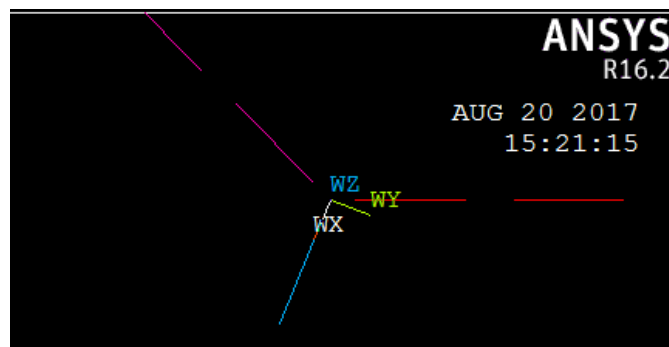


Figure 3.24: Local Cartesian coordinate system.

The nodes belonging to the bisector line, within the bigger circle radius were selected and used to define a path with exception to the nodes belonging to the smaller circle because heavily sensitive to the singularity distortion. In this reference system the stress σ_y act like the $\sigma_{\theta\theta}(r, \vartheta = 0)$ of the NSIF definition, eq. 3.1, so it was plotted in relation to the tip distance, fig 3.25.

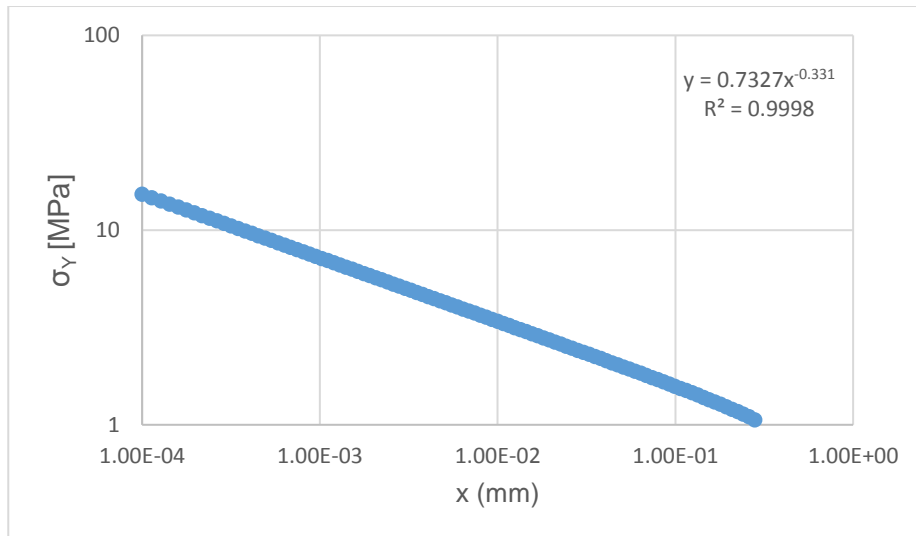


Figure 3.24: Y-stress distribution referred to the local coordinate system in fig. 3.24.

The modulus of exponent of interpolation line (power law) is 0.331 confirming Williams eigenvalue. Having the stress distribution, the Mode I NSIF definition can be applied and what emerges is its finite and constant number within the considered distance.

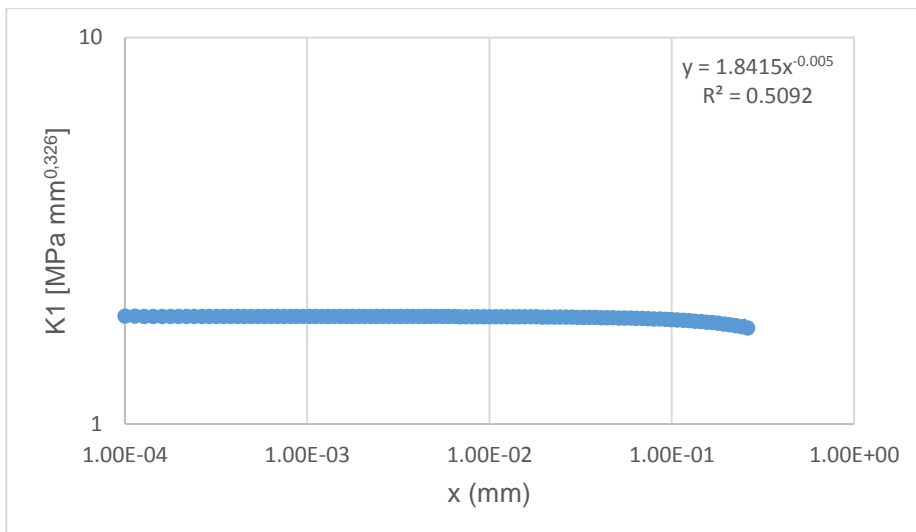


Figure 3.25: NSIF value of the selected nodes belonging to the notch bisector line and within the bigger circle radius.

The exponent of the power of law interpolation line is extremely low, so the NSIF value, considered constant is 1.8415.

3.4 Evaluation of results

The results of the four analyzed models are summarised in the following table, comparing them with the published Mode I NSIF values.

Series	Calculated K1 [MPa mm ^{0.326}]	Published K1 in [10] [MPa mm ^{0.326}]	Percentage error [%]
1	2.6624	2.633	1,116597
12	5.375	5.704	5,767882
16	3.014	3.051	1,212717
23	1.8415	1.793	2,704964

Table 3.5: Comparison of calculated Mode I NSIF with the published ones.

It is worth noting that three out of four models give as an output values with errors below the 3%, confirming the reliability of the FEM analysis. Concerning series 12, the higher value of the error maybe is due to a not-enough refined mesh, however, in this analysis, it is considered acceptable. The radius of the bigger circle was not chosen by chance, but the value of 0.28 mm was selected because it is the control radius suitable to the calculation of the Strain Energy Density (SED) in the steel joints. The Ansys ® software allow us to know the value (called “sene”) of the SED in relation to the applied stress (in our models $\Delta\sigma = 1$ MPa) and referring to a volume or an area (called “volu”). The following equation bring the possibility of calculating the value of the SED and extend it to other stress values:

$$\Delta\bar{W} = \frac{sene}{volu} * \Delta\sigma^2 \quad (3.2)$$

This relation is consistent with the fact that the Strain Energy Density is proportional to the square of the applied stress. Eventually, the experimental data could be studied in terms of SED and K1, using the values obtained by the accurate FE analysis, tab. 3.6.

Series	a [mm]	Nf [cycles]	$\Delta\sigma$ [MPa]	sene ^a [MJ]	volu ^a [m ³]	$\Delta\bar{W}$ ^b [MJ/ m ³]	K1/ σ_{nom} [mm ^{0.326}]	K1 [MPa mm ^{0.326}]
1	13	192000	200	1,43E-06	0,153938	3,72E-01	2,6624	532,48
1	13	507000	140	1,43E-06	0,153938	1,82E-01	2,6624	372,736
1	13	2937000	100	1,43E-06	0,153938	9,31E-02	2,6624	266,24
1	13	4297000	80	1,43E-06	0,153938	5,96E-02	2,6624	212,992
12	100	109000	150	5,65E-06	0,152951	8,31E-01	5,33	799,5
12	100	224000	120	5,65E-06	0,152951	5,32E-01	5,33	639,6
12	100	322000	100	5,65E-06	0,152951	3,69E-01	5,33	533
12	100	1153000	65	5,65E-06	0,152951	1,56E-01	5,33	346,45
12	100	2147000	55	5,65E-06	0,152951	1,12E-01	5,33	293,15
16	100	120000	260	1,82E-06	0,152951	8,03E-01	3,014	783,64
16	100	200000	220	1,82E-06	0,152951	5,75E-01	3,014	663,08
16	100	302000	180	1,82E-06	0,152951	3,85E-01	3,014	542,52
16	100	744000	140	1,82E-06	0,152951	2,33E-01	3,014	421,96
16	100	1180000	120	1,82E-06	0,152951	1,71E-01	3,014	361,68
16	100	2158000	110	1,82E-06	0,152951	1,44E-01	3,014	331,54
23	6	135000	300	6,95E-07	0,152951	4,09E-01	1,8415	552,45
23	6	237000	260	6,95E-07	0,152951	3,07E-01	1,8415	478,79
23	6	407000	200	6,95E-07	0,152951	1,82E-01	1,8415	368,3
23	6	573000	190	6,95E-07	0,152951	1,64E-01	1,8415	349,885
23	6	665000	180	6,95E-07	0,152951	1,47E-01	1,8415	331,47
23	6	1525000	160	6,95E-07	0,152951	1,16E-01	1,8415	294,64
23	6	1534000	150	6,95E-07	0,152951	1,02E-01	1,8415	276,225
23	6	2601000	140	6,95E-07	0,152951	8,91E-02	1,8415	257,81

^a calculated via accurate FE analisys using Ansys ®

^b calculated by means of eq 3.2

Table 3.6: SED and K1 parameters calculated for every series and every load condition.

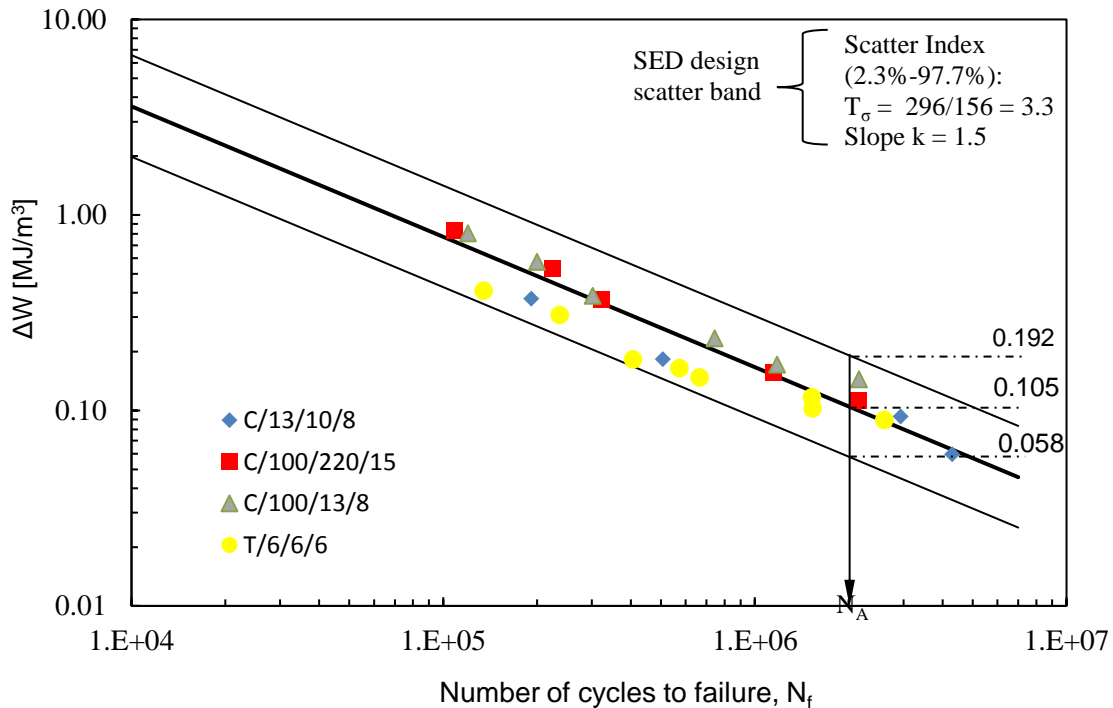


Figure 3.26: Comparison of the experimental data evaluated in terms of Stain Energy Density with the SED design scatter band.

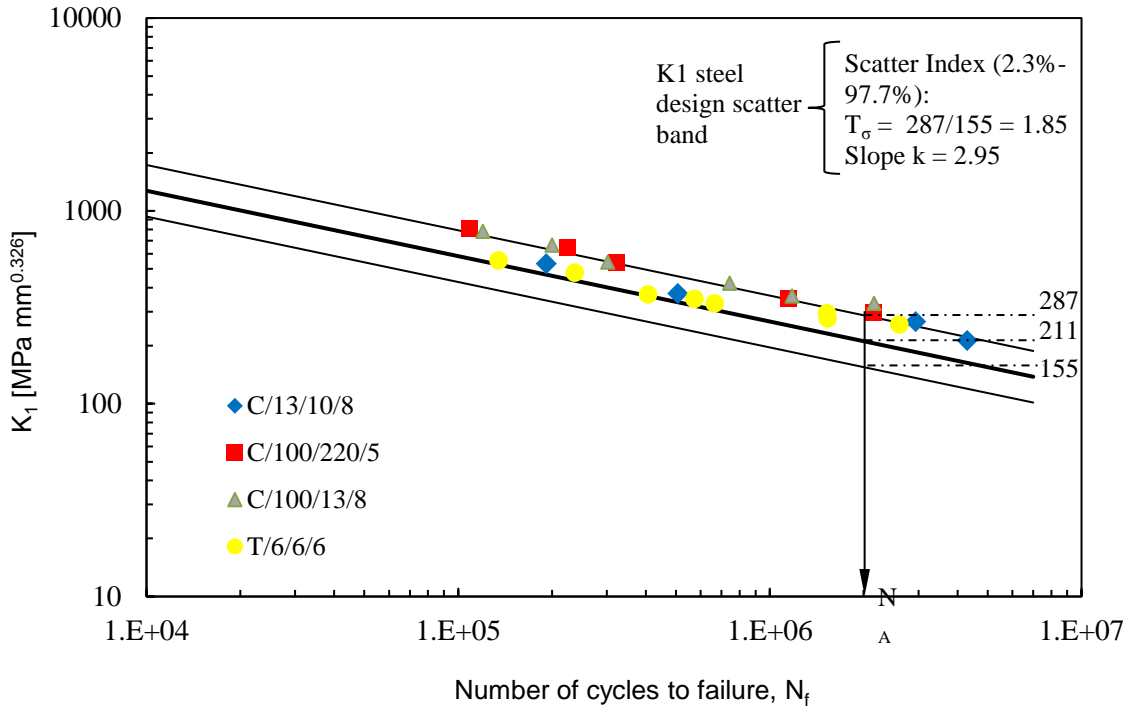


Figure 3.27 Comparison of the experimental data evaluated in terms of Mode I NSIF design scatter band, [24].

These last graphs, figs. 3.26 and 3.27, show that almost every experimental data fall within the calibrated scatter band, confirming the goodness of the analytical procedure and the FEM models. Plotting the SED and the K1 parameters, what emerges is that all the experimental data fall within a unique scatter band, as claimed by the local approach. Also, the inverse slope of the SED is half of the K1 one because of the quadratic dependence of the applied stress. The major result is that the local approach allow all the data to be located in a single scatter band with a great decrease of the scatter index. To emphasize this achievement, both the NSIF approach and the nominal one were plotted in the same graph, figure 3.28.

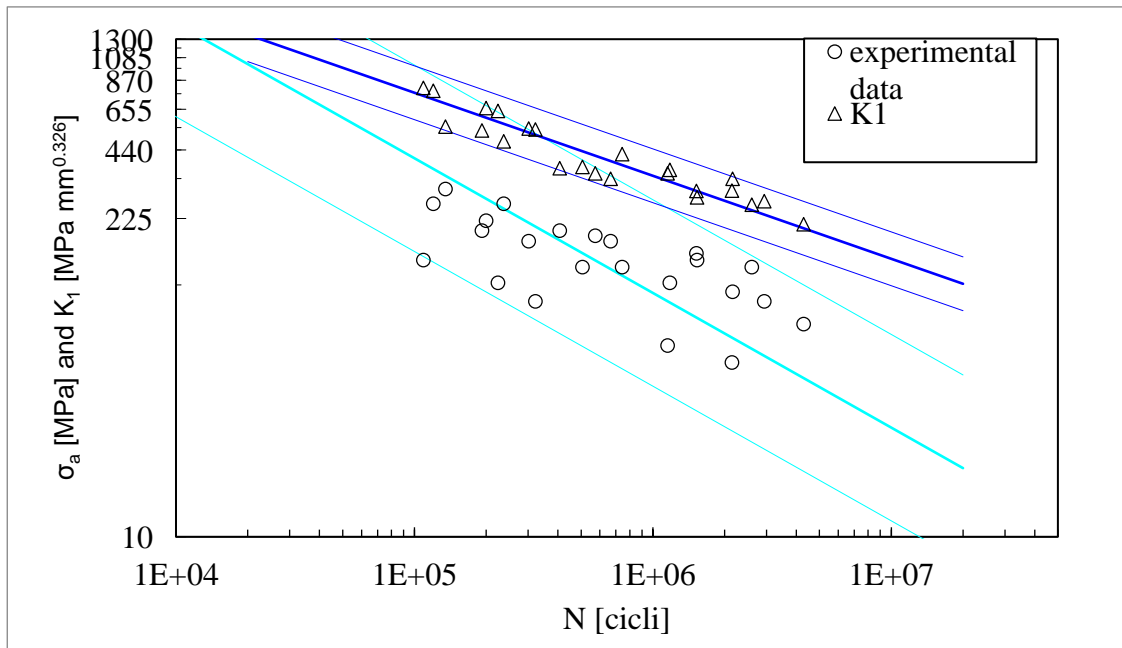


Figure 3.28: Wohler diagram in terms of nominal stress or Mode I NSIF and cycles to failure. The NSIF approach guarantee a scatter index (10%-90%) reduction from 6.19 to 1.69.

As it was previously underlined, these Mode I NSIF values were obtained with a minimum element size of $2 \cdot 10^{-5}$ mm, which is acceptable in two-dimensional cases but, when dealing with 3D models, this would lead to high calculation times. Furthermore, the complexity of the solution, in terms of building the stiffness matrix and its inversion, requires computer with high dynamic memories (RAM). A possible solution to this issue is applying the Peak Stress Method, to calculate the NSIFs approximated values with coarser meshes but still considered valid from an engineering point of view.

3.5 FEM models to estimate the approximated Mode I NSIF value using the Peak Stress Method (PSM).

In order to apply the Peak Stress Method to the four analyzed geometries, new models with coarser meshes have been built. These fulfill all the hypothesis of the PSM and the Mode I constant K_{FE}^* has been calculated to estimate their reliability. First it was necessary to estimate the peak stress at the notch tip. Here it is the first approximation: instead of the $\sigma_{\theta\theta, \theta=0}$, the first principal stress, in relation to the global reference system, was considered $\sigma_{\theta\theta, \theta=0, peak}$. The table 3.1, reports the peak stresses obtained with a global element size of 1 mm; it is authors' opinion that this value leads to over refined meshes for this approach, so the models have been analyzed with this global size but also with a much bigger one.

Then the K_{FE}^* was estimated with eq. 3.3:

$$K_{FE}^* = \frac{K_1}{\sigma_{\theta\theta, \theta=0, peak} d^{1-\lambda_1}} \quad (3.3)$$

Theoretically the result should be:

$$K_{FE}^* = 1.38 \pm 3\% \quad (3.4)$$

Eventually this value will be compared with the ones calculated with the global element size of 1 mm and the ones with the coarser meshes.

3.5.1 Series 1

The FEM characteristics are the same of the previous one, always adopting the PLANE 182 elements with the first keyoption set to "Simple enhanced strain"; what changes is the mesh pattern. A global element size was imposed equal to 2 mm and the free mesh generator algorithm was launched, the result is shown in fig. 3.29.

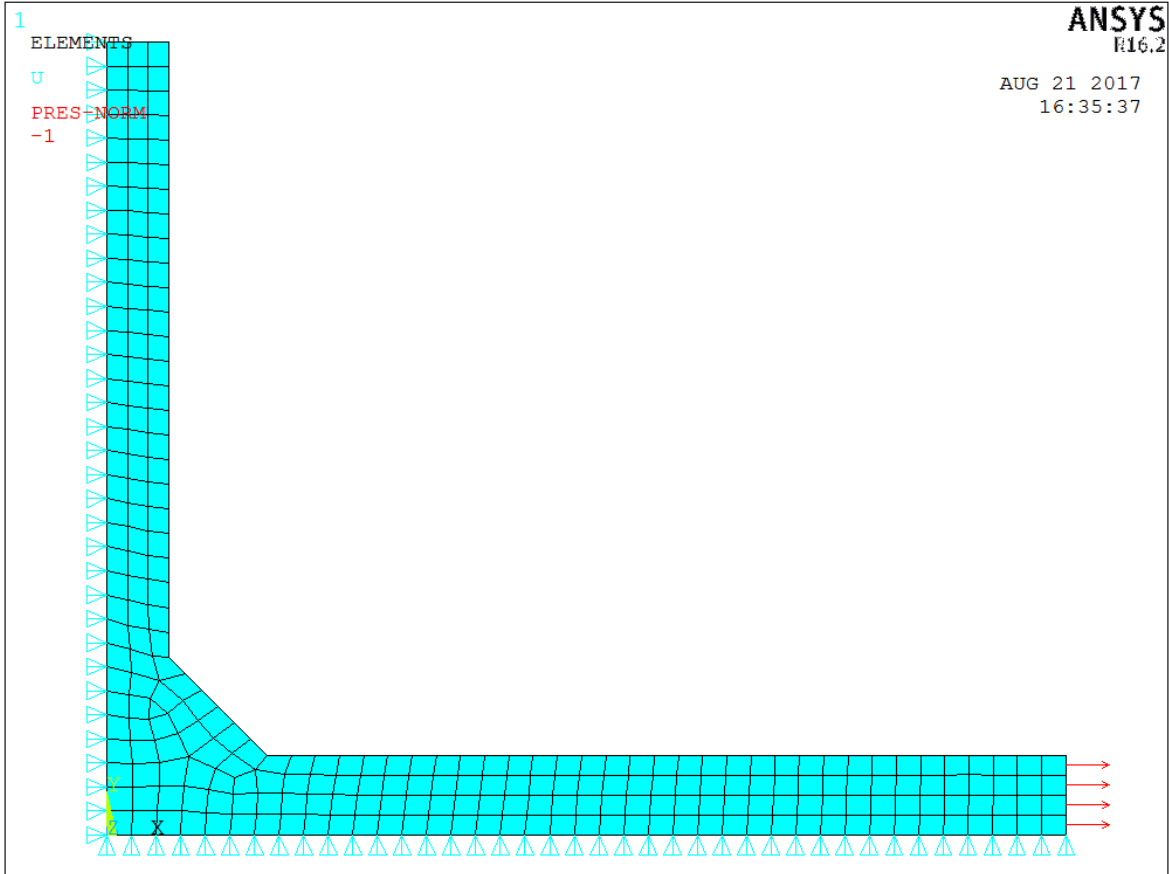


Figure 3.29: mesh pattern of series 1 obtained with a global element size of 2 mm.

3.5.2 Series 12

The FEM characteristics are the same of the previous one, always adopting the PLANE 182 elements with the first keyoption set to “Simple enhanced strain”; what changes is the mesh pattern. A global element size was imposed equal to 15 mm and the free mesh generator algorithm was launched, the result is shown in fig. 3.30.

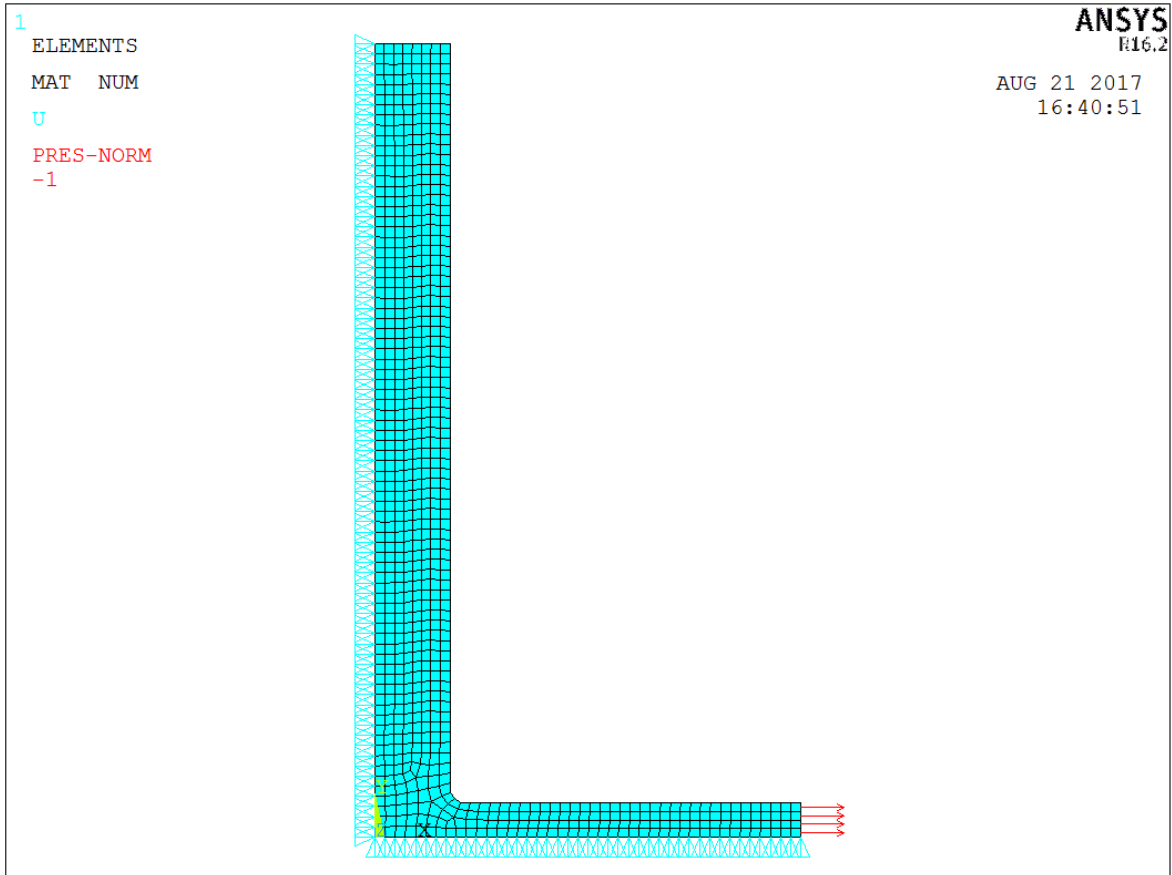


Figure 3.30: mesh pattern of series 12 obtained with a global element size of 15 mm.

3.5.3 Series 16

The FEM characteristics are the same of the previous one, always adopting the PLANE 182 elements with the first keyoption set to "Simple enhanced strain"; what changes is the mesh pattern. A global element size was imposed equal to 5 mm and the free mesh generator algorithm was launched, the result is shown in fig. 3.31.

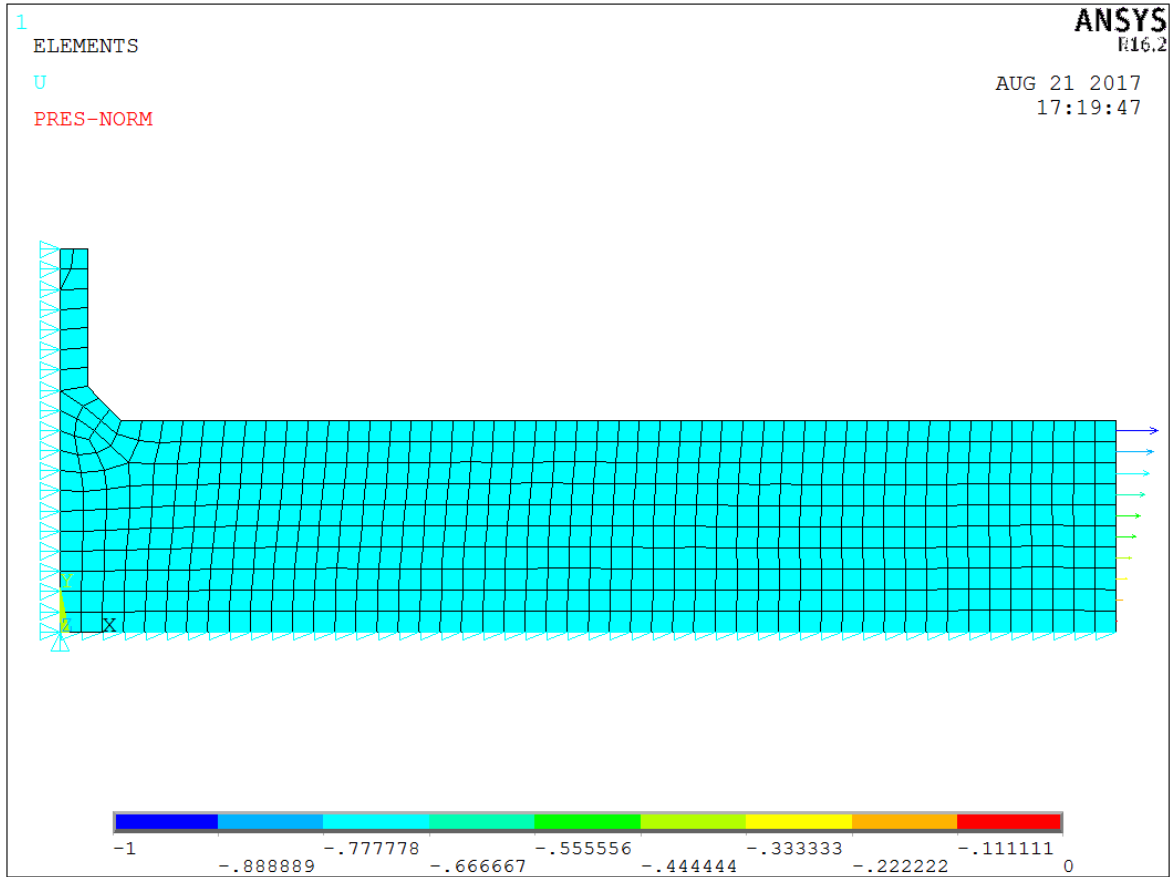


Figure 3.31: mesh pattern of series 16 obtained with a global element size of 5 mm.

3.5.4 Series 23

The FEM characteristics are the same of the previous one, always adopting the PLANE 182 elements with the first keyoption set to “Simple enhanced strain”; what changes is the mesh pattern. A global element size was imposed equal to 2 mm and the free mesh generator algorithm was launched, the result is shown in fig. 3.32.

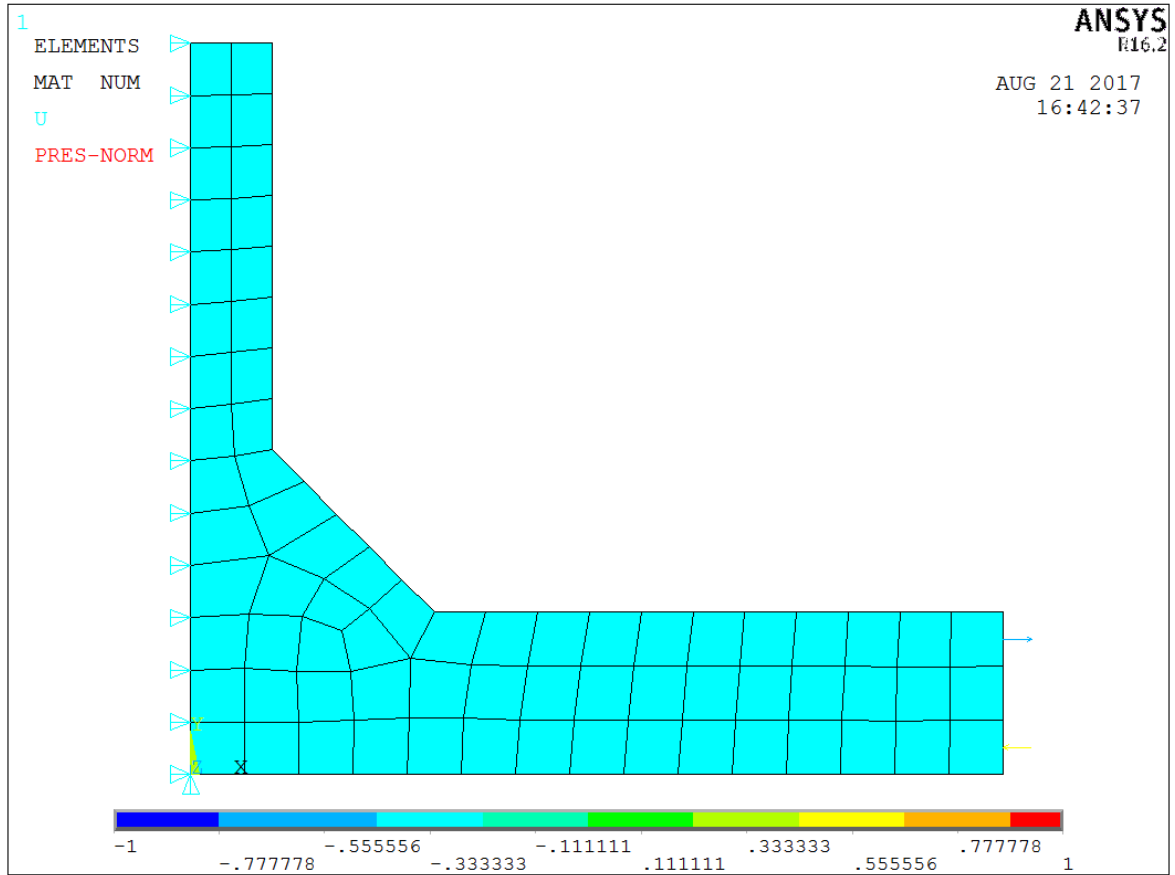


Figure 3.32: mesh pattern of series 23 obtained with a global element size of 2 mm.

3.6 Evaluation of results.

All the series have been analysed by adopting FE models with two different global element sizes. The results, resumed in table 3.7, show a good agreement for series 1 and 23, while the other ones are quite different and exceed the 3% limit of eq. 3.3. In fact the K_{FE}^* should be comprehended between 1,3386 and 1,4214 to be consistent with the definition and series 12 and 16 does not. However it is interesting to remark that the calibration constant obtained with the much coarser meshes is not far away from the correct value, which means that even in this case the PSM is applicable for engineering purposes.

Series	d (mm)	σ_{peak}/σ_g^a	K_{FE}^{*b} [MPa mm ^{0,326}]	d (mm)	σ_{peak}/σ_g^a	K_{FE}^{*b} [MPa mm ^{0,326}]
1	1	1,87145	1,42264	2	1,51882	1,398399
12	1	3,85617	1,3822	15	1,66424	1,324663
16	1	2,17446	1,386091	5	1,1022	1,324071
23	1	1,37595	1,338348	2	1,043555	1,407734

^a $\sigma_g = 1 \text{ MPa}$

^b K_{FE}^* has been calculated by means of eq 3.3.

Table 3.7: Stress parameters for the analyzed steel welded joints.

Eventually the equivalent peak stress was calculated, referring to the peak stress obtained with the coarser mesh and not with the one characterized by a global element size of 1 mm. First from the known tables, see chapter 2 table 2.2, e_1 was found to be 0.118, then the calculation of f_{w1} was carried out with the following equations, eq 3.5.

$$f_{w1} = K_{FE}^* \sqrt{\frac{2e_1}{1-\nu^2}} \left(\frac{d}{R_0}\right)^{1-\lambda_1} \quad (3.5)$$

Then, applying the equivalent peak stress definition in case of only Mode I loading conditions:

$$\Delta\sigma_{eq,peak} = f_{w1} \Delta\sigma_{\vartheta\vartheta,\vartheta=0,peak} \quad (3.6)$$

Finally, all the four values of the equivalent stress were multiplied for the nominal stress range in order to compare the experimental data with the calibrated curve, fig. 3.33.

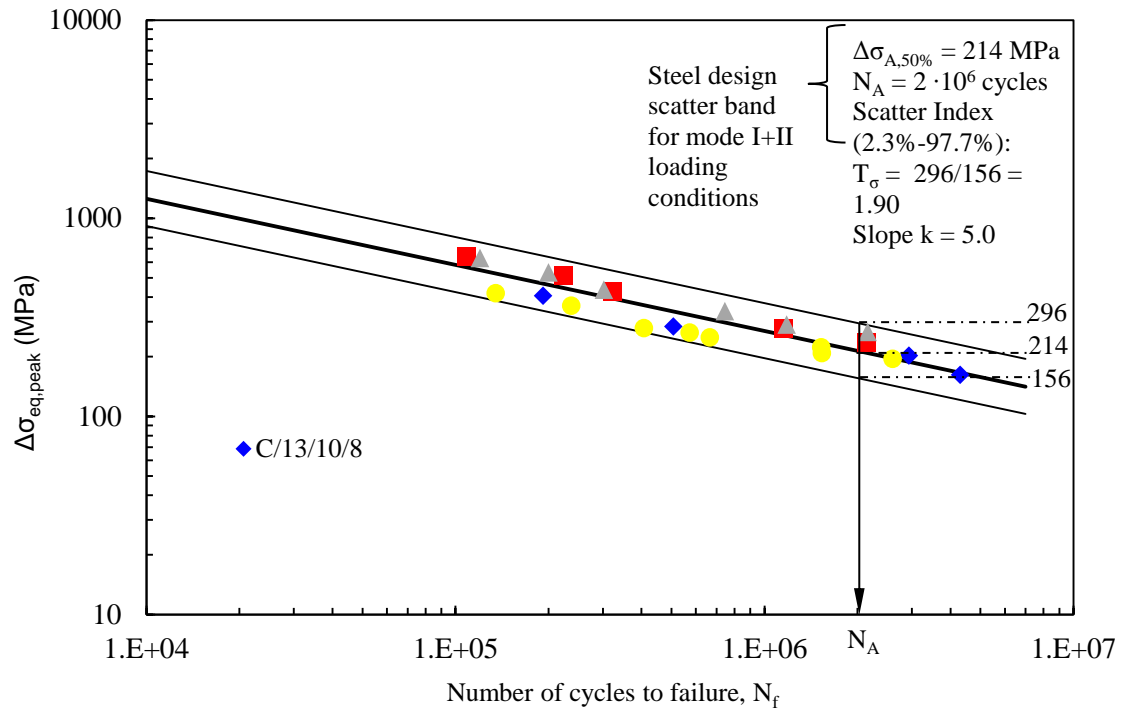


Figure 3.33: Steel design scatter band for mode I+II loading conditions.

Series	N [cycles]	f_{w1}	$\Delta\sigma$ [MPa]	$\Delta\sigma_{eq,peak}$ [MPa]
1	192000	1.334064	200	410.6436
	507000	1.334064	140	287.4505
	2937000	1.334064	100	205.3218
	4297000	1.334064	80	164.2575
12	109000	2.573041	150	621.7725
	224000	2.573041	120	497.418
	322000	2.573041	100	414.515
	1153000	2.573041	65	269.4348
	2147000	2.573041	55	227.9833
16	120000	1.798478	260	604.3359
	200000	1.798478	220	511.3611
	302000	1.798478	180	418.3864
	744000	1.798478	140	325.4116
	1180000	1.798478	120	278.9243
	2158000	1.798478	110	255.6806
23	135000	1.334064	300	426.0443
	237000	1.334064	260	369.2384
	407000	1.334064	200	284.0295
	573000	1.334064	190	269.8281
	665000	1.334064	180	255.6266
	1525000	1.334064	160	227.2236
	1534000	1.334064	150	213.0222
	2601000	1.334064	140	198.8207

Table 3.8: experimental results evaluated in terms of equivalent peak stress

The result is that all the data fall within the calibrated scatter band, confirming the goodness of the calculation process to estimate the equivalent peak stress for all four series.

CHAPTER 4:

Application of the Peak Stress Method to the welded joint

4.1 Axis symmetric model

Before applying the PSM to the 3D geometry, it would be interesting to see if in a 2D model there is a significant influence of higher order terms. In fact, the Peak Stress Method does not consider them and in case of a non-negligible presence of them it cannot be used as originally proposed, but it would require a proper extension. One of the possible alternative way would be the application of the SED approach, because the SED value, calculated by Ansys, takes into account all possible contributes. Considering a polar reference system centred at the V-notch tip, equations 4.1 and 4.2 show that higher order terms could be present in Mode I and II loading conditions but also in the Mode III case.

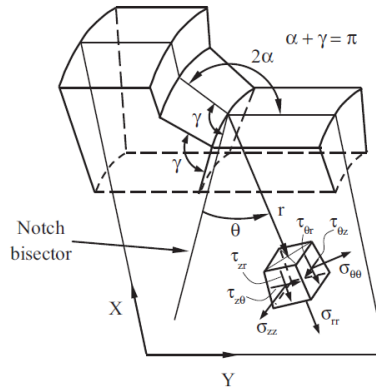


Figure 4.1: Polar reference system centred at the V-notch tip, [9].

$$\begin{Bmatrix} \sigma_{\theta\theta} \\ \sigma_{rr} \\ \tau_{r\theta} \end{Bmatrix} = \frac{K_1}{r^{1-\lambda_1}} \begin{Bmatrix} \tilde{\sigma}_{\theta\theta}(\vartheta) \\ \tilde{\sigma}_{rr}(\vartheta) \\ \tilde{\tau}_{r\theta}(\vartheta) \end{Bmatrix}_1 + \frac{K_2}{r^{1-\lambda_2}} \begin{Bmatrix} \tilde{\sigma}_{\theta\theta}(\vartheta) \\ \tilde{\sigma}_{rr}(\vartheta) \\ \tilde{\tau}_{r\theta}(\vartheta) \end{Bmatrix}_2 + \text{higher order terms} \quad (4.1)$$

$$\begin{Bmatrix} \tau_{\theta z} \\ \tau_{rz} \end{Bmatrix}_{\rho=0} = \frac{K_3}{\sqrt{2\pi}} r^{1-\lambda_3} \begin{Bmatrix} \cos(\lambda_3\vartheta) \\ \sin(\lambda_3\vartheta) \end{Bmatrix} + \text{higher order terms} \quad (4.2)$$

After these considerations, it is clear that two models have to be studied; one loaded with Mode I and II and the other with Mode III.

Dealing with the 2D models an observation has to be done: the specimens' geometry cannot be studied properly with planar geometries because it is not axis symmetric. The weld is not continuous along the outer surfaces but there are two separated welds. However, an axis symmetric geometry was modelled and analysed. Even though it does not simulate exactly the specimen geometry, it allow us to investigate in a simple manner (2D analyses) the higher order terms presence. The planar geometry is the one showed in figure 4.2, where the outer cylinder is considered with its full length, while just 60 mm for the inner one because we are focusing on the root side that is far away from the upper edge. In order to build suitable meshes to apply the SED definition, a particular technique was adopted in both models, consisting in drawing two circles around the notch tip. The bigger circle has a 0.28 mm radius while the smaller one just a 0.0001 mm radius. In the smaller circle, a specific mesh tool of Ansys code called "concentration keypoint" was adopted to guarantee a circular and uniform element disposition around the notch.

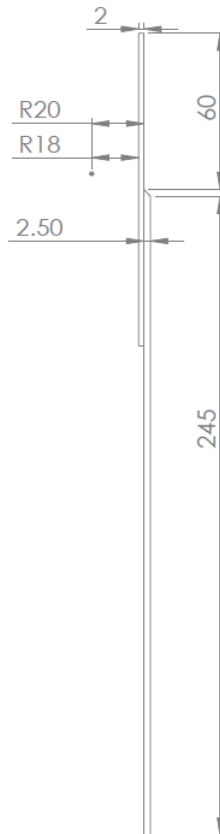


Figure 4.2: Axis symmetric geometry.

FEM characteristics:

- ELEMENT TYPE: PLANE 83 (AXIS SYMMETRIC, HARMONIC)
- MATERIAL PROPERTIES: $E = 206000$ MPa ; $\nu = 0.3$
- Mesh free out of the control radius, after imposing lines divisions.
- Inside the bigger circle the mesh mapped technique was adopted after dividing conveniently the lines.
- Inside the smaller circle the concentration keypoint technique was adopted, parameters showed in figure 4.3.

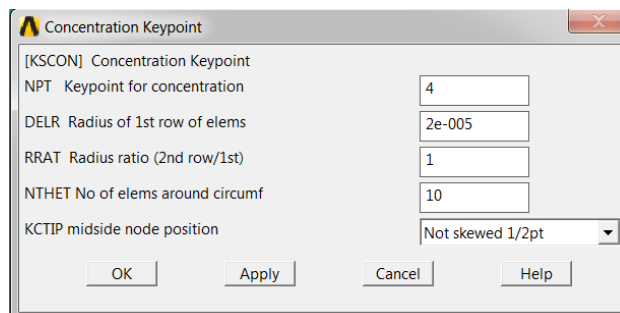


Figure 4.3: Ansys' window for concentration keypoints creation.

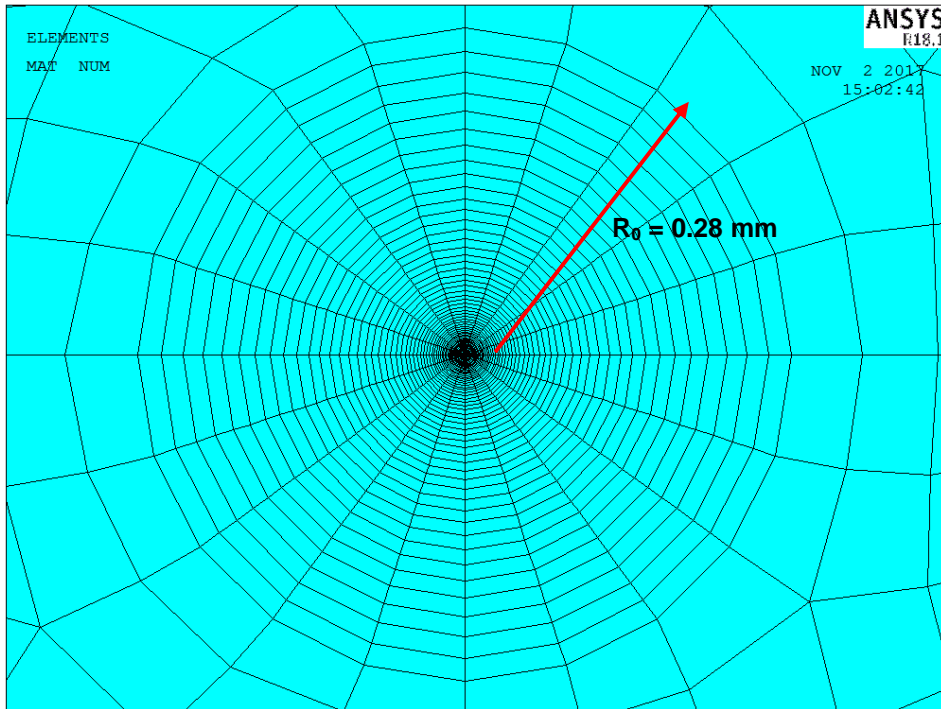


Figure 4.4: Mesh inside the control volume

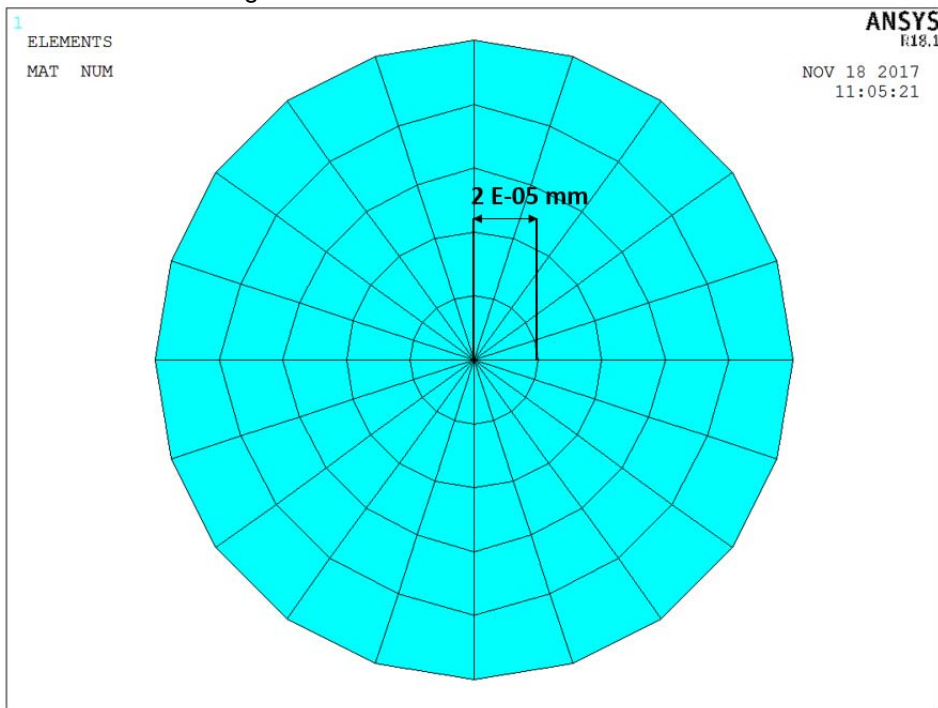


Figure 4.5: Mesh pattern within the minor circle.

The mesh pattern becomes more and more refined near the notch tip, figure 4.6.

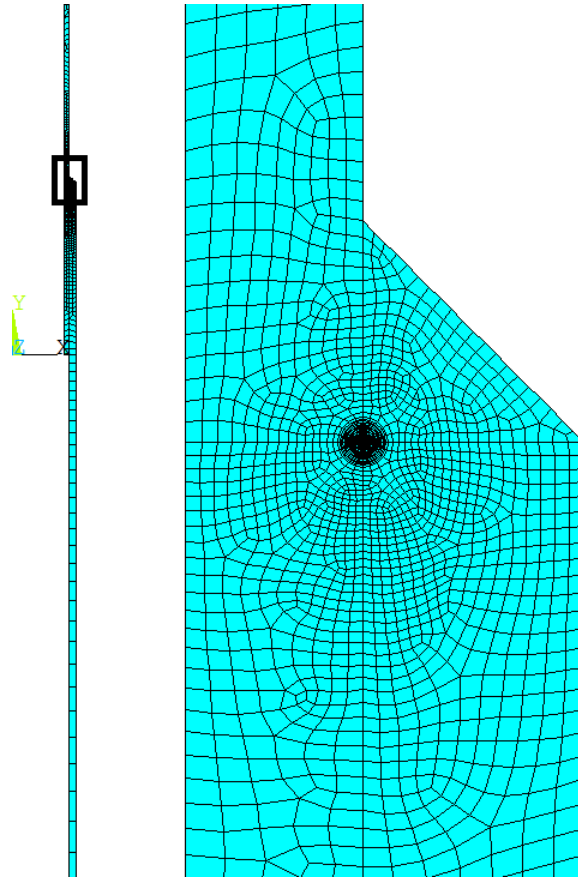


Figure 4.6: Axis symmetric model mesh pattern.

4.1.1 Axis symmetric model: pure axial

With this model we are analysing the Mode I and II loading cases. The main purpose of this work is to calculate the Mode I and II NSIFs K_1 and K_2 , then calculate the analytical SED with these two values and then compare it with the SED value obtained directly with Ansys. In case of a match or a low error the higher order terms influence is negligible. The first step is to define the loads and constraints: all degrees of freedom of the lower line of the outer tube were constrained and a pressure in the x direction of 1 MPa was applied to the upper line of the inner tube, figure 4.7.

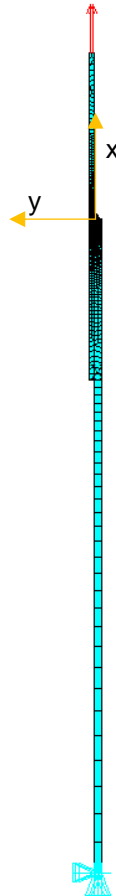


Figure 4.7: pure axial load and constraints.

Considering a Cartesian reference system centred at the root tip the Mode I loading condition is derived from a σ_{yy} stress component and the Mode II from a τ_{xy} stress component. Both have been calculated defining a path selecting the nodes belonging to the notch bisector line in x direction within the control radius. However, in the stress analysis the nodes belonging to the smaller circle were not considered due to numerical errors in detecting the stress singularity. The results of this analysis are shown in figure 4.8.

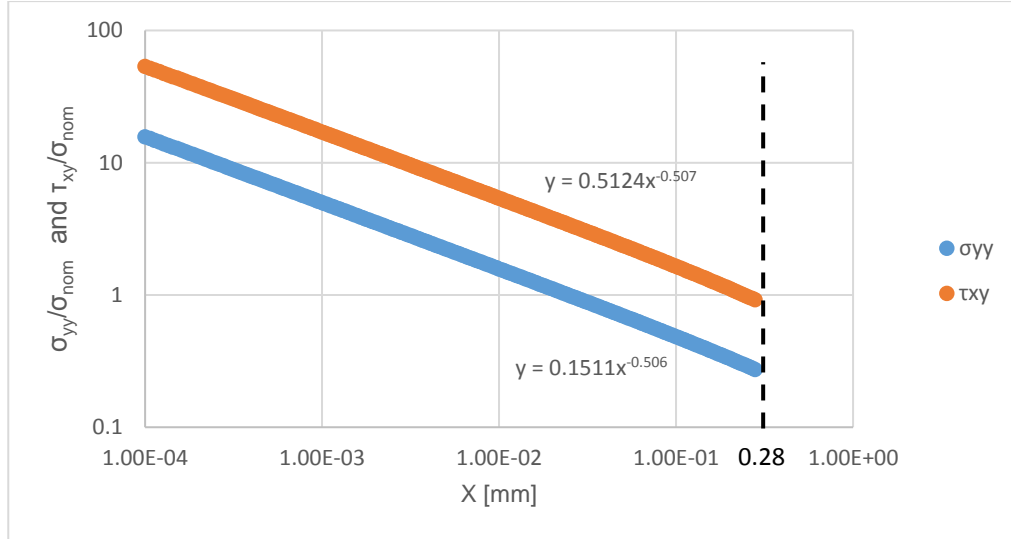


Figure 4.8: stress components path within the control radius, pure axial case.

What emerges from this graph is that adding power law interpolation lines the exponent is more or less 0.5 that is the ideal value for a V-notch with notch opening angle of 0° , typical of the root side. At this point we could apply the NSIFs definitions and plot the result in a graph:

$$K_1 = \sqrt{2\pi} \lim_{r \rightarrow 0^+} r^{1-\lambda_1} \sigma_{yy}(x, y = 0) \quad (4.3)$$

$$K_2 = \sqrt{2\pi} \lim_{r \rightarrow 0^+} r^{1-\lambda_2} \tau_{xy}(x, y = 0) \quad (4.4)$$

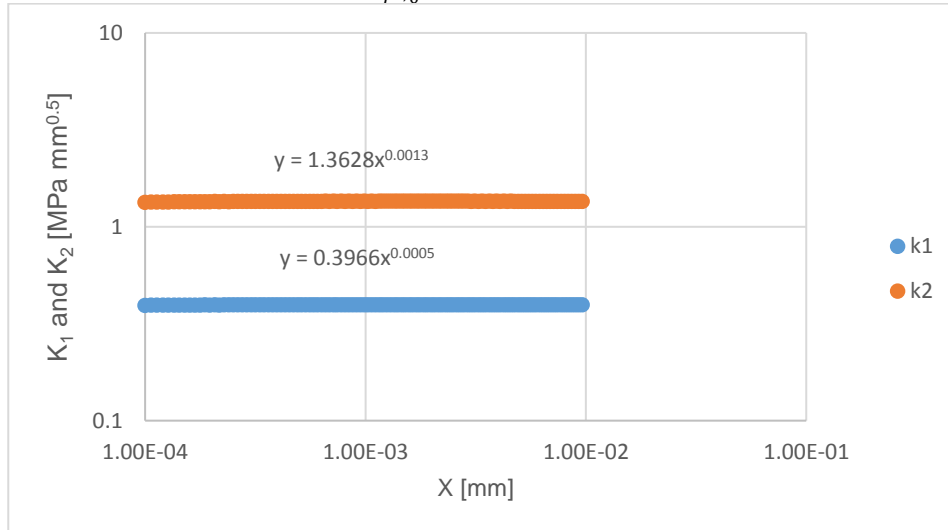


Figure 4.9: Mode I and II NSIFs graph.

In regard of the last plot, the analysis was restricted to a smaller interval because here the NSIFs value is constant. This statement is proved by the very low exponent of the power law interpolation lines, proximal to zero. The Mode I NSIF K_1 is $0.3966 \text{ MPa mm}^{0.5}$ and the Mode II NSIF K_2 is $1.3628 \text{ MPa mm}^{0.5}$. Knowing these parameters the SED definition (2D case) could be applied, eq 4.5.

$$\Delta \bar{W}_{analytical} = \frac{e_1}{E} \left[\frac{K_1}{R_0^{1-\lambda_1}} \right]^2 + \frac{e_2}{E} \left[\frac{K_2}{R_0^{1-\lambda_2}} \right]^2 = 1.131 * 10^{-5} \left[\frac{MJ}{m^3} \right] \quad (4.5)$$

At this point the obtained SED value has to be compared with the one calculated by Ansys, that considers also higher order terms. The Ansys commands are reported below:

```
SELECT => ENTITIES AREAS BY NUM/PICK (pick all areas within the control radius)
SELECT => EVERYTHING BELOW => SELECTED AREAS
```


GENERAL POSTPROCESSOR => ELEMENT TABLE => DEFINE TABLE => ADD => ENERGY
=> SENE => APPLY
GENERAL POSTPROCESSOR => ELEMENT TABLE => DEFINE TABLE => ADD =>
GEOMETRY => VOLU => APPLY
GENERAL POSTPROCESSOR => ELEMENT TABLE => SUM OF EACH ITEM

At this point to calculate the SED value it is necessary to apply the equation 4.6:

$$\Delta \bar{W}_{Ansys} = \frac{sene}{volu} = \frac{3.56 * 10^{-4}}{30.9505} = 1.15 * 10^{-5} \left[\frac{MJ}{m^3} \right] \quad (4.6)$$

The difference between the two values of the Strain Energy Density is very low, see table 4.1:

$\Delta \bar{W}_{analytical}$	$1.131 * 10^{-5} \left[\frac{MJ}{m^3} \right]$
$\Delta \bar{W}_{Ansys}$	$1.15 * 10^{-5} \left[\frac{MJ}{m^3} \right]$
Error (absolute)	1.62 %

Table 4.1: Pure axial case SED comparison.

Eventually, the last consideration is that in the pure axial loading condition, related to the Mode I and II, the higher order terms contribution is negligible and the Peak Stress Method could be applicable.

4.1.2 Axis symmetric model: pure torsion

With this model we are analysing the Mode III loading case. The geometry and the constraints are the same of the previous model, what changes is the load. In order to create a torsional moment, a force orthogonal to the XY plane was applied on the outer keypoint of the upper edge of the inner tube, see the red cross in figure 4.10.

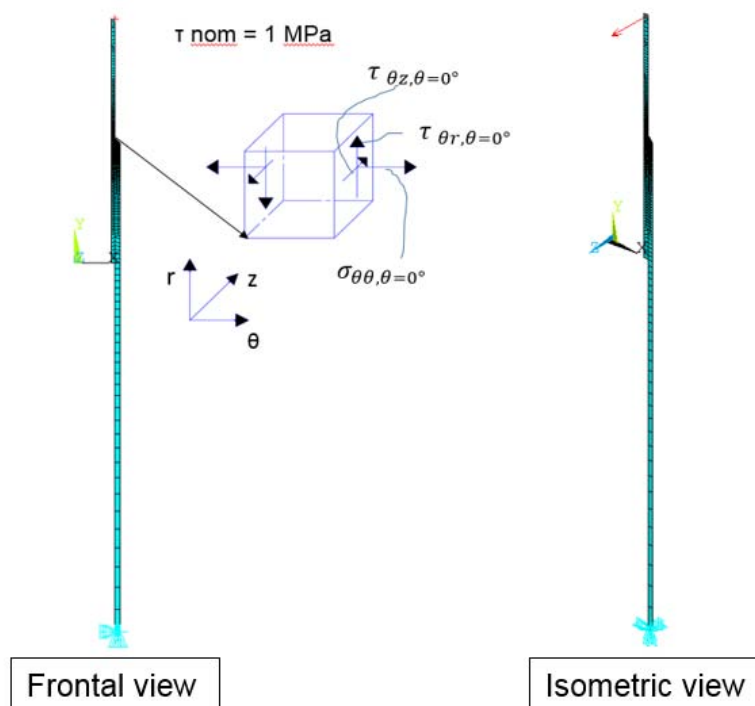


Figure 4.10: pure torsional load and constraints and reference system.

The calculation of the exact force to generate a $\tau_{nom} = 1 MPa$ is reported below and follows the path showed in the Ansys help topics of the axis-symmetric harmonic element adopted in this model. The reference system is shown in figure 4.11, where the 2D model is located on the XY plane.

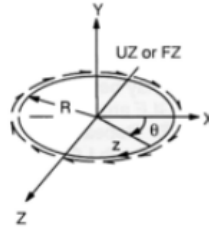


Figure 4.11: axis-symmetric element reference system.

The total applied moment (M) due to a tangential input force (Fz) acting about the global axis is:

$$M = \int_0^{2\pi} (\text{force per unit length}) * (\text{lever arm}) * (\text{increment length}) \quad (4.7)$$

$$M = \int_0^{2\pi} (-Fz/2\pi R) * (R) * (Rd\theta) = -R * Fz \quad (4.8)$$

But:

$$\tau_{nom} = \frac{M}{W_{st}} \quad (4.9)$$

Where W_{st} is the torsional resistance modulus. Isolating M from eq. 4.9 and inserting it in eq. 4.8, it results:

$$Fz = \frac{\tau_{nom} * W_{st}}{R} \quad (4.10)$$

In our case $\tau_{nom} = 1 \text{ MPa}$ and $R = \frac{d_{innertube,ext}}{2}$; so the last relation becomes:

$$Fz = \frac{\frac{\pi}{32} * \frac{d_{innertube,ext}^4 - d_{innertube,int}^4}{d_{innertube,ext}/2}}{\frac{d_{innertube,ext}}{2}} \quad (4.11)$$

$$Fz = \frac{\frac{\pi}{32} * \frac{40^4 - 36^4}{40/2}}{20} = 216,08 \text{ N} \quad (4.12)$$

At this point, once solved the model, we can calculate the stress components typical of the Mode III loading case. Considering equation 4.2 it is clear that with a crack opening radius of 0° only the $\tau_{\theta z}$ should be present as the singular component, but in this particular case there is also a constant τ_{rz} contribute along the crack bisector line, figure 4.12.

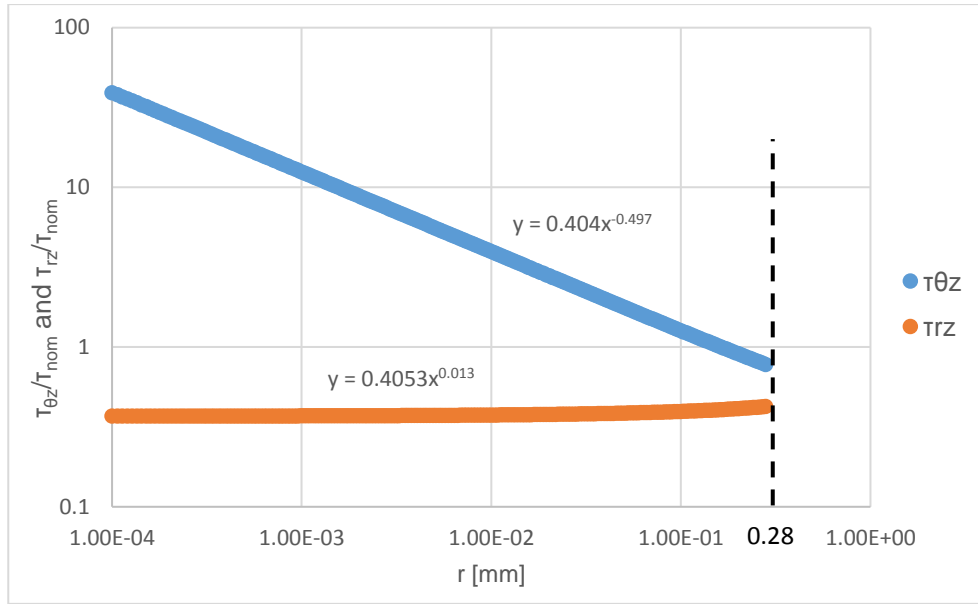


Figure 4.12: stress components path within the control radius, pure torsional case.

Again, in the singular case, the power law interpolation line has an exponent near 0.5, confirming the theoretical behaviour of a 0° opening angle V-notch. Dealing with the non-singular component, the power law interpolation line has an exponent near zero, underlining the fact that there is a constant contribute equal to 0.4053 MPa.

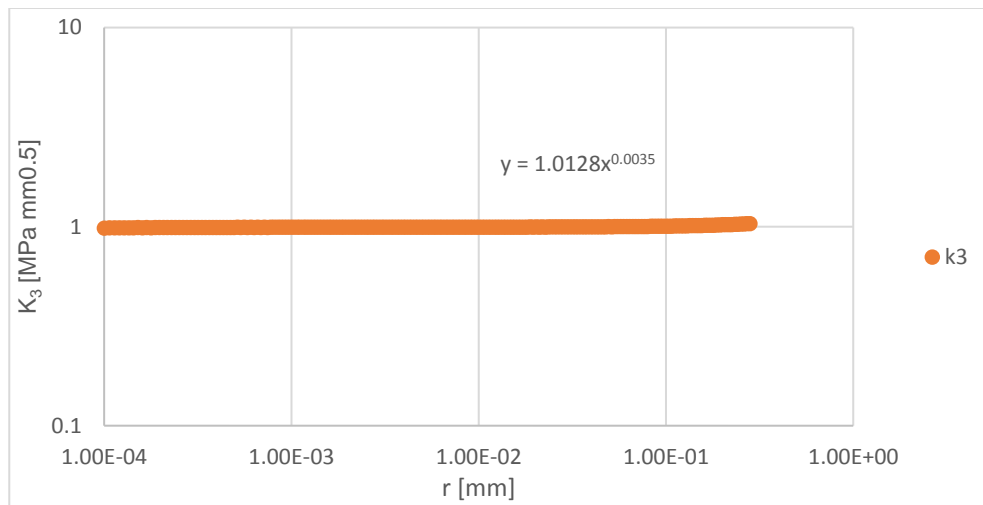


Figure 4.13: Mode III NSIF graph.

The very low value of the power law interpolation line proves that the Mode III NSIF K_3 is constant and equal to $1.0128 \text{ MPa} \cdot \text{mm}^{0.5}$. Proceeding calculating the SED value, it results:

$$\Delta \bar{W}_{analytical} = \frac{e_3}{E} \left[\frac{\Delta K_3}{R_0^{1-\lambda_3}} \right]^2 = 7.36 * 10^{-6} \left[\frac{[MJ]}{[m^3]} \right] \quad (4.13)$$

At this point the obtained SED value has to be compared with the one calculated by Ansys, that includes also higher order terms. The Ansys commands are the same of the previous model. To calculate the SED value it is necessary to apply the equation 4.14:

$$\Delta \bar{W}_{Ansys} = \frac{sene}{volu} = \frac{2.47 * 10^{-4}}{30.9505} = 7.98 * 10^{-6} \left[\frac{[MJ]}{[m^3]} \right] \quad (4.14)$$

The difference between the two values of the Strain Energy Density is bigger than the pure axial case, see table 4.2:

$\Delta\bar{W}_{analytical}$	$7.36 * 10^{-6} \left[\frac{MJ}{m^3} \right]$
$\Delta\bar{W}_{Ansys}$	$7.98 * 10^{-6} \left[\frac{MJ}{m^3} \right]$
Error (absolute)	7.78 %

Table 4.2: Pure torsional case SED comparison.

This error could be partially explained by including the τ_{rz} constant contribute, figure 4.12. It could be taken into account, in an approximate manner, in the Strain Energy Density calculation as follows:

$$\Delta\bar{W}_{\tau_{nom},contribute} = (1 + \nu) * \frac{(\tau_{nom})^2}{E} = (1 + \nu) * \frac{(0.4053)^2}{E} = 1.04 * 10^{-6} \left[\frac{N * mm}{mm^2} \right] \quad (4.15)$$

It should be noted that in the previous expression, the contribution of the τ_{rz} stress component has been assumed as constant inside the whole control volume, while it has been checked that it is constant only along the crack bisector line, here is the approximation. However no other solutions are available for an analytical calculation of the SED value.

Adding this contribute to the analytical SED the difference with the one calculated by Ansys is lower but still bigger than 5%.

$\Delta\bar{W}_{analytical} + \Delta\bar{W}_{\tau_{nom},contribute}$	$8.399 * 10^{-6} \left[\frac{MJ}{m^3} \right]$
$\Delta\bar{W}_{Ansys}$	$7.98 * 10^{-6} \left[\frac{MJ}{m^3} \right]$
Error (absolute)	5.2 %

Table 4.3: Pure torsional case SED comparison considering τ_{nom} contribute.

Eventually, the last consideration is that in the pure torsional loading condition, related to the Mode III, the higher order terms contribute is bigger than the pure axial case. However, the Peak Stress Method is applicable considering that it is proportional to the square root of the Strain Energy Density, so also the error will decrease to an acceptable value, being the error in terms of stress value almost half of the error in terms of energy value.

In conclusion, these 2D axis symmetric analysis show that the Peak Stress Method could be applied with an acceptable error in both loading cases. However, this planar section does not represent well the real geometry behaviour, so this last statement has to be validated once we solved the 3D model. In order to create this three dimensional model we referred to an idealized geometry, the same used by Vormwald in [1] and described in detail in the following paragraph.

4.2 Idealised 3D weld geometry

Vormwald in [1] calculated notch stresses with an idealised weld end model illustrated in previous works [2-4]. The real geometry of weld ends was obtained with high precision using a 3D scanner characterized by a depth resolution of 5 μm . Based on surface scan results volume models were created that contained weld end geometries. In order to validate this model, in [27] it is remarked that comparative calculations with idealised geometries have been performed varying parameters such as the weld angle and the toe radius. Dealing with the weld angle, the best accuracy was achieved with the value of 45° and the geometry shown in figure 4.14.

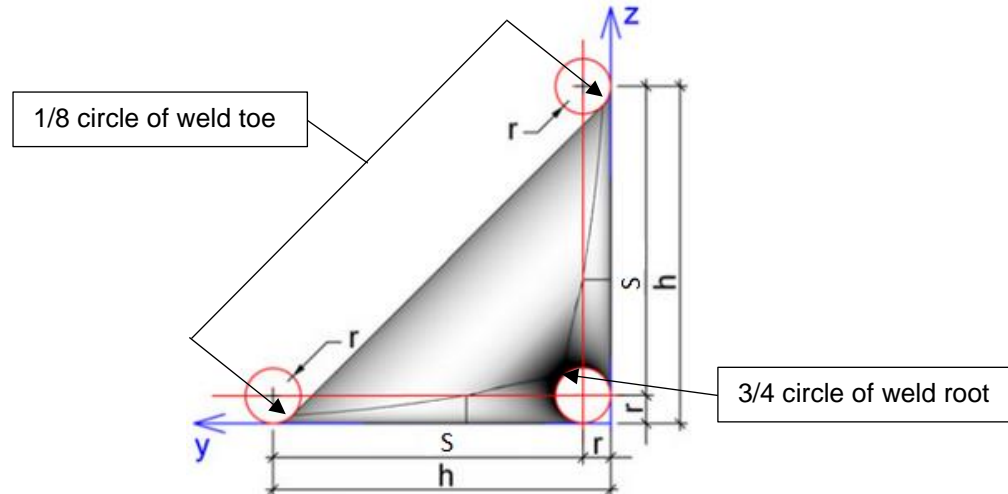


Fig 4.14: Construction of idealised weld end, [27].

In this model the 1/8 circle of the weld toe rounds steadily to 3/4 circle of the weld root, in this way the rounding of the weld toe bends continuously into the weld root. Therefore a unified weld end geometry has been defined with the sheet thickness $S = 2.24 \text{ mm}$ and the radius $r = 0.2 \text{ mm}$. The geometry can be scaled up linearly to the desired sheet thickness (S) according to the following recommendations:

$$\text{for } S \leq 5 \text{ mm:} \quad r = 0.2 \text{ mm} \quad (4.16)$$

$$\text{for } S > 5 \text{ mm:} \quad r = \frac{0.2 * S}{2.24} \text{ mm} \quad (4.17)$$

In the case of the overlapped tube-tube specimens a $r_{\text{root}} = 0.05 \text{ mm}$ was considered after breaking the seam weld at temperatures below the transition from ductile to brittle. In regards of these last changes, a new idealised model was created with different radii values. It is evident that there is a transition zone where the notch radii vary from 0.05 mm to 0.2 mm, shown in fig 4.15.

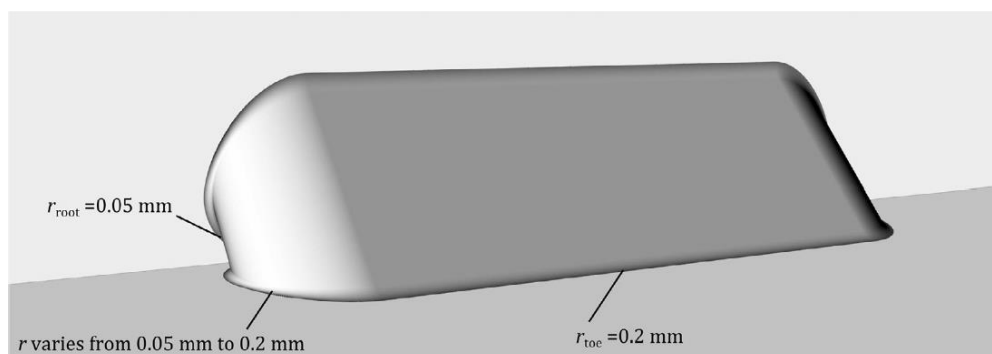


Fig 4.15: idealised weld end model with different radii at weld root and toe, [1].

In order to build the correct geometry, it is necessary to calculate the coordinates of the points in figure 4.16 thanks to the relations shown below in table 4.4.

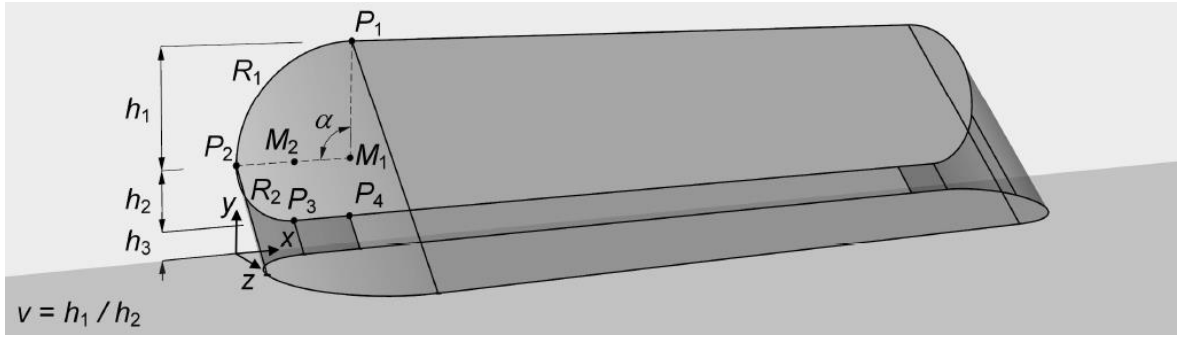


Figure 4.16: Points and angles to create the new idealised weld model with different toe and root radius, [28].

As shown in previous figure, v is defined as follows and its value is established from works [2-4].

$$v = \frac{h_1}{h_2} = \frac{R_1}{R_2} = 2 \quad (4.18)$$

Points	X-coordinates	Y-coordinates
P_1	$\frac{v}{1+v} \cdot \frac{S - r_{root}(\sqrt{2}+1) - r_{toe}(\sqrt{2}-1)}{\tan(\frac{\alpha}{2})}$	$S + r_{root} - r_{toe}(\sqrt{2}-1)$
P_2	0	$\frac{1}{1+v} \cdot \{S + r_{root} \cdot (1 + v \cdot (\sqrt{2}+2)) - r_{toe} \cdot (\sqrt{2}-1)\}$
P_3	$\frac{1}{1+v} \cdot (S - r_{root} \cdot (\sqrt{2}+1) - r_{toe} \cdot (\sqrt{2}-1)) \cdot \tan(\frac{\alpha}{2})$	$r_{root} \cdot (\sqrt{2}+2)$
P_4	$\frac{v}{1+v} \cdot \frac{S - r_{root}(\sqrt{2}+1) - r_{toe}(\sqrt{2}-1)}{\tan(\frac{\alpha}{2})}$	$r_{root} \cdot (\sqrt{2}+2)$
M_1	$\frac{v}{1+v} \cdot \frac{S - r_{root}(\sqrt{2}+1) - r_{toe}(\sqrt{2}-1)}{\tan(\frac{\alpha}{2})}$	$S + r_{root} - r_{toe}(\sqrt{2}-1) - \frac{v}{1+v} \cdot \frac{S - r_{root}(\sqrt{2}+1) - r_{toe}(\sqrt{2}-1)}{2\sin^2(\frac{\alpha}{2})}$
M_2	$\frac{1}{1+v} \cdot (S - r_{root} \cdot (\sqrt{2}+1) - r_{toe} \cdot (\sqrt{2}-1)) \cdot \tan(\frac{\alpha}{2})$	$r_{root} \cdot (\sqrt{2}+2) + \frac{1}{1+v} \cdot \frac{S - r_{root}(\sqrt{2}+1) - r_{toe}(\sqrt{2}-1)}{2\cos^2(\frac{\alpha}{2})}$

Table 4.4: relations useful to calculate the coordinate of the points of the new idealised weld geometry, [28]. “ v ” is not the Poisson ratio, but the ratio defined eq. 4.18.

Eventually, the α parameter is set to 90° in relation to previous works and figure 4.16. The unified weld end geometry consider a value equal to 2.24 mm for the sheet thickness parameter S , but in the case under study it would not be right. In fact from specimens images (see chapter 2, figures 1.3 and 1.11) it is clear that there is no space between the weld toe and the edge of the outer tube. In other words, both welds touch the edge of the bigger tube. The sheet thickness of the outer tube being 2.5 mm, also the overall width of the weld has to be of the same value.

Considering figure 4.14:

$$h = S + r_{root} = 2.5 \text{ mm} \quad (4.19)$$

But the root radius is known:

$$r_{root} = 0.05 \text{ mm} \quad (4.20)$$

So:

$$S = h - r_{root} = 2.5 - 0.05 = 2.495 \text{ mm} \quad (4.21)$$

All parameters' values are recapped in table 4.5.

PARAMETERS	VALUE
r_{root}	0.05 mm
r_{toe}	0.2 mm
S	2.495 mm
v	2
α	90°

Table 4.5: Parameters used to calculate the weld model.

Inserting these values in the relations of table 4.4, it results:

Points	X- coordinates [mm]	Y- coordinates [mm]
P ₁	1.53	2.46
P ₂	0	0.93
P ₃	0.765	0.17
P ₄	1.53	0.17
M ₁	1.53	0.93
M ₂	0.765	0.93

Table 4.6: Points coordinates for the idealised weld model.

Furthermore, the described geometry has been modified in order to apply the PSM, which adopt a sharp geometry both at the weld root and at the weld toe. Accordingly, both r_{toe} and r_{root} have been set to zero to create sharp V-notches. All the coordinates have been calculated with the previous values of the radii, but a few adjustments have been necessary to create a proper geometry. To be precise the Y coordinates of the points P₃ and P₄ have been set to zero and the P₁ to 2.50 mm instead of 2.46 mm. Furthermore, the values of the radii R₁ and R₂ have been modified to create this geometry without changing other parameters. The detailed changes are shown in tables 4.7 and 4.8.

	Original values	Updated values
R_1 [mm]	1.53	1.57
R_2 [mm]	0.76	0.93
$v = \frac{R_1}{R_2}$	2.01	1.7

Table 4.7: New radii values for the idealized weld end model.

In this way at the root we have created a crack where the weld is always attached to the root and the weld width is exactly equal to the thickness of the outer tube.

Points	X- coordinates [mm]	Y- coordinates [mm]
P ₁	1.53	2.50
P ₂	0	0.93
P ₃	0.765	0
P ₄	1.53	0
M ₁	1.53	0.93
M ₂	0.765	0.93

Table 4.8: New points coordinates for the idealised weld model.

4.3 CAD model creation

Due to the non-planar surfaces, it would have been difficult to model the weld geometry directly with the Ansys® software. In order to create the model described in the previous paragraph the software Solidworks® has been adopted. Thanks to the geometry of the specimens, two symmetry planes, orthogonal each other, could be considered and only a quarter of the total geometry will be modelled; so it is necessary to create only half of the weld, figure 4.17.

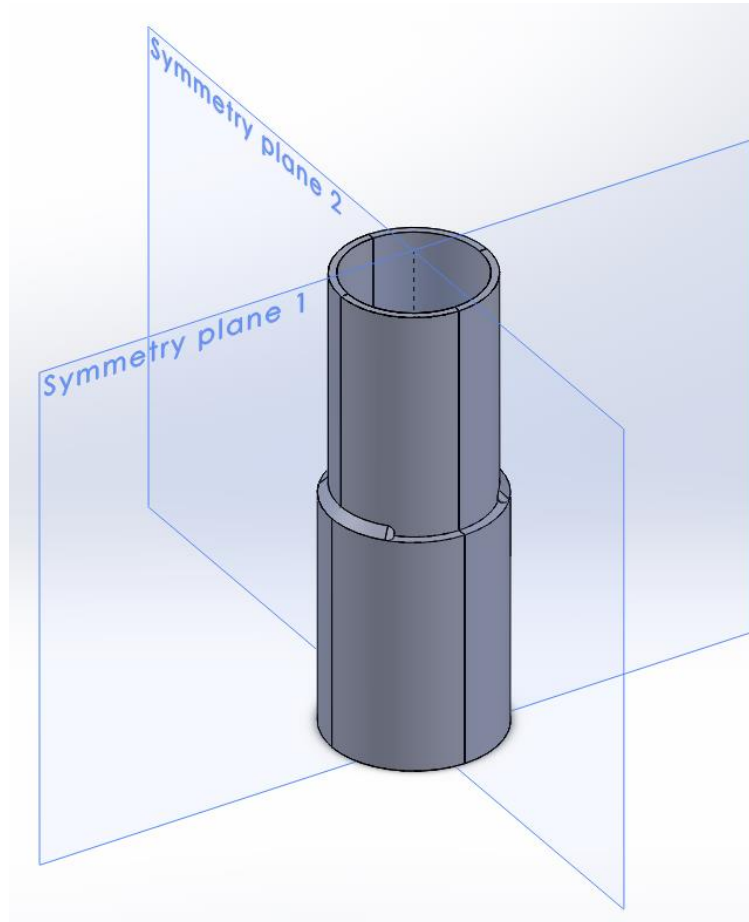


Figure 4.17: CAD geometry with symmetry planes.

First, the profile of the weld seam has been drawn on a plane XZ taking into account the coordinates given in tab 4.8 and considering the Z axis instead of the Y one, see figure 4.18.

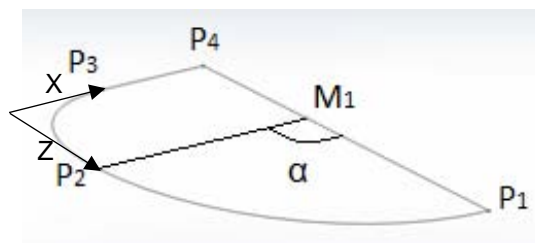


Figure 4.18: 2D sketch of the profile.

Then a volume is created with a revolution considering as an axis of rotation the P_3P_4 line, figure 4.19. The angle of revolution was set to 110° , an overestimated value with respect to the 90° value which could be sufficient to cover the gap between the outer and the inner tube. However, the 110° angle was adopted to be sure that the weld seam intersect the surface of the inner tube, so that the connection between the different volumes is guaranteed.

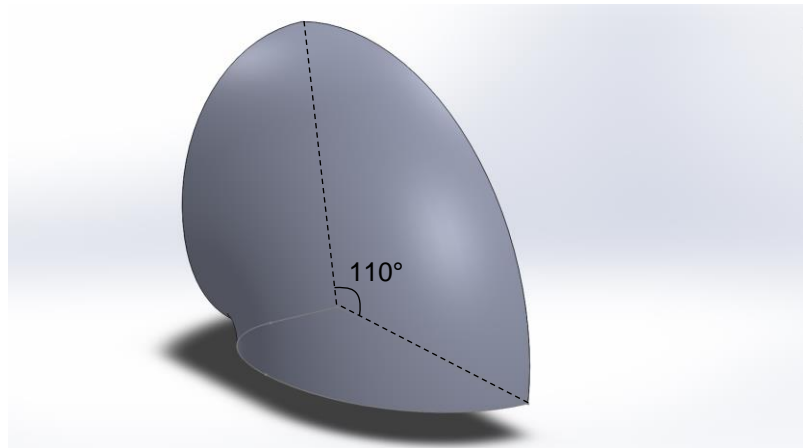


Figure 4.19: Volume created due to revolution along P_3P_4 line.

Now it is necessary to restore the 45° weld angle with an extruded cut, figure 4.20.

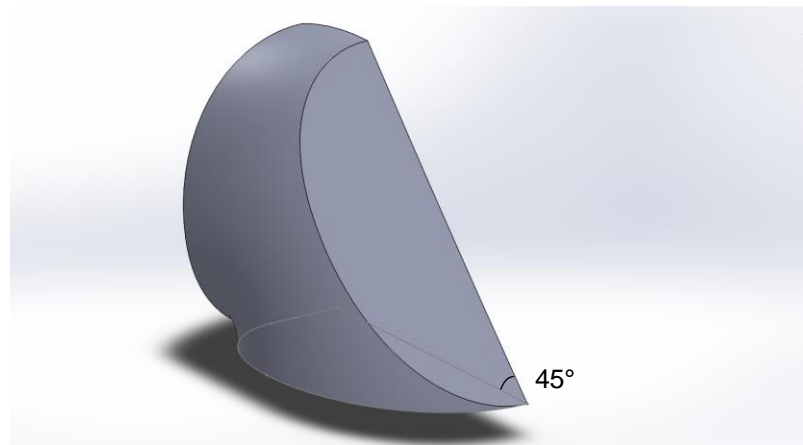


Figure 4.20: Geometry after the first extruded cut.

At this point an extruded cut was used again, but considering a 3D sketch (grey lines in figure below). The cut direction is represented by the red arrow.

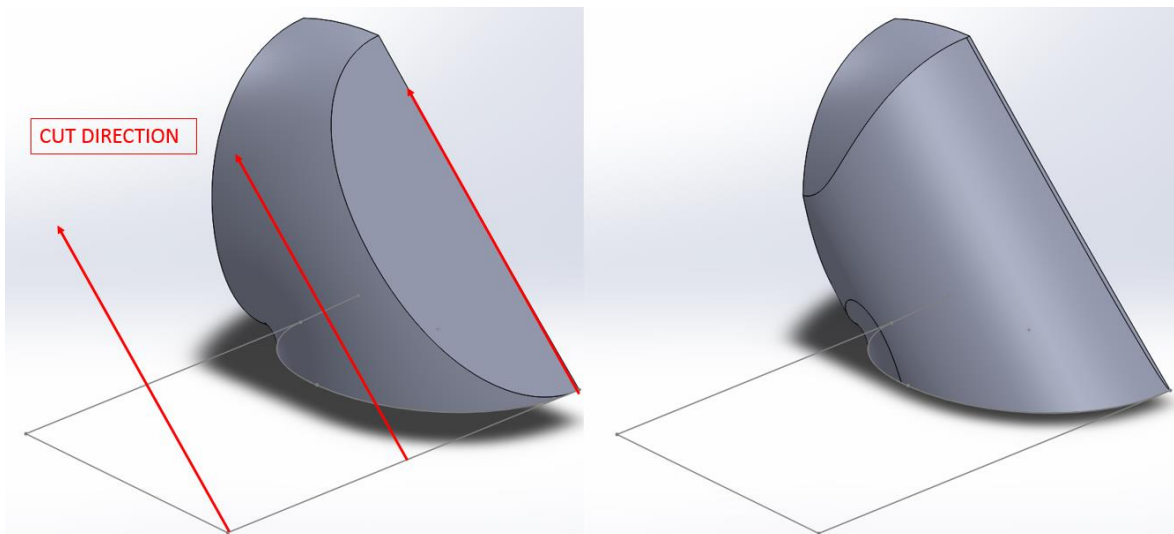


Figure 4.21: Geometry after the second extruded cut

Now with a revolution cut the weld end geometry is finished. Thanks to the 110° revolution of the second step, at this point we are sure that the inner surface is cylindrical (see figure 4.22)

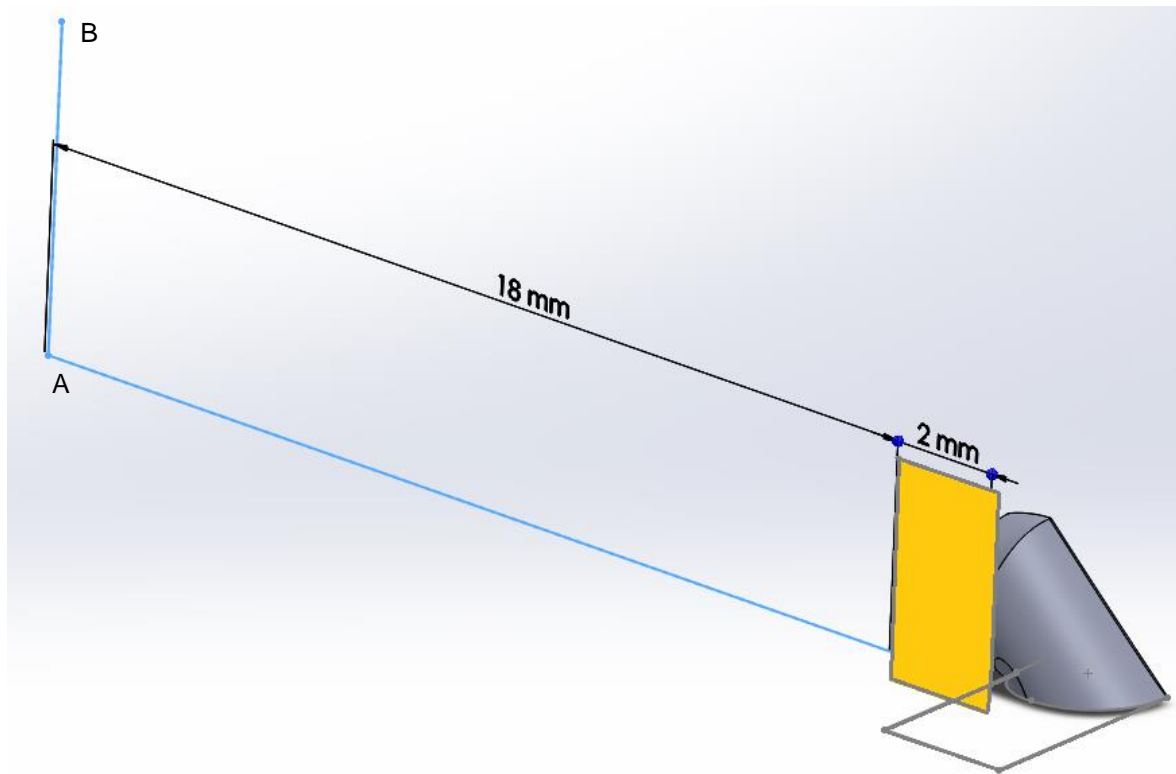


Figure 4.22: Weld end geometry before the revolution cut considering the AB axis.

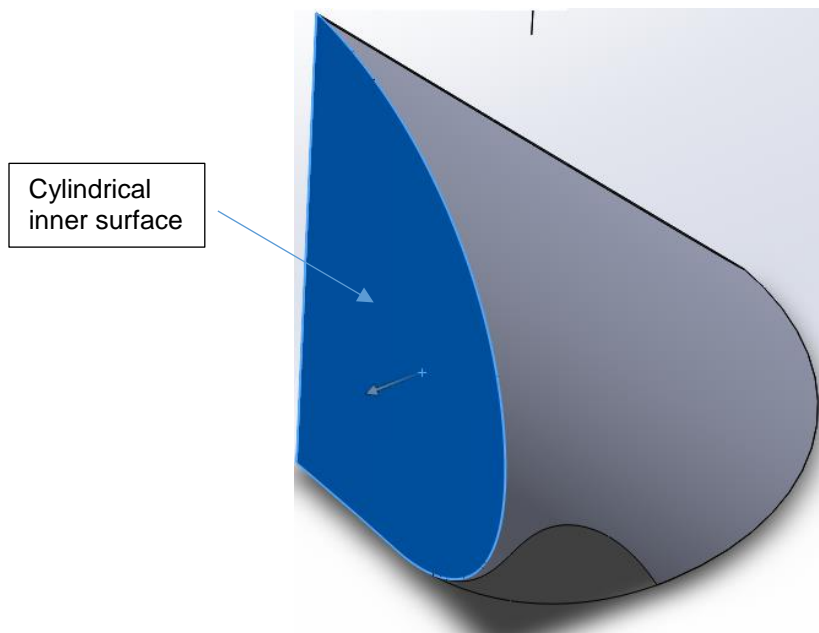


Figure 4.23: Weld end after the revolution cut.

To create the full weld geometry a revolution extrusion was used, figures 4.24 and 4.25.

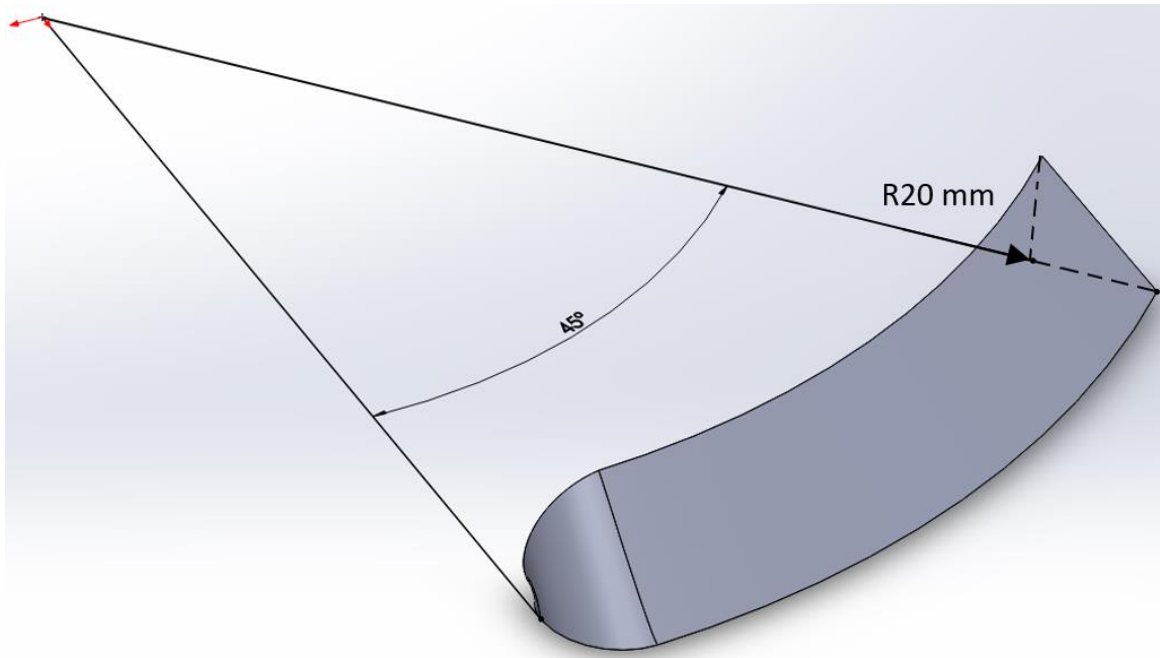


Figure 4.24: Lateral view of the half weld geometry

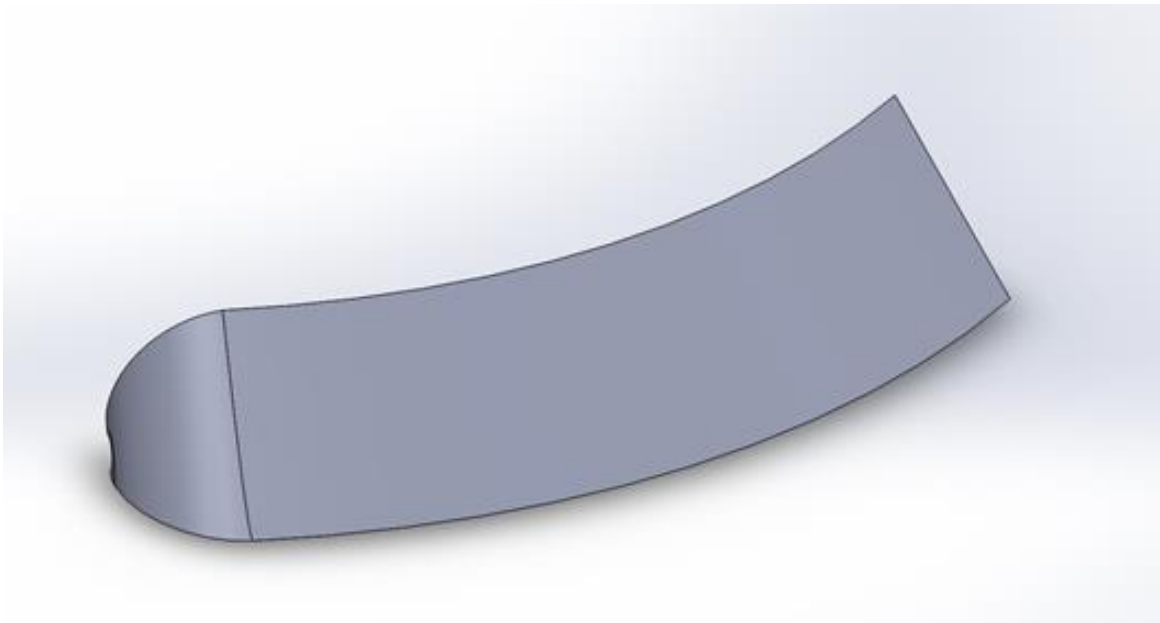


Figure 4.25: Front view of the half weld geometry.

Eventually, the 3D CAD file was saved with the ACIS extension and imported to Ansys. The remaining volumes have been created directly into Ansys to be sure to create attached surfaces and avoid tolerances problems.

4.4 FEM Mainmodel creation

First, after importing the ACIS file it is suggested to check the areas and the volumes created because this particular geometry could lead to visualization issues due to the great changes of surfaces curvatures. To reduce the amount of calculation and simplify the geometry, only a quarter of the total geometry will be modelled considering two symmetry planes, shown with a top view in figure 4.26.

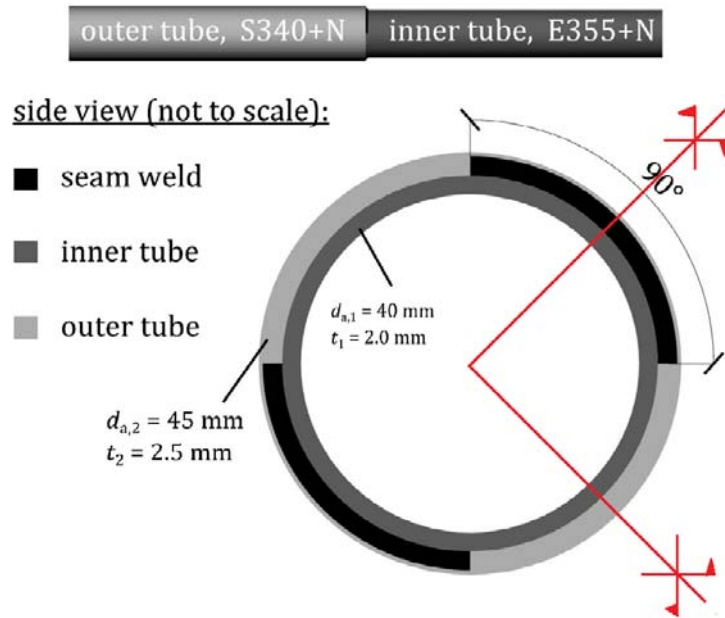


Figure 4.26: Symmetry planes location, [1].

The procedure necessary for the creation of the 3D model now will be described in detail, taking as reference figure 4.27.

An observation has to be done before going on with the modelling procedure. In figure 4.29, it is shown the procedure to create an air wedge between the inner and outer tubes starting from the line passing through the root tip. This wedge has a tip opening angle of just 1 degree and it has been introduced to create a separation of the two tubes to avoid submodelling issues and the adoption of contact elements, which require an iterative solution of the FE model. If they had been attached, there would have been more than one surface in the same place and when it comes the time to apply the boundary condition to the cut boundary of the submodel, the output will be wrong. These happens because without this expedient, the interpolation of the degree of freedom of the submodel could be done both in the outer tube as well as in the inner one.

To create such air edge there are a few operations to be done.

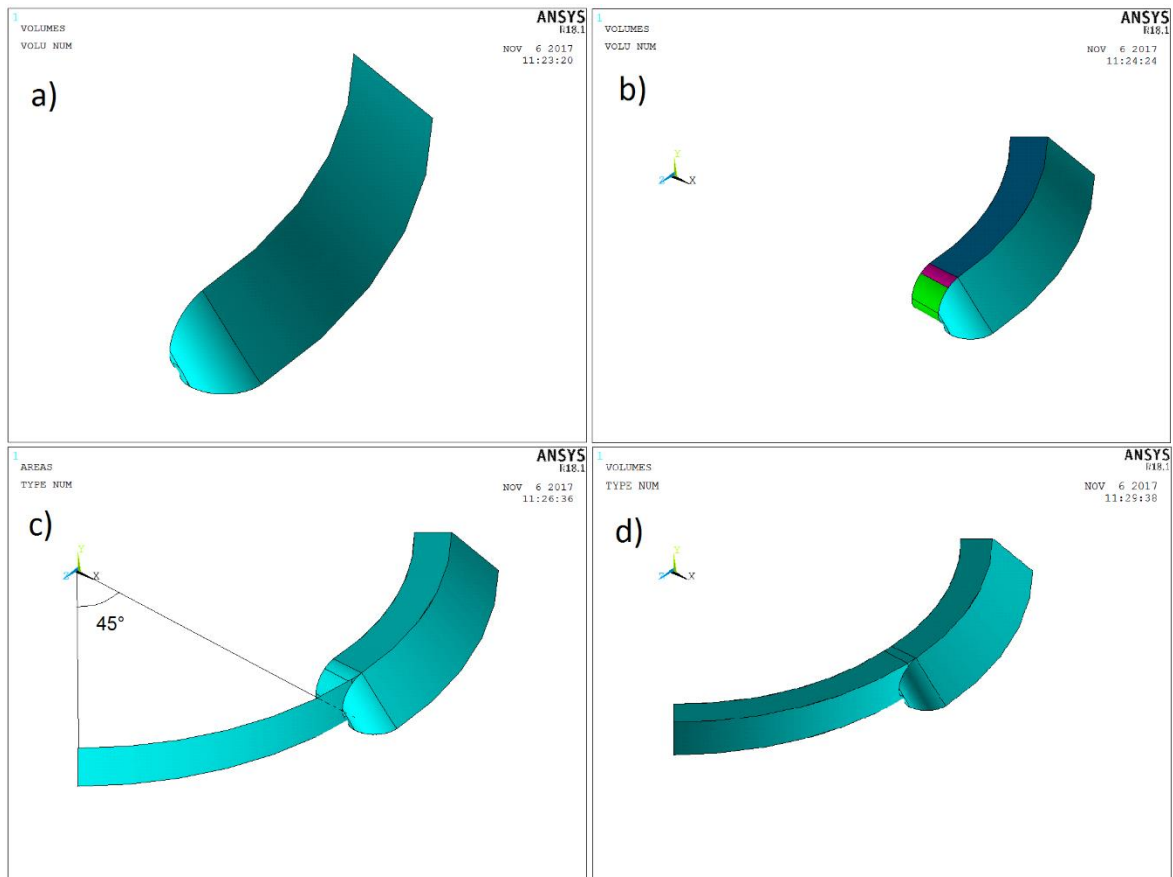


Figure 4.27: Ansys modelling procedure part 1.

- First it is necessary to import the CAD geometry. The Ansys commands are:
FILE => IMPORT => ACIS.
- Now it is possible to create the inner tube, starting from the imported weld geometry. The first step is switching to a global cylindrical coordinate system, then we can extrude the cylindrical inner surface of the weld. The Ansys commands are:
PREPROCESSOR => MODELING => OPERATE => EXTRUDE => AREAS => BY XYZ
OFFSET => (Pick the inner cylindrical surface of the weld model) => OK => DX = - 2 mm.
- The creation of the plotted surface is not immediate. First a global Cartesian system is restored, then an arc was drawn in the XZ plane and extruded in y-direction for 2.5 mm, exactly the "height" of the weld volume. At this point, the profile of the volumes created with the extrusion on point b) can be used to divide the area just created with the command "divide => area by line". Now the area shown in c) is divided in a concave part and a convex one, hidden within the weld. The convex part is useless and has to be throw away, while the concave is kept.

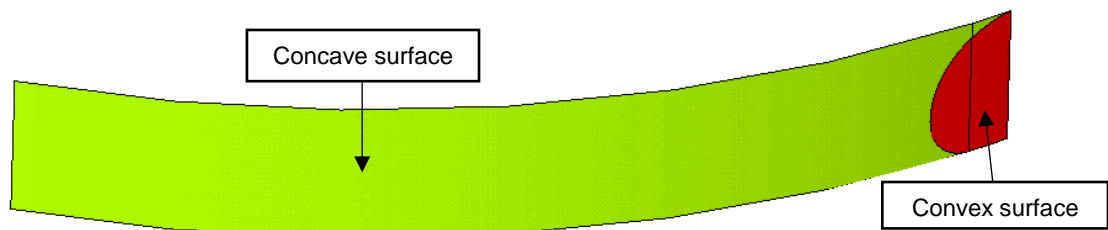


Figure 4.28: Concave and convex surfaces on point c).

- d) Now we need to switch again to a cylindrical coordinate system and the concave area created before can be “extruded by XYZ offset” with a DX of -2 mm. With this articulate procedure, we have created several volumes, but all touching each other, so in the meshing phase they will behave like a unique model, without detachments.
- e) Drawing the upper surface of the outer tube, perfectly attached to the inner tube but not using the same lines, by doing this at the root tip there will be a sharp V-notch, but the two tubes are not connected there, they are just touching.
- f) Create a Local cylindrical coordinate system centred in the global one and rotate of -180° considering a rotation along the X axis and -1° considering another along the Y axis.
- g) Extrude the area created on point e) and the lower surface of the weld with a DZ offset of -3 mm. This value is chosen because this will be the lower edge of the submodel.
- h) Switch to the global Cartesian system and extrude the lower surfaces of the inner tube with an offset DY of -3 mm.
- i) Always considering the Global Cartesian system, extrude the upper surfaces of the inner tube with an offset DY of 3 mm.

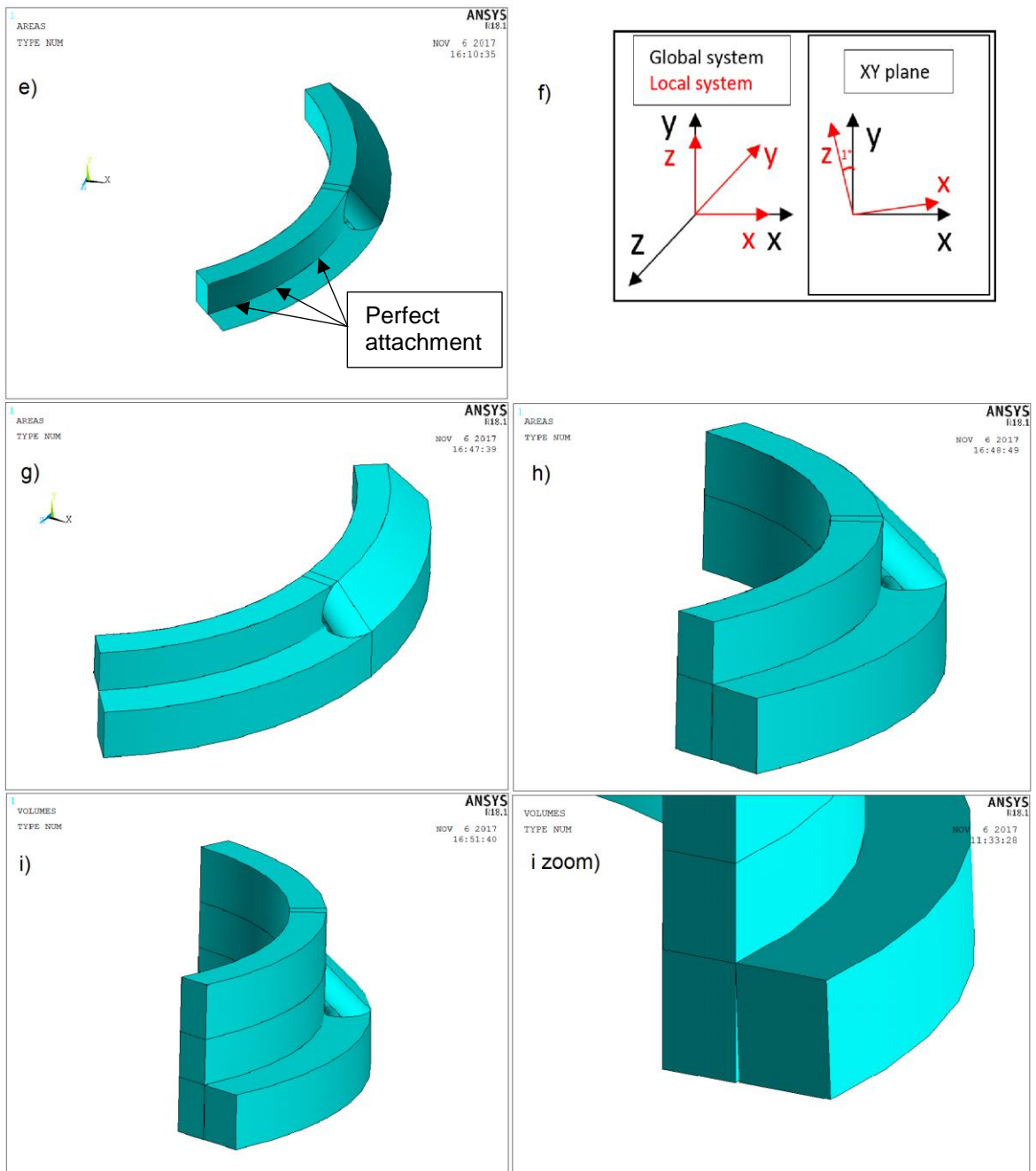


Figure 4.29: Ansys modelling procedure part 2.

- j) Eventually, the full geometry is obtained with a Y-direction extrusion of the upper and lower edges, respectively of the inner and outer tube, with an offset of 60 mm. The real specimens' geometry is longer than this, but it is preferred to model a portion of the total model to reduce the elements count and because the edges are far enough from the weld and their influence is negligible. The quoted final FEM model is shown in figure 4.30.

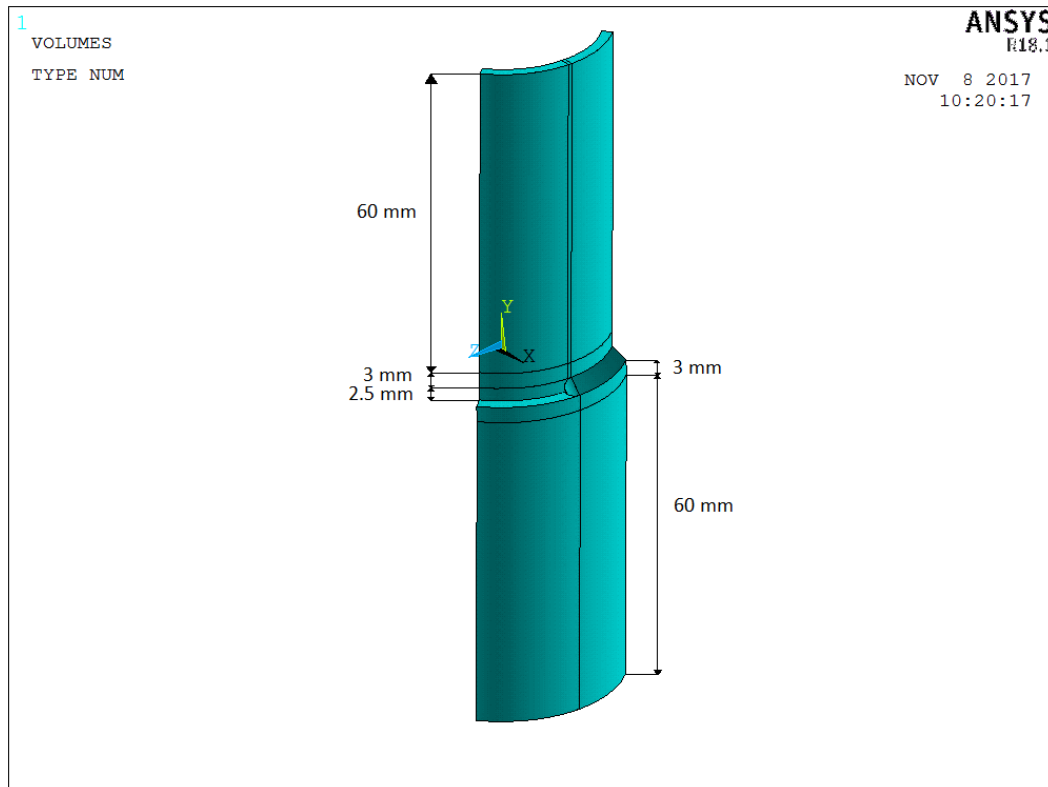


Figure 4.30: Quoted Ansys FEM model.

4.4.1 Mesh characteristics

The mesh pattern creation is quite delicate and a few observations need to be done. First, the global element size has to decrease from the edges to the welded part without evident discontinuities and in a uniform way. Furthermore, the complex curved shape of the weld forces a very small global element size, equal to 0.1 mm, and as a consequence just the solution of this part is particularly time-consuming. In particular, it is not possible to use a bigger global element size because the Ansys meshing algorithm would produce a non-solvable error. Second, the global element size has to be the smallest possible, but this is limited to the calculation power of the computer. This model has been run with a lot of different meshes and the most of the times the output was that the amount of RAM was not sufficient to end all the calculations. After many tries, it was figured out a mesh pattern enough refined, solvable and uniform. The pyramid tetragonal 10 nodes elements were used, meshed with the free technique just imposing the so-called "global element size". In order to be clear, numbers have been assigned to the volumes, figure 4.31, and the mesh characteristics are recapped in table 4.9.

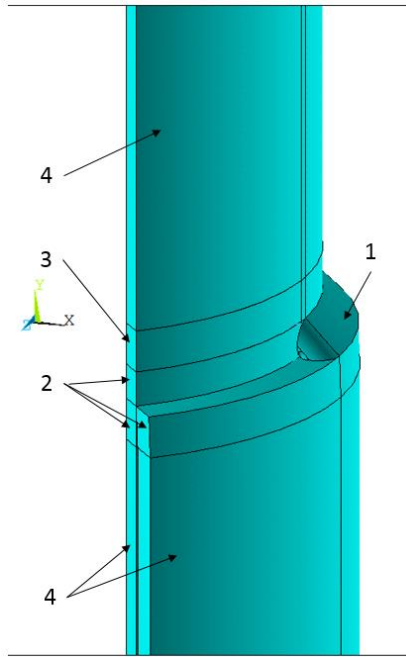


Figure 4.31: Numbers assigned to the volumes

Mainmodel Global element size			
D1	D2	D3	D4
[mm]	[mm]	[mm]	[mm]
0.1	0.4	0.5	1.5

Table 4.9: Volumes global element sizes.

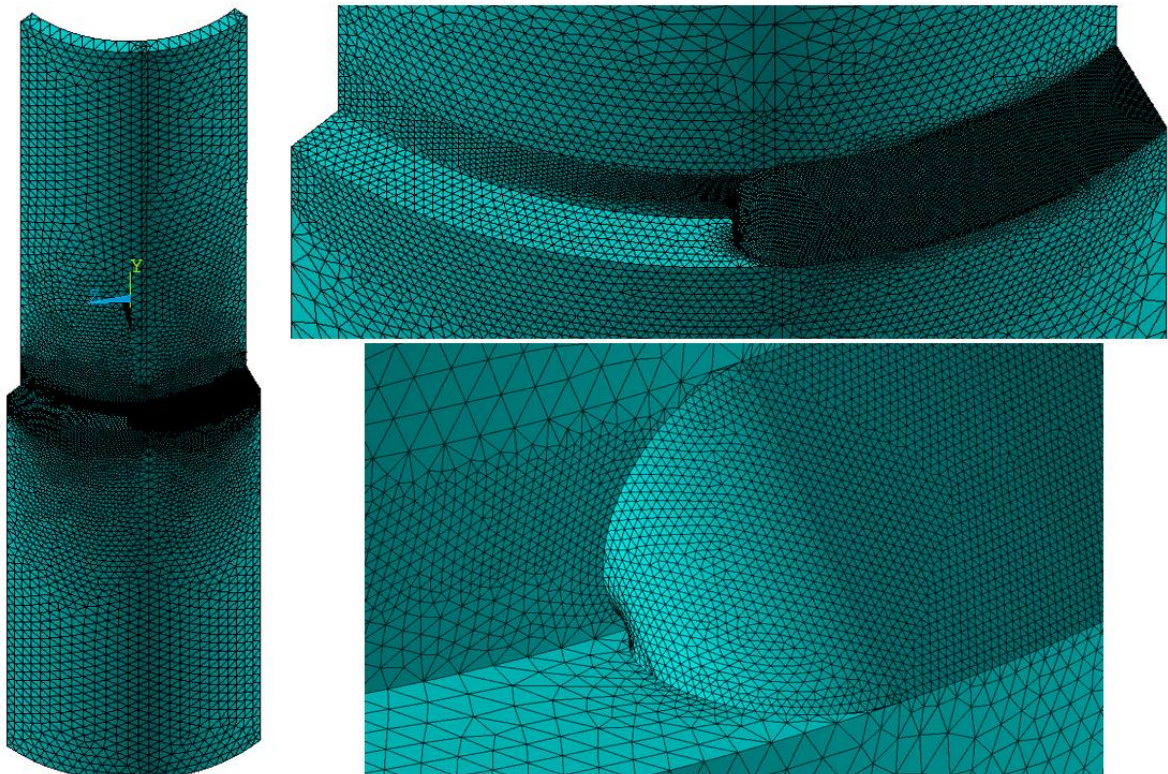


Figure 4.32: Mesh pattern with increasing zooms.

4.4.2 Loads and constraints

Starting from the pure axial loaded model, dealing with the load, a uniform pressure of 1 MPa was applied to the upper surface of the inner cylinder in the Y-direction. In regard of the constraints, symmetry boundary conditions have been applied to surfaces belonging to both geometrical symmetry planes shown in red in figure 4.26. Also, all degree of freedom have been constrained in the lower surface of the outer tube; the lower surface of the inner tube was let free to glide.

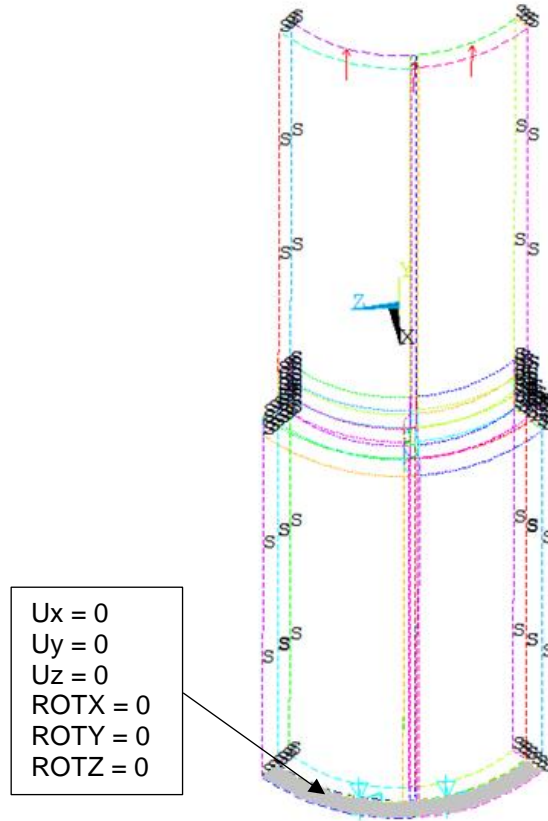


Figure 4.33: Loads and constraints of the pure axial model. The S stand for: Symmetry boundary condition.

Regarding the pure torsional loaded model, dealing with the load, it necessary to calculate a force to create shear stress of 1 MPa in the inner tube.

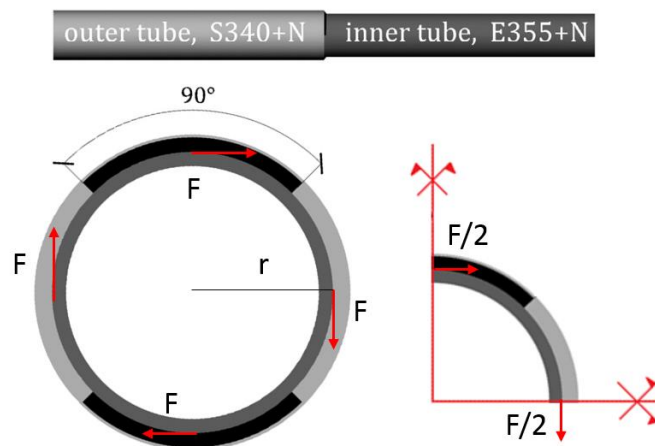


Figure 4.34: Pure torsional case loading condition.

The total applied torsional moment is:

$$M_t = 4F * r \tag{4.22}$$

But:

$$\tau = \frac{M_t}{W_t} = 1 \text{ MPa} \quad (4.23)$$

It results, from eq. 4.24:

$$F = \frac{W_t}{4 * r} = \frac{\frac{\pi}{32} * \frac{d_{innertube,ext}^4 - d_{innertube,int}^4}{d_{innertube,ext}/2}}{4 * r} \quad (4.24)$$

$$F = \frac{\frac{\pi}{32} * \frac{40^4 - 36^4}{40/2}}{4 * 20} = 54 \text{ N} \quad (4.25)$$

$$\frac{F}{2} = 27 \text{ N} \quad (4.26)$$

This Force of 27 N has been applied to the edge keypoints of the upper surface of the inner tube in the tangential direction, as shown in figure 4.34

In regard of the constraints, anti-symmetry boundary conditions have been applied to surfaces belonging to both geometrical symmetry planes shown in red in figure 4.26. In addition, all degrees of freedom have been constrained in the lower surface of the outer tube; the lower surface of the inner tube was let free to glide. Solving this model, the exaggerated deformed shape shows a penetration of the two tubes, however the real one (not scaled) displays that there is a gap between the two cylinders. This positive outcome is also a result of the insertion of the air wedge described in detail previously and gives the possibility not to insert the contact in this analysis. In fact, the insertion of the contact between the two cylinders would make the analysis non-linear and the result less reliable.

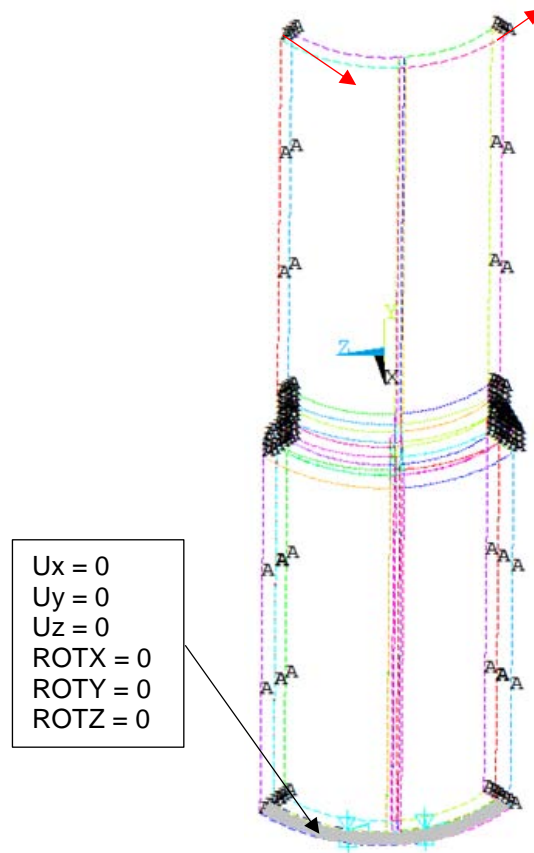


Figure 4.35: Loads and constraints of the pure torsional model. The A stand for: Anti-Symmetry boundary condition.

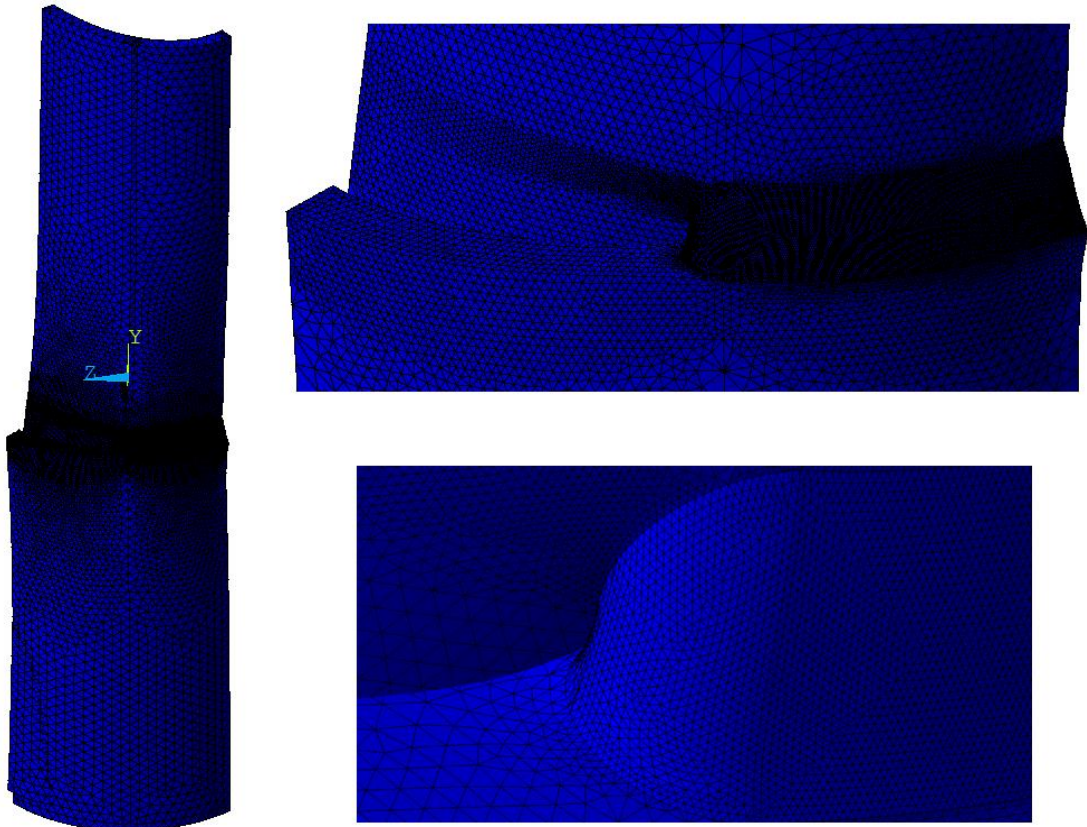


Figure 4.36: Exaggerated deformed shape, axial case

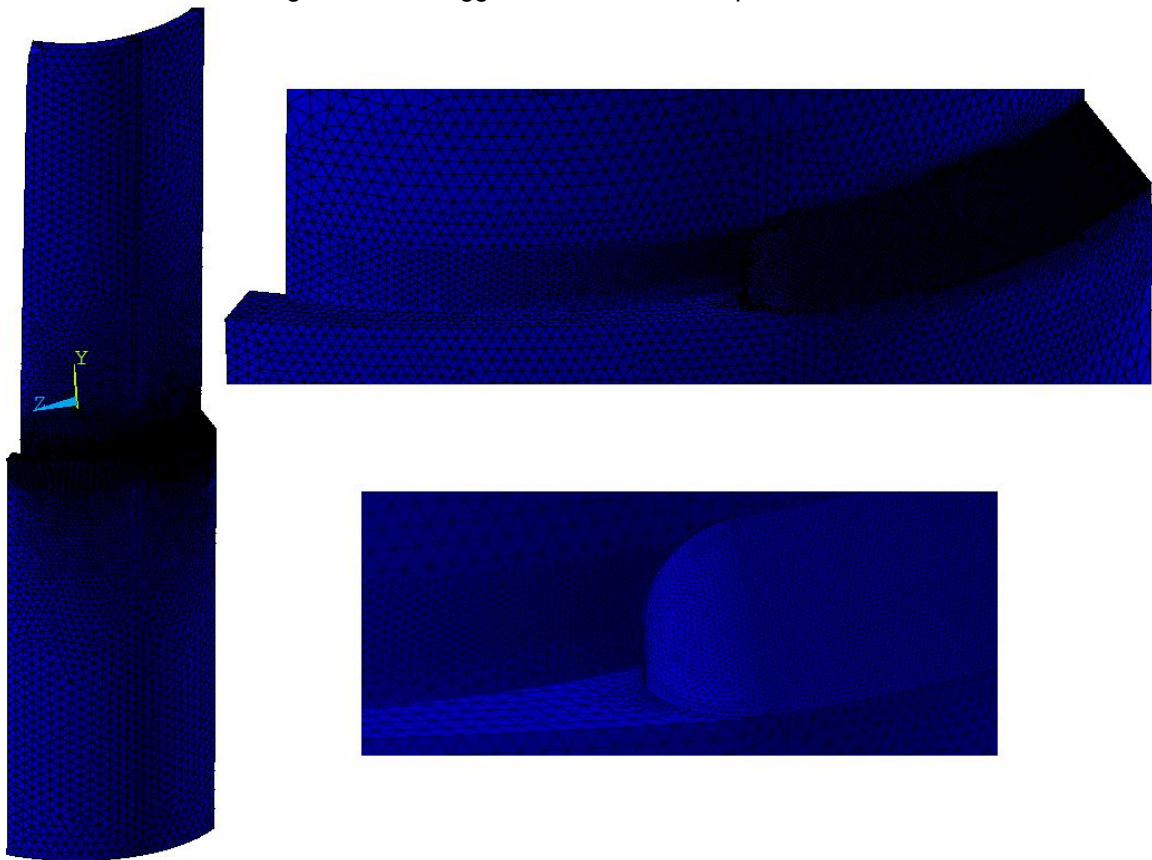


Figure 4.37: Exaggerated deformed shape, torsional case.

4.5 FEM Submodel creation

The submodelling technique was used to analyse with a more refined mesh the critical zone, located at the weld end, in proximity to the separation of the two tubes that is experimentally the crack initiation point in most cases. Considering figure 4.39 some observations could be done:

1. The submodel extension is half of 45° , so a quarter of the total 90° weld. This width angle allow us to use a mesh pattern enough refined and to study the largest portion possible by our calculation power. Previous attempts considered a 45° angle, but the mesh would result gross and leads to non-satisfactory results.
2. The 3 mm distance from the weld is calculated from convergence analysis. At the beginning, model with just 2.5 mm height from the weld have been used, but the outcome was that this distance was not sufficient not to be influenced by the Mainmodel mesh.
3. The Submodel with this characteristics starts exactly from the critical point C. This is forced by the geometry itself, in particular, within the weld, the root tip is constituted by only one line, so by a succession of nodes one after the other and never in the same position, while out of the weld there could be more nodes in the exact same position. The two cylinders are touching at the root tip out of the weld, not merging like within it. If a larger submodel had been created, including the critical point C, in the zone before it, out of the weld, the interpolation procedure would have given a wrong output, because considering the displacement of the outer tube sometimes and of the inner one the other times. This happens because Ansys is not able to understand which one of the two lines has to consider for the interpolation procedure because they are located in the exact same place. This fact leads to the consideration that the nodes belonging to the surface where the submodel starts will be part of the cut boundary. In this way, the resultant stresses and displacements will be deeply influenced by the Mainmodel geometry because deriving from the interpolation of shape functions of very big elements. The solution of this problem is refining the Mainmodel mesh pattern, but we reached the limit of the calculation power.

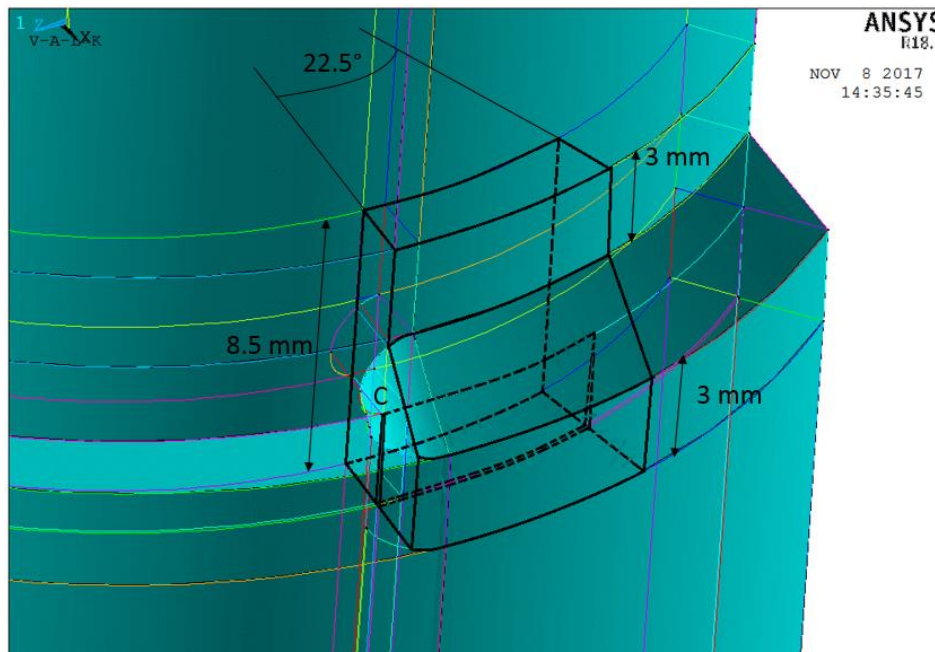


Figure 4.39: submodel geometry and location.

The creation of the geometry of the submodel is here described, step by step:

- a) Starting from the Mainmodel geometry, several volumes have been deleted with the exception of the ones plotted in figure 4.40. The used commands are:
PREPROCESSOR => MODELING => DELETE => VOLUME AND BELOW
- b) To proceed with the submodel creation it is necessary to switch to a cylindrical reference system. Then it is possible to extruded the shaded surfaces with the commands:
PREPROCESSOR => OPERATE => EXTRUDE => AREAS => (Pick shaded areas) => DX = 3 mm.

- c) The result of the previous operations is here shown using the colours to emphasize the volumes edges.
- d) Now we focus only on the just created volumes. The following steps are aimed to keep only their surfaces.
 SELECT => ENTITIES => (Pick the new volumes)
 SELECT => EVERYTHING BELOW => SELECTED VOLUMES
 PREPROCESSOR => MODELING => DELETE => VOLUME AND BELOW => (Pick the new volumes)
- e) The useless areas are eliminated.
 PREPROCESSOR => MODELING => DELETE => AREA AND BELOW => (Pick all areas with exception to the one showed in the figure below)
- f) The outcome of this first part of the submodel modelling procedure is showed with the commands:
 SELECT => EVERYTHING
 PLOT => VOLUMES

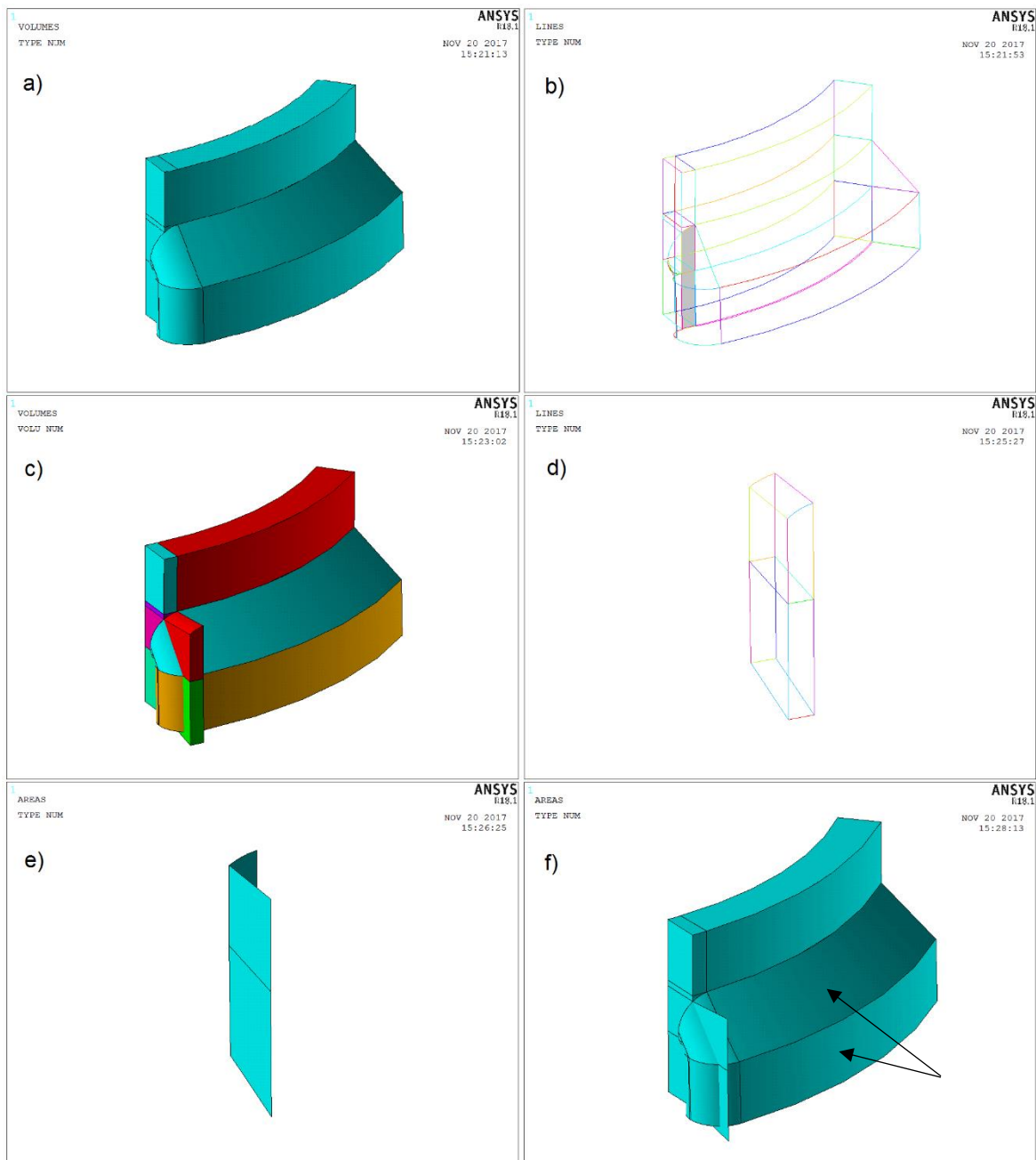
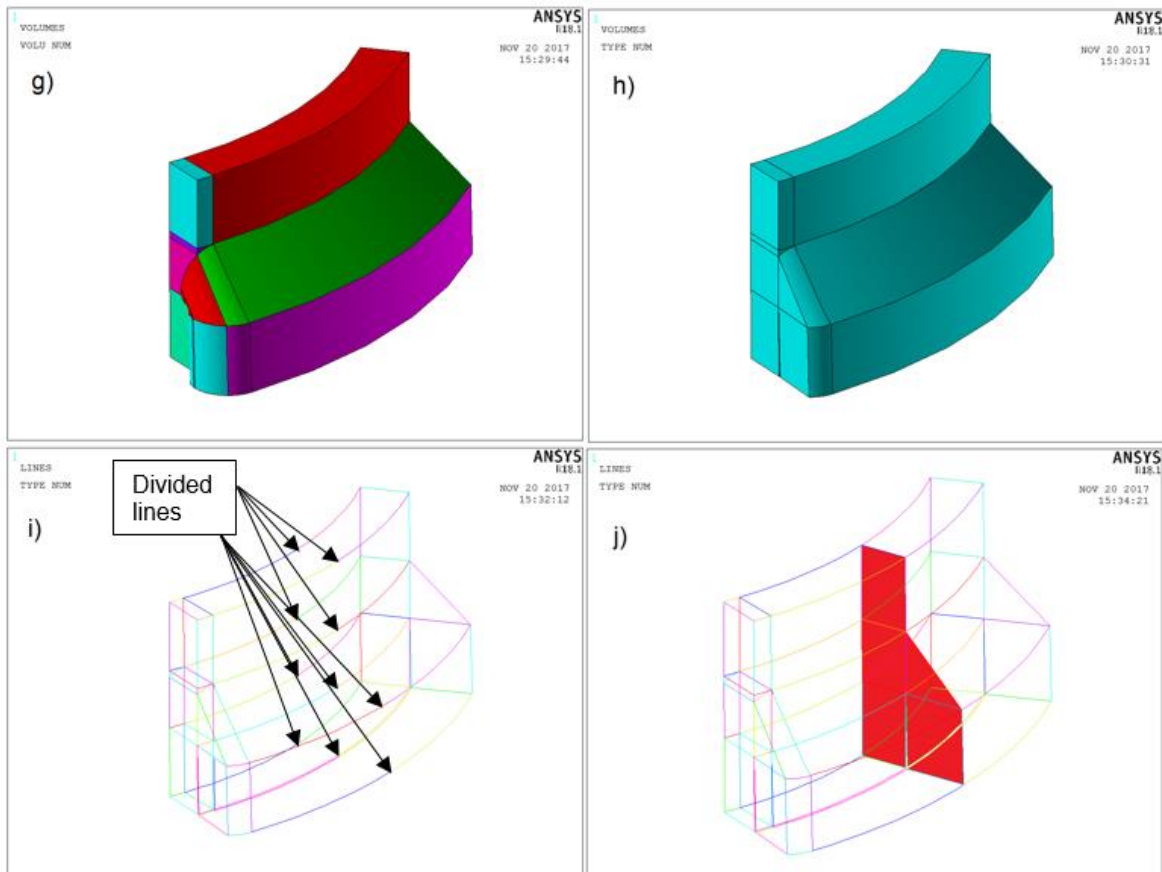


Figure 4.40: Ansys submodel modelling procedure part 1.

- g) The areas shown at point e) are used to slice the volumes indicated by the black arrows on point f). The result is plotted using colours to underline that two new volumes have been created.
 PREPROCESSOR => MODELING => OPERATE => BOOLEANS => DIVIDE => VOLUME BY AREA
- h) The new volumes are useless so they have been eliminated.
 PREPROCESSOR => MODELING => DELETE => VOLUME AND BELOW
- i) The lines indicated by the arrows have been divided in two parts. The path is the following:
 PREPROCESSOR => MODELING => OPERATE => BOOLEANS => DIVIDE => LINES INTO 2 LINES => (Pick every line and repeat the procedure)
- j) Create lines connecting the keypoints derived from previous line division and use them to create an area.
 PREPROCESSOR => MODELING => CREATE => LINES => LINES => STRAIGHT LINE
 PREPROCESSOR => MODELING => CREATE => AREA => ARBITRARY => BY LINES => (Pick the just created lines)
 Use the area painted in red to divide the volumes intersecting it.
 PREPROCESSOR => MODELING => OPERATE => BOOLEANS => DIVIDE => VOLUME BY AREA => (Pick one volume and the corresponding area and repeat the procedure)
 Delete the part of volumes not belonging to the critical point side.
 PREPROCESSOR => MODELING => DELETE => VOLUME AND BELOW
- k) This is the last operation and it is not necessary but aimed to improve the uniformity of the mesh pattern. In particular, the volumes indicated by the arrows are added.
 PREPROCESSOR => MODELING => OPERATE => BOOLEANS => ADD => VOLUMES => (Pick the indicated volumes, both red in the picture)



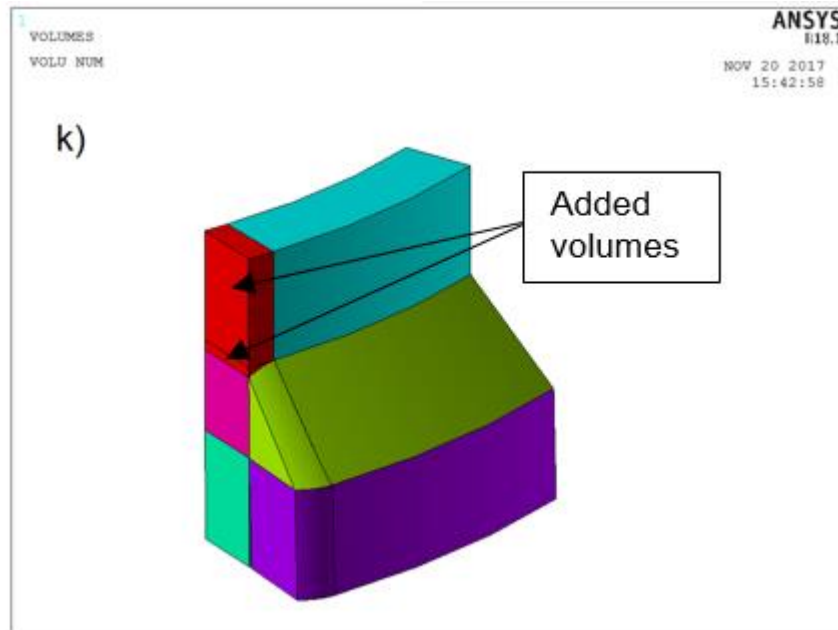


Figure 4.41: Ansys submodel modelling procedure part 2.

4.5.1 Submodel mesh characteristics

In order to apply the Peak Stress Method (PSM) the condition that has to be fulfilled is to mesh mapped with Brick 8 nodes elements. In fact, the meshing technique has to guarantee that in case of a crack with a 0° opening angle four elements are located at its tip, as shown in the figure below.

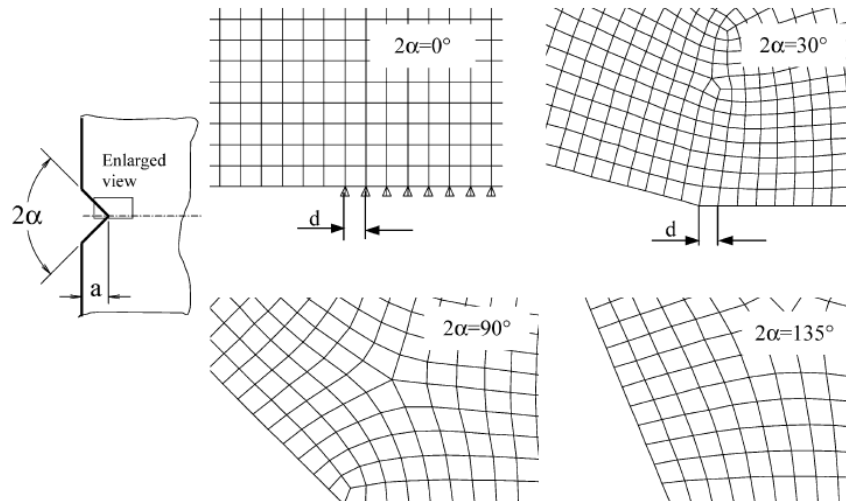


Figure 4.42: Suggested mesh patterns for different opening angle cases to apply the PSM, [10].

However, the particular geometry of the submodel does not allow to mesh mapped, even dividing it into smaller volumes. The reason of this is that we are dealing with curved shapes, in particular the area near the critical point, and Ansys is not able to correlate the opposite surfaces of each volume. There are two different path to follow at this point and at the end of the analysis the results will be compared and discussed.

4.5.2 The two-submodels method

The first idea is to mesh also the submodel with pyramid tetragonal 10 nodes elements and use it to interpolate a second submodel meshed with bricks 8 nodes. This is possible sketching a second submodel with a geometry suitable not give any problems during the mapped meshing. The submodel is modelled around the root tip at a distance of 1 mm and contains the air wedge, like the first submodel. However, since it is starting from the critical point, all the nodes belonging to that surface (shaded in yellow in figure 4.43) are interpolated in the first submodel where this is again a cut boundary that is interpolated in the Mainmodel. To resume, the “frontal” surface of the second submodel interpolated indirectly in the Mainmodel, so the solution of the nodes belonging to that surface will be extremely non-reliable.

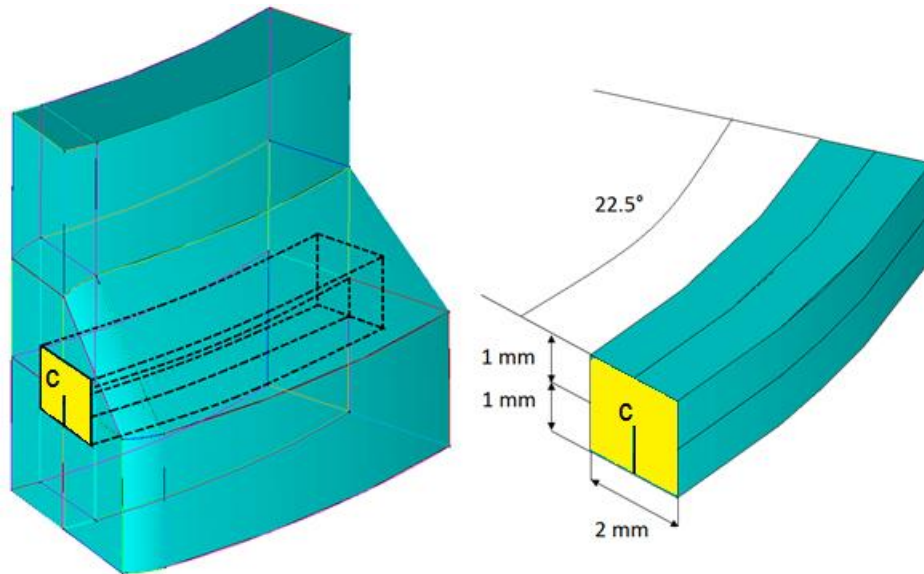


Figure 4.43: Second submodel geometry and location.

The cut boundaries have been applied to all surfaces with exception to the two areas contained within the second submodel. More precisely the two areas are the one connecting the “bottom” of the submodel to the line passing through the root tip.

In order to apply the Peak Stress Method in the second submodel, the mesh density ratio a/d (a = ligament length = 2.5 mm; d = global size) has to assume different values depending in which loading condition we are dealing with; they are recapped in the following table.

	Mode I	Mode II	Mode III (root side)
Minimum a/d	3	14	12
d_{\max} [mm]	0.83	0.18	0.21

Table 4.10: required meshes density ratios for every loading case.

Since the maximum acceptable value for the global element size is 0.18 mm, in this analysis we are investigating dimensions lower that this value and four different mesh cases were studied, table 4.11.

Solution number #	Submodel 1	Submodel 2
	Global element size [mm]	
1	0.15	0.15
2		0.05
3	0.12	0.15
4		0.05

Table 4.11: Convergence analysis of the two submodels technique.

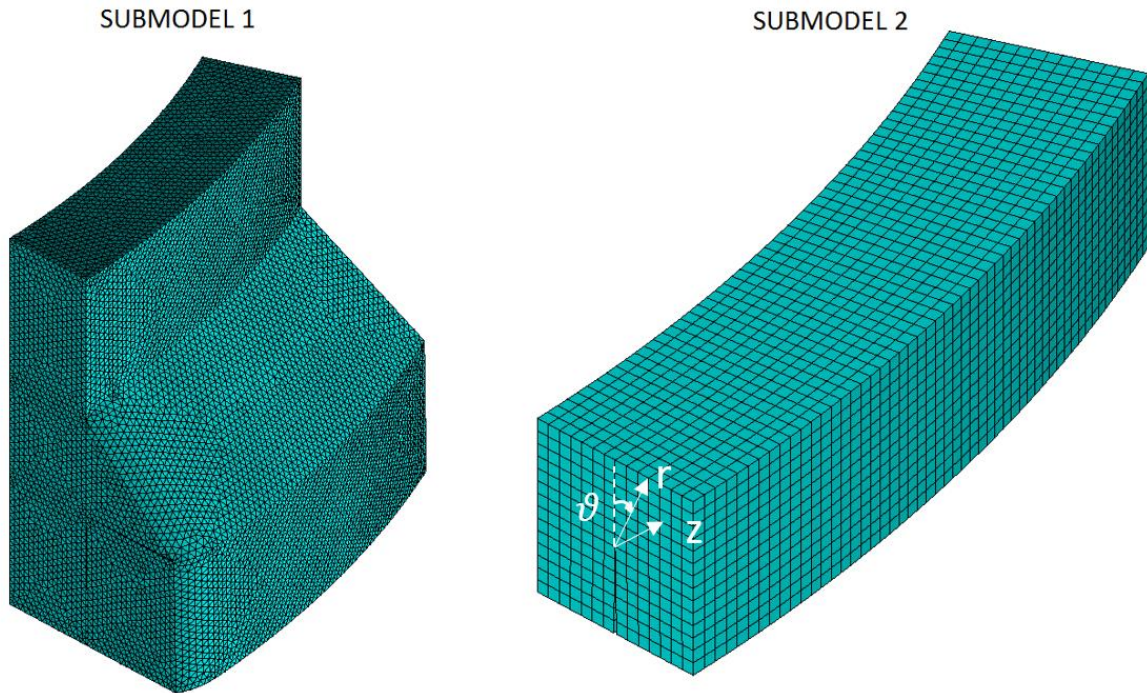


Figure 4.44: solution 1 mesh example. Global element size of 0.15 mm for both models.

All four cases analysis were carried out for the pure axial model as well as the pure torsional one. Starting from the pure axial case, the procedure to calculate the equivalent peak stress is reported step by step:

1. Solve the Mainmodel loaded with the pure axial load.
2. Interpolate the cut boundaries of the first submodel, in the Mainmodel just solved, and solve.
3. Interpolate the cut boundaries of the second submodel, in the first one, and solve.
4. Considering the just solved second submodel, select all nodes belonging to the line located at the root tip and extract the Mode I and Mode II peak stresses. Then it is possible to calculate the equivalent peak stress with equation 4.27, that becomes eq. 4.28 in the as-welded case, since $c_w = 1$:

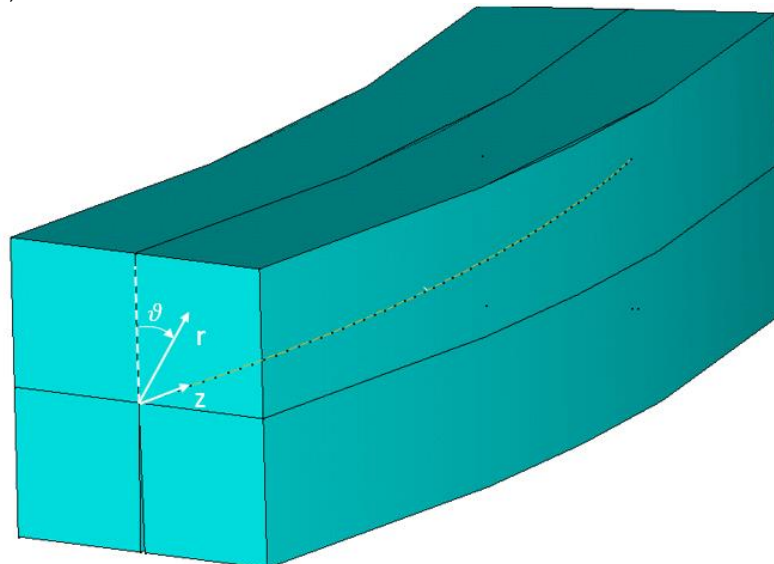


Figure 4.45: Nodes belonging to the line passing through the root tip.

$$\sigma_{eq,peak} = \sqrt{c_{w1}f_{w1}^2 \Delta\sigma_{\theta\theta,\theta=0,peak}^2 + c_{w2}f_{w2}^2 \Delta\tau_{r\theta,\theta=0,peak}^2} \quad (4.27)$$

$$\sigma_{eq,peak} = \sqrt{f_{w1}^2 \Delta\sigma_{\theta\theta,\theta=0,peak}^2 + f_{w2}^2 \Delta\tau_{r\theta,\theta=0,peak}^2} \quad (4.28)$$

Where:

$$f_{w1} = K_{FE}^* \sqrt{\frac{2e_1}{1-\nu^2}} \left(\frac{d}{R_0}\right)^{1-\lambda_1} = 1.38 \sqrt{\frac{2 * 0.133}{1-0.3^2}} \left(\frac{0.05}{0.28}\right)^{0.5} = 0.315 \quad (4.29)$$

$$f_{w2} = K_{FE}^{**} \sqrt{\frac{2e_2}{1-\nu^2}} \left(\frac{d}{R_0}\right)^{1-\lambda_2} = 3.38 \sqrt{\frac{2 * 0.340}{1-0.3^2}} \left(\frac{0.05}{0.28}\right)^{0.5} = 1.235 \quad (4.30)$$

The more refined case, solution 4, is reported as an example considering figure 4.45 reference system:

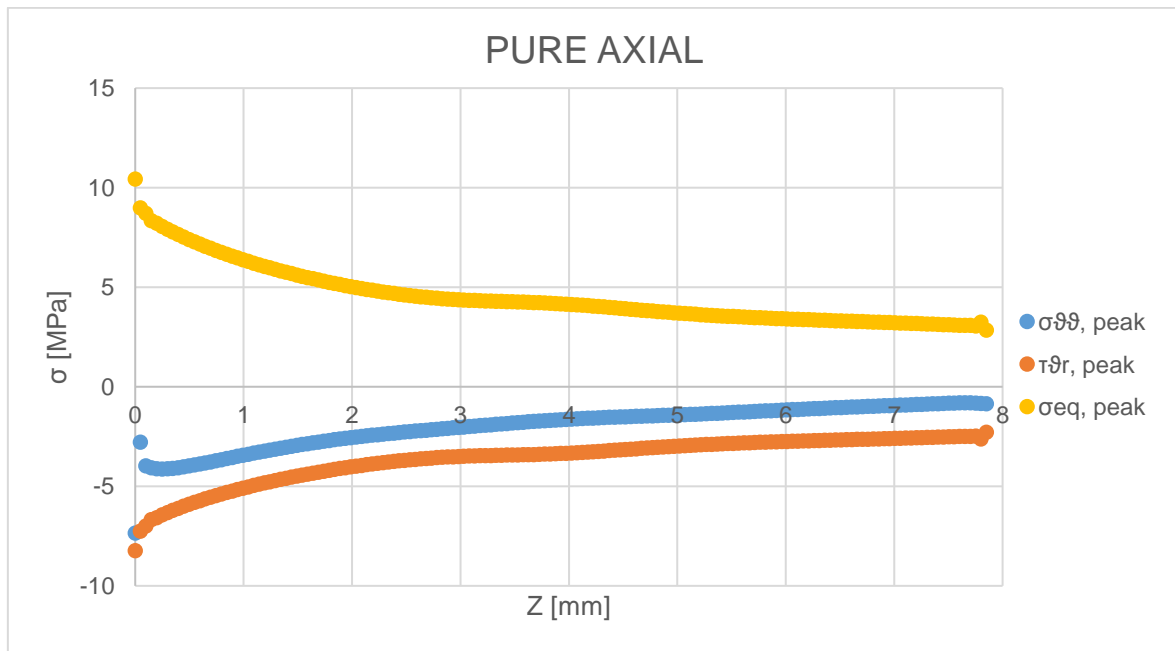


Figure 4.46: Stress analysis in terms of equivalent peak stress of solution 4 mesh case, root side, pure axial loading condition. Global element size of the second submodel = 0.05 mm; nominal applied load $\Delta\sigma = 1$ MPa (to the mainmodel).

The $\sigma_{yy,peak}$ stress component is relate to the Mode I loading case: opening; while the $\tau_{xy,peak}$ refers to the Mode II: in-plane shear. Once multiplied for the correction parameters f_{w1} and f_{w2} , it is clear that the Mode II contribute is by far bigger than the other one, in fact:

$$\frac{Mode\ II}{Mode\ I} = \frac{f_{w2}^2 \Delta\tau_{xy,x=0,peak}^2}{f_{w1}^2 \Delta\sigma_{yy,x=0,peak}^2} = 19.2 \quad (4.31)$$

Furthermore, the $\sigma_{yy,peak}$ is negative, which means that the V-notch, created thanks to the air wedge, is closing and not opening. Eventually, it is remarked how the first node value is unreliable because interpolated indirectly in the Mainmodel. This is the explanation of the discontinuity and as a first estimation of the equivalent stress, it is sufficient to read the value of the second node that is almost 9 MPa.

It would be useful to plot the equivalent peak stresses of the four solution cases in a single graph to study the convergence. In the legend, sub1 stands for submodel 1 and it is followed by the global element size and the same nomenclature was adopted for submodel 2.

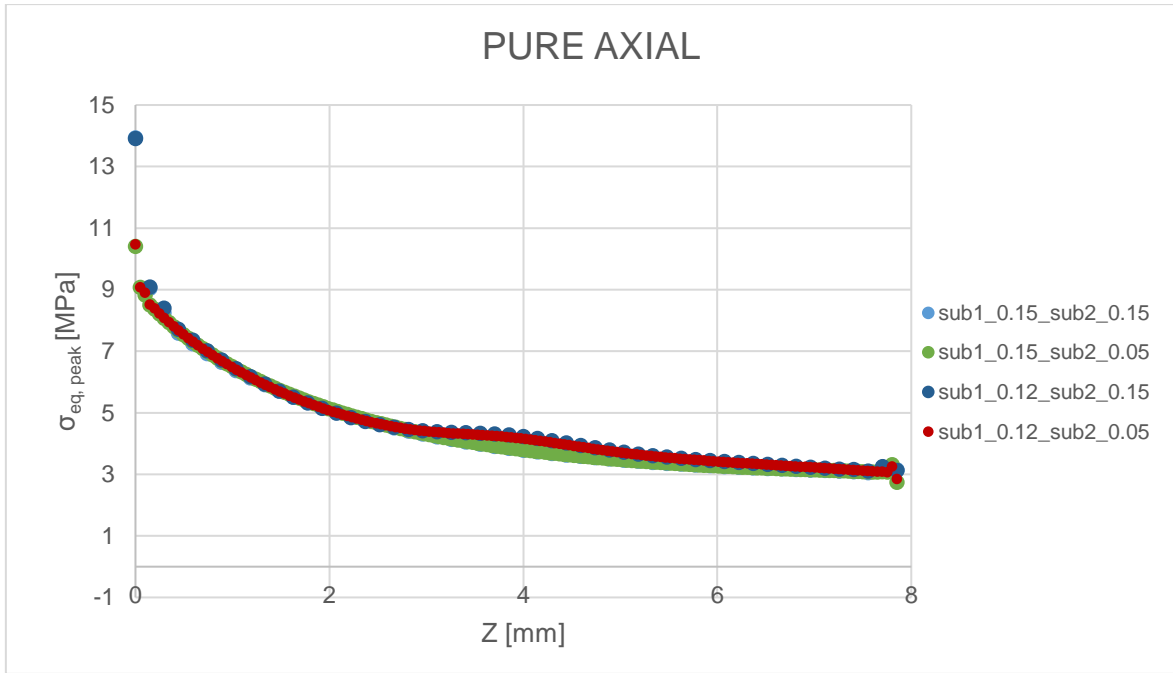


Figure 4.47: Equivalent peak stress calculated along the root tip for the four solution cases. Nominal applied load $\Delta\sigma = 1$ MPa (to the mainmodel)

What emerges from this graph is that all solutions are showing the same path, they are overlapped, with exception to the first point, because of reasons previously discussed, and around 4 mm in z-direction. This is due to the mesh pattern and it would be certainly eliminated with a smaller global element size but this cannot be done because we reached again our calculation limit.

Dealing with the torsional case, the data extraction procedure is exactly the same, what differs is that now there is only the Mode III contribute and the equivalent stress is calculated with equation 4.32, that becomes eq. 4.31 in the as-welded case:

$$\sigma_{eq,peak} = \sqrt{c_{w3} f_{w3}^2 \Delta\tau_{\vartheta z, \vartheta=0, peak}^2} \quad (4.32)$$

$$\sigma_{eq,peak} = \sqrt{f_{w3}^2 \Delta\tau_{\vartheta z, \vartheta=0, peak}^2} \quad (4.33)$$

Where:

$$f_{w3} = K_{FE}^{***} \sqrt{\frac{2e_3}{1-\nu^2} \left(\frac{d}{R_0}\right)^{1-\lambda_3}} = 1.93 \sqrt{\frac{2 * 0.414}{1-0.3^2} \left(\frac{0.05}{0.28}\right)^{0.5}} = 0.778 \quad (4.34)$$

The more refined case, solution 4, is reported as an example, considering the reference system of Figure 4.48:

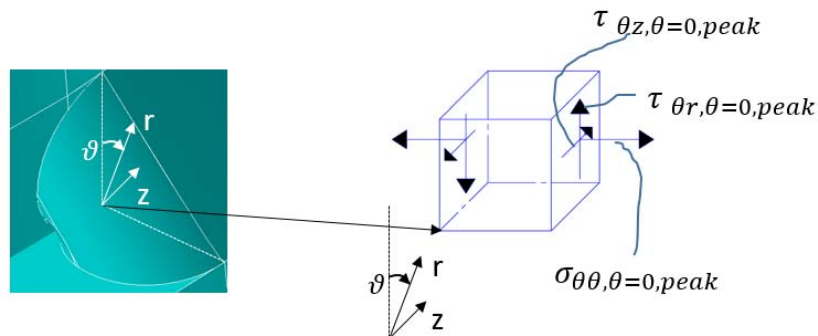


Figure 4.48: Torsional case reference system

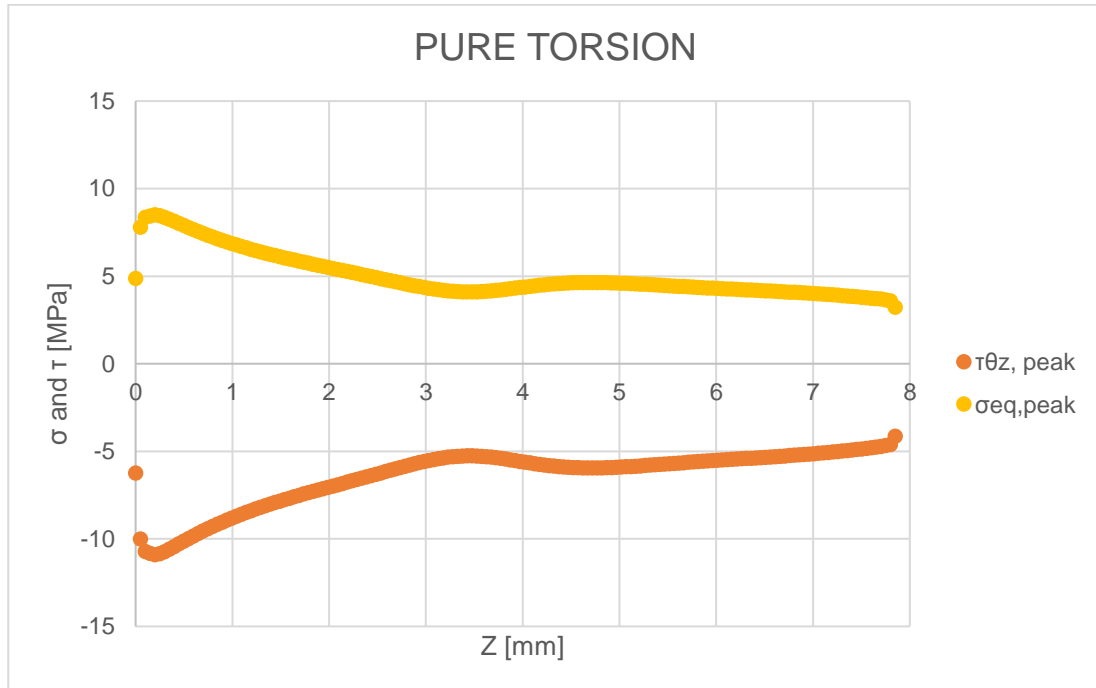


Figure 4.49: Stresses analysis in terms of equivalent peak stress of solution 4 mesh case, root side, pure torsional loading condition. Global element size of the second submodel = 0.05 mm; Nominal applied load $\Delta\tau = 1$ MPa (to the mainmodel).

This graph shows discontinuities and change of concavity that are not physically meaningful. The comparison with the other three solution cases continues to show this unusual slope. The reasons of this strange behaviour are two:

1. The submodel 1 or the submodel 2 should have been enlarged, not to be influenced by the gross mainmodel mesh. However, this is not possible for geometrical problems discussed before and for the reduced calculation power available.
2. The mesh of the first submodel is not enough refined giving a wrong output. The problem is always the same, further mesh refinement is not possible.

These facts lead to the conclusion that the two submodel technique gives positive outcomes only in the pure axial case, while totally unreliable in the torsional loading case. The next step is trying another technique to confirm equivalent stress slope in the pure axial case and find a more accurate stress distribution for the torsional moment loaded model.

4.5.3 The “volume sweep” method

The main achievement of the meshing procedure of the first submodel is to generate an element pattern characterized by having four elements at the root tip. Furthermore, in order to obtain reliable stress distributions, the mesh has to be uniform and not made by very distorted elements. This is not possible with the free mesh generator algorithm but only with the mapped one. However, the mapped mesh generator works only with very simple geometries (like the submodel 2) and it is rarely applicable. A possible alternative to this model is the so-called “volume sweep” method. The main difference from a standard volume meshing technique is that this procedure starts meshing a surface with 2D elements (typically shell elements) with the mapped technique and then with the command volume sweep, the 2D elements are extruded following the volumes shape until reaching a “target” surface. So when the 2D mesh is done and the starting and finishing surfaces are selected, the mesh will be generated automatically. The result is a very regular brick 8 nodes mesh, similar to a mapped one. Once the volumes are meshed it is necessary to clear the surface meshed with 2D elements, in fact this is not belonging to the geometry itself but it was only necessary for the mesh creation. The detailed procedure is here exposed.

1. ELEMENT TYPE => ADD => SHELL181
2. ELEMENT TYPE => ADD => SOLID185 => K1 SIMPLE ENHANCED STRAIN
3. MESHING => SIZE CONTROLS => MANUAL SIZE => GLOBAL => SIZE => 0.12 mm

4. MESHING => SIZE CONTROLS => MANUAL SIZE => LINES => PICKED LINES (divide the lines around the root tip properly to create the four elements of the same size)

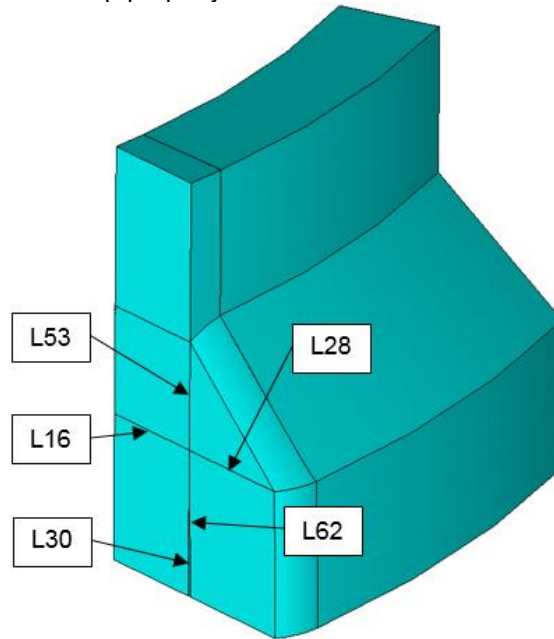


Figure 4.50: Numbers of the lines divided for the meshing procedure.

Line number	Number of divisions	Spacing ratio
L16	17	1
L53	28	1
L28	28	1
L62	30	1
L30	30	1

Table 4.12: Lines characteristics for meshing procedure.

5. MESHING => MESH => AREAS => MAPPED => 4 OR 6 SIDED (pick the areas belonging to the front section, where the critical point is located).

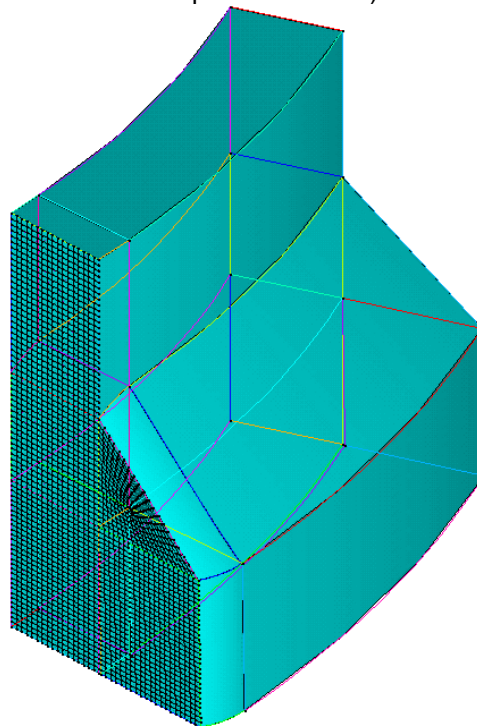


Figure 4.51: 2D shell elements mesh, before volume sweep command.

6. MESHING => MESH => VOLUME SWEEP => SWEEP => (Pick one volume touching the shell elements) => OK (repeat this procedure for every volume, starting from the one touching the 2D meshed elements). The target area is automatically individuated.

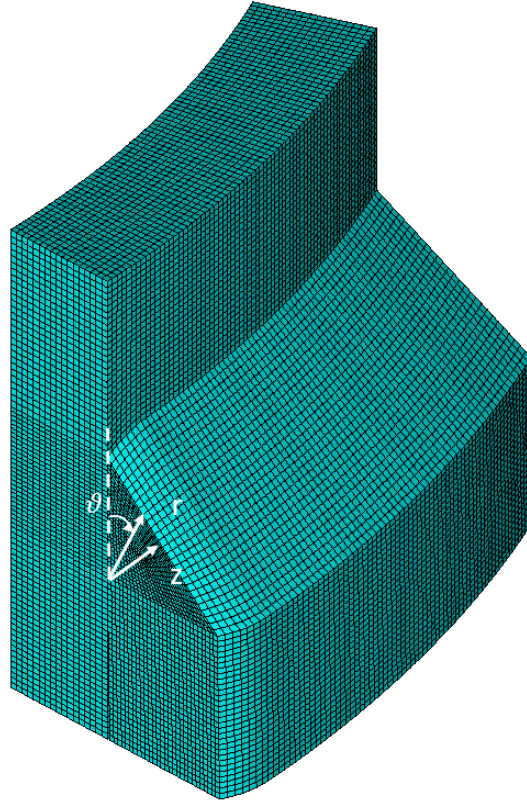


Figure 4.52: meshed submodel 1 with the volume sweep technique. Global element size = 0.12 mm.

7. MESHING => CLEAR => AREAS => ALL (to eliminate the areas meshed with shell elements)

At this point we need to interpolate the degree of freedoms belonging to the cut boundaries nodes, once for the pure axial model and once for the pure torsional one. Starting from the pure axial case, solving the model and selecting the nodes belonging to the line at the root tip, it is possible to analyse the data in terms of equivalent peak stress. The correction parameters values are reported in eqs 4.35 and 4.36.

$$f_{w1} = K_{FE}^* \sqrt{\frac{2e_1}{1-\nu^2}} \left(\frac{d}{R_0}\right)^{1-\lambda_1} = 1.38 \sqrt{\frac{2 * 0.133}{1-0.3^2}} \left(\frac{0.12}{0.28}\right)^{0.5} = 0.488 \quad (4.35)$$

$$f_{w2} = K_{FE}^{**} \sqrt{\frac{2e_2}{1-\nu^2}} \left(\frac{d}{R_0}\right)^{1-\lambda_2} = 3.38 \sqrt{\frac{2 * 0.340}{1-0.3^2}} \left(\frac{0.12}{0.28}\right)^{0.5} = 1.913 \quad (4.36)$$

The results are plotted in the graph below in relation to the coordinate system of figure 4.42.

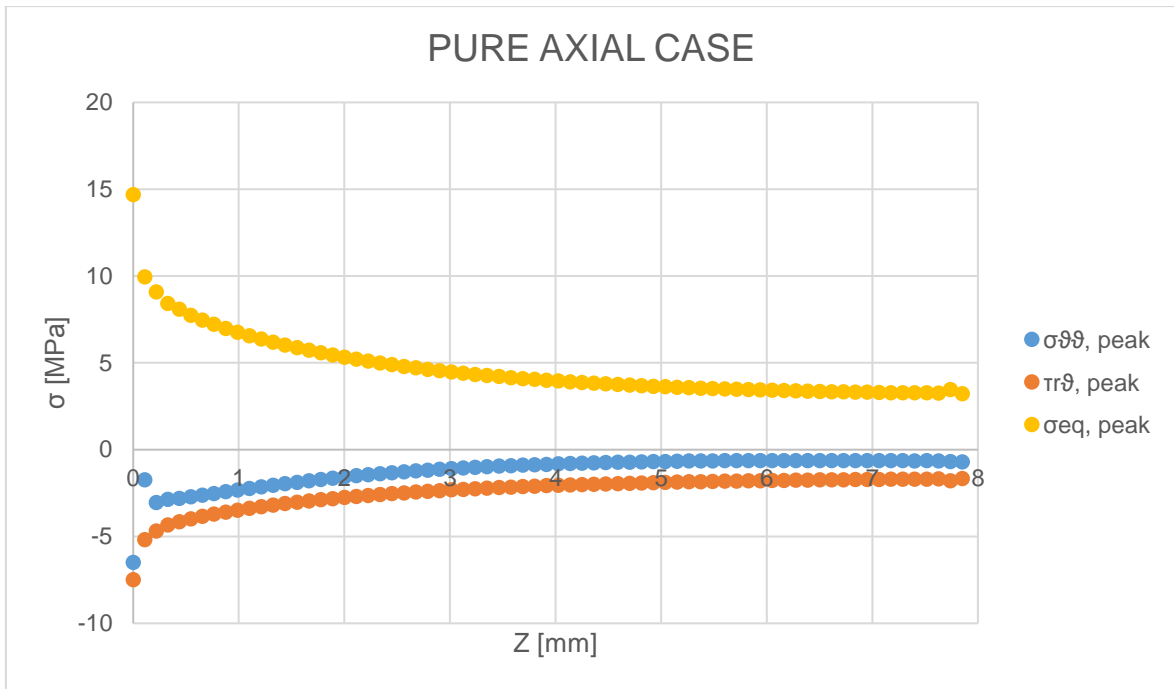


Figure 4.53: Stresses analysis in terms of equivalent peak stress from the submodel meshed with the volume sweep technique, root side, pure axial case. Global element size of the submodel = 0.12 mm; nominal applied load $\Delta\sigma = 1$ MPa (to the mainmodel)

What emerges is that we are confirming the stress distribution obtained with the “two submodel method”: overlapping the two method’s result there would be any visible gaps. However, this last distribution appears more uniform and without any kind of discontinuities or concavity changes; this is due to the very uniform mesh pattern. The first node is again unreliable because of the indirect interpolation in the mainmodel, but considering the value of the equivalent peak stress on the second node we read a value of 10 MPa, not far from the 9 MPa value obtained before.

Dealing with the torsional case, solving the model and selecting the nodes belonging to the line at the root tip, it is possible to analyse the data in terms of equivalent peak stress. The correction parameter value are reported in eq 4.37.

$$f_{w3} = K_{FE}^{***} \sqrt{\frac{2e_3}{1-\nu^2}} \left(\frac{d}{R_0}\right)^{1-\lambda_3} = 1.93 \sqrt{\frac{2 * 0.414}{1-0.3^2}} \left(\frac{0.12}{0.28}\right)^{0.5} = 1.205 \quad (4.37)$$

The results are plotted in the graph below in relation to the coordinate system of figure 4.54.

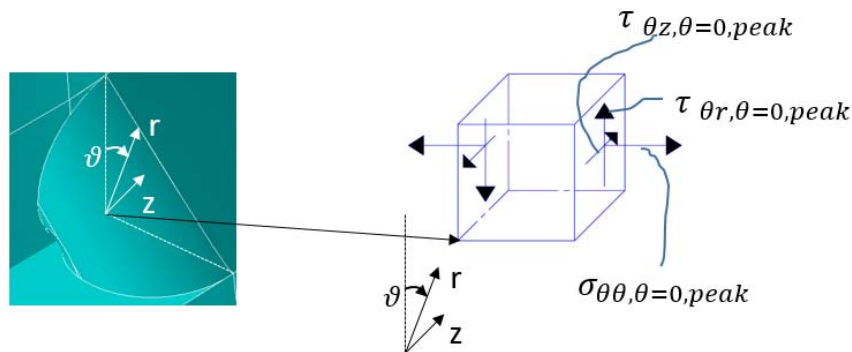


Figure 4.54: Torsional case reference system

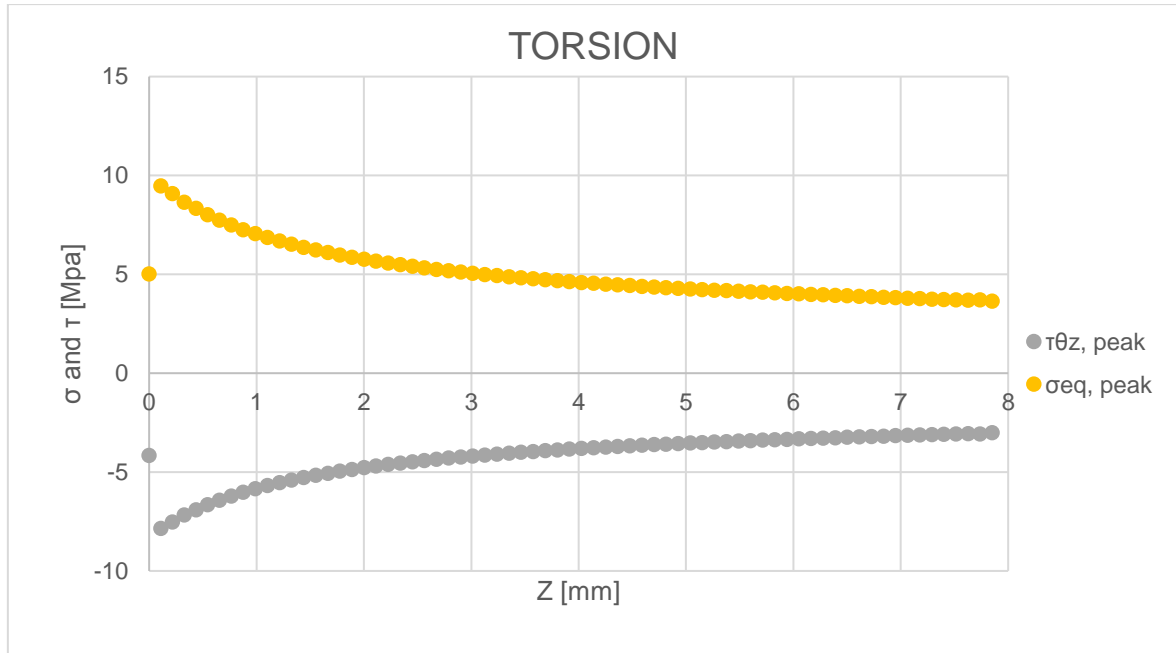


Figure 4.55: Stresses analysis in terms of equivalent peak stress from the submodel meshed with the volume sweep technique, root side, pure torsional loading condition. Global element size = 0.12 mm; nominal applied load $\Delta\tau = 1$ MPa (to the mainmodel).

The first thing that emerges from this stress distribution is that is far way more uniform than the one obtained with the “two submodel technique”. Moreover, this appears to be more truthful, because from a physical point of view the equivalent peak stress has to decrease moving far from the critical point and not to show a fluctuating path. The critical point is always affected by the interpolation problem, so moving to the second node stress we read an equivalent peak stress of 9.5 MPa. Due to the uniformity of the stresses distribution obtained with the “volume sweep technique”, only these last two diagrams will be considered in further analysis. Always considering figure 4.54 reference system now the two loading cases will be combined in a single diagram, figure 4.56. The calculation of the equivalent peak stress was carried out with eq. 4.38.

$$\Delta\sigma_{eq,peak} = \sqrt{c_{w1}f_{w1}^2\Delta\sigma_{\theta\theta,\theta=0,peak}^2 + c_{w2}f_{w2}^2\Delta\tau_{r\theta,\theta=0,peak}^2 + c_{w3}f_{w3}^2\Delta\tau_{\theta z,\theta=0,peak}^2} \quad (4.38)$$

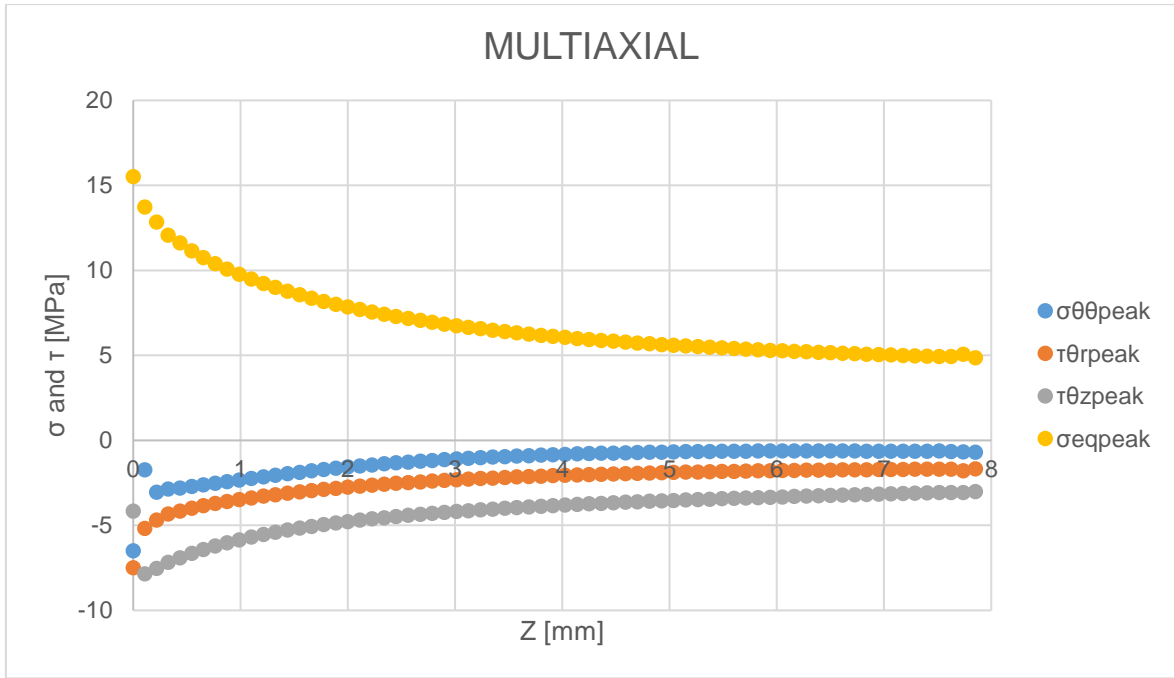


Figure 4.56: Stresses analysis in terms of equivalent peak stress from the submodel meshed with the volume sweep technique, root side, multiaxial loading condition. Global element size 0.12 mm, nominal load $\Delta\sigma = 1$ MPa and $\Delta\tau = 1$ MPa.

It could be interesting to calculate how much is the contribute of Mode I and II in respect to Mode III to the equivalent peak stress, eq. 4.39. Since there are two biaxiality ratio τ_a/σ_a (0.99 and 1.55), we need to distinguish two cases of the solution in table 4.13.

$$\frac{\text{Mode I + II}}{\text{Mode III}} = \frac{[f_{w1}^2 \Delta\sigma_{\vartheta\vartheta, \vartheta=0, peak}^2 + f_{w2}^2 \Delta\tau_{r\vartheta, \vartheta=0, peak}^2] \cdot (\sigma_a)^2}{f_{w3}^2 \Delta\tau_{\vartheta z, \vartheta=0, peak}^2 * (\tau_a)^2} \quad (4.39)$$

$\frac{\tau_a}{\sigma_a}$	$\frac{\text{Mode I + II}}{\text{Mode III}}$
0.99	1.07
1.55	0.44

Table 4.13: Mode I+II contribute in respect to Mode III in terms of biaxiality ratio.

In both cases Mode I and II seems to be more influent in the calculation of the equivalent peak stress. In order to validate the equivalent peak stress graph of both loading cases, a further investigation has been done in terms of Strain Energy Density (SED).

4.6 Validation of results with SED approach

At this point, It is important to check if the influence of higher order terms is negligible or not. This is possible calculating directly the Strain Energy Density on a control volume because it takes into account all possible contributes, not only the singular ones. In order to do this, the two-submodel technique was resumed with some changes regarding the second submodel.

In fact, the cylindrical control volumes, required for the averaged SED calculation, were modelled within it, to bring the possibility of knowing how the SED parameter changes along the root tip line.

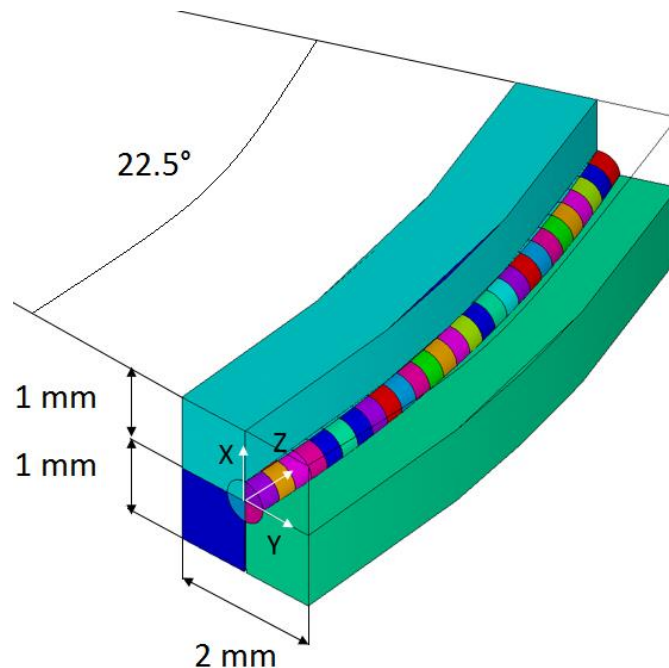


Figure 4.57: Model necessary to the calculation of the SED.

Since we are dealing with structural steel, the control radius is set to 0.28 mm and every cylinder's width is also 0.28 mm. The procedure to create such geometry is here presented in detail.

- a) Resume the second submodel geometry and clear the mesh and the loads.
 PREPROCESSOR => MESHING => CLEAR => VOLUMES => ALL
 PREPROCESSOR => LOADS => DEFINE LOADS => DELETE => ALL LOAD DATA =>
 ALL LOAD DATA AND OPTIONS => OK
- b) For the next step is necessary to move the working plane to the critical point.
 WORKPLANE => DISPLAY WORKING PLANE
 WORKPLANE => ALIGN WITH => KEYPOINTS => (Pick keypoint 5, then 19 and eventually
 23)
- c) To model the control volume, it is necessary to start drawing a circular area around the notch.
 PREPROCESSOR => MODELING => CREATE => LINES => ARCS => BY CENT &
 RADIUS => PICK "WP COORDINATES" => PRESS "0" (keyboard) => ENTER (keyboard)
 => write 0.28 => OK => OK
 PREPROCESSOR => MODELING => CREATE => AREAS => ARBITRARY => BY LINES
- d) This step is aimed to create a geometry to divide internally the submodel 2 geometry.
 PREPROCESSOR => MODELING => CREATE => KEYPOINTS => IN ACTIVE
 COORDINATE SYSTEM (Global Cartesian) => (0;0;0) => OK
 PREPROCESSOR => MODELING => CREATE => KEYPOINTS => IN ACTIVE
 COORDINATE SYSTEM (Global Cartesian) => (0;2;0) => OK
 PREPROCESSOR => OPERATE => EXTRUDE => AREAS => ABOUT AXIS => (Pick the
 circular area just created) => OK => (Pick the keypoints defining the y axis previously
 created) => 45° => OK
 PREPROCESSOR => MODELING => DELETE => VOLUMES ONLY => (Pick the volume
 just created) => OK

- e) Internal division of the submodel 2 geometry.
 PREPROCESSOR => MODELING => OPERATE => BOOLEANS => DIVIDE => VOLUME BY AREA => PICK ALL (Volumes) => OK => (pick the lateral surfaces of the volume eliminated on point g)
- f) Beginning of the creation of several cylindrical volumes to figure out how change the Strain energy density along the line connecting the root tip.
 PREPROCESSOR => MODELING => OPERATE => BOOLEANS => DIVIDE => LINE INTO N LINES => (Pick the indicated lines) => NDIV = 28 => OK (Repeat this procedure for every line indicated by the arrows)

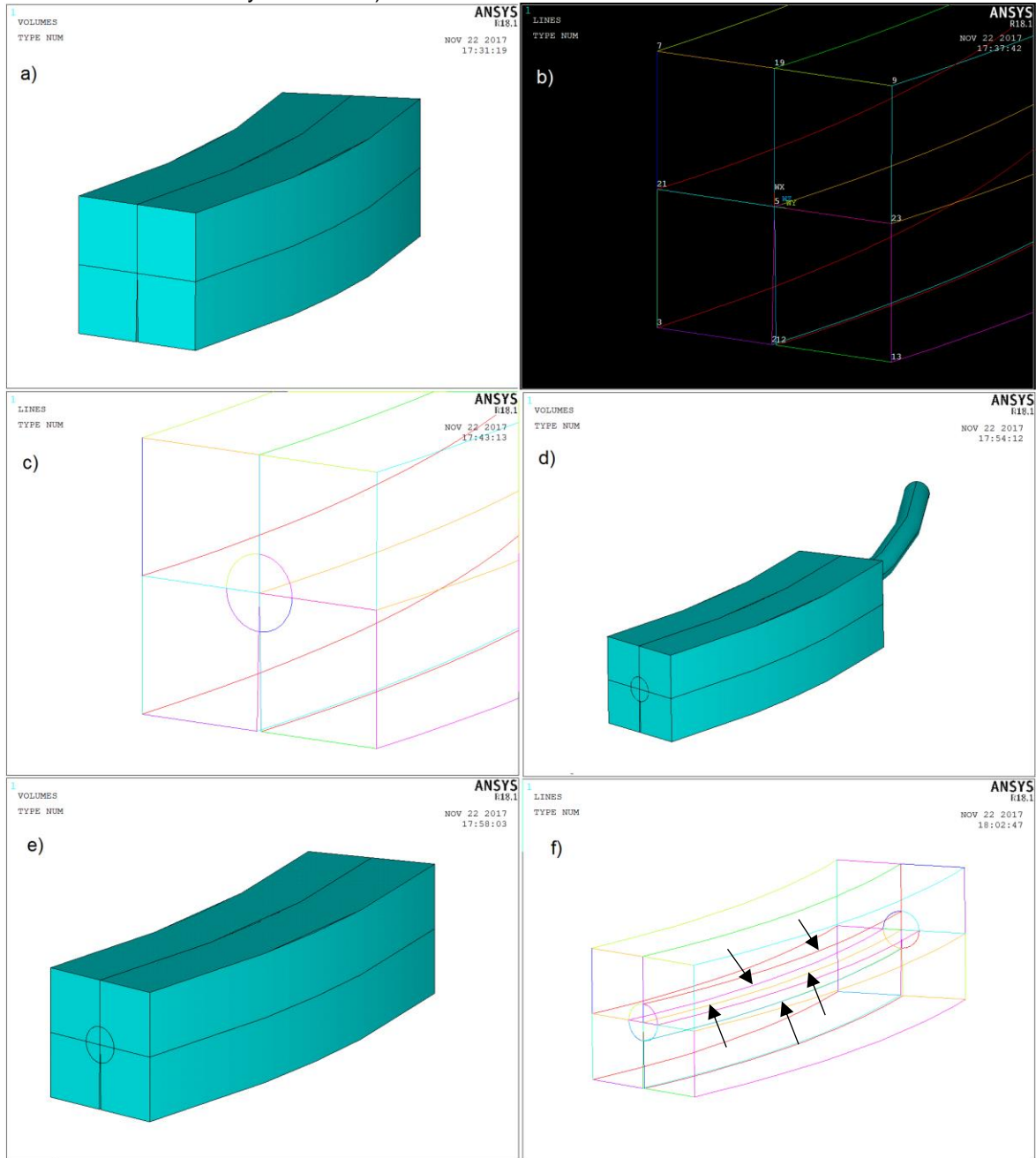


Figure 4.58: Procedure to create the geometry suitable to apply SED approach, part 1.

- g) PREPROCESSOR => MODELING => CREATE => LINES => ARCS => BY END KPs & RADIUS => (Pick keypoints 31 and 61) => OK => (Pick keypoint 88) => RAD = 0.28 => OK
 PREPROCESSOR => MODELING => CREATE => LINES => LINES => STRAIGHT LINE => (Pick keypoints 88 and 61)
- h) At this point the operation described before has to be repeated for every keypoint derived from lines division on point f.

- i) Now, using the just created arcs and lines it is possible to create circular areas that will be used in the next operation. The commands are:
 PREPROCESSOR => MODELING => CREATE => AREAS => ARBITRARY => BY LINES
 => (Pick an arc and two lines to create a circular sector) => OK (Repeat this operation until all arcs and all lines have been used to the areas creation)
- j) Use the areas created on point i to slice the “partial inner toroidal volume” and create 28 different volumes to calculate the SED value.
 PREPROCESSOR => MODELING => OPERATE => BOOLEANS => DIVIDE => VOLUME
 BY AREA => (Pick the partial toroidal volume within the submodel 2 model) => OK => (Pick the areas of point i) => OK
- With this articulate procedure all volumes are perfectly attached each other and to the remaining volumes of submodel 2. In this way, once meshed, there will be no detachments and all volumes will behave like a unique component.

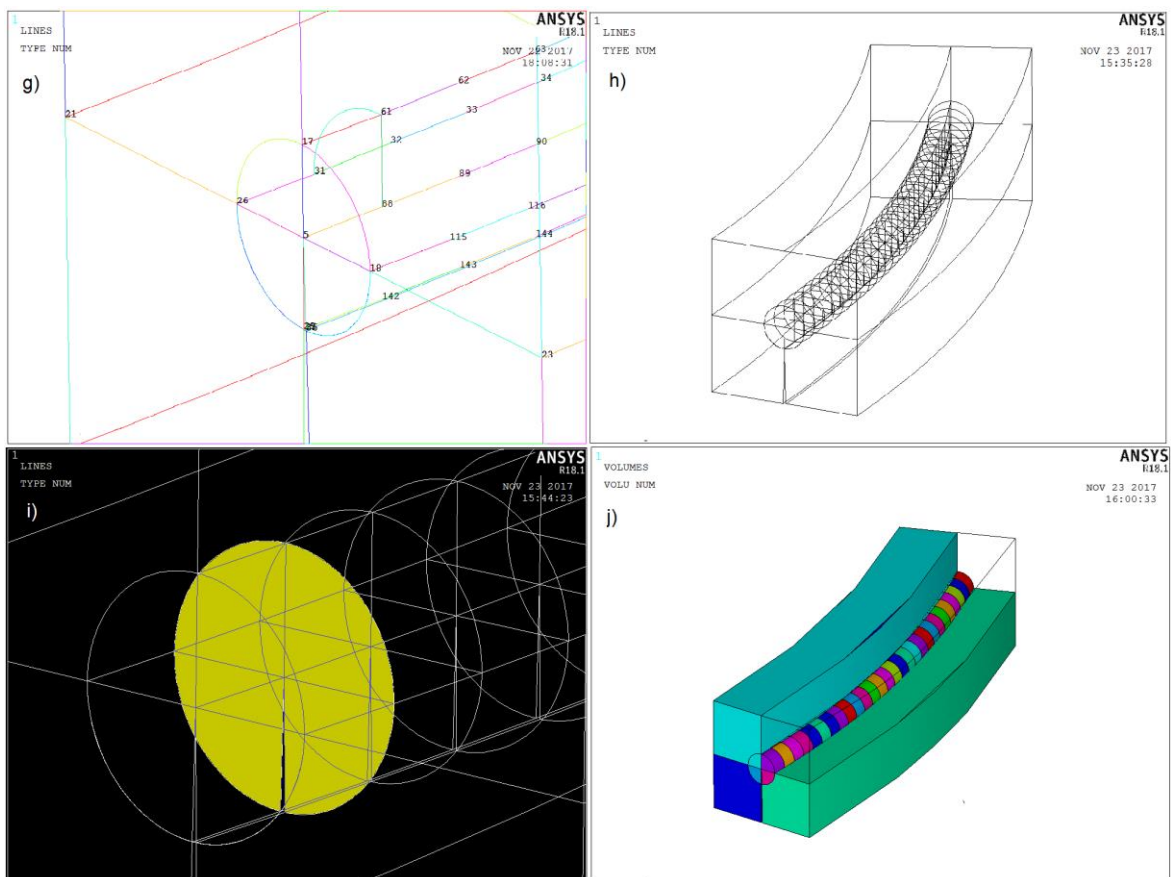


Figure 4.59: Procedure to create the geometry suitable to apply SED approach, part 2.

The meshing procedure was carried out using again the volume sweep technique, so starting meshing the front view with shell elements, running the volume sweep command to mesh the volumes and clearing all areas. Technically the SED calculation is reliable with a few elements within the control volume, but in this case more elements are required; this has been proved empirically running models with coarser meshes.

MESHING => MESH => VOLUME SWEEP => SWEEP => (Pick one volume touching the shell elements) => OK (repeat this procedure for every volume, starting from the one touching the 2D meshed elements). The target area is automatically individuated.

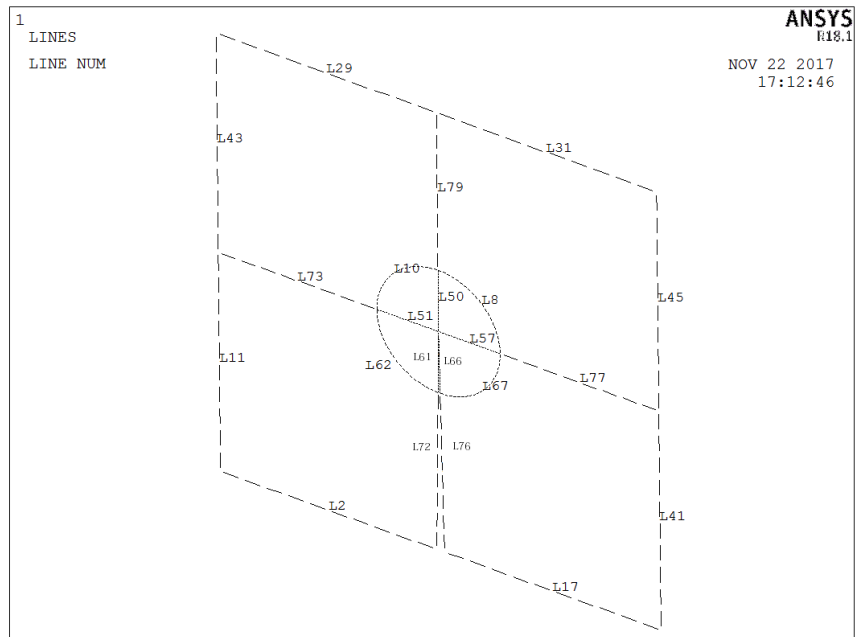


Figure 4.60: Lines division to create the shell mesh pattern on the frontal view.

Lines numbers	Number of divisions	Spacing ratio
L2	10	1
L8	22	1
L10	22	1
L11	10	1
L17	10	1
L29	10	1
L31	10	1
L41	10	1
L43	10	1
L45	10	1
L50	22	1
L51	22	1
L57	22	1
L61	22	1
L62	22	1
L66	22	1
L67	22	1
L72	8	1
L73	8	1
L76	8	1
L77	8	1
L79	8	1

Table 4.14: Lines divisions characteristics.

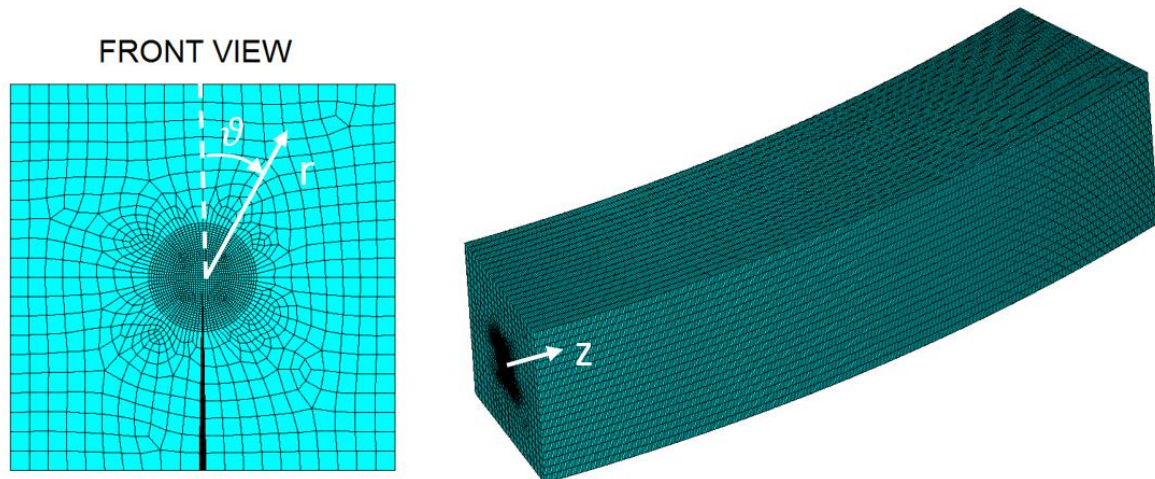


Figure 4.61: Mesh of the model used for the SED calculation

At this point, the cut boundaries have been interpolated in the submodel 1 meshed with the volume sweep technique (fig 4.52), once for the pure axial case and once for the pure torsional one. Now the calculation of the Strain Energy Density was done with the following procedure:

1. SELECT => ENTITIES => BY NUM/PICK => OK => (pick the volumes of the first cylinder) => OK
2. SELECT => EVERYTHING BELOW => SELECTED VOLUMES
3. GENERALPOST => ELEMENT TABLE => DEFINE TABLE => ADD => GEOMETRY => VOLU => OK
4. GENERALPOST => ELEMENT TABLE => DEFINE TABLE => ADD => ENERGY => SENE => OK
5. GENERALPOST => ELEMENT TABLE => SUM OF EACH ITEM
6. SELECT => EVERYTHING

By following these steps, Ansys will give the sum of the “sene” and “volu” of all elements of the first cylinder. To calculate the Strain Energy Density, in an Excel sheet it is sufficient to apply equation 4.40.

$$\text{Strain Energy Density} = \Delta\bar{W} = \frac{\text{sene}}{\text{volu}} \left[\frac{\text{MJ}}{\text{m}^3} \right] \quad (4.40)$$

This procedure has to be redone 28 times to consider every cylinder. Considering the reference system plotted in figure 4.61, the SED development along the volumes located at the root tip line is plotted in figures 4.62 and 4.63. Here the Strain Energy Density value has been assigned to the mid width of each cylinder, so 0.14 mm.

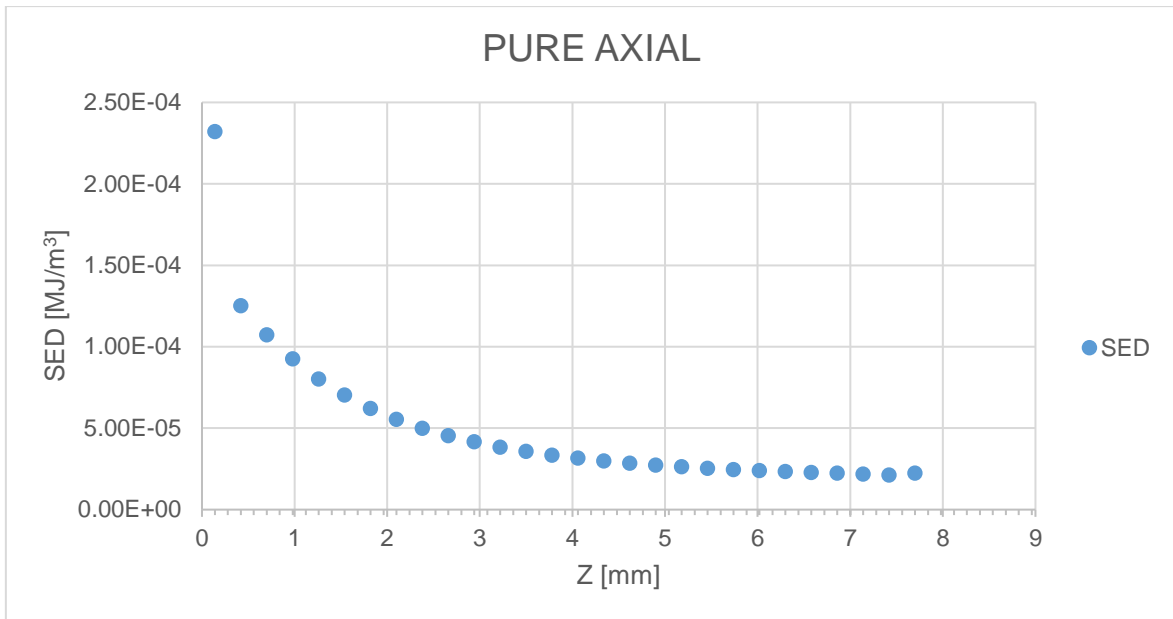


Figure 4.62: SED development along the volumes located at the root tip line, pure axial case. Global element size = 0.1 mm; nominal applied load $\Delta\sigma = 1$ MPa (to the mainmodel)

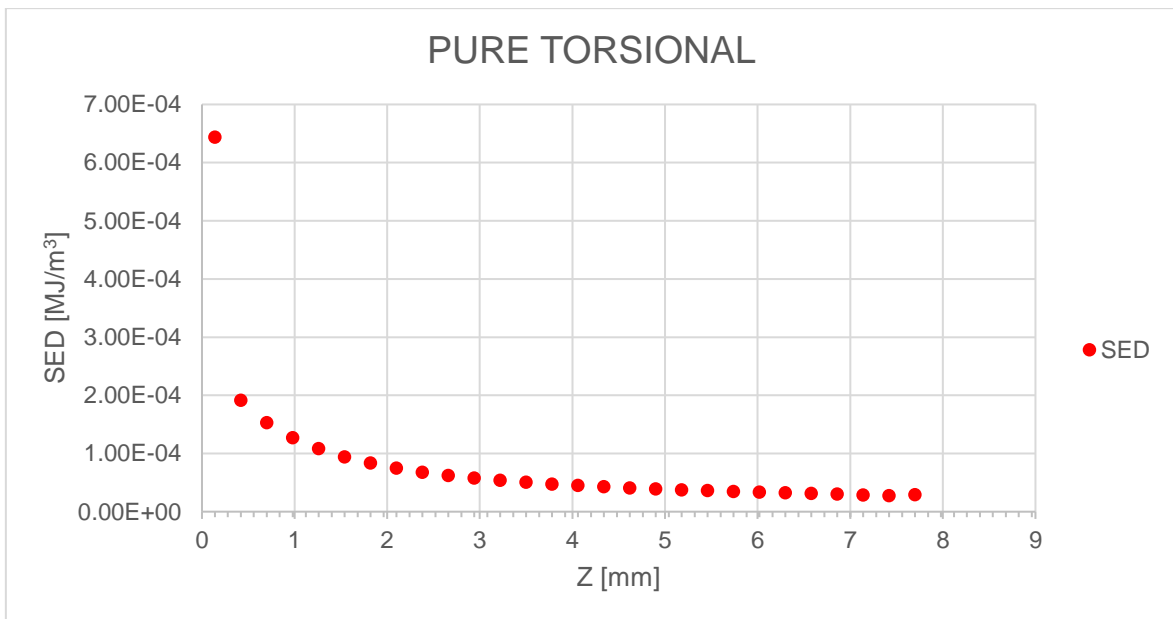


Figure 4.63: SED development along the volumes located at the root tip line, pure torsional case. Global element size = 0.1 mm; nominal applied load $\Delta\tau = 1$ MPa (to the mainmodel)

At first sight, it is clear that there is wide discontinuity between the first and second SED values. The reason is the same of all previous models; also the frontal surface of this model, where the critical point is located, has been interpolated in the mainmodel, where the mesh is not enough refined so the first value is unreliable. While in previous analysis it was sufficient to read the second node value because every node was very near to the following one; here this operation would give an unacceptable error. In fact, every data is distant from the following one by a distance of 0.28 mm, moving to the second data would mean to be too far from the critical point, and the Strain Energy Density calculated in this way would not be representative of the stress state near the singularity. However there is a solution, but first it is interesting to calculate the equivalent peak stress from the SED and compare it to the one calculated with the volume sweep technique. The equivalent peak stress from the SED is derived from equation 4.41:

$$\Delta\bar{W} = \frac{1 - \nu^2}{2E} \Delta\sigma_{eq,peak,SED}^2 \quad (4.41)$$

$$\Delta\sigma_{eq,peak,SED} = \sqrt{\frac{2 * E * \Delta W}{1 - \nu^2}} \quad (4.42)$$

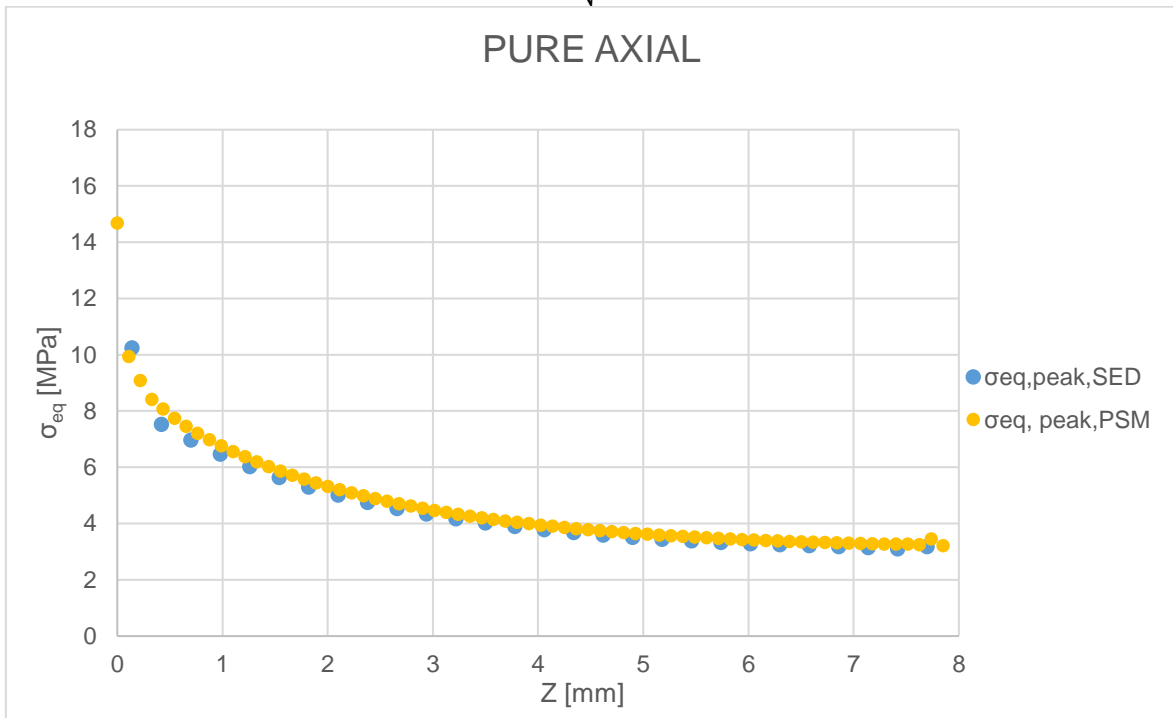


Figure 4.64: Comparison of the equivalent peak stress calculated with the SED approach and the one calculated with the PSM applied to the model meshed with the volume sweep technique, pure axial case. Equivalent Peak stress from SED approach: global element size = 0.1 mm while considering the PSM: global element size = 0.12 mm. Nominal load $\Delta\sigma = 1$ MPa (to the mainmodel for both cases).

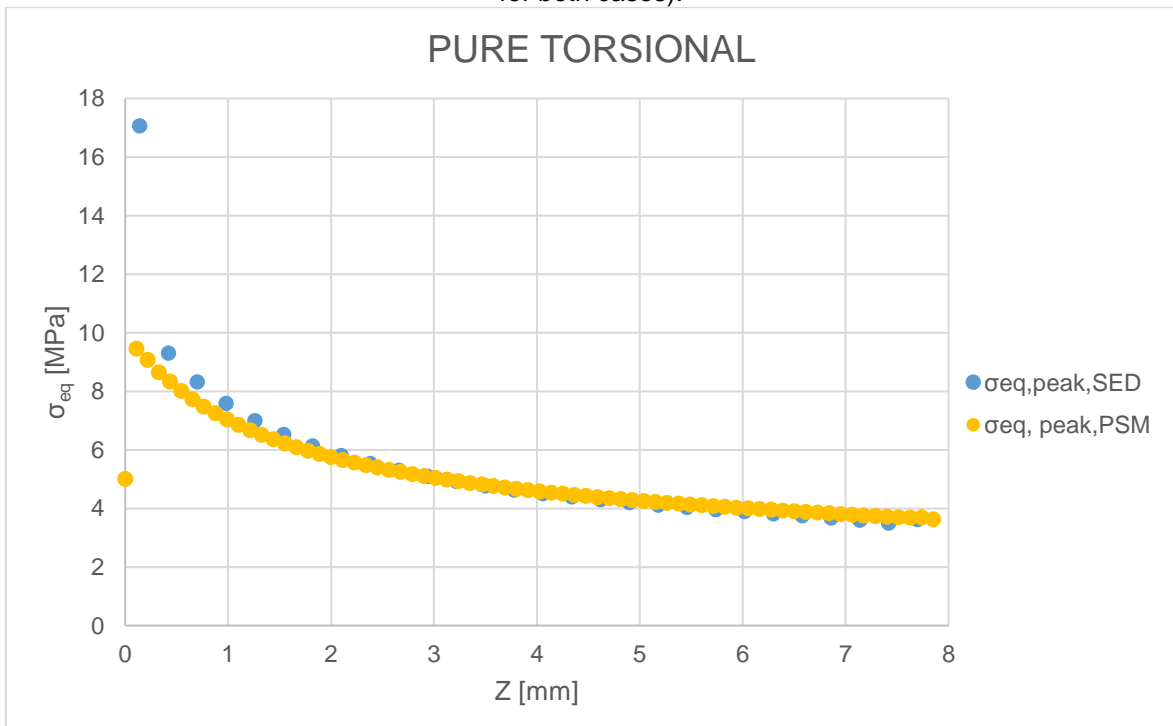


Figure 4.65: Comparison of the equivalent peak stress calculated with the SED approach and the one calculated with the PSM applied to the model meshed with the volume sweep technique, pure torsional case. Equivalent Peak stress from SED approach: global element size = 0.1 mm while considering the PSM: global element size = 0.12 mm. Nominal load $\Delta\tau = 1$ MPa (to the mainmodel for both cases).

Considering the pure axial case, the two slopes are almost perfectly overlapped, validating the equivalent peak stress path. Going to positive z-direction the equivalent peak stress reduces quickly near the singularity and then reaches a constant value at the end of the considered data. This underlines that the submodel extension is sufficient to study the stress field because the analysed data shows completely the transition between a singularity and the reaching of a plateau.

Dealing with the torsional case, the two slopes show a decreasing gap from the critical point until 2 mm distance. This is explained by the evident presence of inducted loading Modes and higher order terms that are taken into account by the SED calculation, but not by the PSM. In fact the equivalent peak stress was calculated only considering the Mode III, even though there are three-dimensional effects that induce Mode I as well as Mode II. In other words, in this case the torsional load is also associated to a notch opening and in-plane shear while we were expecting only out-of-plane shear. These contributions were calculated and retained negligible due to a low percentage error that could be totally absorbed in the Peak Stress Method uncertainty.

Eventually, the estimation of the equivalent peak stress at the critical point is here described distinguishing the two loading cases:

1. PURE AXIAL: In relation to figure 4.64 and previous considerations, it could be affirmed that the equivalent peak stress distribution found with the volume sweep technique is validated. The value of the equivalent peak stress at the critical point is obtained reading its value at the second node from the origin; so it would be of 10 MPa.
2. PURE TORSIONAL: In relation to figure 4.65, the equivalent peak stress value of 9.5 MPa calculated considering the second node value from stress distribution of the model meshed with the volume sweep technique is not exact and needs a revision. To find the correct value a mathematical approach was used, because the finite element analysis could not be refined in any way. Without considering the first node, a polynomial interpolation line was calculated and used to make a prevision of the first value located at a distance $Z = 0.14$ mm, figure 4.52.

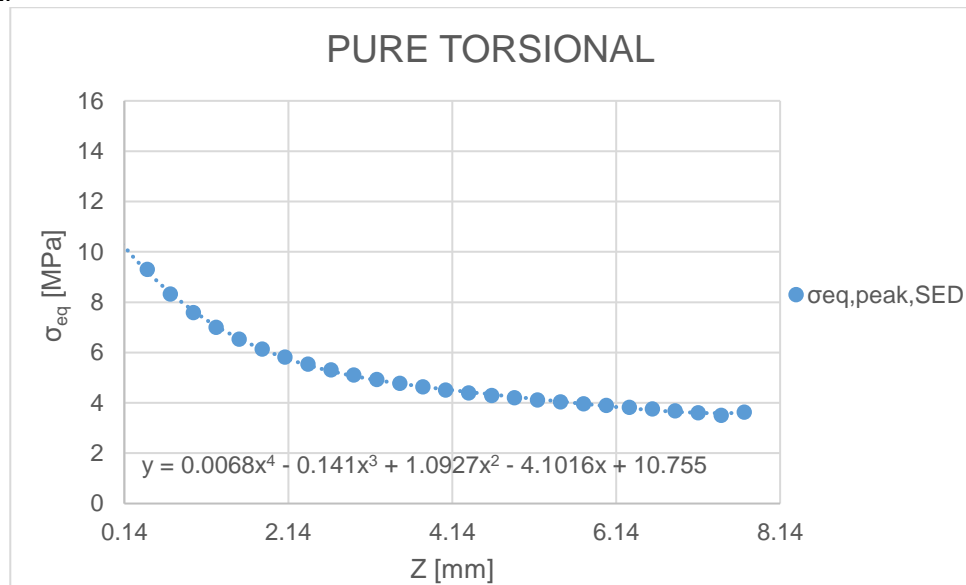


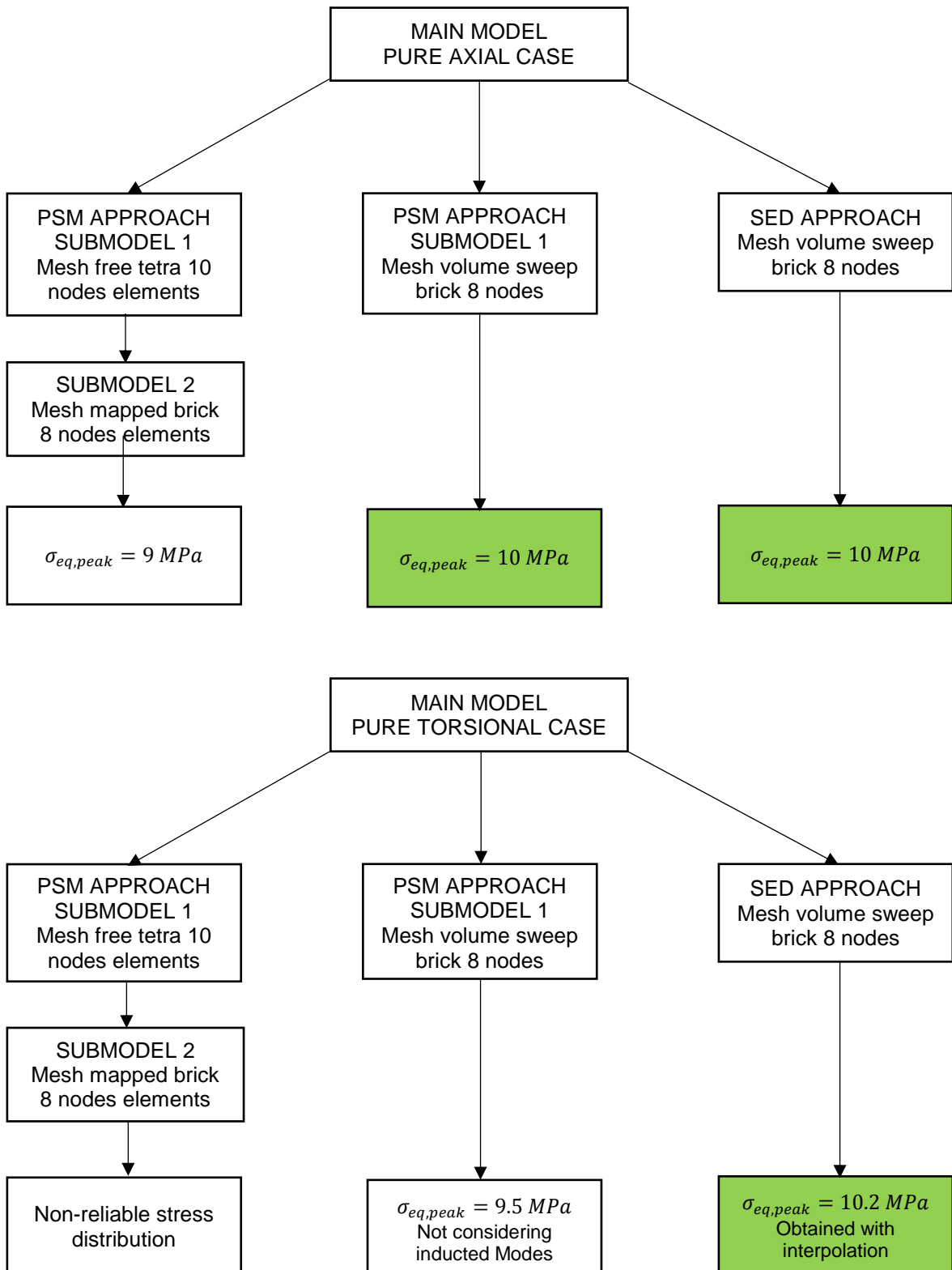
Figure 4.66: Polynomial interpolation line added to the equivalent peak stress graph of the torsional case. Global element size = 0.1 mm; nominal applied load $\Delta\tau = 1$ MPa (to the mainmodel).

Inserting $Z = 0.14$ mm in the interpolation line equation it result an equivalent peak stress value of 10.2 MPa. This was the adopted value for the torsional case.

	PURE AXIAL	PURE TORSIONAL
$\sigma_{eq,peak}$	10.0 MPa	10.2 MPa

Table 4.15: Equivalent peak stress values for both loading cases.

4.7 Procedure flow chart



4.8 Comparison of experimental results with PSM-design scatter bands

To verify the effectiveness of the Peak Stress Method in this particular case, it is necessary to evaluate the experimental data (see chapter 1, table 1.4) in terms of equivalent peak stress. Considering the pure axial case, to calculate the equivalent peak stress, equation 4.43 is used:

$$\Delta\sigma_{eq,peak,axialcase} = \sigma_{eq,peak} * \Delta\sigma_{nom} * \sqrt{c_w} \quad (4.43)$$

Where:

- $\sigma_{eq,peak}$ is the equivalent peak stress derived from the FEM analysis with the volume sweep technique considering the value of the second node, so in this case 10 MPa.
- $\Delta\sigma_{nom}$ is the stress range considering the inner tube:

$$\Delta\sigma_n = \frac{\Delta F}{A_{inner\ tube}} \quad (4.44)$$

- c_w is equal to 1 in all as-welded and stress-relieved cases with cycle ratio $R = 0$, while it is 0.5 in the case of stress-relieved specimens with $R = -1$.

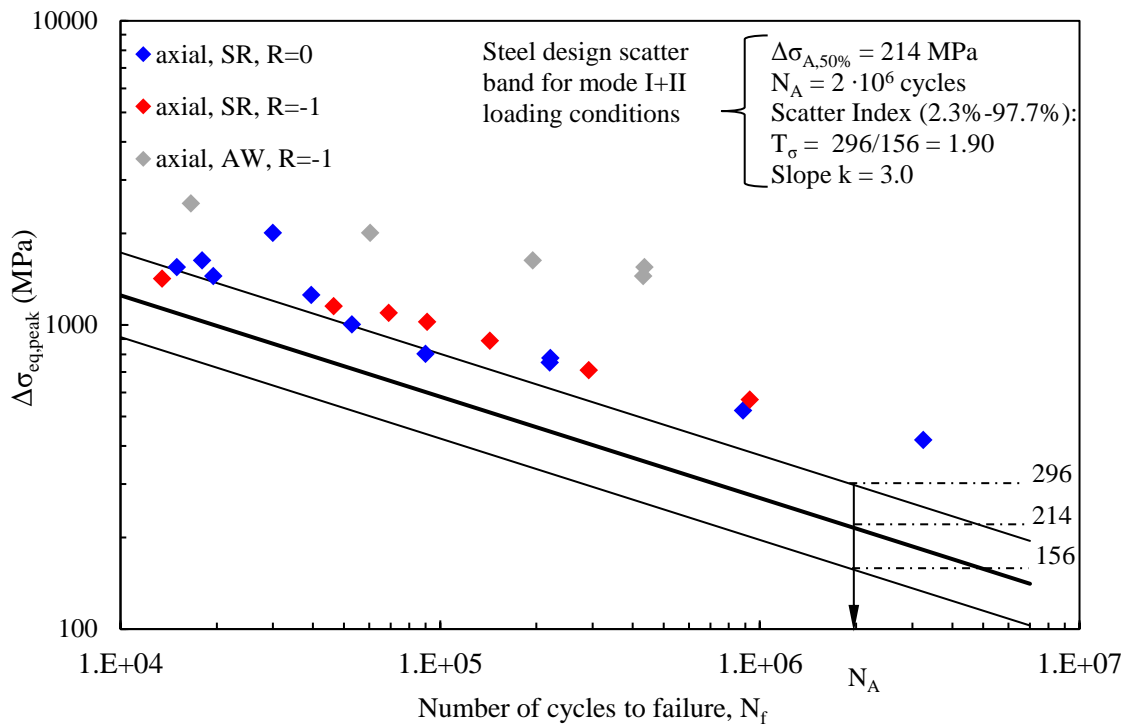


Figure 4.67: Comparison of the experimental data evaluated in terms of equivalent peak stress with the design scatter band: pure axial case.

Considering the pure torsional case, to calculate the equivalent peak stress, equation 4.45 is used:

$$\Delta\sigma_{eq,peak} = \sigma_{eq,peak,torsionalcase} * \Delta\tau_{nom} * \sqrt{c_w} \quad (4.45)$$

Where:

- $\sigma_{eq,peak}$ is the equivalent peak stress derived from the FEM analysis with the SED approach considering the value obtained with interpolation technique, so in this case 10.2 MPa.
- $\Delta\tau_{nom}$ is the stress range considering the inner tube:

$$\Delta\tau_n = \frac{\Delta M_t}{W_{t, inner\ tube}} \quad (4.46)$$

- c_w is equal to 1 in all as-welded and stress-relieved cases with cycle ratio $R = 0$, while it is 0.5 in the case of stress-relieved specimens with $R = -1$.

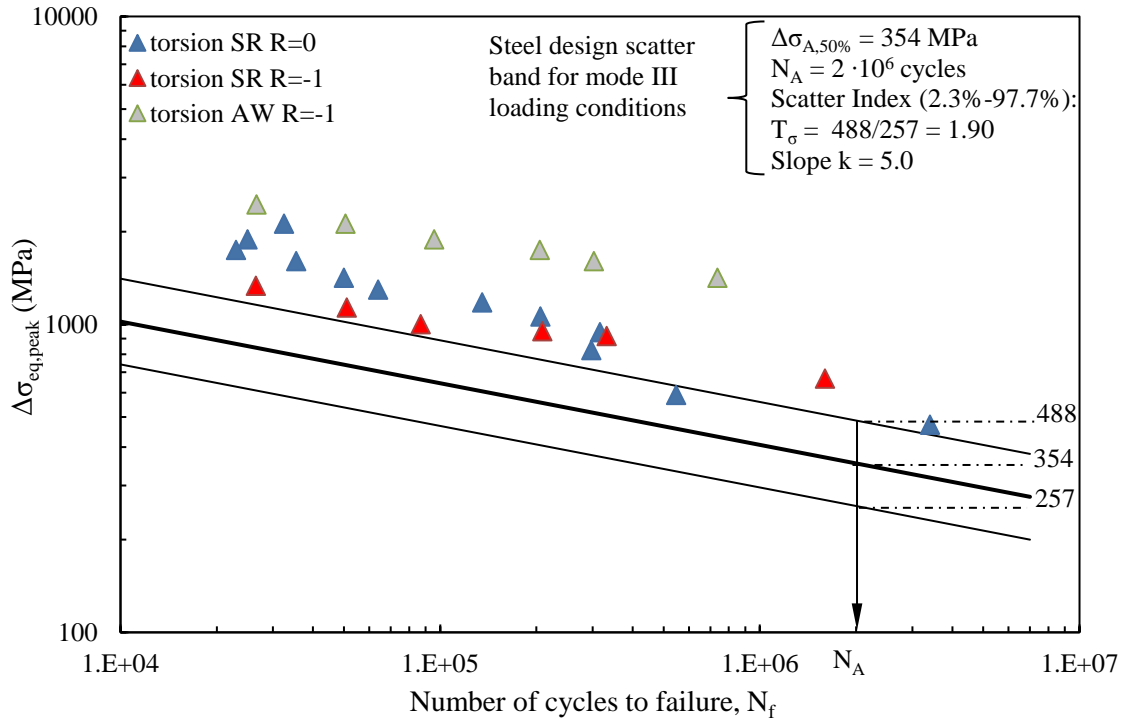


Figure 4.68: Comparison of the experimental data evaluated in terms of equivalent peak stress with the design scatter band: pure torsional case.

Considering the multiaxial case, to calculate the equivalent peak stress, equation 4.47 is used:

$$\Delta\sigma_{eq,peak} = \sqrt{c_{w1}f_{w1}^2\Delta\sigma_{\vartheta\vartheta,\vartheta=0,peak}^2 + c_{w2}f_{w2}^2\Delta\tau_{r\vartheta,\vartheta=0,peak}^2 + c_{w3}f_{w3}^2\Delta\tau_{\vartheta z,\vartheta=0,peak}^2} \quad (4.47)$$

In fact both FEM models, pure axial and pure torsional, are solved considering $\Delta\sigma = 1$ MPa and $\Delta\tau = 1$ MPa and the deriving peak stresses are scaled up considering the range of nominal stress. In equation 4.47: $\Delta\sigma_{\vartheta\vartheta,\vartheta=0,peak}$, $\Delta\tau_{r\vartheta,\vartheta=0,peak}$ and $\Delta\tau_{\vartheta z,\vartheta=0,peak}$ are the stresses extracted from the submodel 1 meshed with the volume sweep technique solved for the axial and torsional case respectively, considering the values of the second nodes. In all as-welded and stress-relieved cases with cycle ratio $R = 0$, $c_{w1} = c_{w2} = c_{w3} = 1$; while in the case of stress-relieved specimens with $R = -1$, $c_{w1} = c_{w2} = c_{w3} = 0.5$. In figure 4.69 all data are distinguished between as-welded, stress-relieved cycle ratio R , biaxiality ratio τ_a/σ_a and phase displacement.

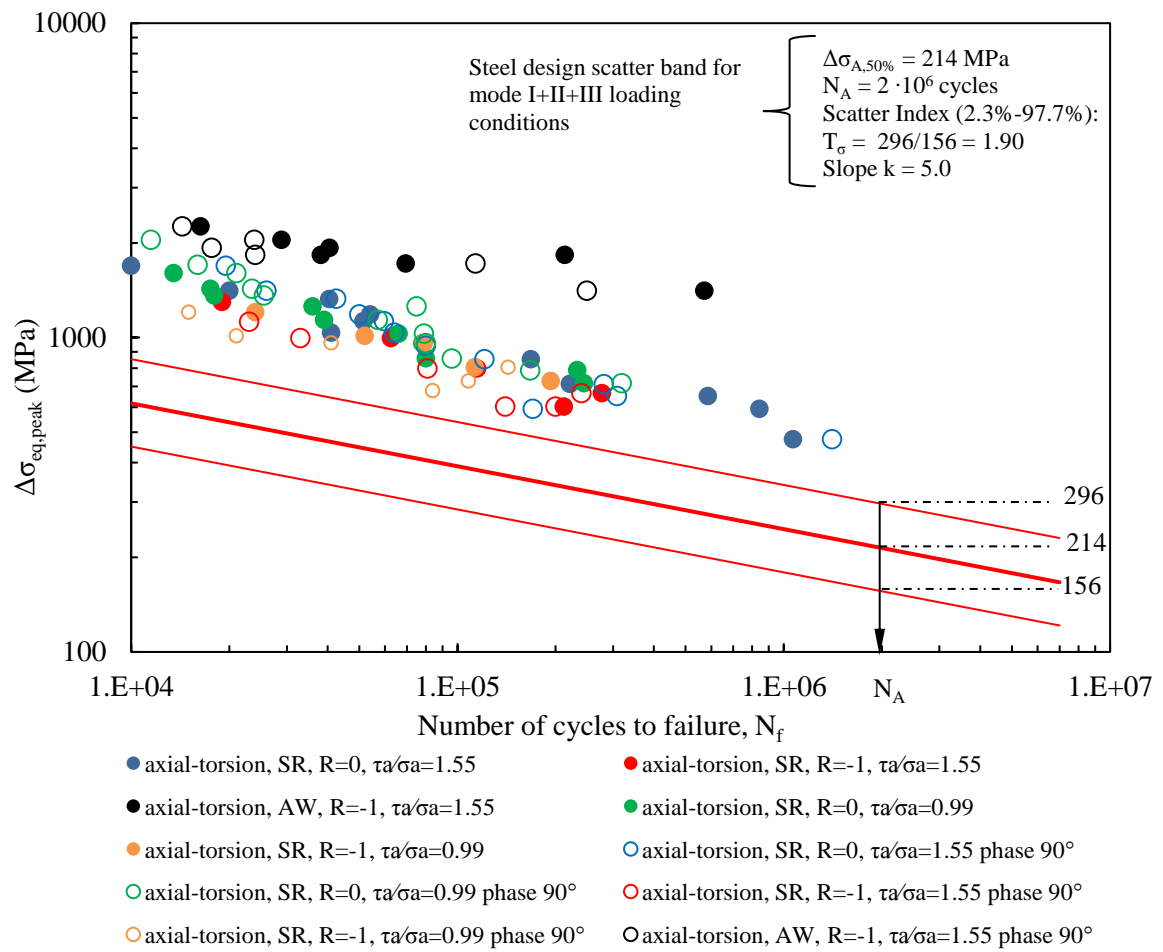


Figure 4.69: Comparison of the experimental data evaluated in terms of equivalent peak stress with the design scatter band: multiaxial case.

Plotting all experimental data evaluated in terms of equivalent peak stress, the outcome will be the one plotted in figure 4.70.

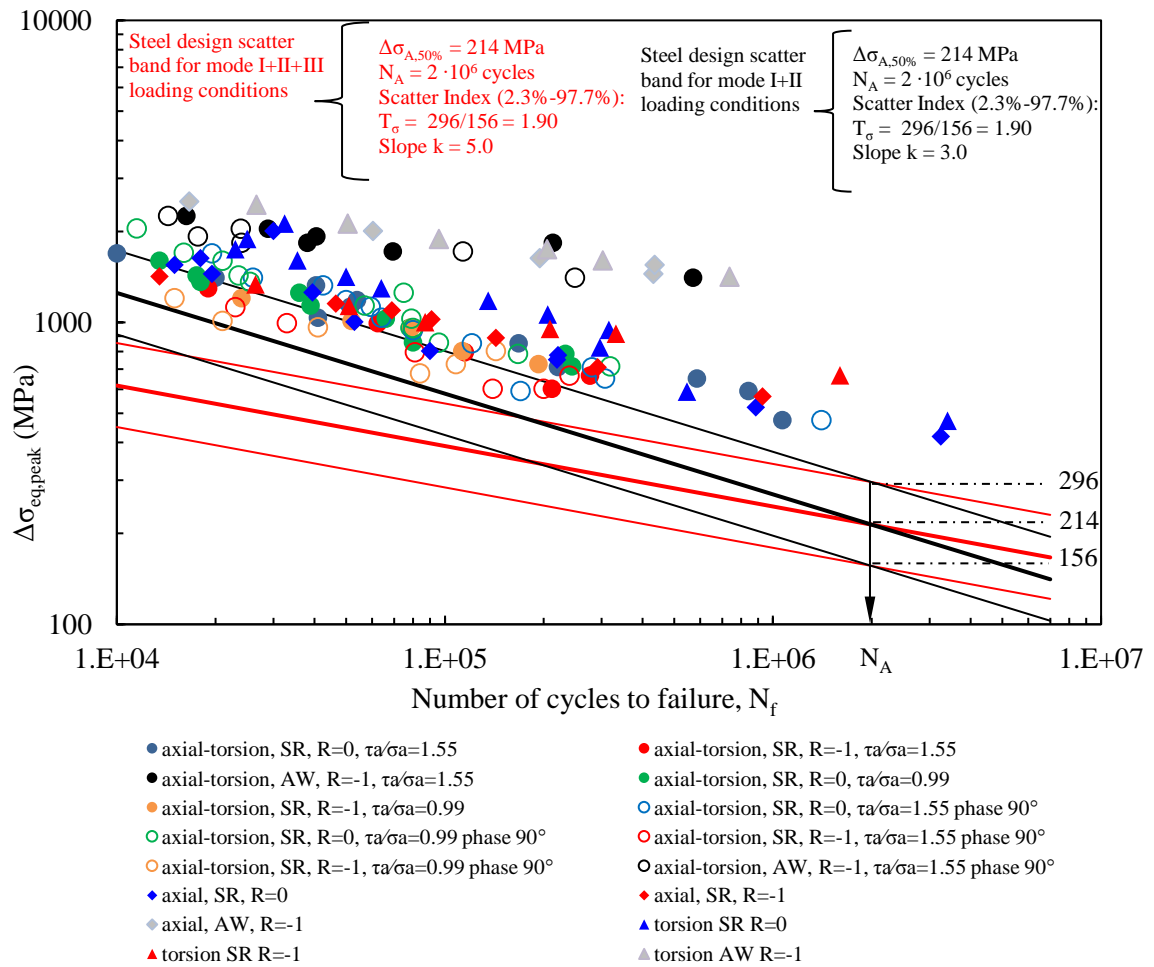


Figure 4.70: Comparison of the experimental data evaluated in terms of equivalent peak stress with the design scatter band: all loading cases.

CONCLUSIONS

Considering the specimens' failures reported in the original paper in terms of figure of crack propagation path, it emerges a strange cracking behaviour under pure axial loading. The crack spreads along the separation between the weld and the outer tube while it was supposed to split the weld. The hypothesis is that there is a lack of penetration and the welded material is not well attached to the outer cylinder.

The Peak Stress Method has been applied and the equivalent peak stress distribution along the root tip has been validated using the Strain Energy Density (SED) approach. What emerges from this comparison is that in the pure axial case, the singular components are representative of the stress state and the higher order terms influence is negligible. On the other hand, this last statement is not valid anymore for the pure torsional case and to find the correct value of the equivalent peak stress a direct calculation of the averaged SED is needed. To be more precise, the percentage error of the equivalent peak stress calculated with the PSM in comparison with the one obtained with the SED approach was around 7%. As a consequence, its value was calculated considering a polynomial interpolation line of the equivalent peak stress distribution derived from the SED path along the root tip line, because this energetic parameter takes into account all stress contributes, not only the singular ones.

All this considerations are based on FEM analysis and it is possible to affirm that these results are reliable due to several convergence analysis and comparisons of stress distributions obtained with different methods.

To summarize, the equivalent peak stress value was obtained by the application of the Peak Stress Method for the axial case and by the application of the Strain Energy Density approach for the torsional case.

Dealing with the design scatter bands of the Peak Stress Method, it emerges that as-welded specimens' failure data are largely located on the safe side. The possible explanation of this phenomenon is the presence of a high compressive residual stress derived from the welding procedure. It is remarkable that Vormwald in his work supposed the presence of this compressive residual stress and it would have been interesting to measure it.

Regarding stress-relieved specimens, the conclusion is similar. In fact, they are also on the safe side and perhaps the reason is that the heat treatment (600° for 6 h and followed by slow cooling) is ineffective and the supposed compressive residual stress is still present.

These observations are shared for uniaxial as well as multiaxial cases, strengthening the hypothesis of the compressive residual stress. Furthermore, running a statistical analysis of the multiaxial experimental data it results a low value of the scatter index, meaning that the Peak Stress Method has been able to summarize SN data of very different loading conditions. The goal of this approach has always been to unify fatigue failures data in a single curve considering the local stress state, so not taking into account the applied load but the deriving stress state near the V-notch.

Eventually, from the analysis of the equivalent peak stress distributions it is clear that there is a very high stress gradient in the hoop direction under both axial and torsion loading. For this reason, it would be helpful to know the exact crack initiation point. In fact, the equivalent peak stress varies significantly just moving a fraction of millimetres far from the critical point. In other words, if the crack was not starting exactly from the so-called critical point, the equivalent peak stress would significantly reduce and in this way the experimental data could fall within the scatter band. However, the exact crack initiation point is not known and maybe this fact would lead to further experimental investigations since the simulation work and computational analysis are accomplished in this thesis.

REFERENCES

- [1] Shams E, Vormwald (2017), M. Fatigue of weld ends under combined loading. *Int J Fatigue*.
- [2] Pedersen, M. M. (2016). Multiaxial fatigue assessment of welded joints using the notch stress approach. *International Journal of Fatigue*, 83(2), 269–279.
- [3] C. M. Sonsino (1995), Multiaxial fatigue of welded joints under in- phase and out-of-phase local strains and stresses, *Int. Journal of Fatigue* 17 (1) 55–70.
- [4] A. Hobbacher (2013), IIW Recommendations for Fatigue Design of Welded Joints and Components, Revised September 2013., IIW- doc. XIII-2460-13.
- [5] J. Wiebesiek, K. Störzel, T. Bruder, H. Kaufmann (2011), Multiaxial fatigue behaviour of laserbeam-welded thin steel and aluminium sheets under proportional and non-proportional combined loading, *International Journal of Fatigue* 33 992–1005.
- [6] M. Kaffenberger, M. Vormwald (2012), Considering size effects in the notch stress concept for fatigue assessment of welded joints, *Computational Materials Science* 64 71–78.
- [7] P. Lazzarin, T. Lassen, P. Livieri (2003), *Fatigue Fract. Eng. Mater. Struct.* 26 (1) 49–58.
- [8] Vormwald M, Schwingfestigkeitsbewertung von Nahtenden MSGgeschweißter Feinbleche aus Stahl unter kombinierter Beanspruchung, VDA.
- [9] Meneghetti Giovanni, De Marchi Andrea and Campagnolo Alberto (2016), Assessment of root failures in tube to flange steel welded joints under torsional loading according to the peak stress method, *Theoretical and applied Fracture Mechanics*, 19-30.
- [10] Meneghetti Giovanni and Lazzarin Paolo (2006), Significance of the elastic peak stress evaluated by FE analyses at the point of singularity of sharp V notched components, *Fatigue Fract Engng Mater Struct* 30, 95-106.
- [11] Lazzarin Paolo and R. Tovo (1998), A notch intensity factor approach to the stress analysis of welds.
- [12] P. Lazzarin, R Zambardi, A finite-volume-energy based approach to predict the static and the fatigue behavior of components with sharp V-shaped notches, *Int.j.Fract.* 133(2005) 247-276.
- [13] Meneghetti Giovanni, Campagnolo A. and D. Rigon (2017), Multiaxial fatigue strength assessment of welded joints using the Peak Stress Method – Part I: Approach and application to aluminium joints. *Int J Fatigue*.
- [14] G. Meneghetti and P:Lazzarin, The peak stress method for fatigue strength assessment of welded joints with weld toe or weld root failures, *Fatigue of Welded components and structures*
- [15] Lazzarin P. and Tovo R.: A notch intensity factor approach to the stress analysis of welds, *Fatigue and Fracture of Engineering Materials and Structures*, 1998, vol. 21, no. 9, pp. 1089-1103.
- [16] Meneghetti G, Guzzella C. and Atzori B, The peak stress method combined with 3D finite element models for fatigue assessment of toe and root cracking in steel welded joints subjected to axial or bending loading, *Fatigue Fract Engng Mater Struct*, 37, 722-739.
- [17] G. Meneghetti (2013), The peak stress method for fatigue strength assessment of tube-to-flange welded joints under torsion loading, *Weld. World.* 57, 265–275.
- [18] Meneghetti Giovanni (2011), The use of peak stresses for fatigue strength assessments of welded lap joints and cover plates with toe and root failures, *Engineering fracture mechanics* 89, 40-51.
- [19] M. Zappalorto, *Appunti del corso di Meccanica dei Materiali*, Vicenza, 2014.
- [20] P. Lazzarin, S. Filippi e Giulio Mattiello, *Tesi di Laurea Magistrale: Riprogettazione di giunzione saldate per presse meccaniche basata su modelli FEM tridimensionali*, Università di Padova - Dipartimento di Tecnica e Gestione dei Sistemi Industriali, 2013-14.
- [21] G. Meneghetti, A. Campagnolo, the Peak Stress Method to assess the fatigue strength of welded joints using linear elastic finite element analysis, *Procedia Engineering* 00 (2017) 000-000
- [22] Meneghetti G., Campagnolo A., *Approcci locali basati sugli NSIFs per la progettazione a fatica dei giunti saldati*, 2016
- [23] Meneghetti Giovanni, Campagnolo A. and D. Rigon (2017), Multiaxial fatigue strength assessment of welded joints using the Peak Stress Method – Part II: Approach and application to steel joints. *Int J Fatigue*.
- [24] Lazzarin and Livieri, Notch stress intensity factors and fatigue strength of aluminium and steel welded joints, *International Journal of Fatigue* 23 (2001) 225–232.

- [25] Kaffenberger M, Vormwald M. Application of the notch stress concept to the real geometry of weld end points. *Materwiss Werksttech* 2011;42:289–97.
- [26] Kaffenberger M, Vormwald M. Fatigue resistance of weld ends – analysis of the notch stress using real geometry. *Materwiss Werksttech* 2011;42:874–80.
- [27] Kaffenberger M, Malikoutsakis M, Savaidis G, Vormwald M. Fatigue resistance of weld ends. *Comput Mater Sci* 2012;52:287–92.
- [28] Vormwald M, Schwingfestigkeitsbewertung von Nahtenden MSGgeschweißter Feinbleche aus Stahl unter kombinierter Beanspruchung, VDA.

APPENDIX

In previous analysis, the experimental data were evaluated in terms of equivalent peak stress considering its value in proximity of the critical point ($Z = 0$ mm) from the distributions obtained with the volume sweep technique, see figures A1 and A2. A further investigation could be done re-analysing the experimental data considering the minimum value of the equivalent peak stress distribution, supposing it constant along the entire weld. Therefore, the experimental data could also be re-analysed considering the mean value of the equivalent peak stress distribution, supposing it constant along the entire weld. It must be underlined that the stress distribution was limited to a quarter of the total weld ($Z \approx 8$ mm), due to the submodel geometry, and to extend it to half of the weld ($Z \approx 16$ mm) the last value was supposed constant. In the axial case, this operation does not represent a big approximation because we had just reached a plateau, while in the torsional case the discontinuity is quite evident and the output of this analysis less reliable.

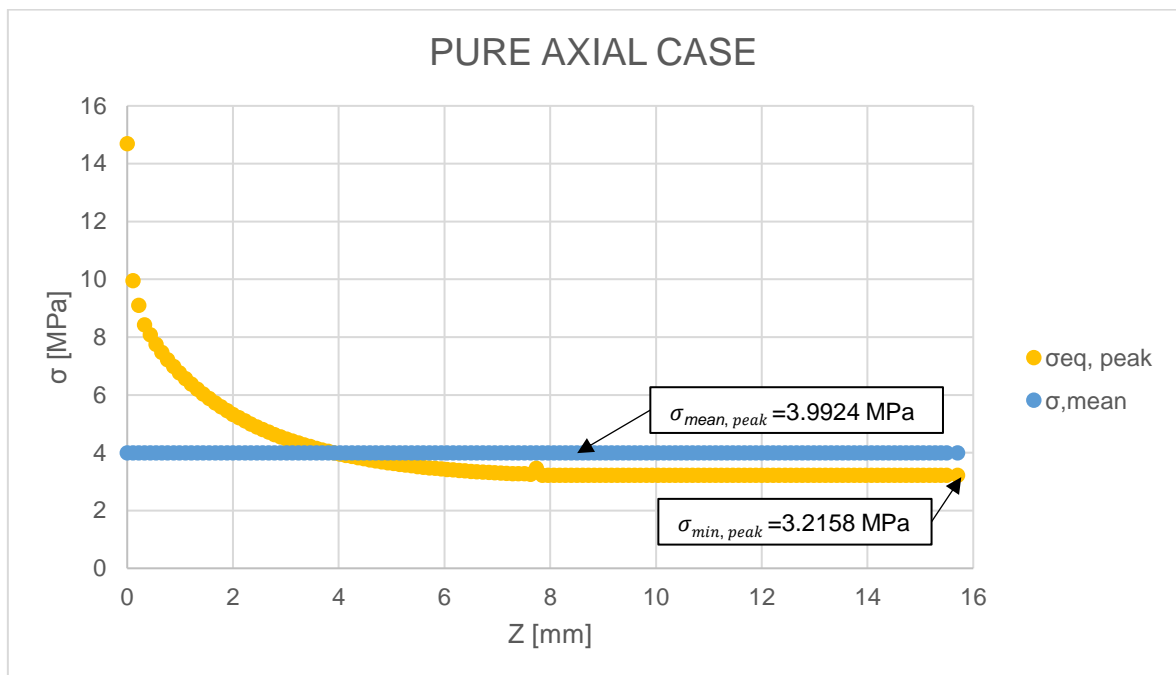


Figure A1: Stresses analysis in terms of equivalent peak stress from the submodel meshed with the volume sweep technique, root side, pure axial case. Global element size of the submodel = 0.12 mm; nominal applied load $\Delta\sigma = 1$ MPa (to the mainmodel). In blue it is represented the mean value of this distribution.

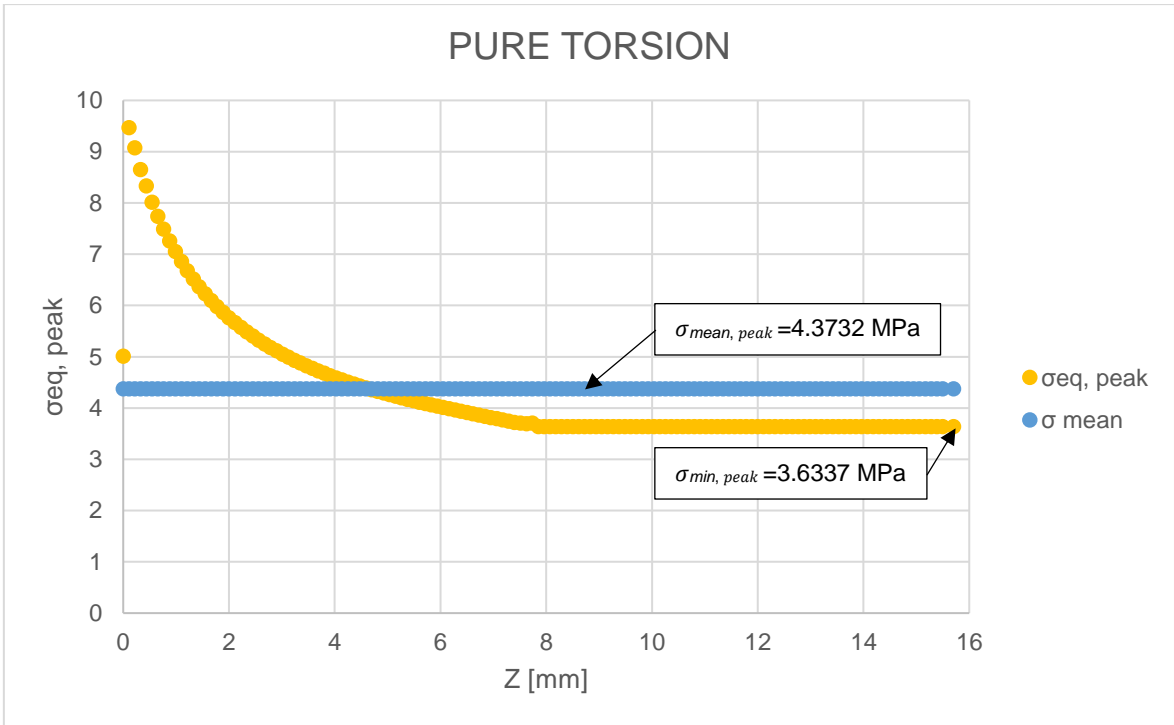


Figure A2: Stresses analysis in terms of equivalent peak stress from the submodel meshed with the volume sweep technique, root side, pure torsional loading condition. Global element size = 0.12 mm; nominal applied load $\Delta\tau = 1$ MPa (to the mainmodel). In blue it is represented the mean value of this distribution.

Evaluation of experimental data in terms of $\sigma_{eq, peak}$ considering $\sigma_{min, peak}$

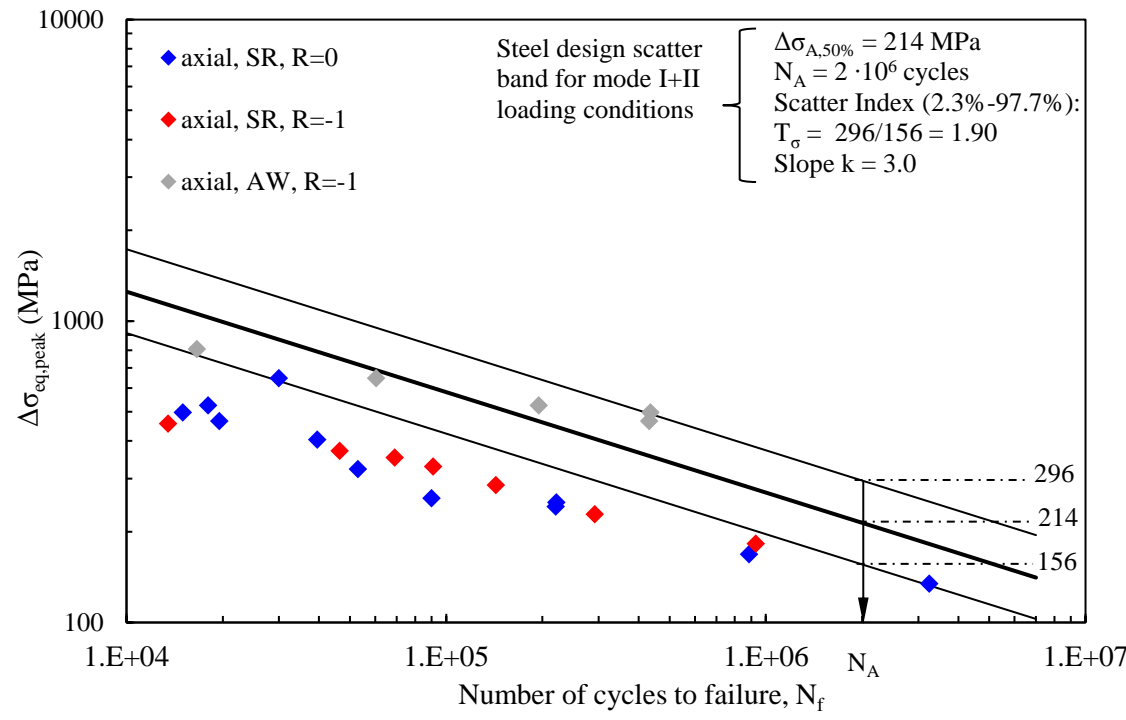


Figure A3: Comparison of the experimental data evaluated in terms of equivalent peak stress with the design scatter band: axial case.

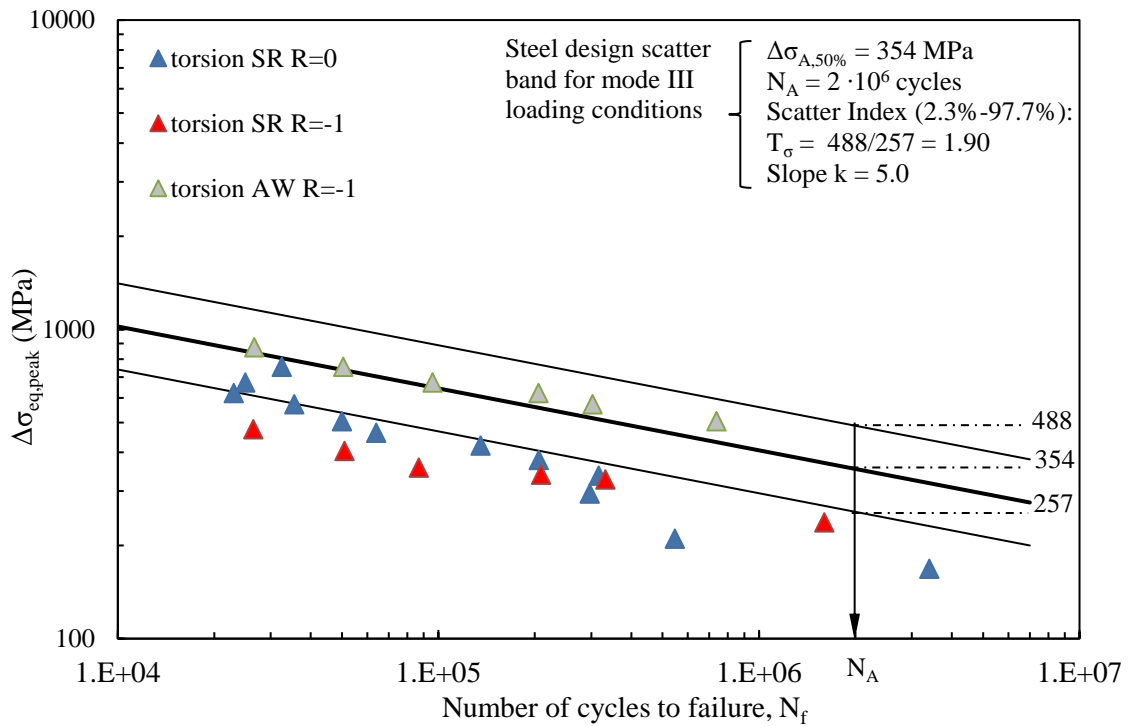


Figure A4: Comparison of the experimental data evaluated in terms of equivalent peak stress with the design scatter band: torsional case.

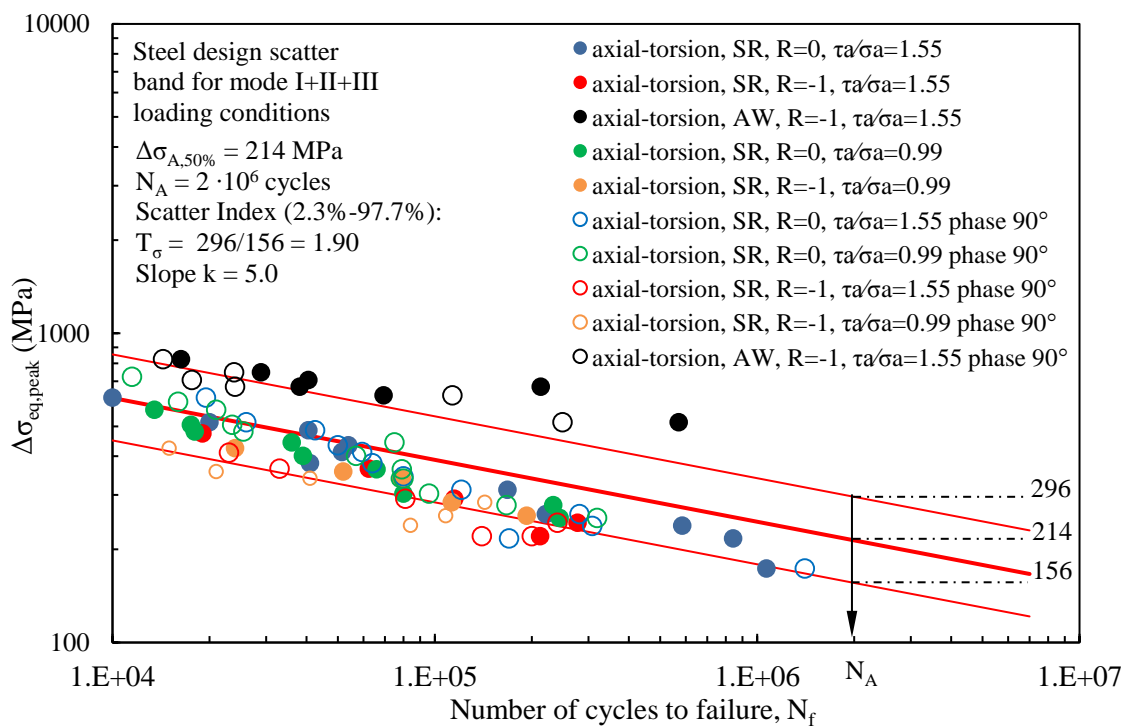


Figure A5: Comparison of the experimental data evaluated in terms of equivalent peak stress with the design scatter band: multiaxial case.

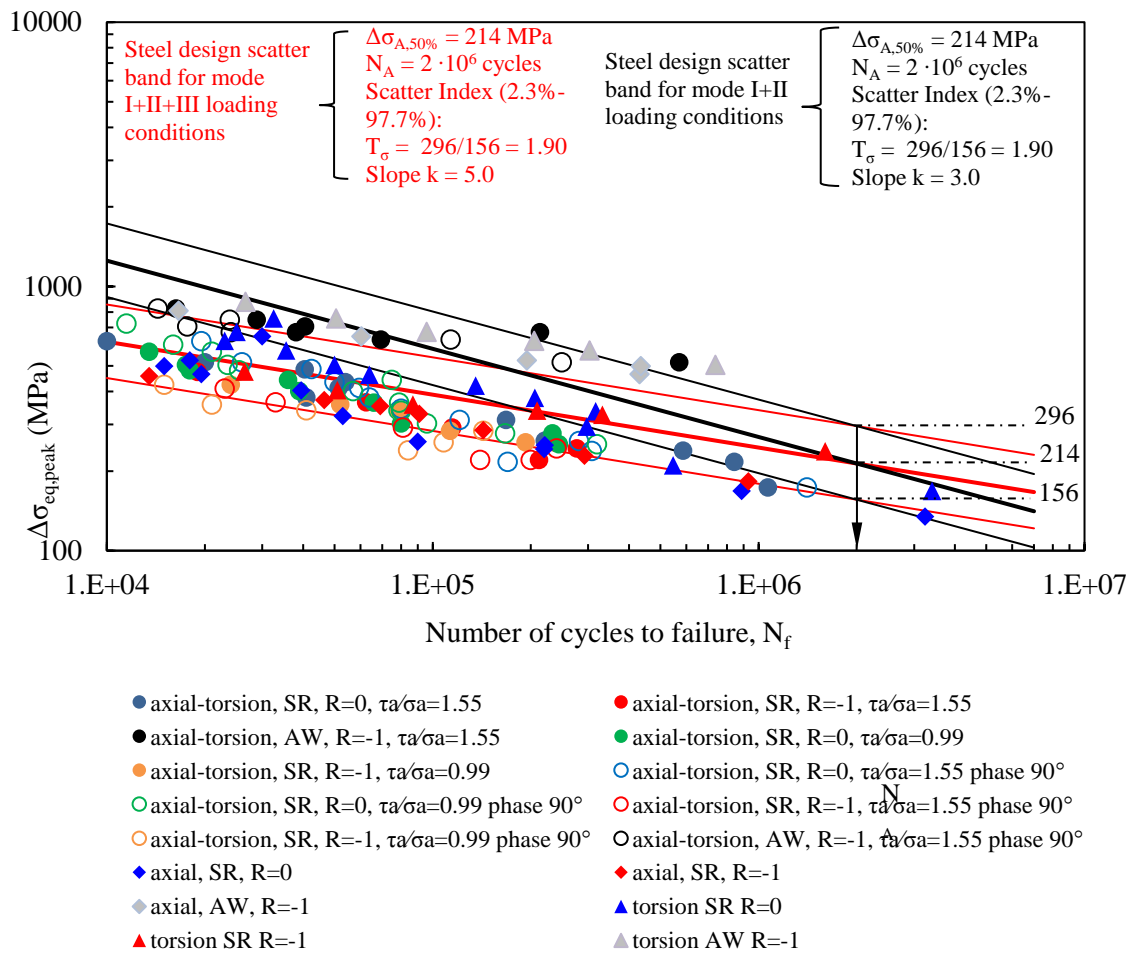


Figure A6: Comparison of the experimental data evaluated in terms of equivalent peak stress with the design scatter band: all loading cases.

Evaluation of experimental data in terms of $\sigma_{eq,peak}$ considering $\sigma_{mean,peak}$

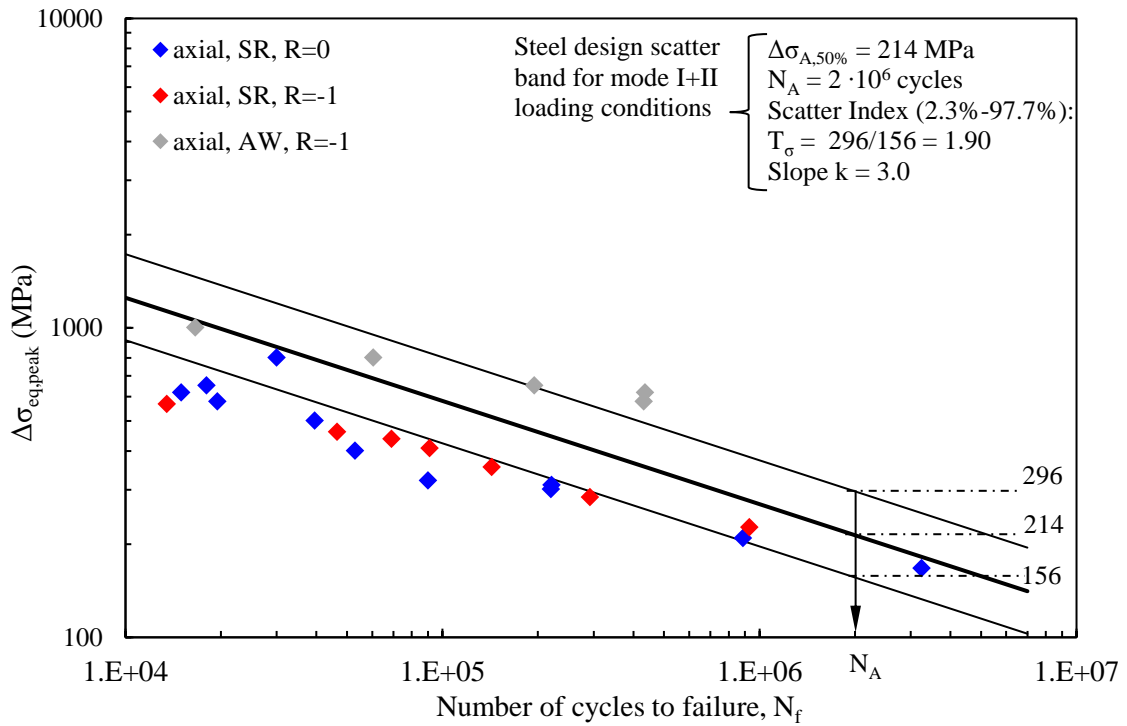


Figure A7: Comparison of the experimental data evaluated in terms of equivalent peak stress with the design scatter band: axial case.

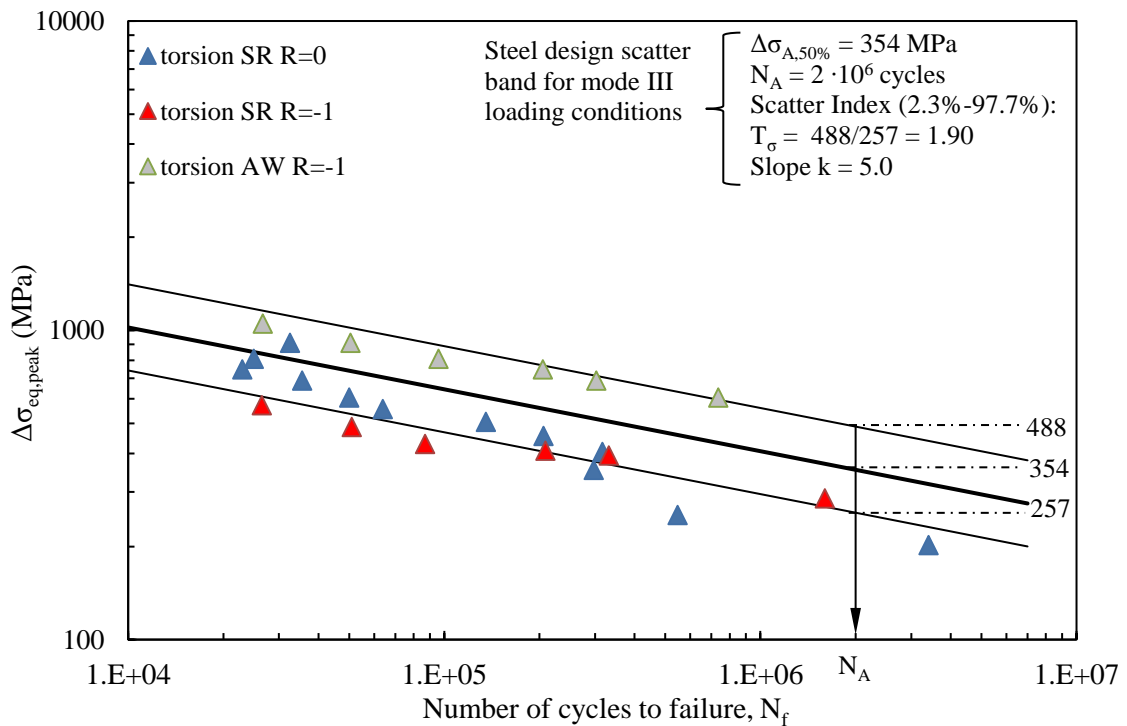


Figure A8: Comparison of the experimental data evaluated in terms of equivalent peak stress with the design scatter band: torsional case.

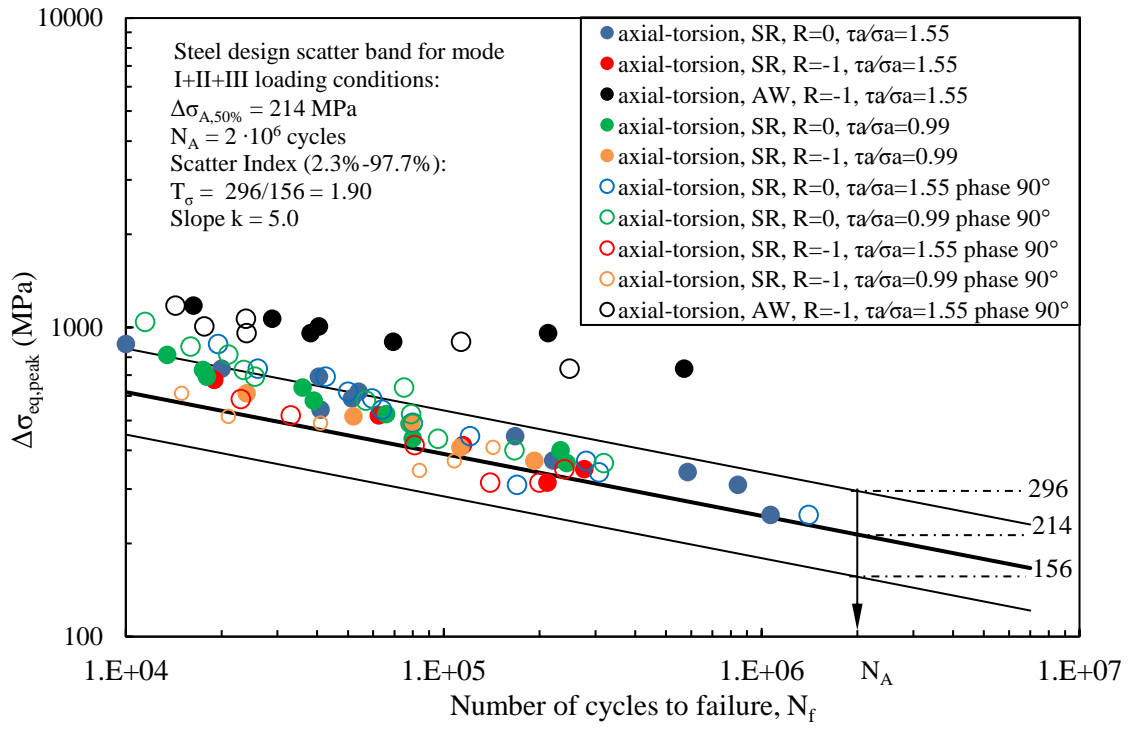


Figure A9: Comparison of the experimental data evaluated in terms of equivalent peak stress with the design scatter band: multiaxial case.

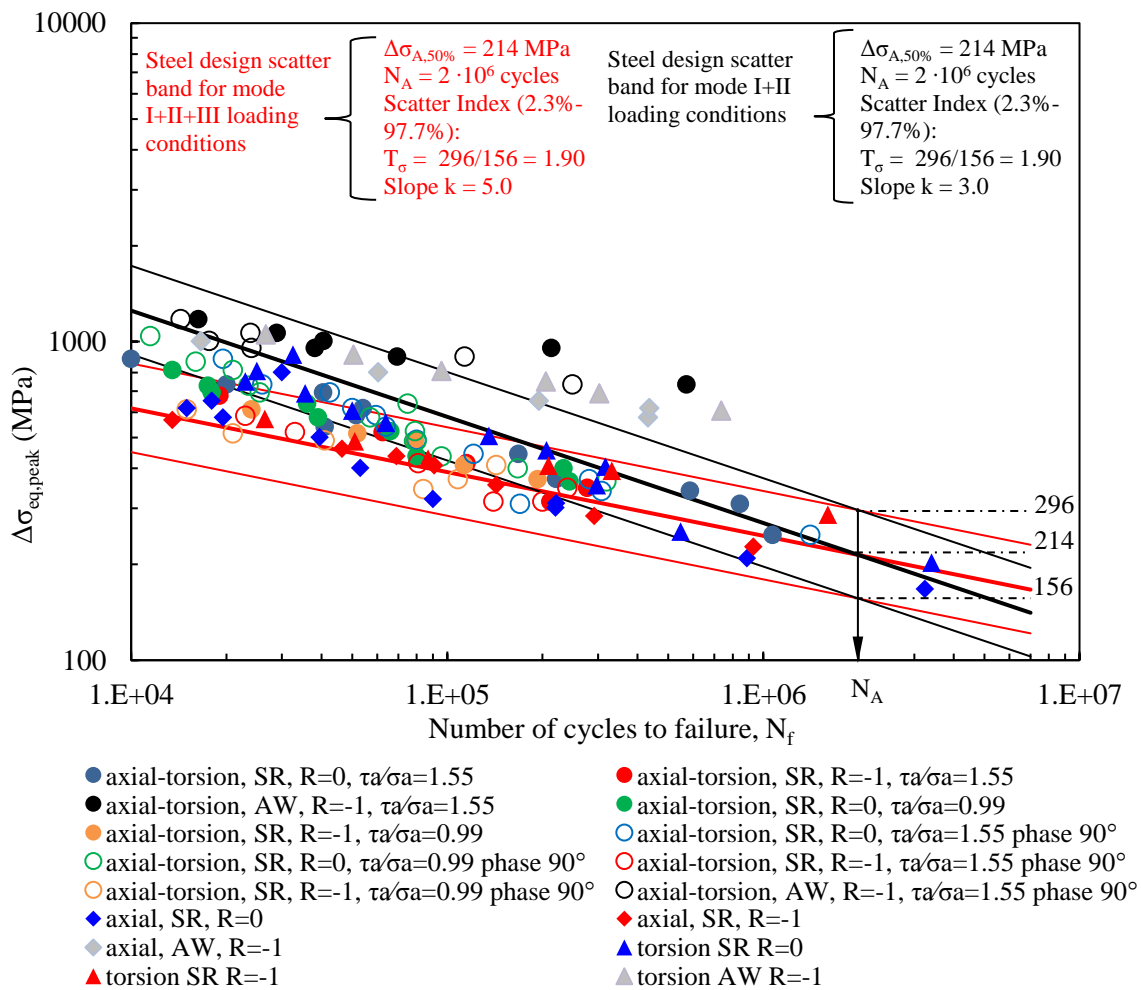


Figure A10: Comparison of the experimental data evaluated in terms of equivalent peak stress with the design scatter band: all loading cases.

Eventually, it could be interesting to compare the areas below the equivalent peak stress distributions with the one that would result considering constant values. In particular the area that would result below a constant $\sigma_{mean,peak}$ and $\sigma_{min,peak}$ within the half weld.

PURE AXIAL CASE		
Area below $\sigma_{eq,peak}$ [MPa * mm]	Area below $\sigma_{mean,peak}$ [MPa * mm]	Area below $\sigma_{min,peak}$ [MPa * mm]
62.13	62.70	51.82

Table A1: Comparison of the areas below the equivalent peak stress slope with the ones obtained considering constant values, axial case.

PURE TORSIONAL CASE		
Area below $\sigma_{eq,peak}$ [MPa * mm]	Area below $\sigma_{mean,peak}$ [MPa * mm]	Area below $\sigma_{min,peak}$ [MPa * mm]
68.70	68.68	57.07

Table A2: Comparison of the areas below the equivalent peak stress slope with the ones obtained considering constant values, torsional case.

From this comparison, it emerges that the constant stress distribution that seems to better represent the real equivalent peak stress distribution is the one obtained considering the mean value $\sigma_{mean,peak}$.

ACKNOWLEDGMENTS

First of all, I would like to express my gratitude to Professor Giovanni Meneghetti, who is able to share with the students his passion for the mechanical analysis. His commitment is present in every lecture and this makes a huge difference from a student point of view. It is truly worth listening every pronounced words because the logical order and the exemplification procedures are extremely useful to create a valuable knowledge.

Then, I would like to thank Alberto Campagnolo, who helped me in first person during the writing of this thesis. Together we face up a lot of problems, but with some patience and further investigations we have been able to come up with the ideas here presented. Without his help, it would have been impossible to finish this research project.

Therefore, a special acknowledgment is dedicated to my parents. They have always been present for me and they helped me during difficult situations supporting me in every way. My personal hope is not to disappoint them in any ways in the future, because they have done far more that what was expected from them.

Last but not the least, my sister, my relatives and all my friends that have been fundamental during my path towards the graduation. All the time spent together opened my mind and made me a better person. In fact, I am no longer a person afraid of changes but someone who want to challenge himself. All of this is due to the experiences we have shared together that allowed me to overcome my shyness, now only a memory.

Eventually, a final though goes to my girlfriend Alessandra who is giving me breath-taking experiences and I am starting to dream a bright future with her. She is not only standing by my side, but she has been able to understand me and making me feel happy like I have never been before.

